University of Cagliari

PhD in Physics

Multidisciplinary studies of pulsar data and applications to Pulsar Timinig Arrays

FIS/05

Tutor:

Prof. Nicoló d'Amico

Co-tutor:

Dr. Andrea Possenti

Coordinator:

Prof. Paolo Ruggerone

PhD Candidate:

Caterina Tiburzi

XXVII Cycle - Academic year 2013/2014

This Thesis was possible in virtue of the strong collaboration with some people who, in practice, acted as co-supervisors for me: in chronological order, Doctor Simon Johnston, Doctor Willem van Straten, Doctor George Hobbs, Doctor Stefan Osłowski.

I want to thank them and Doctor Andrea Possenti for everything they taught to me in these three years.

Contents

Introduction

Pulsars are fast-rotating, highly-magnetized neutron stars, a type of degenerated objects that are the leftovers from the collapse of the core of originally massive (10–25 Solar masses) stars. Pulsars are powered by their rotational kinetic energy, and their radio emission is collimated into one or two beams, which co-rotate with the pulsar: if the line-of-sight of an observer crosses the beam(s), a regular series of pulses is detected, at the pace of the pulsar rotational period. The stable rotation of the pulsars, combined with the possibility of measuring the times of arrival of their pulses with high precision (even less then 100 ns for some sources belonging to the class of the millisecond pulsars) opens the opportunity of constraining the astrometric, kinematics, rotational, orbital (when appropriate) and environmental parameters of a pulsar with high accuracy. In turn, the measurement of these parameters made a wide range of applications to flourish, such as: studies of the neutron star physics, equations of state of the dense matter and emission mechanisms, tests of general relativity, analysis of the properties of the Galaxy like its magnetic field and interstellar medium, pulsar population statistics and distribution. The general concepts about the pulsar physics, the pulsar emission, the effects produced by the interstellar medium, as well as some of the physical applications are summarized in Chapter 1.

Although, by using a procedure called *timing*, it has been possible to achieve exquisite precision in the determination of some pulsar parameters, the underlying emission mechanisms still remain obscure. Among the list of the still unsolved issues, there is the origin of pulsar polarization characteristics, including the presence of two polarized modes of emission. In Chapter 2, after a summary about the definition of the Stokes parameters, it is presented a literature review on the generalities of pulsar polarization, and on the polarized mode composition. We then extract the polarization parameters of a wide sample of pulsars, discovered in the context of the High Time Resolution Universe survey for pulsars and radio transients. We show as well how they can be used to study some properties of pulsars and of the Milky Way. In the second part of the Chapter we outline a new approach to classify the combination of the orthogonal polarized mode and its first application to real data. In the context of this study, we show how the commonly adopted way of subtraction of the noise budget to obtain the Stokes parameters is biased.

Among the surprising large basket of the applications of pulsar timing, and especially of high-precision pulsar timing, Chapter 1 focuses on one of the currently most important experiments in astronomy: the Pulsar Timing Arrays (PTAs). Relying on the very stable, clock-like signal of some millisecond pulsars, the first goal of the PTA experiments is the direct detection of an isotropic and stochastic gravitational wave background (GWB), generated by the summation of the gravitational wave emissions from numerous coalescing, high-redshift, super-massive black hole binaries. No GWB detection has been claimed so far. However, the PTA sensitivity increasing, and in the near future it will start probing the region of the strain versus GW frequency plot in which the aforementioned GWB is theoretically expected. In view of this, it is fundamental to build solid bases for running sanity checks on the data of any possible future detection, in order to state if the detection is genuine or not. In Chapter 3 we describe a study aimed to evaluate the impact, in the GW detection pipeline, due to correlated signals when are unrelated to GW. In particular errors in the clock time standards and in the planetary ephemeris in PTA experiments are investigated and possible mitigation routines proposed and tested. We first give an introduction about these effects and their expected angular correlations. We then outline the adopted method of study, that includes the usage of simulated ToA data sets affected by the selected effects and the tests of the mitigation routines. We next describe the obtained results, before and after the application of the mitigation routines, and the impact of the mentioned mitigation routines on the GWB detection sensitivity.

One of the main hypotheses behind the procedures of high precision timing and for the PTA activities is the stability of the monitored millisecond pulsar template profile. Although several studies (especially in the last years), have been carried out to characterize the short-term variability of the millisecond pulsar profiles, the long term decadal stability has never been systematically studied on a significant sample of objects. In Chapter 4 we test the long-term stability of 10 millisecond pulsar profiles. The data sets were obtained from a 15-year long timing campaign performed with the Effelsberg radio telescope with an unchanged combination of frontend and backend. We first review literature studies about short-term variability in pulsars, and the few cases of long-term ones. We then describe the data sets and the algorithm used to carry on the analyses. We then review the results, paying particular attention to the case of one of the analyzed millisecond pulsars whose profile shows an unexpected, clear temporal evolution.

Finally, we review our results and conclusions.

Chapter 1

Pulsars and Pulsar Timing Arrays

Pulsars are fast rotating, highly magnetized neutron stars which emit radiation in a vast range of frequencies across the electromagnetic spectrum. Although the bulk of this radiation occurs in the high energies (gamma and X-rays), the vast majority of the known pulsars are visible only at radio wavelengths. In a simplified and certainly incomplete representation, beams of radio emission are radiated or from the surroundings of the pulsar magnetic poles or from regions of the pulsar magnetosphere close to what we call "light-cylinder", or from regions close the the last closed line of the pulsar magnetic field. In all cases the emission zone(s) corotate with the star. Therefore, if the rotational and magnetic axes are misaligned, the radio beams sweep the space: when the line-of-sight of an observer crosses one of the beams, at each pulsar rotation the observer receives a bunch of radio waves, which appear as a radio "pulse" (this phenomenon is called "lighthouse effect"). The period of repetition of this pulsating signal coincides with the pulsar spin period.

Besides being very interesting cosmic objects *per sé*, pulsars are invaluable tools to perform a great number of experiments which exploits the Cosmos as a Physics Laboratory. This PhD thesis mainly focuses on their use as cosmic clocks, because of the very high degree of precision that it is possible to achieve in predicting the time-of-arrival of the aforementioned packets of radio waves, at least for a subgroup of pulsars. This property is one of the reasons behind the setting up of one of the major projects in nowadays pulsar astronomy, the Pulsar Timing Arrays, the main aim of which being the direct detection of gravitational waves of very low frequency, typically in the nanohertz regime.

1.1 Pulsar generality

In this section, we summarize the basic properties of pulsars and of their signals, using Lorimer and Kramer 2005, Lorimer 2008 and Salaris and Cassisi 2005 as references, when not otherwise indicated. Details and specific discussion on some of these subjects are then presented in the subsequent Chapters.

1.1.1 Progenitors

Neutron stars are the final stage in the evolution of stars with an initial mass between about 11 and about 25 $M_\odot$. In these stars, the end of the spontaneous thermonuclear activities leaves a degenerate nucleus of Fe^{56}, supported by the pressure generated by free, degenerate electrons. Temperature and pressure conditions in the nucleus, however, trigger the electron depletion via a reaction with protons that generate neutrons and neutrinos. As a consequence, while most of the mass of the evolved star is expelled, the nucleus undergoes a gravitational collapse, that is arrested by the degeneration of the neutrons. The new contribution to the total, outward pressure, due to the degenerate neutrons, allows the stellar nucleus to find an equilibrium as a compact object mainly made of degenerate neutrons, and having a typical radius, mass and density of about 10 km, 1.4 $M_\odot$and 10^{14} g/cm^3, respectively. This new self gravitating structure in hydrostatic equilibrium is what we call a *neutron star*.

Although the details of the collapse of the nucleus are not yet completely understood, heuristic considerations based on angular momentum and magnetic flux conservations during the nucleus collapse lead to account for the facts that the new born neutron stars are characterized by extremely rapid rotational periods (between few milliseconds and tens of seconds) and by the highest magnetic fields ever measured in any astrophysical objects (between 10^8 and 10^{15} Gauss).

To date, about 2400 pulsars are known. The observational bias due to pulsar intrinsic weakness and distance causes an apparent source clustering around the Solar System. However, there is no reason to believe that pulsars are not spread all over the Milky Way and present in other galaxies. The estimate is that the number of Galactic pulsars is at least an order of magnitude greater then the currently known pulsar population. At first approximation the birthrate of the radio pulsars appears also compatible with the rate of occurrence of their supernova progenitors.

1.1.2 Emission & Energetics

Pulsars were discovered in 1968 by J. Bell (Hewish et al., 1968). These objects were firstly interpreted as oscillating white dwarves, and only eventually as fast-rotating and highly-magnetized neutron stars. Shortly after that, the discovery of a radio pulsar in the Crab nebula also established the connection between the pulsar birth and the supernova explosion.

Pulsar magnetic field is dipolar at the first order. The corotation of the magnetic field with the rapidly spinning pulsar body generates an extraordinarily intense electric field at the star surface, that largely exceeds the neutron star gravitational attraction and can extract charged particles from the surface itself. The charged particles form a plasma, called magnetosphere, surrounding the pulsar, part of which (the one permeated by the closed field lines of the magnetic field, and thus also known as *closed magnetosphere*) is corotating with the star as well. The processes triggering the emission of radio waves, high energy photons and charged particles are thought to mostly occur somewhere in the *open magnetosphere* (where the lines of force of the magnetic field, to which the magnetospheric plasma is attached, cannot be closed for not violating causality) or at the border between the open and the closed magnetosphere.

Remarkable progresses have been obtained in recent years in the interpretation of the process of emission of the gamma-rays from the pulsar, mostly thanks to the observations of last generation gamma-ray satellites, like *Fermi* and *AGILE*. However, after more than 40 years of attempts, a coherent picture for the pulsar emission mechanism at the radio wavelengths is still lacking and several competing models have been proposed, calling for various possible regions of the pulsar magnetosphere from where the radio-waves are finally released. Among the reasons for the difficulties in the modeling of the radio emission, it is possible to mention the tiny fraction of energy emitted in the radio band with respect to the gamma-ray and X-ray bands, as well as the coherent nature of the radio emission (having brightness temperature of order $10^{26} - 10^{34}$ K), which contrasts the simpler incoherent emission mechanisms invoked for the gamma-ray and X-ray bands.

Despite the unsolved uncertainties on the detailed emission mechanisms across the electromagnetic spectrum, the global energetics of pulsars, and neutron stars in general, is well known. In particular, their energy reservoir is represented by their own rotational kinetic energy and the emission of radiation over a broad range of frequencies (as well as the acceleration of charged particles) are both associated with a spin-down of the neutron star.

In fact, pulsar observations extended over a long enough timespan show that pulsar period P tends to slow down with time. If we assume that the pulsar slow-down (represented by the pulsar spin period derivative $\dot{P}$) is completely driven by the kinetic energy radiated by the pulsar, we can compute the total energy loss simply as $\dot{E} = 4\pi^2 I\dot{P}P^{-3}$, where I is the moment of inertia of the neutron star. Also assuming that the energy is released according to that of a rotating magnetic dipole in vacuum (i.e. the Larmour formula), some other useful quantities can be derived, such as the pulsar spin-down (or characteristic) age $\tau = P/(2\dot{P})$, and the magnetic field strength at the surface $B_s = 3.2 \times 10^{19}\sqrt{P\dot{P}}$ G, where the following reference values for the moment of inertia, the radius and the mass of the neutron star have been assumed: $I = 10^{45}$ g cm^2, $R = 10^6$ cm and $M = 1.4\ M_\odot$. We stress that the hypotheses used to compute these quantities certainly are not fully accounting for the complex pulsar emission processes and thus these parameters are only to be considered as illustrative of the underlying physics of the neutron stars. However, they are also very useful for a first order classification of the various categories of pulsars.

1.1.3 Profile phenomenology

A relatively small number of pulsars has sufficiently high flux densities to distinguish the individual pulses with respect to the background noise. Detailed studies of these single pulses show that they are extremely variable in shape, brightness and polarization.

In general, however, pulsar flux densities are too faint to allow the identification of individual pulses. In fact, pulsars are a population of in general weak radio sources, characterized by a median value of the mean flux density at 1.4 GHz of about 0.47 mJy (computation based on the Australian Telescope National Facilities - ATNF - public pulsar catalogue[1]). For this reason, the flux density of a single pulse from one of these objects often does not exceed the intrinsic noise of the detection system, making a direct detection impossible. It is then usually necessary to coherently add up to few hundreds or few thousands (depending on the specific pulsar) of the single pulses in order to clearly detect and then to study the pulsar signal. Such a process, called *folding*, produces an *integrated light curve* of the flux from the pulsar with respect to its rotational phase, called *pulse profile*.

While the single pulses are highly variable, an integrated profile appears stable in time at a fixed observing frequency, i.e., it does not usually undergo significant temporal changes over the timespan of interest for the specific experiment. This amazing characteristic has made pulsars extremely valuable tools for a large number of physical applications. However, in view of the new experiments planned in the context of the Pulsar Timing Arrays (see later on in this Chapter) it is important to carefully revisit and/or put limits to this assumption in the case of ultra long data-spans. This is the aim of one of the investigations performed in this Thesis.

Pulse profile shape is pulsar-specific: once stabilized thanks to the coherent addition of several single pulses, pulse profiles of different pulsars are different as well, although they can share some common characteristics and can be divided into classes depending on the number of pulse components. Moreover, although being statistically stable at a fixed observing wavelength, the pulse profiles often present dramatic variations with frequency: typically, they are wider at lower frequencies and narrower at higher frequencies, and the profile component number, as well as the polarization characteristics of the various components, can vary with the frequency. In fact, pulsars are also among the most polarized objects known in the radio sky. Although integrated profiles are

---

[1] http://www.atnf.csiro.au/people/pulsar/psrcat/

usually less polarized then the single pulses, the degree of linear polarization can reach up to 100% in the youngest sources, and averages around 20% in the oldest.

As reported in the previous subsection, a satisfactorily and comprehensive physical picture of the mechanism(s) of radio emission from the pulsars is still lacking. As a consequence the vast phenomenology associated with the pulsar profiles is usually interpreted in term of heuristic and/or phenomenological models. For instance, the shape of the profiles can be explained according to the pulsar-specific distribution of the radio emission regions within the radio beams which are cut at every pulsar rotation by the line-of-sight to the observer (e.g. Lyne and Manchester 1988; Rankin 1993). As to the frequency evolution of the widths of the profiles, a simple phenomenological model, the radius-to-frequency mapping (RFM) model (Cordes, 1978), assumes that the border of the emission cone are given by the last open magnetic field line in the pulsar magnetosphere and then calls for the fact that low radio frequencies are emitted at higher altitudes, thus implying a wider emission cone, with respect to the higher frequencies. Also, the Rotating Vector Model (RVM) aims to account for the S-shaped trend shown by the polarization position angle across a pulsar profile (Radhakrishnan and Cooke, 1969). Despite various improvements over the years, these and other models are still hardly capable of capturing all the phenomenology and can still be regarded only as first approximation guidelines for orienteering in the large complexity and variety shown by the catalogue of the pulsar profiles.

1.1.4 The effects of the Interstellar Medium

The pulsar signal has to cross the interstellar medium (ISM, from few tens of parsecs up to few tens thousand parsecs, depending on the pulsar distance), before reaching the observer. The ISM exerts a variety of actions on the pulsar radiation, the most evident of which is the frequency dispersion of the broad band electromagnetic waves associated to each pulse. In particular, radiation at lower frequencies is delayed with respect to radiation at higher frequencies. This dispersion of the broadband radiation can be corrected applying a procedure which is called de-dispersion of the signal. This is based on the knowledge of a physical quantity, the *dispersion measure* (DM), which represents the equivalent electron column density along the source line of sight and is computed as a path-integral:

$$\mathrm{DM} = \int_0^d n_e(l) dl \tag{1.1}$$

where d is the source distance with respect to the Earth and n_e is the electron density along the path leading from the source to the observer. Two kinds of de-dispersion can be adopted: (i) the *in-coherent* de-dispersion, in which the pulsar signal is independently detected in a large number of frequency channels in which the entire observing band is split, and then suitable time delays (calculated on the basis of the value of DM) are applied to the channels in order to shift the pulses in all the channels at a fixed rotational phase; (ii) the *coherent* de-dispersion, in which the observing bandwidth is converted to base-band and Nyquist sampled, then the whole data are transformed by applying a transfer function (built on the basis of the value of DM) which mirrors, but with an opposite effect, the dispersion experienced by the radio signal in its traveling across the ISM. At this point the data have ideally gained immunity from the effect of the dispersion and can be folded with no loss of information. Although much more computationally demanding, the second approach leads to the best results in getting rid of the dispersive effects of the ISM and in general allows one to obtain smaller uncertainties (than the in-coherent method) when determining the time of arrival of the pulses (see below the section devoted to the timing procedure).

Other ISM effects on the pulsar emission occur as a consequence of the fact that the medium is not uniform: interstellar scattering and scintillation.

Interstellar scattering happens when inhomogeneities in the ISM modify the optical path of part of the waves, in dependence of the wave frequency and the local amount of variation in the free electron density at the site of the inhomogeneities. This effect translates into a delay for part of the signal, whose effect is to introduce a one-sided exponential tail in the pulse profile.

Interstellar scintillation is given by constructive or disruptive interference between the delayed waves in a train. These interactions induce an enhancement or a decrement of the pulsar flux. Scintillation is as more dramatic as closer is the pulsar to the Earth, whereas, along larger distances, the flux fluctuations induced by the interstellar scintillation are averaged and thus significantly neutralized.

In presence of a magnetic field, the ionized component of the ISM also changes the plane of polarization of linearly polarized incoming radio waves, realizing a rotation of the plane itself. This phenomenon, called *Faraday rotation*, has larger effects at longer wavelengths, according to the formula:

$$\psi(\lambda) = \psi_\infty + \mathrm{RM}\lambda^2 \tag{1.2}$$

where ψ is the polarization angle in radians observed at the wavelength λ and ψ_∞ is the polarization angle at a supposedly infinite frequency. The quantity RM, acronym for *Rotation Measure*, is pulsar-specific and can be determined by observing ψ at two different wavelengths. On a theoretical side, RM results from a path-integral involving both the equivalent free electron density and the component of the ISM magnetic field along the line of sight (usually indicated as the parallel component $B_\parallel$):

$$\mathrm{RM} = \frac{e^3}{2\pi m_e^2 c^4}\int_0^d n_e(l)B_\parallel(l)dl \tag{1.3}$$

where e is the electron charge and m_e the electron mass.

1.1.5 Millisecond pulsars

The inspection of the $P - \dot{P}$ *diagram* (i.e. the diagram reporting the values of the spin period and of the spin period derivative for the known pulsars, see Figure 1.1) represents a very useful tool for the classification of these objects, as well as for describing their evolution.

The bulk of the known pulsar population has a spin period and spin period derivative larger then, respectively, 0.1 s and 10^{-17} s/s. These sources have been identified as *ordinary* pulsars. As pulsar spin period is observed to increase because of the radiated rotational kinetic energy, it is reasonable to deduce that among them, the *young pulsars* are characterized by the smallest spin periods, and older pulsars by the longest. It is possible to notice from the

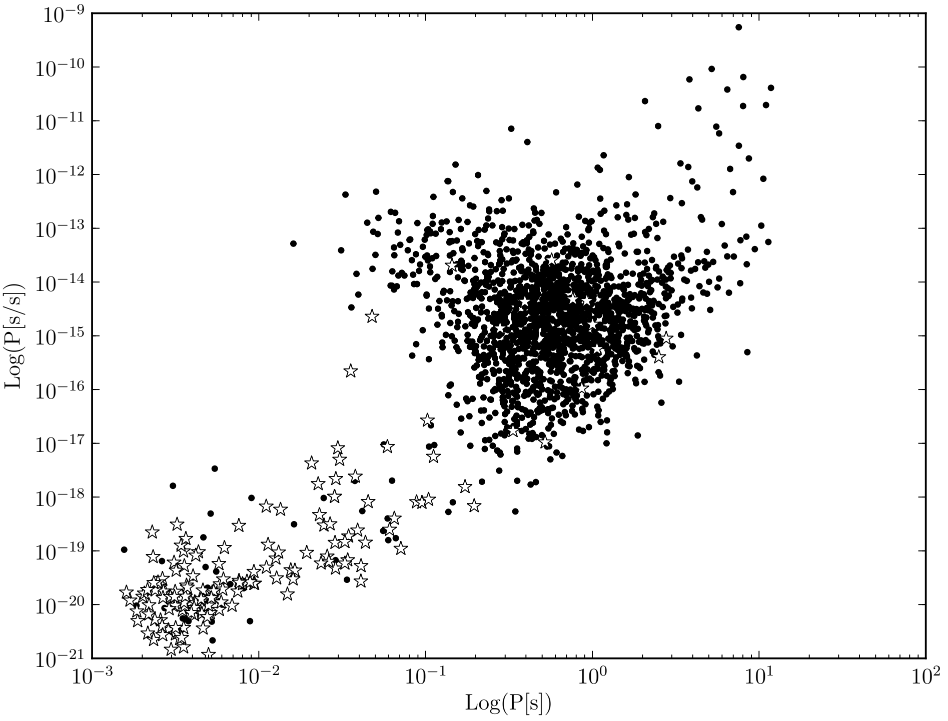

Figure 1.1: On the x and y axes are reported, respectively, spin period and spin period derivative. Black dots indicate isolated pulsars, white-filled stars indicate pulsars included in binary systems. The diagram includes 2031 objects and results from the data of the ATNF public pulsar catalogue on at the 5th of December, 2014. Few hundreds additional pulsars are known, but the values of their $\dot{P}$ has not been determined and/or published yet and therefore they cannot appear in the plot to date.

diagram that the vast majority of these ordinary pulsars are isolated objects.

A pulsar minority, however, presents extremely rapid spin periods, of the order of the milliseconds, and smaller spin period derivatives (between 10^{-18} and 10^{-21} s/s) than the ordinary pulsars. Moreover, pulsars included in this subgroup are very often included in binary systems. They are associated with a distinct population of neutron stars and are called *millisecond pulsars*.

The current paradigm (supported by a growing body of observational facts, see for example Alpar et al. 1982; Bhattacharya and van den Heuvel 1991; Papitto et al. 2013) is that we identify millisecond pulsars as pulsars that have been spun up by the accretion of mass and angular momentum from a companion star in a binary system. In view of that, and in spite of their rapid spin, they are not young neutron stars. On the contrary, it is likely that many millisecond pulsars are even extremely old sources, of age comparable to that of the Galaxy, and whose physical parameters and radiation activity received a refurbishment thanks to the aforementioned mass and angular momentum transfer.

Given the significantly higher spin rate with respect to that of the ordinary pulsars, the typical size of the light cylinder for the millisecond pulsars is much smaller and their magnetosphere is expected to be more compact with respect to that of the ordinary pulsars (Xilouris et al., 1998). As for their emission properties, millisecond pulsars show pulse profile shapes that, as a population, are similar to normal pulsars (Kramer et al., 1998). However, in average they are usually less luminous than normal pulsars (e.g. Lorimer et al. 2007), with isolated millisecond pulsars weaker than the ones included in binary systems (e.g. Burgay et al. 2013 and reference therein). Millisecond pulsar profiles show smaller evolution with the observing frequency with respect to the ordinary pulsars, although they present a similar degree of depolarization at high frequencies (Kramer et al., 1999a) and, apparently, wider emission beams. In any case, as for the case of the ordinary pulsars, the phenomenology is very ample, and the profile characteristics, as well as the polarization features, of each millisecond pulsar must be investigated on a one-by-one basis.

1.2 Pulsar timing procedure

Each pulsar is associated to a series of physical parameters, overall referred under the name of *ephemeris*: according to their physical meaning, they can be grouped in various categories: i.e. the rotational parameters (the spin period, and a certain number of spin period derivatives), the positional and kinematics parameters (i.e. the celestial coordinates right ascension and declination, plus the proper motion and, when measurable, the trigonometric parallax), the parameters linked with the effects of the interstellar medium (the DM and its times derivatives and the RM), plus the orbital parameters (classical and relativistic) when the pulsar is included in a binary system. The exact number of the measurable parameters depend on a variety of factors, ranging from some intrinsic properties of the pulsar (e.g. the brightness of its signal, the shape of the pulse profile, the rotational stability of the neutron star, the environment of the pulsar), to the sensitivity of the used radio telescope and to the capabilities of the data acquisition system, as well as the rate and duration of the performed observations.

Typically, at the time of the discovery only 4 parameters are roughly known: the spin period the DM, and the celestial coordinates, the latter with an uncertainty which is of the order of the primary beam of the telescope which led to the discovery. These parameters, as well as the additional ones mentioned above, can later be determined with increasing precision thanks to a process called *pulsar timing*. This analysis is based on measuring the time-of-arrival (ToA) of the pulses that a pulsar emits at every rotation to the telescope and then modeling them by including the minimum suitable number of parameters, which are usually chosen in the list above. Once a model satisfactorily reproduces the already collected ToAs, one says that the adopted model and the associated ephemeris represent a coherent timing solution for the pulsar: in other words, all the pulsar rotations since the beginning of the data-span can be accounted for if using the computed model. However, pulsar timing is an iterative and in principle never-ending procedure, in which new ToAs are always checked against the temporarily valid ephemeris and the latter are improved for better reproducing the extended dataset and thus increasing the predictive capabilities of the model.

We usually measure ToAs from the integrated profiles. This is mainly due to two reasons: the intrinsic weakness of the pulsars as radio sources, and the extreme variability (in shape, flux, polarization etc.) that characterizes the pulsar individual pulses. An integrated profile $\mathcal{P}$ is obtained folding an observation that begins at a certain time t_i. The ToA associated to $\mathcal{P}$ is measured with respect to a fiducial point of the pulsar flux profile. Once the fiducial point is chosen, a ToA is properly measured by cross-correlating $\mathcal{P}$ with a *template profile* $\mathcal{T}$. The latter is a high signal-to-noise (S/N) profile, obtained through a coherent addition of numerous integrated profiles, and it is thus assumed to be absolutely stable. Each integrated profile $\mathcal{P}$ can be written as:

$$\mathcal{P}(t) = a + b\mathcal{T}(t - \tau) + \mathcal{N}(t) \tag{1.4}$$

where a is a flux offset, b is a rescaling factor, τ is the time shift between $\mathcal{P}$ and $\mathcal{T}$ and $\mathcal{N}$ is the instrumental and sky noise contributions. The ToA associated to $\mathcal{P}$ can then be computed as:

$$\text{ToA} = t_i + \tau \tag{1.5}$$

The measurement of a ToA take place at the telescope site. This is suboptimal, mainly because the Earth is a non-inertial reference frame. Thus the ToAs must undergo a process of baricentrization, in order to go from *topocentric ToAs*, measured on the Earth at the site of the radio telescope, to the barycentric ToAs, measured at the Solar System barycenter (SSB). This conversion has the additional advantage that all the ToAs measured from different sites on the Earth can be easily compared. The conversion from topocentric ToAs (t_t) to barycentric (t_b) requires the introduction of several correction addenda:

$$t_b = t_t + t_{time} - \frac{d \times \text{DM}}{c^2} + \Delta_R + \Delta_S + \Delta_E \tag{1.6}$$

Element t_{time} include the conversion to get from the local time at the the telescope site to the time of a reference frame comoving to the SSB (Barycenter Coordinate Time, TCB). At first, the local time at the telescope is converted to a time standard referred to the Earth geoid, the *Terrestrial Time* (TT). TT is achieved through the combination of the atomic clocks distributed from several world-spread countries. These atomic clocks are used to produce the International Atomic Clock (TAI) by the Bureau International des Poids et Mesures (BIPM), as well as a version of the TT called TT(TAI). However, as TAI never undergoes corrections once it is published, BIPM also provides yearly corrections to it, and new versions of the TT are thus produced: TT(BIPM2011), TT(BIPM2012), TT(BIPM2013) etc. The latest version of TT is thus converted into the TCB.

Element $(d \times \mathrm{DM})/c^2$ corrects for the delay with respect to an infinite frequency given by the dispersion in the ISM.

Elements Δ_R, Δ_S, Δ_E - respectively Roemer, Shapiro and Einstein delays - actually operate the conversion of the ToAs from the telescope to the SSB. In particular, Δ_R takes into account the light travel time between the telescope site and the SSB position. Δ_S corrects for the space curvature induced by Solar System bodies, while Δ_E applies the time dilation corrections for the Earth motion and the gravitational redshift caused by the Solar System bodies as well. Δ_S and Δ_E are relativistic terms.
To compute the last three elements it is clearly necessary to have extremely precise information about the SSB position, and the Solar System objects positions, trajectories and masses. The most used planetary ephemeris are the Development Ephemeris (DE), regularly released by the NASA's Jet Propulsion Laboratory, indicated with crescent numerical indexes: DE404, DE414, DE421 etc. Other planetary ephemeris are released by the Integrateur Numérique Planétaire de l'Observatoire de Paris (INPOP) and by the Institute of Applied Astronomy (IAA) of the Russian Academy of Science (RAS).

As mentioned at the beginning of this Section, every pulsar is characterized by an ensemble of parameters, its ephemeris. We usually assess the achieved quality factor for each ephemeris set by analyzing the trend of the residuals versus the epoch of the various observations, obtained from the comparison between the predicted ToAs (on the basis of the known ephemeris) and the observed ToAs. An ephemeris set is considered good when the series of the residuals mentioned above (often referred to as *timing residuals*) do not show any recognizable structure and has a small value of the root-mean-square (rms.). In this case, we commonly say that the residuals are *white*, with a reference to the corresponding nature of their power spectrum.

When one of the ephemeris parameters is poorly determined, it generates recognizable features in the timing residuals: an error in the pulsar spin period and spin period derivative would produce, respectively, a linear and a quadratic trend, an error in the pulsar position generates a sinusoidal trend with an yearly period, etc. It is possible to correct for the errors in the ephemeris parameters via the timing procedure. As anticipated, this includes the iterative linear fit of the residuals for the presumably wrong parameters until the spurious "structures" are neutralized and the parameters are corrected. This procedure seems simple in principle, but it encounters several issues in the concrete application. Firstly, some timing parameters are covariant. This means that even if the residuals look white at the end of the timing procedure, the ephemeris parameters could have been wrongly inferred. Secondly, as we usually perform a linear fit of the residuals we need to guarantee that the post-fit timing residuals are white, otherwise we have to supply a thorough description of the post-fit noise in order to ensure a correct measurement of the parameters' uncertainties (these descriptions are commonly called *noise models*). This is linked with another issue. The majority of pulsars, in particular the young sources, are affected by what we call *timing noise*: a source of features in the residuals that cannot be ascribed to any error in the ephemeris parameters and shows a power spectrum with amplitudes typically increasing towards low frequencies. Timing noise possibly reflects irregularities in the pulsar rotation, inhomogeneities in the ISM, errors in the data manipulation, etc. The study of timing noise grew significantly in the last years, and its thorough description is extremely important in the context of the experiments that involve high-precision pulsar timing.

Under the fundamental assumption - which is commonly adopted - that the radio emission beams are strongly coupled with the underlying rotating neutron star, the cadence of the crossings between the emission beams and the line-of-sight exactly maps the rotational behavior of the star. It results that, as a population, millisecond pulsars are much more stable rotators than the ordinary pulsars. As a matter of fact, they are much less prone to rotational irregularities, like glitches (i.e. a sudden increase in the neutron star spin frequency, likely related to a re-adjustment in the internal structure of the star) and/or the aforementioned timing noise, which on the contrary can affect the ordinary pulsar population. This is commonly ascribed to their being associated to old neutron stars, which had enough time for their interiors to relax. In view of that, and of the much higher spin rate of millisecond pulsars with respect to ordinary pulsars (implying much shorter radio pulses and hence a potentially much better determinations of the time of arrival of the pulses themselves), the former are, as a population, much better *timers* (i.e. clocks) than the ordinary pulsars. In term of the quality of the timing residuals, one can simply state that, in general, millisecond pulsars are characterized by a significantly smaller rms in the timing residuals than the ordinary pulsars.

1.3 Pulsars as detectors of gravitational waves

Einstein theory of general relativity (Einstein, 1916) affirms that a biunivocal link exists between mass and space curvature: space curvature is defined by the mass potential, and mass traveling paths are constrained by the space curvature itself. In particular, general relativity predicts the existence of *gravitational waves*. Gravitational waves are time-dependent deformations of the space-time. Once sufficiently far away from any source of space-time curvature (that is, in the linear, Minkowskian space), and in the extremely reasonable hypothesis that the perturbation of the space-time itself that they induce is small, it can be demonstrated that they propagate at the light speed as transversal quadrupole waves. Gravitational waves have never been directly detected. However, their presence was indirectly assessed firstly thanks to the measurement of the orbital decay occurring in the relativistic double neutron star binary of Hulse and Taylor (Hulse and Taylor, 1975), that follows with very high precision the rate predicted assuming the existence of gravitational radiation. More recently, the measurements of the orbital decay in the Double Pulsar (Burgay et al., 2003; Lyne et al., 2004; Kramer et al., 2006) led to an even more constraining validation of the predictions of the Einstein theory.

For the principles of mass and momentum (corresponding to the monopole and dipole moments) conservation, the lowest moment the time-variation of which can induce the production of gravitational waves is the quadrupole moment. Higher moments too can generate gravitational waves, but their intensities would be extremely lower. In Astrophysics, the most likely sources of gravitational waves are thus those that, during their evolution, break the constancy of the quadrupole moment as, for example, the binary systems. The amplitude of a gravitational wave can be represented by the fractional distortion that it induces in the crossed time-space called *strain*, h. Assuming a binary system of equally massive stars in a circular orbit, the strain of the generated gravitational wave increases with the power $5/3$ of the mass of the stars and with the power $2/3$ of the orbital frequency and linearly decreases with the distance of the system to the observer. That is, the more massive and the faster are the bodies in the binary system and the closer is the system itself to the Earth, the higher is the gravitational wave strain. However, the order of magnitude of the constants in the formula that defines the strain h is about 10^{-54} (cgs). This means that even with extremely massive stars that can reach very tight orbits (thus we speak of compact objects), the strain of the produced gravitational waves is tiny. Concerning the frequency of the emitted gravitational waves, it is twice the orbital frequency itself. To give a reference example, if we assume a coalescing binary system that is made of two supermassive black holes with a mass of 10^9 $M_\odot$located at a distance of 1 Gpc and having a coalescent time shorter than a Hubble time, the frequency range of the emitted gravitational waves is included approximately between 10^{-6} and 10^{-10} Hz, and the strain amplitude between 10^{-14} and 10^{-17} (Jaffe and Backer, 2003; Sesana et al., 2009; Sesana, 2013). We stress that due to the slow inspiraling of such a kind of sources, the generated gravitational waves can be considered monochromatic.

Since their discovery, pulsars unique characteristics made them amazing tools that can be used to explore several fields of Physics. Given their extreme conditions of degenerate matter and gravitational field associated to these objects, they are laboratories to constrain the equation of state of the superdense nuclear matter and to test strong-field gravity. They are used to probe the Milky Way structure, the ISM density, magnetism and turbulence, as well as to understand binary star evolution and globular cluster dynamics (Cordes et al., 2004; Kramer, 2004; Lorimer and Kramer, 2005). Beyond, and on top of all the aforementioned applications, the last years saw the exponential development of a Nobel-prize class experiment, called *Pulsar Timing Arrays*, that exploits the amazing rotational stability and clock-like behavior of pulsars, and in particular of the millisecond pulsars, to search for a direct detection of the gravitational waves.

1.3.1 The basics concepts and practicabilities of the Pulsar Timing Array experiments

The effect of the passage of a gravitational wave (GW) in the space-time among a pulsar and an observer is a periodic quadrupolar deformation of the space-time, whose fractional amount given by the strain amplitude of the gravitational wave itself. Since radio pulses travel along geodesics in the space-time, the space-time distortions leave a signature in the observed ToAs from a millisecond pulsar. If the GW sources were powerful and close enough to the Milky Way, the aforementioned signature would be easily detectable even when performing ordinary timing observations of a particularly stable millisecond pulsar. As a rule-of-thumb, and in absence of other effects/biases, timing observations repeated along a timespan T_{span} of a millisecond pulsar having a typical ToA uncertainty σ_{ToA} could unveil a GW characterized by a dimensionless strain $h(f_{gw})$ at the frequency $f_{gw} \sim 1/T_{span}$ if $\sigma_{ToA}/T_{span} < h(f_{gw})$. As an example, the existence of a supermassive black hole (SMBH) binary in a short period orbit, that had been claimed in 2003 to be hosted in the radio galaxy 3C66, located at a redshift $z = 0.02$ (Sudou et al., 2003), was soon excluded at 95% confidence level, simply by looking at the timing residuals of the observations of the millisecond pulsar PSR B1855+09 (Jenet et al., 2004). In fact, the ripples in the space-time caused by the claimed GW source would have left clearly visible trends (with an amplitude of order 5 μs and a period of $\sim$ 1 year) in the timing residual, which on the contrary appeared to be flat, once a standard model for the pulsar rotation (i.e. a model which did not account for any by-passing GW) was applied and fit to the data.

However, it appears very unlikely to have a strong emitter of GWs at a frequency f_{gw} detectable via the timing residual analysis of an individual pulsar (i.e. typically $f_{gw};<;10^{-7}$ Hz, see below) that is also located in the surroundings of our Galaxy. What is much more probable is that any GW signal in that frequency range will be very weak: hence, the signature left in the timing residuals will be marginal. In this case, it becomes extremely difficult to achieve an unambiguous detection of a GW by using the data only from one pulsar, also because of the difficulties in perfectly accounting for other effects (e.g. timing noise, errors in the reference clock(s), uncertainties in the Solar System ephemeris needed for barycentering the ToAs) which could be intrinsically related to the given pulsar, or for the ISM traveled by the radio pulses, or for the instrumentation used to collect and/or model the data.

Most of these problems can be alleviated by studying an *ensemble* of millisecond pulsars, located at different positions in the sky. In fact, since a by-passing gravitational wave would affect the entire space-time surrounding the Earth, it is expected that the signatures imprinted in the ToAs of each pulsar will be correlated in a predictable way (depending on the specific source of the searched GWs), when simultaneously inspecting the ToAs from a number of pulsars. This is the basic idea behind the concept of a Pulsar Timing Array (PTA): searching, over decade-long timescales, for correlations among the timing residuals of an ensemble of millisecond pulsars, distributed at various celestial coordinates and regularly monitored. In a pictorial way, one can imagine the array as if it were an interferometer with many arms (one for each targeted pulsar), with the length of the various arms being stretched and/or shrunk according to the mutual orientation of the arms with respect to the direction of propagation of the GWs.

In fact, at first approximation, the frequency range over which a PTA can be sensitive to the occurrence of GWs is set on one side (the upper frequency) by the typical minimum cadence between two successive observations of the pulsar ensemble, i.e. once every few weeks. On the other side, the lower detectable GW frequency is given by the duration T_{span} of the longest pulsar data sets, which is nowadays of the order of some tens years. Those limits correspond to the interval between $f_{gw} \sim 10^{-9}$ and $f_{gw} \sim 10^{-7}$ Hz and explain why the operational frequency range for a PTA is often reported as that of the nanoHertz, that is, gravitational waves whose period is approximately one-ten year(s). In this range, by assuming white residuals from the fitting of a pulsar model to the collected ToAs, it is possible to show that the best sensitivity is reached at the frequency $f_{best} \sim 1/T_{span}$, i.s. at the lowest frequency edge of the interval.

As it was anticipated above, an expected source of low-frequency gravitational waves is typically represented by SMBHs, the frequency of emission of which being $f_{gw} = 3(M/10^9\ M_\odot)^{1/2}(a/0.01\ \mathrm{pc})^{-3/2}$ nanoHz where M is the mass of the BH and a the orbital separation. The current paradigm for most of the models for the formation of the large structures in the Universe states that *mergers* represent an essential part in the formation and evolution of the galaxies, and that massive BHs (with mass above 1 million solar masses) can be found in the nuclei of most (if not all) the galaxies. Given these premises, there should exist a huge number of SMBH binaries in the early stage of the Universe. Their fate is to progressively approach each other, while also sinking towards the center of their host galaxies, as a consequence of a not yet completely assessed mechanism, likely involving dynamical friction and/or the effects of a gaseous component in the environment. Once they reach orbital separation of order 1 pc, the emission of GWs become the dominant mechanism of additional shrinking of the binary. In this scenario, there should be plenty of super massive BH binaries emitting in the frequency range $1-10$ nanoHz. However, only a very small number of them is expected to be nowadays located close enough to the Earth for them to be detectable as single sources of GW (e.g. Yardley et al. 2011; Sesana et al. 2014).

On the contrary, the most probable GW source to be detected through pulsar timing is an incoherent superposition of low-frequency gravitational wave originated from a large number of the aforementioned coalescing SMBH binaries, which populated the early universe. This superposition generates an isotropic and stochastic background of gravitational waves (GWB; Sesana et al., 2009; Ravi et al., 2014).

It has been shown since a while (Detweiler, 1979), that the power spectrum of this GWB, $P_{GWB}(f_{gw})$, should have a specific shape as well:

$$P_{GWB}(f_{gw}) = \frac{A^2}{12\pi^2}\left(\frac{f_{gw}}{f_{gw,\mathrm{yr}}}\right)^{2\alpha-3} \tag{1.7}$$

where A is the GWB amplitude for a frequency $f_{gw} = f_{gw,\mathrm{yr}} = (1\mathrm{yr})^{-1}$, while

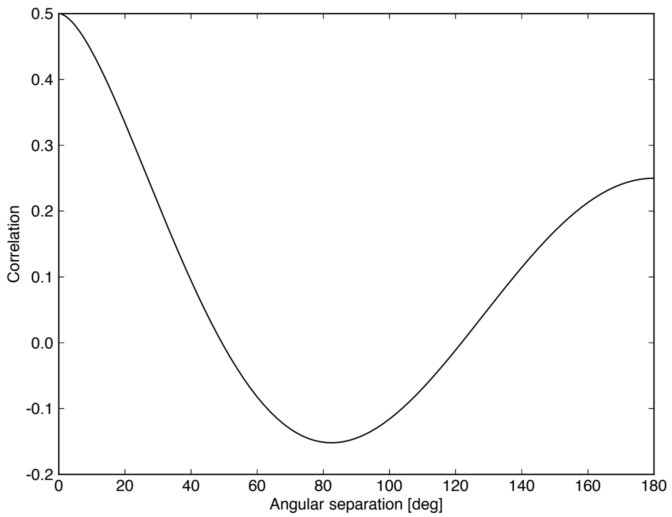

Figure 1.2: The Hellings and Downs curve

α sets the slope of the power-law spectrum associated with the dimensionless strain h, and it is predicted to be $-2/3$ for an isotropic and stochastic GWB (Phinney, 2001; Jaffe and Backer, 2003). More recent investigations, based on population synthesis of SMBH from merging of galaxies hosting seed massive BHs (Sesana et al., 2008), indicate that the highest contribution to the total GWB signal results from binaries located around $z = 1$. When dealing with a cosmological background, in place of the dimensionless strain, it is often preferred to indicate the GW spectrum in term of Ω_{gw}, i.e. the energy density per logarithmic frequency interval normalized to the critical energy density ρ_c needed for closing the Universe $\rho_c = 3H_o^2/8\pi G$, where H_o is the Hubble constant and G the Newton constant. It turns out that:

$$\Omega_{gw} = \frac{1}{\rho_c}\frac{\mathrm{d}\log\rho_{\mathrm{gw}}}{\mathrm{dlog}\,\mathrm{f}_{\mathrm{gw}}} \tag{1.8}$$

and hence, if the spectrum of the strain h of the aforementioned GWB scales as a power-law with $\alpha = -2/3$, the related spectrum of $\Omega_{gw}(f_{gw})$ goes like a power-law with index $2/3$, i.e. $\propto f_{gw}^{2/3}$.

It has also been demonstrated more than 30 years ago (Hellings and Downs, 1983) that, given a PTA, an isotropic and stochastic GWB leaves a recognizable trend in the angular correlation between the timing residuals of independent pulsar pairs, separated by an angular distance θ_{ij}. This trend, called *Hellings and Downs curve* is analytically given as:

$$C(\theta_{ij}) = \zeta(\theta_{ij}) = \frac{3}{2} x \log(x) - \frac{x}{4} + \frac{1}{2} \tag{1.9}$$

where $x = [1 - \cos(\theta_{ij})]/2$. The Hellings and Downs curve is reported in Figure 1.2: inspecting that Figure it is possible to notice that the correlation at an angular separation of zero degrees (that means that the sources are coincident on the sky projection) is 0.5 instead of unitary. This is because the ToA delays induced by the passage of a GW include two contributions (Lommen, 2012): the effect of the GW passing the Earth (often known as the *Earth term*) and also the effect of the GW passing the pulsar (the *pulsar term*). The Earth term is angularly correlated between pulsar pairs, and it is the dominant component in shaping the Hellings and Downs curve shown in Figure 1.2. On the other hand, the pulsar term of a GWB will induce uncorrelated noise characterized by a low-frequency ("red") power spectrum in the pulsar timing residuals. In fact, the pulsar term would give a spatial correlation, but as we do not know the distances of pulsars with a sufficient accuracy, we cannot make any use of a spatial correlation, that thus carries away half of the total amount of correlation between the timing residuals.

In summary, by fully exploiting an idea which was first proposed by Romani 1989; Foster and Backer 1990, the first target of the current PTA experiments is the direct detection of a gravitational wave background generated by supermassive black hole binaries in the early Universe through pulsar timing. On the practical side, the first step is a careful choice of a possibly large number (for having a good angular coverage of different directions in the sky) of millisecond pulsars that present both a bright and suitably peaked pulse profile (thus allowing the observer to determine the ToA associated to a single observation with a low level of uncertainty) and an excellent rotational stability, i.e. a low level of timing noise. The combination of these factors with the present observational capabilities, leads to select some tens (typically from ∼10 to ∼30) of millisecond pulsars, having timing solutions with a rms in the range from tens of nanoseconds for the best timers up to 1 microsecond for still useful objects. However, pulsar search experiments are keeping on running at the largest single-dish radio telescopes (e.g. Arecibo, Effelsberg, Parkes at about 1400 MHz, and Green Bank and Lofar at lower radio frequencies) in order to discover new millisecond pulsars suitable to enter a PTA and/or capable to replace in the array(s) some of the targets with the poorest properties. Simulations shows that very high quality millisecond pulsars will be finally available after the first stage of the Square Kilometer Array (SKA1) will be commissioned (Janssen et al., 2015).

Secondly, it is necessary to maintain a regular observing cadence in order to ensure an as much as possible uniform sampling along the time span (Levin et al., 2012). In this context, the availability and coordinated use of multiple telescopes, like is the case for the NanoGrav organization (see below) and, even better, for the EPTA community (see later), gives certainly an edge.

A third very important point is the accurate development of pipelines of data reduction and statistical investigation of the data to check for the presence of the signature of a GWB in the angular correlations between the timing residuals. In this context, many approaches to the data analysis have been proposed: from the Sperical Harmonic Decomposition (Detweiler, 1979; Jaffe and Backer, 2003) to the Two Points Correlation, focusing either on the time derivative of the residuals (Hellings and Downs, 1983) or directly onto the residuals themselves (Jenet et al., 2005; Hobbs et al., 2012). As far as the used statistics, the works can also be approximately distinguished in two large categories, i.e. those relying on a frequentists approach and those largely using Bayesian inference. Nowadays few pipelines and codes, independently developed, have been checked and are available. Moreover, a large effort have been undertaken by the whole PTAs' community (e.g. the IPTA organization, see later) in order to cross check their capabilities. The results of this comparison are expected to be published soon.

Although the work developed and reported in this Thesis (see Chapter **??**) will also focus on the issues related with the detection of the GWB described above, it is worth mentioning here that there are other GW sources which could be potentially interesting for the PTAs and/or the physics of which can be constrained by the observations of the PTAs. For instance, a background of GWs released from Cosmic Strings when Loops are formed and then oscillate (Caldwell et al., 1996; Maggiore, 2000; Damour and Vilenkin, 2005), or a background of relic GWs resulting from the inflationary era, via rather speculative mechanisms, like quantum fluctuation and/or inflationary generated fields, as well as produced during Phase Transitions, associated with bubble collisions, topological defects, primordial turbulence (Grishchuk, 2005; Boyle and Buonanno, 2008). As earlier discussed, besides the case of the cosmological backgrounds (i.e. the effect of the superposition of a large number of similar sources), PTAs have also the potentiality of directly detecting the GW emitted by a single discrete source, like a SMBH binary orbiting in a ∼ yr-long orbit in the nucleus of a not too far galaxy. Although the probability of detecting this kind of event is not very high with the present telescopes and instrumentation, with new generation telescopes, like SKA, the perspectives appears very good, with detection probability above 90% (Janssen et al., 2015) assuming the current theoretical models for the distribution of SMBH binaries in the Universe. Other sporadic events which could also be detected are the *GW bursts with memory* (Favata, 2009), which, in astrophysics, typically occur in events which are accompanied by large amount of mass or radiation ejected in an asymmetric fashion (Braginskii and Thorne, 1987); the same effect is called *Christodoulou effect*, if the ejected particles were gravitons (Christodoulou, 1991; Blanchet and Damour, 1992). In this case, the jump in the metric of the space-time is permanent and thus it produces a linear increasing of the pulsar timing residuals with time, likewise a pulsar glitch (see above), but easily recognizable by a PTA since it will involve all the observed pulsars. van Haasteren and Levin 2010 have shown that they are detectable with current facilities for SMBH binaries of $10^8\ M_\odot$ up to ∼1 Gpc, or everywhere in the Universe for $10^{10}\ M_\odot$.

It is also important to note that the interval of GW-frequencies at which the PTAs are sensitive is nicely complementary to the ranges on which both the original and the advanced versions of the ground-based interferometric GW detectors, like LIGO and VIRGO, are tuned, i.e. GW-frequencies between 10 and 1000 Hz. Also, the new planned eLISA space interferometer will operate (since the early '30) approximately in the range between 10^{-4} and 10^{-1} Hz, just in the spectral region between that of the PTAs and of LIGO/VIRGO. Moreover, experiments devoted to exploit the Polarization properties of the

Cosmic Microwave Background are potentially sensitive to GWs at much smaller frequencies than the PTAs.

Finally, it is interesting to mention that the detection of GWs is not the only target of the PTA experiments. Given the nature of the collected data and the search for a common signal underlying the timing residuals, at least two other studies can be carried on: the search for errors in the time standard conversion chain and the attempt to improve the planetary ephemeris, both of which are strongly linked with the timing procedure, as described in Section 1.2.

1.3.2 Pulsar Timing Arrays in the world

At the moment, three collaborations are carrying on PTA experiments.

European Pulsar Timing Array, EPTA – the EPTA (Kramer and Champion, 2013) joins members from several institutes in Europe (in Germany, UK, France, the Netherlands and Italy) and has access to the five major radio telescopes in Europe to collect pulsar observations:

- the Effelsberg radio telescope (Germany), a 100-mt single dish telescope. It has been performing coherently de-dispersed pulsar observations, first with the Effelsberg Berkeley Pulsar Processor (EBPP) and later with Asterix, a backend based on Reconfigurable Open Architecture Computing Hardware (ROACH) boards.
- the Lovell telescope at the Jodrell Bank Observatory (U.K.), a 76.2-mt single dish radio telescope. The observations are simultaneously performed with two backends, a Digital FilterBank (DFB) and a ROACH that is able to perform a coherent de-dispersion of pulsar data;
- the Westerbork synthesis radio telescope (the Netherlands), an interferometer made of 12 antennas with a diameter of 25 mt, corresponding to a 93-mt single dish. A backend performing the coherent dedispersion of the data is available, know as Pulsar Machine II (PuMa II);
- the Nançay decimetric radio telescope (France), a transit telescope with a surface equivalent to that of a 90-mt single dish telescope. Coherently de-dispersed pulsar observations started with the Berkeley Orléans Nançay

(BON) backend, and later with the Nançay-Ultimate-Pulsar-Processor-Instrument (NUPPI);

- the Sardinia radio telescope (Italy), a 64-mt single dish telescope. Currently under commissioning, it can perform incoherently de-dispersed observations with a DFB backend, and coherently de-dispersed observations with a ROACH board.

A subset of the observations are simultaneously performed by the 5 radio telescopes above, in the framework of a EU-funded project known as LEAP (Large European Array for Pulsars, Kramer and Champion 2013). These observations are expected to produce the best series of pulsar timing data taken ever for most of the inspected millisecond pulsars, since the equivalent collecting area of the 5 telescopes is that of a single dish of more than 200mt diameter, comparable with the effective area of the Arecibo dish (the largest single dish available so far), but able to look at a much larger number of millisecond pulsars than Arecibo.
Nowadays, the EPTA follows 41 millisecond pulsars, 18 of them with high priority due to their timing precision. ToAs are combined from the different telescopes in order to obtain a unique data set for each pulsar. The codes developed to search for the presence of a GWB typically work in the frame of the Bayesian statistics (van Haasteren et al., 2009, 2011).

Parkes Pulsar Timing Array, PPTA – the PPTA (Hobbs, 2013) joins members from various institutes mainly located in Australia. It collects pulsar observations with the 64-mt Parkes single dish radio telescope (NSW, Australia) simultaneously using typically four backends, two DFBs that perform an incoherent de-dispersion as well as two devices able to perform a coherent de-dispersion of the incoming data: the ATNF Parkes Swinburne Recorder (APSR) and the CASPER (Center for Astronomy Signal Processing and Electronics Research) Parkes Swinburne Recorder (CASPSR). 20 millisecond pulsars currently made the top priority group of sources monitored by the PPTA. The detection code typically adopted by this collaboration (Yardley et al., 2011) is based on the frequentist statistics.

North American Nanohertz Observatory for Gravitational Waves (Nanograv) – Nanograv (McLaughlin, 2013) joins members from different North American institutes. It collects pulsar observations with two different telescopes:

- the Green Bank radio telescope (West Virginia, USA), a 100-mt single dish telescope. Coherently de-dispersed observations are carried on with the Green Bank Ultimate Pulsar Processing Instrument (GUPPI);
- the Arecibo radio telescope (Puerto Rico), a 300-mt, not fully steerable single dish telescope. Coherently de-dispersed observations are performed with the Puertorican Ultimate Pulsar Processing Instrument (PUPPI).

Nanograv observes 36 millisecond pulsars, and makes major use of Bayesian statistics-based codes to search for a GWB in the collected data (Ellis et al., 2013).

These three collaborations refer to a more global organization, the *International Pulsar Timing Array, IPTA* (Manchester and IPTA, 2013), that has been established with the aim to maintain and foster the communications between the various groups, discussed common data format and exchange properly formatted ToAs collected by the various collaborations, cross-check the data and the detection pipelines, setting up key experiments and projects making use of shared data and expertise.

1.3.3 The limits obtained so far

To date, no detection of GWB was made by any of the three collaborations listed above; however, progressively more constraining upper limits on the strain amplitude of the GWB has been determined. All the values reported below refers to upper limits at 95% confidence level, for the case of a background of GWs measured at a reference frequency $f_{gw} = 1/\text{yr}$ and generated by SMBH binaries, the collective effect of which results in a GW spectrum with spectral index $\alpha = -2/3$.

Nanograv published its sensitivity limit in 2013 (Demorest et al., 2013), claiming that the amplitude of the GWB was less than 7×10^{-15}. This result confirmed what showed by the EPTA two years earlier (van Haasteren et al., 2011), with a sensitivity limit of approximately 6×10^{-15}. In 2013, the PPTA estimated that their used observational setup yields an upper limit of about 2.4×10^{-15}, which is the best sensitivity limit published so far (Shannon et al., 2013).

Although the reported upper limits are not discriminating yet for constraining the expected properties of the population of SMBH binaries, their values are now really approaching the range predicted by the most updated scenarios for the formation and evolution of these systems (Sesana, 2013). That in turn means that the current PTAs are about to reach a sensitivity which may finally lead them to obtain the first direct detection of a gravitational wave background.

In this perspective, it becomes now very urgent to properly identify and investigate, on a one-by-one basis, the major spurious effects which could mimic in the data the presence of a GWB. In a more quantitative approach, it is necessary to quantify the level at which these effects can increase the so-called False Alarm Probability (FAP), that is the probability for the data analysis pipeline(s) to recognize in the data the signature of a GWB when no real gravitational wave signal is indeed present. This is one the studies performed in the context of this Thesis.

Chapter 2

Polarization influence in pulsar data

Based on:

- *The High Time Resolution Universe Survey - IX: Polarimetry of long-period pulsars*, C. Tiburzi et al. 2013, MNRAS, Vol. 436, p.3557-3572
- *Erratum: The High Time Resolution Universe Survey - IX: Polarimetry of long-period pulsars*, C. Tiburzi et al. 2014, MNRAS, Vol. 445, p.3009-3510
- *The statistics of radio astronomical polarimetry: superposition and partial coherence of polarized modes*, W. van Straten & C. Tiburzi, in preparation.

In this Chapter we discuss several aspects of pulsar polarization, including two techniques to evaluate the Stokes parameters and some of their applications. In Section 2.1 we briefly summarize the general concepts about the Stokes parameters. In Section 2.2 we give an overview of pulsar polarization literature, emphasizing the discussion that compares the composition state of orthogonal polarized modes. In Sections 2.3 and 2.4 we describe one of the two techniques to compute the Stokes parameters, that is particularly suitable for low signal-to-noise sources, and its application to a numerous sample of pulsars. In Sections 2.5 and 2.6 we describe how the study of the fourth moment of the electric field allows to newly classify the orthogonal polarized mode composition, and a preliminary application to real data that opens to the possibility of a far more precise way to subtract the noise bias in the computation of the fourth moment of the electric. In Section 2.7 we summarize the practical results of the Chapter.

2.1 Stokes parameters in a nutshell

For sake of completeness, we summarize some general concepts and definitions about polarization. We follow the IAU and IEEE conventions (Hamaker and Bregman, 1996), and we use Rybicki and Lightman (1979) and Rohlfs and Wilson (2000) as references when not otherwise indicated.

2.1.1 Monochromatic waves

Let us consider a Cartesian tern of orthogonal axes, x, y and z. Let us also consider an electric field $\overrightarrow{E}$, part of a monochromatic, electromagnetic wave characterized by a wavelength λ, a wavenumber $\beta = 2\pi/\lambda$ and an angular frequency $\omega = 2\pi c/\lambda$, that propagates along z and can be decomposed in two components E_{x} and E_{y} along the x and y axes:

$$\begin{array}{rcl} E_{\mathrm{x}} & = & E_1 \cos(\omega t - \beta z - \delta_1) \\ E_{\mathrm{y}} & = & E_2 \cos(\omega t - \beta z - \delta_2) \end{array} \tag{2.1}$$

with E_1 and E_2 being the constant amplitudes of the two components. In a monochromatic wave, the phase difference $\delta = \delta_2 - \delta_1$ between E_{x} and E_{y} is also time-independent: this (or also if E_1 or E_2 is zero) states that a monochromatic wave is always 100% polarized.

It is possible to demonstrate that Equations 2.1 lead to the parametric representation of a ellipse rotated by an angle χ with respect to the x and y axes, whose eccentricity e is tied to an angular coordinate ϵ such as: $\tan\epsilon = \sqrt{1-e^2}$, and centered on the origin of the reference system if we impose that:

$$\begin{array}{r} E_1 \cos\delta_1 = \sqrt{E_1^2 + E_2^2}\cos\epsilon\cos\chi \\ E_1 \sin\delta_1 = \sqrt{E_1^2 + E_2^2}\sin\epsilon\sin\chi \\ E_2 \cos\delta_2 = \sqrt{E_1^2 + E_2^2}\cos\epsilon\sin\chi \\ E_2 \sin\delta_2 = -\sqrt{E_1^2 + E_2^2}\sin\epsilon\cos\chi \end{array} \tag{2.2}$$

This means that, with time, $\overrightarrow{E}$ draws an ellipse in a plane that is perpendicular to z. Special instances of elliptical polarization are circular and linear polarization. Circular polarization occurs if $E_{\mathrm{x}} = E_{\mathrm{y}} = E_0$ and $\delta = \pm\pi/2$: in this case, $\overrightarrow{E}$ draws a circumference of radius E_0. The circumference is drawn clockwise (as seen by the observer) if $\delta = -\pi/2$ or counter-clockwise if $\delta = \pi/2$. A clockwise circular polarization is defined as *left-handed*, an anti-clockwise circular polarization is defined as *right-handed*. Linear polarization occurs if $\delta = 0$ or $\delta = \pi$: in this case, $\overrightarrow{E}$ oscillates along a constant direction in time, that forms an angle θ with $\hat{x}$. θ is called *position angle* (PA; or *polarization angle*), and it is defined as:

$$\theta = \tan^{-1} \frac{E_\mathrm{y}}{E_\mathrm{x}} \tag{2.3}$$

Four quantities, called *Stokes parameters*, are introduced to describe the polarized state of the electromagnetic radiation, although in the case of fully polarized radiation (i.e., the monochromatic wave chase), only three are independent. They are defined as:

$$\begin{array}{rcl} I & = & E_1^2 + E_2^2 = E^2 \\ Q & = & E_1^2 - E_2^2 = E^2 \cos 2\epsilon \cos 2\chi \\ U & = & 2E_1E_2 \cos\delta = E^2 \cos 2\epsilon \sin 2\chi \\ V & = & 2E_1E_2 \sin\delta = -E^2 \sin 2\epsilon \end{array} \tag{2.4}$$

where Stokes parameter I clearly represents the total intensity. It is common to express the Stokes parameters as elements of a four-vector $S = (I, Q, U, V)$. As only elements Q, U, V contain polarization information, it is useful to introduce the *polarization vector*, $p = (Q, U, V)$. The tridimensional space whose axes are represented by Stokes Q, U, V (sometimes by $Q/I, U/I, V/I$) is called *Poincaré sphere*, and it is extremely useful to study some very interesting polarization features that will be introduced along in the Chapter.

In the case of a monochromatic wave, that is always 100% polarized, we have that $I^2 = p^2$ (only three out of four Stokes parameters are independent). The most general polarization state for a monochromatic wave is to be elliptically polarized: this implies that Q, U and V are all non-zero. If the monochromatic wave is circularly polarized ($E_1 = E_2, \delta = \pm\pi/2, \epsilon = \pm\pi/4$), we have that $Q = U = 0$, and $V = \pm I$. If it is linearly polarized ($\delta = 0$ or $\delta = \pi$ and $\epsilon = 0$), we obtain that $V = 0$ and $I^2 = Q^2 + U^2$. This demonstrates that Stokes parameter V is only tied to circularly polarized radiation, while Stokes Q and U characterize linearly polarized radiation.

2.1.2 Quasi-monochromatic waves

A monochromatic wave is, by definition, 100% polarized. However, this is an ideal, non-existing case in nature.

The radiation we receive from astrophysical sources is never monochromatic, and always partially polarized. That is, the phase difference δ between components E_{x} and E_{y} is time-dependent (possibly completely random), as well as the amplitudes E_1 and E_2, and the received emission is composed of a part of polarized radiation and a part of unpolarized radiation. In this case, all four Stokes parameters must be defined as averages over a statistical sample of the electric field vector:

$$\begin{aligned} I &= \langle E_1^2 + E_2^2 \rangle \\ Q &= \langle E_1^2 - E_2^2 \rangle \\ U &= \langle 2E_1E_2 \cos\delta \rangle \\ V &= \langle 2E_1E_2 \sin\delta \rangle \end{aligned} \tag{2.5}$$

where the angular brackets $\langle\rangle$ indicate a time average.

The computation of the time averages of Equations 2.5 is not obvious, and requires some complex algebra. For this reason, it is easier and more useful to express the electric fields using their complex-valued analytic representation (van Straten, 2003):

$$\begin{aligned} V_{\mathrm{x}} &= E_{\mathrm{x}} + i\hat{E}_{\mathrm{x}} = E_1 e^{i(\omega t - \delta_1)} \\ V_{\mathrm{y}} &= E_{\mathrm{y}} + i\hat{E}_{\mathrm{y}} = E_2 e^{i(\omega t - \delta_2)} \end{aligned} \tag{2.6}$$

where we always assume $z = 0$ for sake of simplicity and $\hat{E}_{\mathrm{x}}$ and $\hat{E}_{\mathrm{y}}$ are the Hilbert transform of E_x and E_y. Through this representation, the definition of the Stokes parameters in the presence of quasi-monochromatic radiation is given by the second moments of the electric field:

$$\begin{aligned} I &= \langle V_{\mathrm{x}}, V_{\mathrm{x}}^* \rangle + \langle V_{\mathrm{y}}, V_{\mathrm{y}}^* \rangle \\ Q &= \langle V_{\mathrm{x}}, V_{\mathrm{x}}^* \rangle - \langle V_{\mathrm{y}}, V_{\mathrm{y}}^* \rangle \\ U &= \langle V_{\mathrm{x}}, V_{\mathrm{y}}^* \rangle + \langle V_{\mathrm{y}}, V_{\mathrm{x}}^* \rangle \\ V &= \tfrac{1}{i}\left(\langle V_{\mathrm{x}}, V_{\mathrm{y}}^* \rangle - \langle V_{\mathrm{y}}, V_{\mathrm{x}}^* \rangle \right) \end{aligned} \tag{2.7}$$

In the case of quasi-monochromatic radiation, we have that $I^2 \geq p^2$.

2.1.3 Matrix representation of the Stokes parameters

Given a measurement ensemble of the transverse (with respect to the observer) electric field $\overrightarrow{e}$ emitted by a source, the second order statistics can be also studied via the coherency matrix ρ, which is a 2×2 complex matrix given by (Born and Wolf, 1980):

$$\rho = \langle \overrightarrow{e} \otimes \overrightarrow{e} \rangle \tag{2.8}$$

where the $\otimes$ symbol indicates a tensor product. In the previous paragraphs we presented the four Stokes parameters of an ensemble of transverse electric fields as the elements S_k $(0 \leq k \leq 3)$ of a vector S. Elements S_k can be defined from ρ after introducing the Pauli matrices σ_i:

$$\begin{aligned} \sigma_0 &= \begin{bmatrix} 1 & 0 \\ 0 & 1 \end{bmatrix} & \sigma_2 &= \begin{bmatrix} 0 & 1 \\ 1 & 0 \end{bmatrix} \\ \sigma_3 &= \begin{bmatrix} 0 & -i \\ i & 0 \end{bmatrix} & \sigma_1 &= \begin{bmatrix} 1 & 0 \\ 0 & -1 \end{bmatrix} \end{aligned} \tag{2.9}$$

as (Britton, 2000; van Straten, 2009):

$$\begin{aligned} \rho &= S_\mathrm{k}\sigma_\mathrm{k}/2 \\ S_\mathrm{k} &= Tr(\sigma_\mathrm{k}\rho) \end{aligned} \tag{2.10}$$

where Tr is the matrix trace operator and repeated indexes imply a summation along the ranges spanned by the indexes themselves.

As the Pauli matrices are a base of traceless Hermitian matrices, and satisfy specific multiplication rules, the Stokes four-vector S is associated to the Lorentz group (Britton, 2000). We can then define an inner product between two Stokes four-vectors A and B as:

$$A \circ B \equiv A^k B_\mathrm{k} = \eta^{kk} A_\mathrm{k} B_\mathrm{k} = A_0 B_0 - \mathbf{A} \cdot \mathbf{B} \tag{2.11}$$

where we recall that $\mathbf{A} = (A_1, A_2, A_3)$ (and likewise $\mathbf{B}$) and η is the Minkowski metric written as:

$$\begin{bmatrix} 1 & 0 & 0 & 0 \\ 0 & -1 & 0 & 0 \\ 0 & 0 & -1 & 0 \\ 0 & 0 & 0 & -1 \end{bmatrix} \tag{2.12}$$

From Equation 2.11 it is possible to introduce the Lorentz invariant of a Stokes four-vector:

$$S^2 \equiv S \circ S = S_0^2 - |\mathbf{S}|^2 = 4|\rho| \tag{2.13}$$

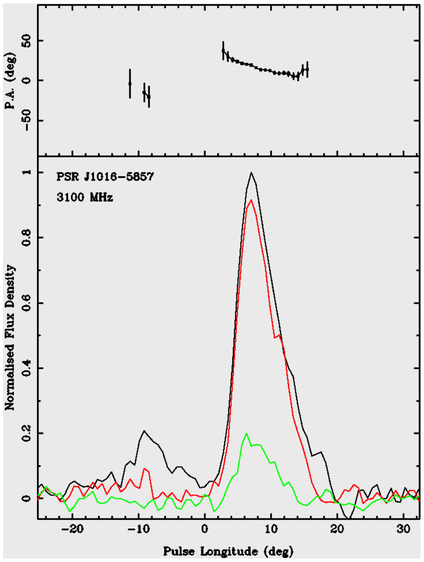

Figure 2.1: Detail from Figure 2 of Johnston and Weisberg (2006): flux versus pulse phase plot of PSR J1016−5857. The black, red and green lines represent, respectively, the pulse profiles in I, L and V.

where $|\rho|$ indicates the determinant of matrix ρ and, again, we recall that $\mathbf{S}$=(S_1, S_2, S_3) as well as an Euclidean norm:

$$\|S\|^2 = S_0^2 + |\mathbf{S}|^2 = 4\|\rho\|^2 \tag{2.14}$$

where $\|\rho\|$ is the Frobenius norm.

These definitions will be useful in Section 2.5.

2.2 Polarization emission as a tool in pulsar science

Polarization is one of the most striking features of pulsar radio emission. High degrees of linear polarization, typically higher than those seen in other astrophysical sources, can be found in integrated profiles (see Figure 2.1 from Johnston and Weisberg 2006 and also Crawford et al. 2001).

In sources with a spin-down luminosity ($\dot{E}$) less than 5×10^{33} erg s^{-1}, the average degree of linear polarization L reaches 20%, while it exceeds 50% in those where $\dot{E} > 2 \times 10^{35}$ erg s^{-1} (see Figure 2.2 of Weltevrede and Johnston 2008 and Gould and Lyne 1998; von Hoensbroech et al. 1998).

Single pulse observations can be even more polarized, with the degree of linearly polarized emission sometimes reaching 100% (Levin et al., 2012). The fraction of circular polarization is lower, around 10%. L is typically anti-

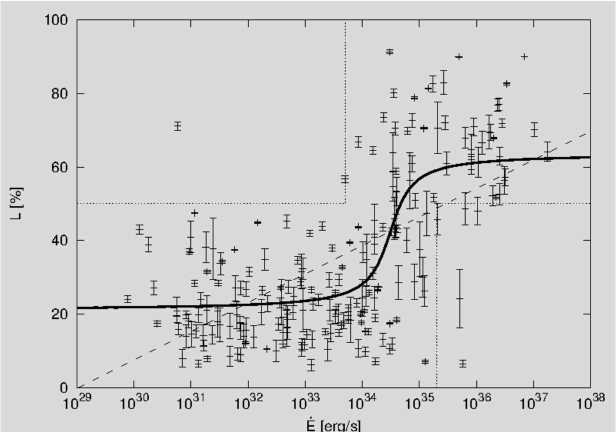

Figure 2.2: Figure 8 of Weltevrede and Johnston (2008): percentage of L versus $\dot{E}$.

correlated with observing frequency (see Figure 2.3 from Keith et al. 2012 and Johnston et al. 2008). Circular polarization is usually brighter in the center (or core) of a pulse profile (Rankin 1993, Gould and Lyne 1998). It often shows handedness variability as a function of pulse longitude (Radhakrishnan and Rankin, 1990), and in many cases hand reversal also occurs near the profile center (see Figure 2.4 from Karastergiou and Johnston 2004).

A thorough understanding of the complex nature of pulsar polarization is a fundamental ingredient to give a unique insight into the emission beam structure above the polar caps (Rankin, 1983; Lyne and Manchester, 1988; Han and Manchester, 2001; Karastergiou and Johnston, 2007; Beskin and Philippov, 2012).

One of the first features noted soon after the discovery of pulsars (Hewish et al., 1968) was that some of these objects displayed a rapid sweep of the polarization angle across the pulse profile, resulting in an S-shaped trend. This behavior was successfully explained by the Rotating Vector Model (RVM) introduced by Radhakrishnan and Cooke (1969) and Lyne et al. (1971). In the RVM, the PA is determined by the orientation of the magnetic field lines. As the pulsar turns, the line of sight crosses the magnetic field lines with a continuously changing orientation (see Figure 2.5). It is thus expected that the phase resolved PA trend follows a S-shaped swing described by the following formula:

$$\mathrm{PA} - \mathrm{PA}_0 = \frac{\sin\alpha \sin(\phi - \phi_0)}{\sin(\alpha + \beta)\cos\alpha - \cos(\alpha + \beta)\sin\alpha\cos(\phi - \phi_0)} \tag{2.15}$$

where PA_0 is the PA value at a pulse longitude $\phi = \phi_0$ which is defined as the pulse phase at which the pulsar magnetic axis, the rotational axis and the

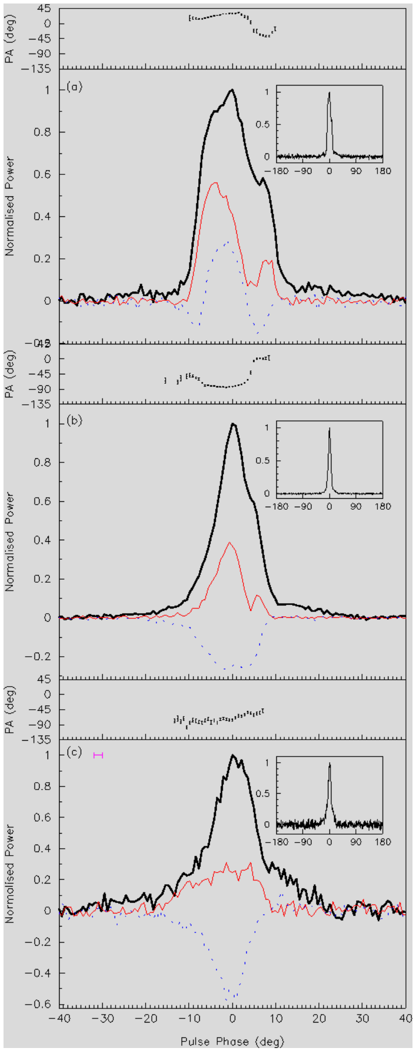

Figure 2.3: Figure 5 of Keith et al. (2012): polarization profiles of PSR J1017−7156 at (a) 732, (b) 1369 and (c) 3100 MHz, showing phases within ±40° of the pulse peak. The black, red and blue lines show, respectively, I, L and V. The inset figures show the profile over the full 360° of pulse phase.

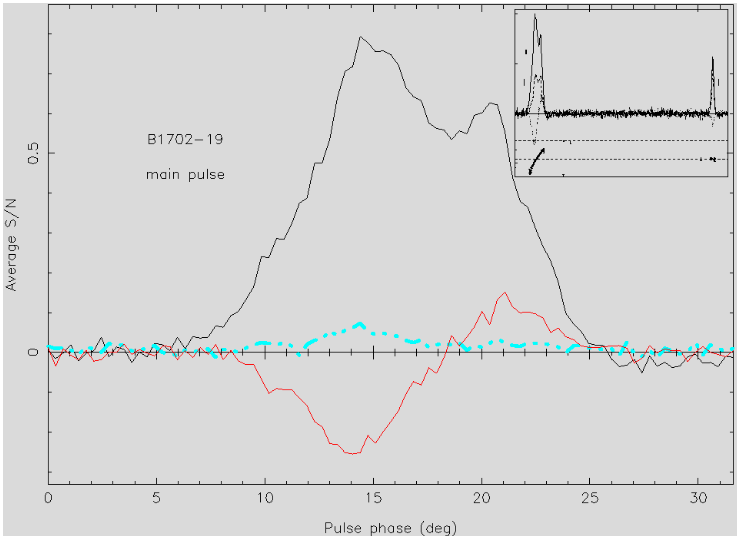

Figure 2.4: Detail from Figure 5 of Karastergiou and Johnston (2004): integrated profile of PSR B1702−19 at 1.41 GHz (both the main pulse and interpulse). The black, red and light blue lines show, respectively, the average S/N of the I, V and $|V|$. The insert represents the full polarization profile, including L (dashed line), and the PA ranging from $-90°$ to $90°$.

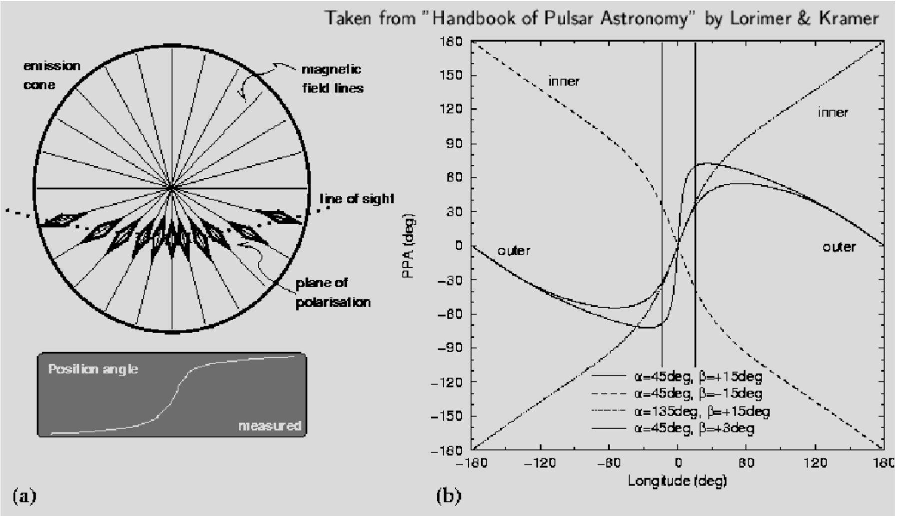
Taken from "Handbook of Pulsar Astronomy" by Lorimer & Kramer

Figure 2.5: Rotating vector model, figure taken from the *Handbook of pulsar astronomy* (Lorimer and Kramer, 2005). In the upper part of Figure a) is reported a pole-on view scheme of the emission beam and the pulsar magnetic field line. The line-of-sight sweeps the magnetic field lines, and the observed PA (in the lower part of the Figure) mirrors the change in their orientation. Figure b) reports the expected polarization angle swings as a function of different combinations of the angular separation between magnetic and rotational axes, α, and the impact parameter β.

observer's line-of-sight are coplanar (often referred at as *fiducial plane*), α is the angular separation between the two aforementioned axes and β is the impact parameter (i.e., the smallest angular separation between the line-of-sight and the magnetic axis). Thus, in principle, the PA can be used to determine the orientation of the rotational and magnetic axis (see e.g. Everett and Weisberg 2001).

Moreover, from the delay in longitude between the PA swing and the total power peak due to retardation and aberration effects (Blaskiewicz et al., 1991; Hibschman and Arons, 2001; Gupta and Gangadhara, 2003), it is possible to infer the emission altitude (von Hoensbroech and Xilouris, 1997; Johnston and Weisberg, 2006).

However, it was immediately clear that this simple and elegant model could not be applied to every pulsar. In particular, old pulsars and millisecond pulsars often display complicated PA profiles that are inconsistent with the RVM predictions, see e.g. Johnston and Weisberg (2006); Johnston et al. (2008); Xilouris et al. (1998); Stairs et al. (1999); Yan et al. (2011). A vast number of pulse profiles show abrupt jumps in the polarization angle that break the S-shape sweep (Clark and Smith, 1969; Ekers and Moffet, 1969). The amplitude of these discontinuities is usually 90° (Backer et al., 1976). This phenomenon arises because the polarized radiation of a pulsar may occur in one of two orthogonal states (Manchester et al., 1975) called *orthogonally polarized modes* (OPM). The PA of an integrated pulsar profile that shows one or more orthogonal jumps mirrors a switch in the dominance[1] of one OPM over the other (Stinebring et al., 1984). Also several cases of non-orthogonal jumps in the PA have been reported (Karastergiou et al., 2005; Karastergiou, 2009).

Since the OPMs were discovered, a wide debate arose in the literature about how they are composed.

First of all, their composition can be coherent (Gangadhara, 1997) or incoherent (McKinnon, 2006). A coherent addition between two waves means that there exists a certain relationship between the wave phases: if we can measure individually the two signals (and not only their sum), we thus expect that the mean value of the cross-multiplied voltages is non-zero. On the other hand, an incoherent addition between two waves implies that there is no link

---

[1] The meaning of *mode dominance* depends on the applicable polarization regime.

between their phases. As a physical example, if the individual sources behave collectively we expect coherent emission. On the other hand, if the individual sources are independent we expect incoherent emission. Usually, incoherent modes are considered because this is the simplest assumption until evidence to the contrary arises.

Secondly, at a given phase longitude the modes can occur at the same time or mutually excluding each other. In the first case, the modes were defined *superposed* (Karastergiou et al., 2005), in the second they were defined *disjoint* (Cordes et al., 1978). As it seems that the first regime is the favorite state for the pulsar majority, scarce evidence in support of mode disjointness have been given so far.

Cordes et al. (1978) first claimed the existence of mode disjointness, studying single pulse observations at 430 MHz of PSR B2020+28 obtained with the Arecibo Observatory. They first showed that a high degree of correlation between the handedness of V and the individual occurrence of one or the other of the OPMs can be computed from the data (asserting a clear link between V and the OPMs). They then found that both the average fractional linear polarization ($[|\langle L_1\rangle| - |\langle L_2\rangle|]/\langle I_1 + I_2\rangle$) and its second moment ($\langle|L^2|\rangle/\langle I\rangle$) are large, and interpreted these observations as evidence for mode disjointness in PSR 2020+28. Stinebring et al. (1984), however, argued the rarity of mode disjointness and favored a mode superposition regime. They carried on a single pulse study on 11 pulsars (including PSR B2020+28) at 1404 MHz with the Arecibo Observatory, and they deduced that if the modes are 100% linearly polarized and disjoint, then a similar percentage of linear polarization should be observed pulse per pulse at any phase longitude: this was found to be very rare. On the other hand, if the modes are superposed, a low degree of linear polarization should be computed pulse per pulse in those longitudes at which both the OPMs can be seen over a large number of pulsar rotations, as observed. In practice, since the Stinebring et al. (1984) analysis almost no additional evidence of mode disjointness has been published. On the other hand, mode superposition was supported by numerous studies. For example, Johnston et al. (2001) discovered a rare, transient and bright component in the leading edge of the Vela pulsar profile, using single pulse observations at 660 and 1413 MHz obtained with the Parkes radio telescope. The component is orthogonally polarized with respect to the persistent radio emission at the longitude range where it occurs. When present, it induces an orthogonal jump in the PA and a decrease of the linearly polarized emission. Furthermore, Johnston (2004) found that, in the trailing edge of PSR B1641-45, observed at 1413 MHz with the Parkes radio telescope, single pulses were depolarized where orthogonally polarized modes occur. In a recent single pulse study of PSR J0738-4042, observed at 1404 MHz at Parkes, Karastergiou et al. (2011) identified a transient component in this pulsar profile, characterized by an orthogonal polarization state: this result is similar to the discovery of Johnston et al. (2001). These studies all support mode superposition as defined by Cordes et al. (1978).

From a more theoretical point of view, comparing with data from the literature, McKinnon (1997) indicated mode superposition as the principal cause of depolarization at high observing frequencies, based on the assumption of a birefringent pulsar magnetosphere. McKinnon and Stinebring (1998) proposed a statistical model to describe pulsar polarization in presence of superposed OPMs, representing them as random variables and assuming fully linearly polarized modes. They computed the expected probability distributions for total intensity, linear polarization and PA, and they compared them with the B2020+28 observations collected by Stinebring et al. (1984), finding that the observed PA distribution is wider than the theoretical one. This was later explained by McKinnon (2004) with the occurrence of randomly polarized radiation. Always assuming mode superposition, McKinnon and Stinebring (2000) elaborated a method to separate the two mode profiles, while McKinnon (2002) explained the broadening in the longitude resolved distribution of fractional circular polarization derived from single pulses. McKinnon (2003) obtained the joint probability distribution of the polarization vector's amplitude, longitude and colatitude in the Poincaré sphere for several polarization states, OPM included. The latter work was generalized by McKinnon (2006) and McKinnon (2009). In these three papers, OPMs were considered superposed, and their flux densities were represented as Gaussian random variables with additional instrumental noise. The obtained distributions yield extremely realistic results, e.g. the model presented by McKinnon (2009) can describe complicated trends of the polarization vector in the Poincaré sphere, such as bowties and bars. The expected distribution of the polarization vector's colatitude, agrees extraordinarily well with the

Stinebring et al. (1984) data of PSR B2020+28.

Most of the considerations above rely on the assumption that the identification of the OPM combination regime is somewhat independent from instrumental effects. However, there exists observational evidence that how we distinguish between disjoint and superposed OPMs depend on the temporal resolution of the instrument (Gangadhara et al., 1999). In Sections 2.5 and 2.6 we explore this aspect and its potential consequences. As an introduction to this topic, in Sections 2.3 and 2.4 we present one of the typical methodologies to derive the Stokes parameters and polarization percentages, especially in presence of low signal-to-noise ratio (S/N) pulsars, and a some of studies that it is possible to perform with its outcomes.

2.3 A standard polarimetry method for low S/N pulsars

We present a method, based on Noutsos et al. (2008), to obtain an optimal evaluation of the Rotation Measure (RM) and polarization degree while dealing with low S/N pulsars, and in general with data-sets made of folded observations.

Let us assume that, for a given pulsar, we can collect numerous, folding-mode observations that retain their maximum resolution in frequency, time and phase, and were built on a good timing solution for the pulsar. We also assume that radio frequency interference (RFI) was carefully excised and that thorough polarization and flux calibrations were applied.

The first step of the analysis is to collapse each observation in time. The pulsars of this sample are generally weak, and we notice a high variation of the detected S/N with the observations. For these reasons, we conclude that it is optimal to sum the observations weighting them according to their own S/N, with the aim to obtain an integrated profile:

$$w = \frac{\mathrm{S/N}(I)}{\mathrm{rms}(I)} \tag{2.16}$$

where w is the weight we applied and $\mathrm{S/N}(I)$ and $\mathrm{rms}(I)$ are, respectively, the S/N and the off-pulse root-mean-square (rms) of the pulsar profile in Stokes I.

This results in a higher S/N for the final, integrated profile with respect to adding profiles based solely on the integration time. We collapse this average profile in time: it thus still retains the full frequency information.

We now compute the RM when possible. We collapse the frequency channels to four, in order to enhance the S/N, and we compute an average PA across the bins of the pulse for each channel as in Noutsos et al. (2008):

$$\mathrm{PA}_{\mathrm{ave}} = \frac{1}{2}\arctan\left(\frac{\sum_{i=n_{\mathrm{start}}}^{n_{\mathrm{end}}} U_{\mathrm{i}}}{\sum_{i=n_{\mathrm{start}}}^{n_{\mathrm{end}}} Q_{\mathrm{i}}}\right) \tag{2.17}$$

where Q_{i} and U_{i} are the Stokes parameters that quantify linear polarization for the i-th phase bin, and n_{start} and n_{end} are the phase bins of the pulse edges.

In order to calculate the PA error bars we first measure the linear polarization as:

$$L_{meas} = \sqrt{\left(\sum_{i=n_{\mathrm{start}}}^{n_{\mathrm{end}}} U_{\mathrm{i}}\right)^2 + \left(\sum_{i=n_{\mathrm{start}}}^{n_{\mathrm{end}}} Q_{\mathrm{i}}\right)^2} \tag{2.18}$$

Since it is a positive definite quantity, the average value L_{meas} is biased. We follow the method of Wardle and Kronberg (1974) to obtain a better determination of the value of the linear polarization L_{true}:

$$L_{\mathrm{true}} = \begin{cases} 0.0 & \text{if } p_0 < 2.0 \\ \sqrt{L_{\mathrm{meas}}^2 - (\mathrm{rms}(I)\sqrt{n_{\mathrm{on}}})^2} & \text{otherwise} \end{cases} \tag{2.19}$$

where $p_0 = L_{\mathrm{meas}}/\mathrm{rms}(I)\sqrt{n_{\mathrm{on}}}$, with n_{on} being the on-pulse number of phase bins.

Simmons and Stewart (1985) showed that this is the best method to be applied whenever p_0 is greater than 0.7 (see also Noutsos et al. 2008). This is often the case for low S/N pulsars.

As for the estimates of the uncertainties on $\mathrm{PA}_{\mathrm{ave}}$, $\sigma_{\mathrm{PA}_{\mathrm{ave}}}$, for high values ($P_0 > 10$) of $P_0 = L_{\mathrm{true}}/\mathrm{rms}(I)\sqrt{n_{\mathrm{on}}}$, we use the formula from Everett and Weisberg (2001):

$$\sigma_{\mathrm{PA}_{\mathrm{ave}}} = \frac{1}{2P_0} \tag{2.20}$$

For lower values of P_0, we numerically compute the error by integrating the PA probability distribution between $\pm\sigma_{\mathrm{PA}_{\mathrm{ave}}}$ in order to obtain 0.68, as in Naghizadeh-Khouei and Clarke (1993) and Everett and Weisberg (2001):

$$G(\mathrm{PA} - \mathrm{PA}_{\mathrm{true}}; P_0) = \frac{1}{\sqrt{\pi}}\left\{\frac{1}{\sqrt{\pi}} + \eta_0 \mathrm{e}^{\eta_0^2}[1 + \mathrm{erf}(\eta_0)]\right\} \times \mathrm{e}^{-(\mathrm{P}_0^2/2)} \tag{2.21}$$

where $\mathrm{PA}_{\mathrm{true}} = \mathrm{PA}_{\mathrm{ave}}$ in our case, $\eta_0 = (P_0\sqrt{2})\cos 2(\mathrm{PA} - \mathrm{PA}_{\mathrm{true}})$, erf is the Gaussian error function. We obtain the RM and its error by implementing a least squares fit through the following equation:

$$\mathrm{PA}(f) = \mathrm{PA}_{\mathrm{ref}} + \mathrm{RM}c^2 \times \left(\frac{1}{f^2} - \frac{1}{f_{\mathrm{ref}}^2}\right) \tag{2.22}$$

where $\mathrm{PA}(f)$ is the PA at a certain frequency f, $\mathrm{PA}_{\mathrm{ref}}$ is the PA at a reference frequency f_{ref} and c is the speed of light. If the pulsar profile has two recognizable components in the linearly polarized profile, we fit for the RM separately for each component and we compare the obtained results *a posteriori*.

Once the RM is computed, we can correct the observations for it and sum over the frequency channels to produce a final integrated profile.

A further useful quantity when considering pulsar polarization is the total amount of circular polarization irrespective of the handedness. The measured quantity $|V|_{\mathrm{meas}}$ is biased because it is positive definite. We follow Karastergiou and Johnston (2006) to obtain an unbiased value via:

$$|V|_{\mathrm{true}} = \begin{cases} 0.0 & \text{if } |V|_{\mathrm{meas}}/b < 2.0 \\ \sqrt{|V|^2_{\mathrm{meas}} - b^2} & \text{otherwise} \end{cases} \tag{2.23}$$

where:

$$b = \sqrt{\frac{2}{\pi}} \times \mathrm{rms}(V). \tag{2.24}$$

Here, $\mathrm{rms}(V)$ is the off-pulse rms of the V profile.

In order to quantify the luminosity and the percentage of polarization of the analyzed pulsar, we compute the quantities S_0, $L\%$, $V\%$ and $|V|\%$ as:

$$\begin{aligned} S_0 &= \frac{1}{n_{\mathrm{bins}}} \sum_{i=n_{\mathrm{start}}}^{n_{\mathrm{end}}} I_{\mathrm{i}} \\ L\% &= \frac{1}{n_{\mathrm{bins}}} \sum_{i=n_{\mathrm{start}}}^{n_{\mathrm{end}}} L_{\mathrm{true,i}} \times \frac{100}{S_0} \\ V\% &= \frac{1}{n_{\mathrm{bins}}} \sum_{i=n_{\mathrm{start}}}^{n_{\mathrm{end}}} V_{\mathrm{i}} \times \frac{100}{S_0} \\ |V|\% &= \frac{1}{n_{\mathrm{bins}}} \sum_{i=n_{\mathrm{start}}}^{n_{\mathrm{end}}} |V|_{\mathrm{true,i}} \times \frac{100}{S_0} \end{aligned} \tag{2.25}$$

where $n_{\rm bins}$ is the total number of phase bins that are present in the observations, $L_{\rm i,true}$, $V_{\rm i}$ and $|V|_{\rm i,true}$ are the (unbiased, in the cases of $L_{\rm i,true}$ and $|V|_{i,true}$) values of linear, circular and absolute circular polarization in the i-th phase bin. These definitions are consistent with those adopted by Gould and Lyne (1998).

2.4 A case of study: application to 49 pulsars from the HTRU survey

The southern component of the High Time Resolution Universe survey for pulsars and fast transients (HTRU, Keith et al. 2010) was carried out at the 64-metre Parkes radio telescope. It is divided into three parts with different integration times depending on the Galactic latitude: low, medium and high. To date, it has led to the discovery of more than one hundred pulsars. Among them there is a remarkable sample of millisecond pulsars (Bates et al., 2011; Keith et al., 2012; Burgay et al., 2013; Levin et al., 2013; Ng et al., 2014). However, the majority of them are normal pulsars (Bates et al. 2012, Ng et al. in preparation). Following the presentation of the millisecond pulsar polarimetry (Keith et al., 2012; Burgay et al., 2013), in this Section we present a systematic polarization analysis of 48 long-period pulsars discovered in the medium latitude part of the survey, and one discovered in the high latitude part.

2.4.1 Observations and Analysis

The examined sample of 49 long-period pulsars shows spin periods range from a few hundred milliseconds to about two and a half seconds. They were all discovered during the mid-latitude part of the HTRU survey (Keith et al., 2010; Bates et al., 2012) apart from PSR J1846–4249 that has been discovered in the high latitude survey. PSR J1237–6725 and PSR J1539–4835 were originally thought to be new discoveries of the mid-latitude part of the HTRU survey but were first published by Kramer et al. (2003) and Eatough et al. before 2010.

After discovery and confirmation, the pulsars were followed-up with with the third Parkes Digital Filterbank, observing them for at least one year to allow the determination of a complete timing solution. The typical length of the timing observations ranges from ∼100 to ∼600 seconds. The data were acquired over a 256 MHz bandwidth centered at 1369 MHz, split into 1024 frequency channels, each 0.25 MHz wide. The collected samples were folded on-line forming pulse profiles with 1024 bins for all four Stokes parameters in each frequency channel. To calibrate the target pointings for the differential gain and phase between the linear feeds, we made observations of noise diode coupled to the receptors in the feeds.

We reduce the data using the PSRCHIVE software package (Hotan et al., 2004b). For each individual observation, we first excise the RFIs from the data. The observations are polarization-calibrated using a square wave signal in order to produce true Stokes parameters, and flux-calibrated using an averaged observation of Hydra A. In addition, corrections are made to the polarization impurity of the feed following the method in van Straten (2004). Finally, the observations are aligned using the best-fit ephemeris.

RM (when possible) and polarization parameters are obtained following the procedure explained in Section 2.3. A combination of low signal-to-noise and/or low polarization fraction meant that we are unable to compute the RM for a number of pulsars in our sample. In these cases, we simply set the RM to zero before summing over frequency.

Referring to Equation 2.19, we note that: 1) for a handful of pulsars in our sample we accept a lower threshold for p_0, either in agreement with Everett and Weisberg (2001) or by visually inspecting that the PAs in the frequency channels where p_0 resulted less than 2 follow the trend predicted by Equation 2.22; 2) in all the pulsars of our sample $p_0 > 0.7$.

2.4.2 Polarimetric Results

The main results are given in Tables 2.1 and 2.2 along with the full Stokes profiles of the pulsars in Appendix 4.5.3. Table 2.1 includes information for pulsars for which we are able to determine the RM and Table 2.2 contains the sample for which RMs are not constrained. We can notice from Table 2.1 and Table 2.2 that only $\sim$ 9% of the pulsars with a computable RM shows a DM value higher than 200 pc cm^{-3}. On the other hand, $\sim$33% of the pulsars for which we are not able to compute a RM exhibits DM $>$ 200 pc cm^{-3}. This is not totally unexpected: in fact, large values of DM can be associated with high values of RM, provided that a uniform field is present along the line of sight. Collapsing the total bandwidth in 4 sub-bands, as we do to compute the RM, depolarizes the signal if the RM is large enough (note that the low S/N of the pulsars in our sample forces us to not increase the number of sub-bands). For the high-DM pulsars, we attempt a different method to compute RM which involved a search in the RM space of values to maximize the linearly polarized flux. Unfortunately, the low S/N of the pulsars implies that we are unable to determine a reliable RM in any of the cases.

Below, we briefly give a qualitative description of the profiles in total power, linear and circular polarization and the PA curves of the analyses pulsars, except for *PSRs J0919–6040, J1054–5946, J1143–5536, J1539–4835, J1625–4913, J1634–5640, J1647–3607* and *J1700–4422*, for which we are not able to obtain a RM value, and that show very low linear and circular polarization and no interesting features.

PSR J0807–5421: The profile is relatively narrow, but the total intensity shows two clear, though blended components, with the trailing being the brightest. In contrast, the linear polarization peaks in the center of the profile and is significantly narrower than the total intensity. The circular polarization displays a sign change towards the trailing component. The PA curve does not exhibit the swing expected from the RVM, but rather a sort of an arch.

PSR J0905–6019: The profile is relatively narrow and it shows an asymmetric single peak. Although the linear polarization is low, we are able to derive a RM. The circular polarization is faint and left-handed.

PSR J0912–3851: The profile shows two distinct, narrow components, with the leading component being brighter than the trailing one. The linear polarization also shows two peaks, narrower than in total intensity. The circularly polarized signal displays a sign change in the center of the profile. We compute a RM value for each of the linear polarization peaks and we find them to be compatible with only overlapping the extremes of the respective 1 σ error bar.

PSR J0949–6902: This bright integrated profile shows two almost completely blended, relatively narrow components. The linear polarization is faint, and the circular polarization exhibits a change of sign in the profile center.

PSR J1036–6559: The total intensity, the linear and the circular profiles all show a single component. The PA curve appears to increase with the phase longitude, and to decrease at its very end.

PSR J1105–4353: The total intensity is noisy and single-peaked. The linear polarization is noisy as well, and the circular polarization is basically absent. The PA curve has no real pattern.

PSR J1237–6725: The profile shows two blended components, with the leading component being the brightest. There is a faint signature of the presence of linear polarization. Note that the observations were folded with a period that is half the real one, which was discovered at a later time. This can have affected the quality of the observations.

PSR J1251–7407: The total intensity profile is narrow and asymmetric, made of at least three blended components. Linear and circular polarization appear to be significant under the trailing component. The PA profile presents three changes of slope in the first half of the pulse profile. After that, it follows a smooth swing with a positive slope that covers about 50° before changing the sense of the slope at its very end.

PSR J1331–5245: This noisy profile shows at least two blended components, where the leading is the brightest. The linear and circular polarization profiles follow the total intensity to a large extent. However, the linear polarization is larger under the leading component whereas the circular polarization is more significant under the trailing components. The PA profile is flat along the leading component, and it shows a steep swing with a negative slope across the trailing one covering about 100°. An almost orthogonal jump occurs between these two parts of the PA profile.

PSR J1346–4918: The profile shows a single, asymmetric component. The circular polarization exhibits a sign change against the maximum of the total intensity profile. The PA profile presents a very smooth decrease in the first half of the pulse profile.

PSR J1409–6953: This noisy total intensity profile is box-shaped. It is perhaps a blended double, although this could be an effect of the occurrence of more than two components. The linear polarization is as well noisy and the PA values have no real pattern. The circularly polarized profile exhibits a right-handed maximum against the profile trailing component.

PSR J1416–5033: This noisy profile shows at least two components, whereof the leading one is the brightest. The linear polarization profile is noisy, and there is no hint of circularly polarized signal.

PSR J1432–5032: The total intensity profile is box-shaped. The linear polarization is noisy but significant, and the left-handed circularly polarized profile is mainly present close to the leading edge of the total intensity curve. The PAs exhibit a smooth swing across the profile covering about 70°. Note that the observations were folded with a period that is half of the real one, discovered at a later time. This can have affected the quality of the observations.

PSR J1443–5122: This noisy and relatively broad profile is asymmetric and shows a single component. The linearly polarized profile is significant when close to the leading edge, and another peak occurs at the center of the profile. There is almost no circular polarization. The PAs exhibit a smooth swing with a positive slope, covering about 120°.

PSR J1517–4636: The profile displays a narrow, single component. The linear polarization largely follows the total intensity but it is narrower. The PA curve exhibits a change of slope close to the leading edge of the pulse profile, followed by a steep swing with a positive slope, that extends over ∼50°.

PSR J1530–6336: The total power profile shows two principal components, with the leading being the brightest. The circular polarization follows the total power, but it is narrower. On the contrary, the linear polarization is characterised by at least three components. The first two of them are almost blended and occur before the trailing peak of the total intensity profile. The PAs show two swings with similar slopes under the two leading components of the linear polarization. They are separated by an OPM jump. The third part of the PA profile is a swing with a flatter slope.

PSR J1534–4428: The total intensity profile extends over more than 40° and consists of a bright leading component followed by a flat structure. There is a significant degree of linear polarization which largely tracks the total intensity profile. If we interpret this structure as a zone of partially overlapping components, the depolarization can be explained thanks to the fact that the linearly polarized profile is narrower than the total power one. The PA curve is largely flat but rises steeply in the middle of the profile before flattening off again.

PSR J1551–4424: This profile is affected by interstellar scattering, and it shows a typical steep rising edge to a peak followed by a more gradual decay. The small linear polarization fraction is concentrated towards the leading edge of the profile. The PA swing is remarkably flat, an effect that is induced by the scattering (Li and Han (2003)).

PSR J1552–6213: The total intensity profile is single-peaked and slightly asymmetric, with the trailing edge being steeper than the leading. The circular polarization is barely visible and slightly right-handed in the second part of the profile. The linear polarization shows two components, with the brightest roughly corresponding to the maximum of the total power. The first part of the PA profile is followed by a non-orthogonal jump. The second part shows a generally rising trend.

PSR J1607–6449: The profile is made of at least two almost completely blended components. The linear polarization is noisy. There is a significant occurrence of the right-handed, circularly polarized signal, that is mostly present in the first half of the pulse profile.

PSR J1612–5805: The total intensity profile shows three features: a narrow, slightly asymmetric leading component and blended, fainter central and trailing components. The linearly polarized profile is mainly present beneath the leading component, and its peak almost coincides with the maximum of the total power. The circular polarization shows a change of sign between the leading and the central component. The PA curve starts flat and exhibits a very steep swing with negative slope across almost the entire leading peak, followed by a slightly increasing curve toward the center of the pulse profile. The two parts of the PA profile are separated by a jump of ∼110°.

PSR J1614–3846: The total intensity profile is noisy, box-shaped and symmetrical, and these attributes are largely mirrored by the linear polarization. The circular polarization is almost absent. The PA curve exhibits a smooth swing, with a positive slope that covers about 50°.

PSR J1622–3751: The profile is a blended double with the trailing component being the brightest. The linear polarization, in contrast, is more significant in the leading component. The circular polarization changes sign in the center of the profile. Unusually amongst this sample, the PA profile shows the classic RVM signature: a flat beginning followed by a wide swing beneath the linearly polarized leading and trailing peaks, and flatter again at the end of the profile. The swing center coincides with the minimum in the total intensity. It covers about 120°. Despite of the fact that the pulse profile is narrow, the steep swing of PA lends itself to the RVM fitting. We find that, although the angle between the spin and magnetic axis is unconstrained, the impact angle must be less then 4°. Interestingly also, the inflexion point of the RVM (the magnetic pole) aligns with the midpoint of the profile to within 0.5°. The lack of significant offset implies a low emission height of less than 100 km. Such a low emission height favors a non-orthogonal rotator with preferred values of $\alpha \lesssim 40°$.

PSR J1626–6621: The profile shows two distinct, relatively narrow components, with the leading component being significantly brighter. The linear and the circular polarizations occur in correspondence of the profile's leading component. The PA profile exhibits a steep swing across this peak, which covers about 50°.

PSR J1627–5936: This broad profile extends over more than 100° of longitude. It shows an asymmetric, relatively narrow leading component followed by a central structure and a broader and fainter trailing component that is probably a blended double. The linear and circular polarization profiles roughly follow the total power. However, while all three approximately peak at the same longitude in the leading component, in the trailing one the maxima of linear and circular polarizations are shifted. In the central structure, both circular and linear depolarizations occur. A change of handedness is displayed by the circular polarization between the two main components. The PAs are mainly flat beneath the leading component, and show a swinging behavior compatible with the RVM predictions in correspondence of the trailing component.

PSR J1629–3636: The total power shows two peaks, with the asymmetric trailing being the brightest and narrowest. The linearly polarized profile mirrors the total intensity but it is narrower, while the circular polarization is visible just in correspondence of the trailing component and it is left-handed. The PA profile is flat for both of the linearly polarized components.

PSR J1648–6044: The profile has a single, asymmetric peak. However, the linear polarization displays two clear components. The PA curve starts with a smooth swing that covers about 50°, and continues with an almost orthogonal jump between the two components of the linearly polarized profile. The last part of the PAs value is practically flat.

PSR J1705–4331: The profile shows a classic double structure with the trailing component slightly brighter than the leading component. There is some circular polarization in the leading component.

PSR J1705–5230: The profile is relatively broad and box-shaped, possibly a blend of several components. The linear polarization shows a first, weak peak followed by a brighter one close to the total power trailing edge. In correspondence of the main, linearly polarized component, the PAs exhibit a practically flat trend.

PSR J1705–6135: The profile is noisy, broad and box-shaped, and it is possibly a blended double. The fraction of linear polarization is relatively high, particularly against the leading part of the profile. The PA curve exhibits a smooth swing across the profile, with a positive slope that covers $\sim$130°.

PSR J1709–4401: The profile of this intermittent pulsar shows a single, relatively narrow and pretty symmetrical peak. The linear polarization has a main component close to the total intensity trailing edge, and it shows a hint of a minor peak on the leading side. The flux density is about one third of the total power one, and their maxima are misaligned. The circular polarization is scarce and noisy. Beneath the weak leading component in the linearly polarized profile, the PA curve starts flat and follows a steep trend with a positive slope. The PA profile under the main linear polarization peak is separated from the leading one by an almost orthogonal jump. It has a flat start too, followed by two swings with positive and negative slopes, respectively.

PSR J1710–2616: This broad profile shows emission over nearly 180° of longitude. A broad leading component is followed by a bridge of emission linking it to a blended double. The linear polarization mostly follows the total intensity but the circular polarization remains low throughout. Although the low linear polarization in the profile center, the characteristic S-shape from the RVM is recognizable. In fact, the large longitude coverage of the pulse profile and the smooth PA swing lends itself well to RVM fitting. Results show that α must be less than 30°, with an impact parameter of ∼20° or less. The location of the inflexion point of the RVM is coincident with the profile center. The pulsar therefore appears to be an almost aligned rotator.

PSR J1716–4711: The profile shows a single, relatively narrow component possibly flanked by two outriders. The circular polarization displays a clear change of sign in correspondence of the profile center.

PSR J1733–5515: The profile shows two blended components of almost equal amplitude. Very small linear or circular polarization can be discerned.

PSR J1744–5337: The profile is affected by the interstellar scattering. It shows a broad and asymmetric leading component blended with a second one. The linear polarization profile is significant especially in the second half of the pulse profile. The PA curve is flat.

PSR J1745–3812: The profile shows a single and slightly asymmetric component with low circular polarization. In spite of a moderate degree of linear polarization, we are not able to obtain a RM value for this pulsar.

PSR J1749–4931: This single-peaked profile shows no clear signs of circular polarization, while the linear polarization is present but weak.

PSR J1802–3346: This noisy and box-shaped profile shows at least two blended components. The linear polarization profile follows the total intensity but it is narrower, and the PA curve displays a swing with negative slope that covers ∼90°.

PSR J1805–2948: This noisy profile shows a single, relatively broad and asymmetric component. There appears to be a linearly polarized component on the leading edge of the profile with a flat PA swing.

PSR J1811–4930: The profile of this intermittent pulsar is a blended double with the trailing component brighter. The linear polarization follows the total power, though it is narrower. On the other hand, the circular polarization peaks where L is fainter. The PA profile shows a steep swing with negative slope in correspondence of the leading component that covers about 130°, while it is flat beneath the trailing.

PSR J1846–4249: This profile shows two blended peaks. The linear and circular polarizations, however, exhibit a single, box-shaped component at the center of the pulse profile. The PA curve shows a steep swing spanning 80°.

2.4.3 Discussion

In our sample, the percentage of the linear polarization, $L\%$, ranges from a few percent to almost 40%. However, only two of the sources (PSR J1614–3846 and PSR J1705–6135) approach the aforementioned upper limit: the mean of $L\%$ is ∼16.

The dependence of $L\%$ on the pulsar spin-down luminosity:

Name	P [s]	W_{10} [ms]	W_{50} [ms]	Log $\dot{E}$	S0 [mJy]	$L\%$	$V\%$	$\|V\|\%$	RM [rad m^{-2}]	DM [pc cm^{-3}]	Distance [kpc]	$< B_{\|\|} >$ [μG]	Log τ_C
J0807−5421	0.527	17	11	32.0	0.35(1)	14.5(7)	3(1)	5.8(6)	−65(3)	165	0.26	−0.48	7.3
J0905−6019	0.341	14	6	32.7	0.36(1)	5.8(7)	1(1)	1.3(7)	−63(23)	91	2.9	−0.85	7.0
J0912−3851	1.526	48	38	31.6	0.14(1)	24(1)	−1(1)	10(1)	85(16)	71	0.5	1.47	6.8
J0949−6902	0.64	10	4	32.0	0.31(1)	6.5(8)	2(1)	3.6(7)	−58(14)	93	2.9	−0.77	7.2
J1036−6559	0.534	16	9	32.5	0.27(1)	12(1)	3(1)	5.2(9)	−88(20)	158	4.0	−0.69	6.8
J1237−6725	2.111	40	30	31.0	0.48(2)	4.8(9)	0(1)	1.6(8)	24(14)	176	3.9	0.17	7.2
J1251−7407	0.327	14	3	32.6	0.24(1)	23(1)	6(2)	6(1)	−121(9)	89	2.4	−1.66	7.2
J1331−5245	0.648	43	27	31.9	0.32(2)	30(1)	16(1)	17(1)	83(5)	148	4.2	0.69	7.3
J1409−6953	0.529	31	24	32.4	0.26(2)	16(1)	−3(2)	8(1)	−51(10)	168	4.5	−0.37	7.0
J1432−5032	2.035	52	33	31.4	0.29(2)	18(1)	4(1)	4(1)	11(3)	113	2.8	0.13	6.7
J1443−5122	0.732	117	47	31.5	0.68(3)	22(1)	1(1)	2.6(9)	43(6)	87	1.9	0.61	7.5
J1517−4636	0.887	27	16	32.1	0.37(1)	19.6(9)	5(1)	5.0(8)	−68(7)	126	3.1	−0.66	6.8
J1530−6336	0.91	11	32	31.6	0.43(1)	23.2(8)	17(1)	17.2(7)	195(7)	206	5.0	1.16	7.2
J1534−4428	1.221	178	14	30.6	0.55(3)	28(1)	−2(1)	3(1)	24(6)	137	3.9	0.22	8.0
J1551−4424	0.674	129	27	31.4	1.14(3)	17.1(6)	2(1)	3.2(6)	−32(5)	66	2.4	−0.6	7.8
J1552−6213	0.199	7	3	32.1	0.34(2)	24(1)	0(1)	1(1)	42(14)	122	2.66	0.43	8.1
J1612−5805	0.616	22	4	32.2	0.31(2)	16(1)	3(1)	9(1)	−21(12)	172	3.6	−0.15	7.0
J1614−3846	0.464	45	17	32.6	0.18(2)	31(2)	3(3)	3(2)	45(9)	111	2.7	0.51	6.9
J1622−3751	0.731	48	24	32.4	0.20(1)	30(1)	7(2)	9(1)	85(7)	154	3.9	0.69	6.7
J1626−6621	0.451	39	3	32.5	0.19(2)	20(1)	12(3)	14(1)	39(12)	84	2.2	0.58	7.0
J1627−5936	0.354	159	85	30.8	1.62(4)	22.2(6)	1.3(9)	7.0(6)	89(5)	99	2.2	1.11	8.9

Table 2.1: Pulsars for which RM can be determined. We show the spin period (P), the profile widths at 10% (W_{10}) and 50% (W_{50}) of the total intensity peak, the logarithm of the spin down luminosity (Log$\dot{E}$), the total intensity flux ($S0$), the percentages of the linear, the circular and the absolute value of the circular polarizations ($L\%$, $V\%$, $|V|\%$), the rotation and the dispersion measures (RM and DM), the DM derived distance from the Sun (via the NE2001 electron density model from Cordes and Lazio, 2002, that gives uncertainties up to about 30%), the average value of the average magnetic field along the line of sight ($< B_{||} >$) and the logarithm of the characteristic age (Log τ_C). 1 σ errors on the last digit(s) are reported in parentheses. 3 σ errors are reported for $S0$.

Name	P [s]	W_{10} [ms]	W_{50} [ms]	Log $\dot{E}$	S0 [mJy]	$L\%$	$V\%$	$\lvert V\rvert\%$	RM [rad m^{-2}]	DM [pc cm^{-3}]	Distance [kpc]	$< B_{\lvert\lvert} >$ [μG]	Log τ_C
J1629−3636	2.988	41	12	31.0	0.20(2)	29(1)	2(2)	2(1)	0(4)	101	2.4	−0.001	6.8
J1648−6044	0.584	31	12	31.9	0.66(2)	19.7(7)	0(1)	0.3(6)	59(3)	106	2.6	0.69	7.3
J1705−5230	0.231	14	21	32.2	0.60(2)	15.6(9)	1(1)	3(1)	−20(11)	164	3.8	−0.15	7.9
J1705−6135	0.809	85	43	30.6	0.30(3)	34(1)	2(3)	5(1)	75(11)	95	2.5	0.98	8.4
J1709−4401	0.865	12	24	32.7	1.15(3)	21.5(5)	7.9(8)	7.9(5)	−122(2)	225	4.4	−0.67	6.3
J1710−2616	0.954	393	99	30.0	1.40(5)	32.5(8)	2(1)	4.4(7)	−9(3)	111	2.6	−0.1	8.9
J1744−5337	0.356	49	18	32.2	0.39(2)	25(1)	4(1)	6(1)	38(9)	109	3.0	0.43	7.5
J1749−4931	0.446	8	13	32.4	0.15(1)	11(2)	0(3)	0(2)	41(19)	55	1.4	0.93	7.1
J1802−3346	2.461	77	120	30.5	0.20(2)	28(2)	1(3)	1(2)	236(17)	217	5.4	1.35	7.5
J1805−2948	0.428	22	10	32.4	0.18(1)	16(1)	1(2)	1(1)	23(21)	167	3.77	0.17	7.2
J1811−4930	1.433	39	11	31.5	0.46(2)	23.2(8)	−8(1)	11.0(8)	42(6)	44	1.2	1.19	7.0
J1846−4249	2.273	67	60	30.6	0.29(1)	13.6(9)	8(1)	8.0(8)	82(10)	62	1.8	1.63	7.5

Table 2.1: (continued)

Name	P [s]	W_{10} [ms]	W_{50} [ms]	Log $\dot{E}$	S0 [mJy]	L%	V%	|V|%	DM [pc cm^{-3}]	Log τ_C
J0919−6040	1.217	52	26	29.3	0.23(1)	2(1)	7(1)	7(1)	82	9.3
J1054−5946	0.228	29	7	32.8	0.23(2)	5(2)	3(2)	5(1)	253	7.2
J1105−4353	0.351	22	12	33.4	0.17(2)	21(2)	4(3)	4(2)	46	6.3
J1143−5536	0.685	24	12	31.8	0.25(1)	0(1)	2(1)	2(1)	185	7.3
J1346−4918	0.3	18	10	31.7	0.70(2)	6.9(6)	3.9(9)	5.6(5)	74	8.1
J1416−5033	0.795	25	12	31.0	0.13(1)	14(2)	0(3)	3(2)	58	8.0
J1539−4835	1.273	91	18	31.4	0.21(2)	0(1)	2(3)	8(1)	118	7.2
J1607−6449	0.298	19	3	31.6	0.22(2)	10(1)	−6(2)	12(1)	89	8.3
J1625−4913	0.356	23	9	33.8	0.22(2)	1(2)	2(3)	2(2)	720	5.9
J1634−5640	0.224	15	8	32.2	0.24(2)	2(1)	1(2)	3(1)	149	7.9
J1647−3607	0.212	15	5	32.7	0.17(2)	11(2)	−2(4)	2(2)	222	7.4
J1700−4422	0.756	72	45	30.6	0.24(3)	7(2)	7(3)	13(2)	425	8.5
J1705−4331	0.223	23	6	32.4	0.43(2)	3(1)	3(1)	3(1)	185	7.7
J1716−4711	0.556	15	4	32.3	0.31(2)	5(1)	6(1)	19.3(9)	287	7.0
J1733−5515	1.011	69	45	31.3	0.38(3)	6(1)	0(2)	1(1)	84	7.5
J1745−3812	0.698	24	11	32.4	0.28(2)	11(1)	5(2)	5(1)	160	6.7

Table 2.2: Pulsars for which no RM can be determined. Parameters and errors like in Table 2.1.

$$\dot{E} \simeq 3.95 \times 10^{31} erg\ s^{-1} \left(\frac{\dot{P}}{10^{-15}}\right) \left(\frac{P}{s}\right)^{-1} \tag{2.26}$$

where $\dot{P}$ is the spin period derivative (Lorimer and Kramer, 2005), is reported by von Hoensbroech and Xilouris (1997), Crawford et al. (2001) and Johnston and Weisberg (2006). These authors noticed that higher values of $\dot{E}$ gave higher values of $L\%$. This trend was better modeled by Weltevrede and Johnston (2008), who found that the correlation between the two quantities is not linear. They identified two main regions, a low $\dot{E}$ (less than 5×10^{33} erg s^{-1}), low $L\%$ (less than 50%) area and a high $\dot{E}$ (more than 2×10^{35} erg s^{-1}), high $L\%$ (exceeding 50%) one, divided by a narrow transition zone. As can be seen from Figure 2.6, the results derived from our low $\dot{E}$ sample do not conflict with Weltevrede and Johnston (2008): all of the pulsars (except one) belong to the low $\dot{E}$ interval and show $L\%$ smaller than 40%. Moreover, no clear correlation of $L\%$ vs. $\dot{E}$ is present over the low $\dot{E}$ sample.

In Figure 2.7 we show the characteristic age, τ_C:

$$\tau_C = \frac{P}{2\dot{P}} s \tag{2.27}$$

plotted versus $L\%$ and $|V|\%$ (that is the percentage of the absolute circular polarization) and compare our results with Gould and Lyne (1998). Since τ_C of the pulsars in our sample (except PSR J1625–4913) exceeds 1 Myr, according to the results of Gould and Lyne (1998), values of $L\%$ around 20% are expected. Although a large degree of scatter is present in the sample, the average values of $L\%$ are in fact between 10% and 20%. Regarding the percentage of $|V|$, we find a less pronounced degree of scatter in the data, and generally lower values of the average $|V|\%$ with respect to the results of Gould and Lyne (1998). We expected values around 8% for 10^6 Myr $\leq \tau_{\rm C} \leq 10^7$ Myr, and slightly higher results for older ages. We instead find a generally flat trend when the values of $|V|\%$ are averaged over the six bins in τ_C, into which our sample has been split. In particular, the average $|V|\%$ is $\sim$6$\pm$3 for pulsars with $\tau_C \geq 10^7$ Myr yrs, fully compatible with the value of $\sim$6$\pm$5 for pulsars with $\tau_C \leq 10^7$ Myr yrs.

For the majority of the pulsars in our sample, we can recognize the presence of more than one component in the profiles. This is not unexpected since pulsars of an advanced age typically have more complicated profiles than younger

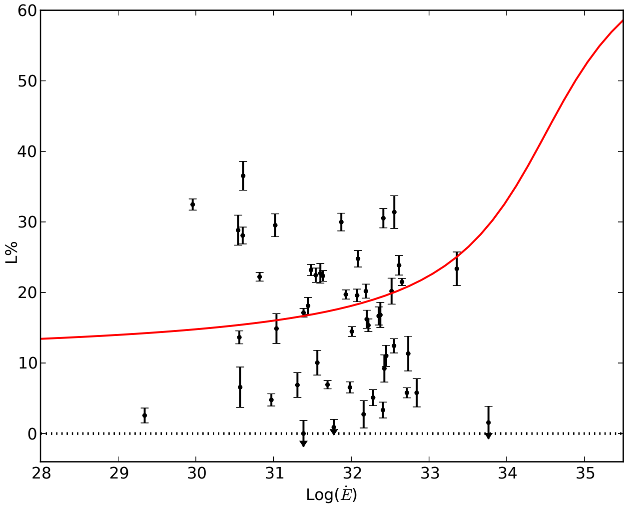

Figure 2.6: Percentage of linear polarization against the spin-down luminosity $\dot{E}$. The black points represent the individual pulsars of our sample with 1 σ error bars (the arrows imply an upper limit), while the red line is the fit reported in Weltevrede and Johnston (2008).

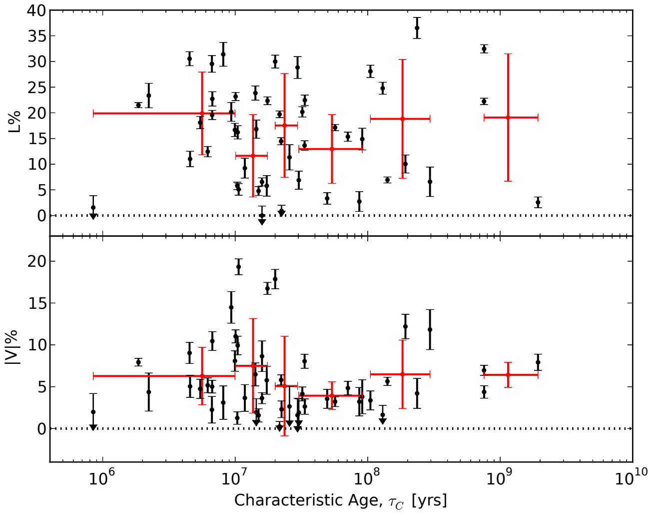

Figure 2.7: Percentage of linear polarization against the characteristic age in the top panel, and percentage of absolute circular polarization against the characteristic age in the bottom panel. The black points represent the individual pulsar of our sample with 1 σ error bars (the arrows imply an upper limit), while the red points and the vertical and horizontal bars represent the average over suitable groups of pulsars, the scatter and the range of age involved in the computation of the mean, respectively.

objects (Rankin, 1983; Lyne and Manchester, 1988; Rankin, 1993; Johnston and Weisberg, 2006; Karastergiou and Johnston, 2007). Karastergiou and Johnston (2007) attribute this evidence to the location of the emitting regions crossed by the line of sight, assuming that each of them corresponds to one component in the profile. In particular, at a fixed observing frequency, the radio emission in young pulsars should be produced from a limited range of altitudes above the neutron star surface. This range widens and descends to lower heights in the magnetosphere with increasing age of the pulsar. According to the model presented by Karastergiou and Johnston (2007), this naturally increases the number of emitting regions crossed by the observer line of sight, and hence the number of components in the profile. A large fraction of the profiles in our sample show a blended double, i.e. the superposition of two main components that ranges from barely distinguishable (as in PSR J0807–5421) to well (as in PSR J0912–3851) visible. There is also a tendency for the trailing component to be brighter than the leading one. According to literature (i.e. Rankin 1983), a double component profile should indicate a mainly conal emission. Emission structures that are not well-defined are also observed, the clearest example of which is for PSR J1534–4428. Emission bridges are also exhibited among otherwise separated components, as in PSRs J1627–5936 and J1710–2616. Given the relatively small S/N of the majority of the pulsars, it is not easy to distinguish the occurrence of multiple components from the case of pure double profiles. Nevertheless, some objects certainly show at least three components, e.g. PSRs J1251–7407, J1607–6449 and J1802–3346.

The linear polarization, when present, follows the total intensity in the majority of the cases, although it often shows a general edge depolarization that causes a narrowing in the polarization profile, as illustrated in PSRs J1517–4636 and J1811–4930. The phenomenon of the linear depolarization is usually explained via the superposition of two emission modes that are in competition in pulsars (Stinebring et al., 1984).

The circular polarization profiles are often barely visible, but show some cases of change in handedness between the components (as in PSRs J0807–5421, J1612–5805, J1627–5936) or across the profile (as in PSRs J1346–4918 and J1716–4711).

As mentioned in Section 2.3, in those pulsars (9 over the total sample of 34 objects for which RM has been determined) that show more than one peak in the linear polarization profile, we separately fit for the RM component by component. In the majority of the cases, we obtain fully compatible (at 1 σ) RM values. In PSRs J0912–3851 and J1629–3636 the agreement is marginally accomplished only by the overlap of the extremes of the respective 1 σ uncertainties intervals. However, this is expected on a statistical bases given the available sample of 9 sources.

Pulsars RM and Galactic Magnetic Field

One of the uses of polarization analysis is in probing the magnetic field structure of the medium crossed by the radiation. A polarized signal that propagates through an ionized and magnetized medium (see §3) undergoes differential propagation velocity between its (right- and left-handed) components. This effect, known as Faraday rotation, that is a birefringence phenomenon, induces a rotation in the PA. This is quantified through the RM, which depends on the ionized medium density and the magnetic field component along the line of sight. For pulsars, the polarized signal passes across three different kinds of ionized and magnetized medium: the pulsar magnetosphere, the Milky Way interstellar medium and Earth ionosphere. In pulsars, we can also quantify the average density of the ionized medium along the line of sight via the dispersion measure (DM) parameter and a combination of the RM and DM allows a direct measurement of the magnetic field along the line of sight.

Several attempts have been made to apply pulsar polarization analysis to probe the Galactic magnetic field structure (Manchester, 1972; Manchester and Taylor, 1977; Thomson and Nelson, 1980; Lyne and Smith, 1989; Weisberg et al., 2004). In particular, the results obtained by Han and Qiao (1994); Han et al. (1999); Han et al. (2002, 2006) and Noutsos et al. (2008) suggest that the large scale in the magnetic field structure of the Milky Way disk is compatible with a bi-symmetric spiral, where the magnetic field in the spiral arms is mainly counter-clockwise if seen from the Galactic north, and the field in between the arms is chiefly clockwise (Sofue and Fujimoto, 1983). On the other hand, the work of Vallée (2005) supports a general clockwise orientation of the large scale Galactic magnetic field, with the presence of a counter-clockwise annulus included between 4 and 6 kpc from the Galactic Centre. It is clearly necessary to increase the RM sample in order to discriminate among

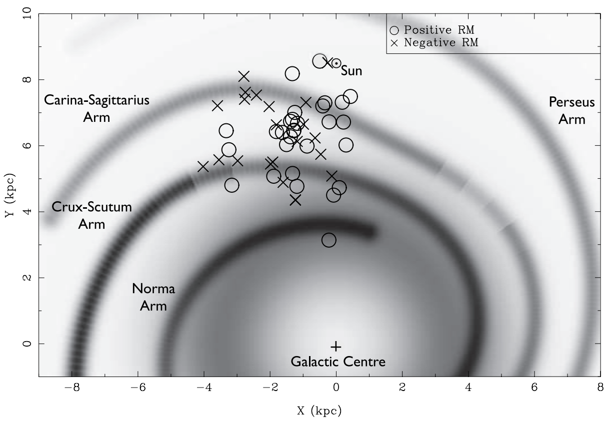

Figure 2.8: A scheme of the Milky Way seen from the North Galactic Pole. In dark grey are shown the galaxy arms as from Taylor and Cordes (1993). The symbol ⊙ indicates the Sun, the circles and the crosses indicate the pulsars of our sample with positive and negative values of RM, respectively. The distances of the pulsars have been computed using the NE2001 electron model (Cordes and Lazio, 2002), prone to errors on the calculated distance up to the 30%

the various hypotheses, and to guard against interstellar medium fluctuations and local turbulence in the magnetic field that could bias the RM estimation. An additional complication in this framework is RM fluctuation as a function of the pulse longitude. In particular, three sources of additional PA rotation beyond the large scale Galactic magnetic field have been identified (Li and Han, 2003; Ramachandran et al., 2004; Karastergiou, 2009; Noutsos et al., 2009): the incoherent superposition of quasi-orthogonal polarization modes, the pulsar magnetosphere and scattering in the interstellar medium. In particular the latter is indicated as the most probable reason for the detected fluctuations.

We have collected all the sources discovered so far by the HTRU southern survey and having a measured value of RM. The list totals 51 pulsars, resulting from the present work, as well as from Bailes et al. (2011); Keith et al. (2012) and Burgay et al. (2013). These values can be used to obtain an estimate of the average intensity and sign of the projection of the Galactic magnetic field vector ($< \mathrm{B}_{||} >$) along the 51 lines of sight to the pulsars. In fact, the RM is defined as:

$$\mathrm{RM} = \frac{e^3}{2\pi {m_\mathrm{e}}^2 c^4} \int_0^\mathrm{d} n_\mathrm{e}(l) B_{||}(l)\, dl \qquad (2.28)$$

where e is the electron charge, m_e is the electron mass, d is the distance between the emitting object and the observer, $n_{\rm e}$ is the electron column density and $\rm B_{||}$ is the projection of the magnetic field vector along the line of sight. Since the DM is defined as:

$$\mathrm{DM} = \int_0^{\rm d} n_{\rm e}(l)\,dl \tag{2.29}$$

is it possible to obtain $< \rm B_{||} >$ as:

$$\begin{aligned} < \mathrm{B}_{||} > \quad &= 1.232 \frac{\int_0^d n_{\rm e}(l)\mathrm{B}_{||}(\mathrm{l})\mathrm{dl}}{\int_0^d n_{\rm e}(l)dl} \\ &= 1.232 \left(\frac{\mathrm{RM}}{\mathrm{m^{-2}rad}}\right) \left(\frac{\mathrm{DM}}{\mathrm{cm^{-3}pc}}\right)^{-1} \mu\mathrm{G}. \end{aligned} \tag{2.30}$$

The resulting values of $< B_{||} >$ are reported in the second last column of Table 2.1. For each of the considered objects, we also derive a measurement of the distance (see Table 2.1) using the DM value of each object and the NE2001 electron density model (Cordes and Lazio, 2002). Assuming these distances, all the selected pulsars are located within 2 kpc in height from the Galactic plane and thus the lines of sight to all of them are expected to be useful to investigate the behavior of the Galactic magnetic field in the proximity of the Galactic disk (Noutsos et al., 2008). In Figure 2.8 we report the positions - projected onto the Galactic plane - of the objects of our sample.

Our sample does not support the hypothesis suggested by Vallée (2005) of a prevailing counter-clockwise direction of the Galactic magnetic field in an annulus included between 4 and 6 kpc from the Galactic center and a prevailing clockwise direction outside the annulus. First, looking at Figure 2.8 it is evident the occurrence of opposite signs for the values of RMs for many pairs of pulsars which are very close to each other. As already pointed out by other authors (e.g. Noutsos et al. 2008), this is an indication for variations of intensity and direction of the Galactic magnetic field also over small scales. To be more quantitative, we also compute (as first suggested by Lyne and Smith 1989), the average intensity of the magnetic field in the intermediate region between pairs of pulsars:

$$< \mathrm{B}_{||} >_{\rm d_1-d_2} = 1.232 \frac{\Delta\mathrm{RM}}{\Delta\mathrm{DM}} \mu\mathrm{G} \tag{2.31}$$

where $\rm d_1$ and $\rm d_2$ are the distances of the two sources from the Sun and ΔRM and ΔDM are the differences between the RM and the DM values of the two

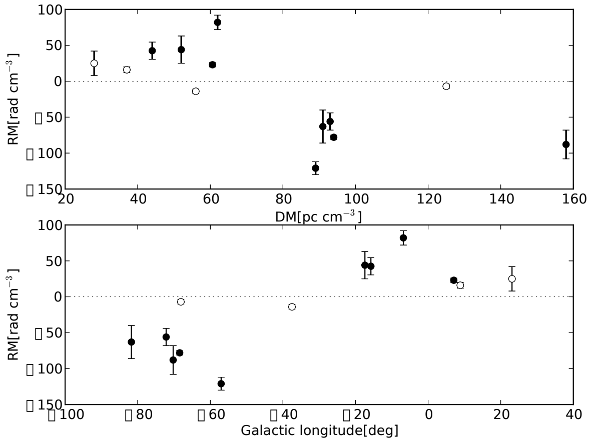

Figure 2.9: In the top panel are shown the RM values for the pulsars the projected positions of which are in agreement with their belonging to the Carina-Sagittarius arm, plotted in function of their DM. In the bottom panel are shown the RM values for the same pulsars plotted in function of their Galactic longitude. Empty circles indicate pulsars with positive Galactic latitude, whereas filled circles are associated with pulsar located at negative Galactic latitude. 1 σ error bars are overlapped to the data points. Note that the error bar associated with some of the data points are too small to be visible.

considered pulsars, respectively. In doing that, we follow the prescription of Noutsos et al. (2008), i.e. investigating pairs of pulsars the projected positions of which are closer than 5° in Galactic longitude. For the limited range in distances and Galactic longitudes of our sample, a counter-clockwise direction for the Galactic magnetic field would correspond to a prevalence of positive values of $< \mathrm{B}_{||} >_{\mathrm{d}_1-\mathrm{d}_2}$ for pairs located in the first Galactic quadrant (Galactic longitudes between 0° and 90°) and a prevalence of negative values of $< \mathrm{B}_{||} >_{\mathrm{d}_1-\mathrm{d}_2}$ for pairs in the fourth Galactic quadrant. At variance with the expectations of the model of Vallée (2005), no trend is recognizable in our sample. In particular, within the annulus mentioned above, the values of $< \mathrm{B}_{||} >_{\mathrm{d}_1-\mathrm{d}_2}$ for 6 pairs of pulsars are compatible with a counter-clockwise direction of the Galactic magnetic field, whereas a clockwise direction is preferred on the basis of 6 other pairs. Similarly, the results for 24 pairs of pulsars would favor a clockwise direction for the region outside the annulus, whilst the consideration of 26 other pairs would suggest the opposite direction[2].

---

[2] The total number of pairs is larger than the number of pulsars of our sample since few pulsars of the sample enter more than one pair.

We also perform a preliminary investigation of the compatibility of our sample with the model of Han et al. (2006), which states the occurrence of a counter-clockwise direction for the Galactic magnetic field along the arms and an opposite direction of that in the inter-arm regions. Given the distances of the pulsars in our sample (typically spanning the range $1-4$ kpc) and the relatively small number of available objects, our investigation focused on the case of the closest arm, i.e. the Carina-Sagittarius arm (see Figure 2.8). We then selected those pulsars whose projected position is compatible with them belonging to the area of the Carina-Sagittarius arm or close (within 0.5 kpc) to that. That choice left us with 13 objects, whose Galactic longitudes span the range between -82° and 23°. Adopting the same criteria as mentioned above, 8 pairs of pulsars can be selected in this region and the related values of $<\mathrm{B}_{||}>_{\mathrm{d}_1-\mathrm{d}_2}$ measured. It results a prevalence of pairs (6 vs 2) indicating a counter-clockwise direction of the Galactic magnetic field along the Carina-Sagittarius arm, nominally in agreement with the model of Han et al. (2006). Figure 2.4.3 indicates that some large scale ordered component of the Galactic magnetic field can indeed be present in the Carina-Sagittarius arm, being reflected in the overall trend for the RM values, which change from positive to negative values with increasing values of DM. Unfortunately our sample is not suitable to test the detailed dependence of RM vs DM inferred by Han et al. (2006) for the objects belonging to the Carina arm and having DM $<$ 200 pc cm^{-3}, i.e. RM $\propto -0.6$ DM, for the pulsars with Galactic longitudes between -76° and -68°. In fact Han et al. used only pulsars at Galactic latitude less than $|8|°$, which are too rare in our sample (resulting from a survey at intermediate and high Galactic latitudes) for a meaningful comparison. However, Figure 2.4.3 also shows that the status of the magnetic field in the Carina-Sagittarius arm is more complex than described by the relatively simple model of Han et al., with a large scatter of values of RM for similar values of DM and the trend in Figure 2.4.3 which is much more evident for the pulsars below the Galactic plane than for the ones at positive Galactic latitudes. As a consequence, additional components in the Galactic magnetic field are likely needed, like those investigated by Noutsos et al. (2008). A significant improvement in the modeling is expected when the sample presented here will be complemented by the discoveries resulting from the low-latitude part of the HTRU survey (Ng et al., in preparation).

2.5 Using the fourth moments of the electric field to study orthogonally polarized modes of pulsar emission

We describe a technique, based on the procedure presented by van Straten (2009), to evaluate the covariance of the Stokes parameters while dealing with data-sets made of single pulses.

As already outlined in Section 2.1, given a statistical sample of electromagnetic waves whose transverse electric field is $\overrightarrow{e}$, the mean Stokes four-vector S describes its second order statistics. If we consider an ensemble of mean Stokes vectors, we can introduce the fourth moment statistics of the electromagnetic waves, represented by the covariance matrix C of the mean Stokes vectors. To refer to a concrete example in pulsar observations, let us assume to observe a pulsar for N of its rotations. As we typically compute phase-resolved averages of the Stokes parameters, let us also fix the phase bin corresponding to the ϕ-th phase longitude of the i-th rotation, ϕ_i. We can thus compute a mean Stokes four-vector, $S_{\phi_{\mathrm{i}}}$, that describes the polarization state at phase bin ϕ_{i}. Collecting all the N mean Stokes four-vectors at the same phase, one can compute the covariance matrix C related to the queried phase longitude as:

$$C_\phi = \frac{\sum_{\mathrm{i}} \left(S_{\phi_{\mathrm{i}}} - \overline{S_\phi}\right) \otimes \left(S_{\phi_{\mathrm{i}}} - \overline{S_\phi}\right)}{N-1} = \left\langle \left(S_\phi - \overline{S_\phi}\right) \otimes \left(S_\phi - \overline{S_\phi}\right) \right\rangle \tag{2.32}$$

where $\overline{S_\phi}$ is:

$$\overline{S_\phi} = \frac{\sum_{\mathrm{i}} S_{\phi_{\mathrm{i}}}}{N} \tag{2.33}$$

We will show that it is not possible to distinguish certain basic properties of the polarized emission from a pulsar using only the second order statistics given by the Stokes parameters. We will demonstrate that features of OPM may be constrained using its fourth order statistics. In fact, as for each phase longitude we have an ensemble of mean Stokes four-vectors ($S_{\phi_{\mathrm{i}}}$ in the above example) we have also a distribution of points in the Poincaré sphere. Solving the eigenvector problem of the $Q-U-V$ minor of the covariance matrix C_ϕ, and thus obtaining the eigenvectors S_1, S_2, S_3 and corresponding eigenvalues $\lambda_1 > \lambda_2 > \lambda_3$, it is possible to characterize the distribution geometry. This geometrical characterization, derived from the fourth order statistics of $\overrightarrow{e}$, allows to constrain OPM features that the second order statistics alone can not distinguish. We note that the eigenvalues of the covariance matrix obtained from the Stokes parameters are the variances of the Stokes parameters themselves. We will also show that the polarization state introduced in Section 2.2 as "superposed OPMs" is more correctly described as "disjoint unresolved OPMs".

We are going to consider different combinations of pulsar polarization states, and derive the expected covariance matrix of each combination.

Hereafter we will consider independent (incoherent and with uncorrelated intensities) OPM populations of electromagnetic waves, $\mathfrak{A}$ and $\mathfrak{B}$, whose population mean Stokes parameters are A and B, that characterize N_{A} and N_{B} ensembles of statistical samples of transverse electric fields $\overrightarrow{e_{\mathrm{A}}}$ and $\overrightarrow{e_{\mathrm{B}}}$. Note that with large values of N_{A} and N_{B}, population mean Stokes parameters A and B tend to a multivariate normal distribution (van Straten, 2009). The mean Stokes four-vector of the i-th statistical sample of $\overrightarrow{e_{\mathrm{A}}}$ is A_{i}. The covariance matrices of the ensembles are C_{A} and C_{B}.

In the following we will also use the inner product, Lorentz invariant and Euclidean norm definitions introduced in Equations 2.11 2.13 and 2.14:

$$\begin{aligned} A \circ B &\equiv A^{\mathrm{k}} B_{\mathrm{k}} = \eta^{\mathrm{kk}} A_{\mathrm{k}} B_{\mathrm{k}} = A_0 B_0 - \mathbf{A} \cdot \mathbf{B} \\ A^2 &\equiv A \circ A = A_0^2 - |\mathbf{A}|^2 \\ \|A\|^2 &= A_0^2 + |\mathbf{A}|^2 \end{aligned} \tag{2.34}$$

As a preliminary consideration, we note that the covariance matrix that we expect to compute from unpolarized radiation is proportional to the unity matrix. In fact, as the eigenvectors and eigenvalues of the $Q-U-V$ minor of the covariance matrix describe the geometry of the polarization vector distribution in the Poincaré sphere, a distribution obtained by unpolarized radiation is not supposed to have any preferential direction or shape (that would denote the presence of polarized emission). It would then result in a spheroid, centered on the axis origin. As the three dimensions of a sphere are equivalent, its eigenvalues should be as well.

All of the above considerations result in a covariance matrix proportional to the unity matrix.

Single mode regime, we refer to a single mode regime when the electromagnetic waves in all the considered stochastic samples are only $\overrightarrow{e_{\mathrm{A}}}$ or $\overrightarrow{e_{\mathrm{B}}}$, let us say $\overrightarrow{e_{\mathrm{A}}}$. The elements of the covariance matrix that corresponds to this polarization regime is (van Straten, 2009):

$$C_{\text{single}} = \zeta^2 \left(2A \otimes A - \eta A \circ A\right) \tag{2.35}$$

where η is the Minkowski metric tensor defined as in Equation 2.12, ζ^2 is a dimensionless variance defined as $1/2N$, where N is the number of independent and identically distributed Stokes parameters (van Straten, 2009) and the inner product $S \circ S$ is defined as in Equation 2.13.

As from definition in Equation 2.35, assuming that the mode population we are considering is, for simplicity, linearly polarized:

$$A = (I, pI, 0, 0) \tag{2.36}$$

where p is an arbitrary polarization degree (note that, if the mode population is circularly polarized, it is always possible to rotate the base so that $A = (I, pI, 0, 0)$, see Section 2.2 in van Straten 2009), C_{single} is:

$$C_{\text{single}} = \zeta^2 \begin{bmatrix} I^2(1+p^2) & \pm 2I^2 p & 0 & 0 \\ \pm 2I^2 p & I^2(1+p^2) & 0 & 0 \\ 0 & 0 & I^2(1-p^2) & 0 \\ 0 & 0 & 0 & I^2(1-p^2) \end{bmatrix} \tag{2.37}$$

this means that the polarization vector distribution in the Poincaré sphere resembles a prolate ellipsoid, whose major axis is parallel to the average polarization vector $\overrightarrow{p}$. Also notice that this regime predicts a covariance between Stokes I and the eigenvector S_1.

Superposition regime, we refer to a superposition regime when every sample of the electromagnetic wave $\overrightarrow{e}$ is given by:

$$\overrightarrow{e} = \overrightarrow{e_{\mathrm{A}}} + \overrightarrow{e_{\mathrm{B}}} \tag{2.38}$$

that is, the OPM combination occurs at the electric field level. In this case, the mean Stokes parameters $\overrightarrow{S}$ are simply given by:

$$S_{\text{superposed}} = A + B \tag{2.39}$$

Note that if the two modes are orthogonal and have equal polarized fluxes, it is impossible to distinguish the Stokes four-vector representative of the superposed regime with respect to the Stokes four-vector one would expect to compute from unpolarized radiation. As in van Straten (2010), we can define the covariance matrix that corresponds to this polarization regime via Equation 2.35:

$$C_{\text{superposed}} = C_{\text{A}} + C_{\text{B}} + \Xi + \Xi^T \tag{2.40}$$

where C_{A} and C_{B} are defined by Equation 2.35, and Ξ is the cross-covariance matrix:

$$\Xi = \zeta_{\text{A}}\zeta_{\text{B}} \left(2A \otimes B - \eta A \circ B\right) \tag{2.41}$$

As from definition in Equation 2.40, assuming that the mode populations we are considering are, for simplicity, linearly polarized, with similar dimensionless variances ζ^2 and similar intensities:

$$\begin{aligned} A &= (I, pI, 0, 0) \\ B &= (I, -pI, 0, 0) \end{aligned} \tag{2.42}$$

where p is an arbitrary polarization degree, $C_{\text{superposed}}$ is:

$$C_{\text{superposed}} = \zeta^2 \begin{bmatrix} 4I^2 & 0 & 0 & 0 \\ 0 & 4I^2 & 0 & 0 \\ 0 & 0 & 4I^2 & 0 \\ 0 & 0 & 0 & 4I^2 \end{bmatrix} \tag{2.43}$$

that is, it is impossible to distinguish between unpolarized radiation and the superposition of orthogonal modes with equal polarized fluxes.

Composite regime (or **disjoint unresolved regime**), we refer to a composite regime when each sample of the electromagnetic wave is either $\overrightarrow{e_{\text{A}}}$ or $\overrightarrow{e_{\text{B}}}$. That is, the electromagnetic waves from the two modes are not superposed, but both modes contribute to a certain stochastic sample: this is what have been called *superposed regime* in the past OPM literature. The mean Stokes vector of a stochastic sample of electromagnetic wave instances is:

$$S_{\text{composite}} = f_{\text{A}} A + (1 - f_{\text{A}})\, B \tag{2.44}$$

where f_{A} is the fraction of electromagnetic wave instances that belong to mode $\mathfrak{A}$ in a stochastic sample. Note that if $f_{\text{A}} = 0.5$ and the two modes are orthogonal with equal polarized fluxes it is impossible to distinguish the Stokes four-vector representative of the composite regime with respect to the Stokes four-vector one would expect to compute from unpolarized radiation. The covariance matrix that corresponds to this polarization regime is:

$$C_{\text{composite}} = f_{\text{A}} C_{\text{A}} + (1 - f_{\text{A}})\, C_{\text{B}} \tag{2.45}$$

where C_{A} and C_{B} are defined as in Equation 2.35.

As from definition in Equation 2.45, assuming that the mode populations are described by the mean Stokes four-vectors of Equation 2.42 and that the occurrence frequencies of modes $\mathfrak{A}$ and $\mathfrak{B}$ in the same stochastic sample are equal ($f_{\text{A}} = 0.5$), we have that $C_{\text{composite}}$ is:

$$C_{\text{composite}} = \zeta^2 \begin{bmatrix} I^2(1+p^2) & 0 & 0 & 0 \\ 0 & I^2(1+p^2) & 0 & 0 \\ 0 & 0 & I^2(1-p^2) & 0 \\ 0 & 0 & 0 & I^2(1-p^2) \end{bmatrix} \tag{2.46}$$

That is, as for the single mode regime, we expect the polarization vector distribution in the Poincaré sphere to be a prolate ellipsoid whose major axis is directed along the semi-Stokes parameter that represent the predominant polarization. In contrast with the single mode regime, no covariance is predicted between Stokes I and eigenvector S_1.

Disjoint regime, we refer to a disjoint regime when a fraction F_{A} of entire stochastic samples contains only instances $\overrightarrow{e_{\text{A}}}$ and the complementary fraction $(1 - F_{\text{A}})$ contains only instances $\overrightarrow{e_{\text{B}}}$. The past OPM literature too refers to this regime as “disjoint”, however, it would be more correct to call it “disjoint resolved regime”. In this case, the mean Stokes vector of a stochastic sample is either A or B, depending on which mode is present in the considered sample. An average over all the mean Stokes vectors would give:

$$S_{\text{disjoint}} = F_{\text{A}} A + (1 - F_{\text{A}})\, B \tag{2.47}$$

Again, note that if $F_{\mathrm{A}} = 0.5$ and the two modes are orthogonal with equal polarized fluxes it is impossible to distinguish the Stokes four-vector representative of the disjoint regime with respect to the Stokes four-vector one would expect to compute from unpolarized radiation.
The covariance matrix that corresponds to this polarization regime is:

$$C_{\mathrm{disjoint}} = F_{\mathrm{A}} C_{\mathrm{A}} + (1 - F_{\mathrm{A}})\, C_{\mathrm{B}} + F_{\mathrm{A}} (1 - F_{\mathrm{A}})\, D \tag{2.48}$$

where $D = (A - B) \otimes (A - B)$, C_{A} and C_{B} are defined as in Equation 2.35.

Note that, in the hypotheses assumed at the beginning of the dissertation (that is, the polarized modes are orthogonal and incoherent), only in the disjoint regime it is possible that the variance along the eigenvector S_1 exceeds the variance in Stokes I. This happens because of the contribution of the D matrix.
Assuming that the mode populations are described by the mean Stokes four-vectors of Equation 2.42, and that the stochastic samples characterized by mode $\mathfrak{A}$ or $\mathfrak{B}$ occur with the same frequencies ($F_{\mathrm{A}} = 0.5$), we have that D is:

$$D = \begin{bmatrix} 0 & 0 & 0 & 0 \\ 0 & 4p^2 I^2 & 0 & 0 \\ 0 & 0 & 0 & 0 \\ 0 & 0 & 0 & 0 \end{bmatrix} \tag{2.49}$$

this shows that matrix D only inflates the variance in Stokes Q. The covariance matrix C_{disjoint} is:

$$C_{\mathrm{disjoint}} = I^2 \zeta^2 \begin{bmatrix} 1 + p^2 & 0 & 0 & 0 \\ 0 & 1 + p^2 + 4\zeta^{-2} p^2 & 0 & 0 \\ 0 & 0 & 1 - p^2 & 0 \\ 0 & 0 & 0 & 1 - p^2 \end{bmatrix} \tag{2.50}$$

As we stated at the end of Section 2.2, in the literature there has been a misunderstanding at the basis of the discussion about the composition state of the OPMs - superposed versus disjoint -. What the literature means with OPM *superposition* is what we call, in the above text, *composite regime*: an addition of the Stokes parameters given by the electric field instances that are present in the considered phase bin. We have shown that addition of the Stokes parameters (the composite regime) is not equivalent to the addition of the electric field vectors (the superposed regime). Although the two regimes result in the same mean Stokes parameters, they can be distinguished by the fourth moments of the electric field. Moreover, the fact that the literature *superposed OPMs* is kind of dependent on the phase bin resolution has never been properly taken into account. Our guess is that increasing the phase resolution of the instrument (virtually at an infinitesimal level), the composite regime would disappear, leaving only the unpolarized, the superposition or the disjoint regime.

2.6 A case of study: a first application to real data

The Vela pulsar (PSR J0835-4510) is one of the brightest pulsars ever known. Discovered in association with a supernova remnant (Large et al., 1968) in the southern sky, it is a young (11.2 kyr, Taylor et al. 1993) close (290 pc, Caraveo et al. 2001) and glitchy (Urama and Okeke, 1999; Yu et al., 2013) pulsar, characterized by a spin period of 89 ms. The linear polarization percentage of its single pulses is extraordinarily high (Manchester et al., 1980), close to 100% at the peak, and the behavior of the polarization angle motivated the development of the RVM (Radhakrishnan and Cooke, 1969). Nevertheless, it also presents deviations from the classical S-swing of the position angle, such as an orthogonally polarized, bright component that occurs with a very low frequency in the trailing edge of the pulse profile (Johnston et al., 2001). Moreover, its "giant micropulses" (Palfreyman et al., 2011) and microstructures (Kramer et al., 2002) have been studied in great detail.

We test the method presented in Section 2.5 on the Vela pulsar. Using a single pulse data set obtained with the Parkes radio telescope. The data set is 1 hour-long, and it was collected in July 2012 at an observing frequency and bandwidth of, respectively, 3 GHz and 400 MHz with the CASPER Swinburne Parkes (CASPSR) backend. The single pulses were coherently dedispersed, isolated using an up-to-date ephemeris, calibrated in polarization and flux and split in 512 frequency channels. Due to a failure of one of the CASPSR disks during the observations, about 2×10^4 pulses can be used instead of 4×10^4. Figure 2.10 shows a waterfall plot of the first 20 pulses in the data set.

We apply the method described in Section 2.5 to study the polarization state. At first, we grouped the individual single pulses into 8-second segments. We then obtain the covariance matrix of the Stokes parameters from the approximately 90 pulses included in each group after integrating them in

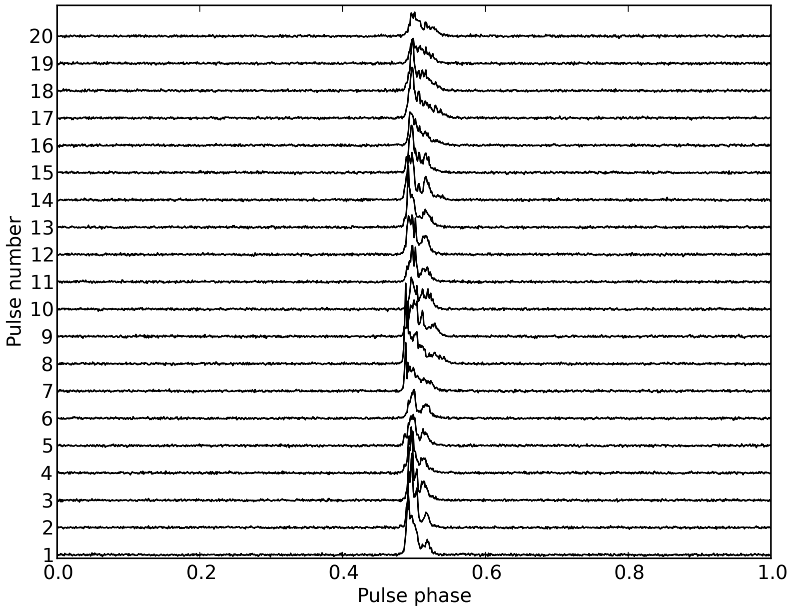

Figure 2.10: First 20 pulses of the data set as shown in a waterfall plot.

frequency, and solve the eigenvector problem for the $Q-U-V$ minor to obtain its eigenvalues. The computed values, however, do not correspond exactly to the unbiased variances in Stokes Q, U and V. In fact, the obtained measures are artificially increased by the instrumental noise, which contributes to inflate the variances in the Stokes. For this reason, once obtained the phase per phase variances in Stokes I, Q, U and V, we computed an off-pulse, mean variance to be subtracted as noise contribution to each of the on-pulse eigenvalues:

$$\begin{aligned}
\sigma^2_{\mathrm{noise,I}} &= \frac{1}{n_{\mathrm{off,end}}} - n_{\mathrm{off,start}} \sum_{i=n_{\mathrm{off,start}}}^{n_{\mathrm{off,end}}} \left(I_{\mathrm{i}} - \bar{I}\right)^2 \\
\sigma^2_{\mathrm{noise,Q}} &= \frac{1}{n_{\mathrm{off,end}}} - n_{\mathrm{off,start}} \sum_{i=n_{\mathrm{off,start}}}^{n_{\mathrm{off,end}}} \left(Q_{\mathrm{i}} - \bar{Q}\right)^2 \\
\sigma^2_{\mathrm{noise,U}} &= \frac{1}{n_{\mathrm{off,end}}} - n_{\mathrm{off,start}} \sum_{i=n_{\mathrm{off,start}}}^{n_{\mathrm{off,end}}} \left(U_{\mathrm{i}} - \bar{U}\right)^2 \\
\sigma^2_{\mathrm{noise,V}} &= \frac{1}{n_{\mathrm{off,end}}} - n_{\mathrm{off,start}} \sum_{i=n_{\mathrm{off,start}}}^{n_{\mathrm{off,end}}} \left(V_{\mathrm{i}} - \bar{V}\right)^2
\end{aligned} \tag{2.51}$$

Thus, what we assume to be our unbiased, on-pulse variances are:

$$\begin{aligned}
\sigma^2_{\mathrm{I}} &= \sigma^2_{\mathrm{on,I}} - \sigma^2_{\mathrm{off,I}} \\
\sigma^2_{\mathrm{Q}} &= \sigma^2_{\mathrm{on,Q}} - \sigma^2_{\mathrm{off,Q}} \\
\sigma^2_{\mathrm{U}} &= \sigma^2_{\mathrm{on,U}} - \sigma^2_{\mathrm{off,U}} \\
\sigma^2_{\mathrm{V}} &= \sigma^2_{\mathrm{on,V}} - \sigma^2_{\mathrm{off,V}}
\end{aligned} \tag{2.52}$$

However, we are aware that this procedure is not sufficient to subtract the noise bias. In fact, the instrumental noise is added to the signal in the context of the superposed regime, as they sum together as electric fields:

$$\overrightarrow{e} = \overrightarrow{e}_{\mathrm{signal}} + \overrightarrow{e}_{\mathrm{noise}} \tag{2.53}$$

where $\overrightarrow{e}$ is the electric field that reaches the backend, e_{signal} and e_{noise} are, respectively, the electric fields of the signal and of the system equivalent flux density.
Where N and S are the Stokes four-vectors given by the instrumental noise and the unbiased signal, the Stokes four-vector that we compute, S_{biased}, is:

$$S_{\mathrm{biased}} = S + N. \tag{2.54}$$

Whereas a direct subtraction of the noise contribution is sufficient to debias the Stokes parameters, this is not enough to debias the covariance matrix. This can be shown using the covariance matrix formula of Equation 2.40:

$$C_{\mathrm{biased}} = C_{\mathrm{S}} + C_{\mathrm{N}} + \Xi + \Xi^T \tag{2.55}$$

where C_{S} and C_{N} are the covariance matrices for the unbiased signal and the noise as defined by Equation 2.35, and Ξ is given by:

$$\Xi = \zeta_{\mathrm{S}}\zeta_{\mathrm{N}} \left(2S \otimes N - \eta S \circ N\right) \tag{2.56}$$

Therefore, the debias applied using Equations 2.52 compensates for only part of the noise contribution. This inaccuracy in debiasing for the noise contribution is particularly severe if it is highly time-dependent. Figure 2.11 shows the temporal trend of the noise baseline as computed over 30-second sub-integrations of data in the four Stokes parameters. By eye, it is possible to notice how dramatically the baseline varies in only 30 minutes of data-acquisition, especially in Stokes I. The reasons for this behavior are still

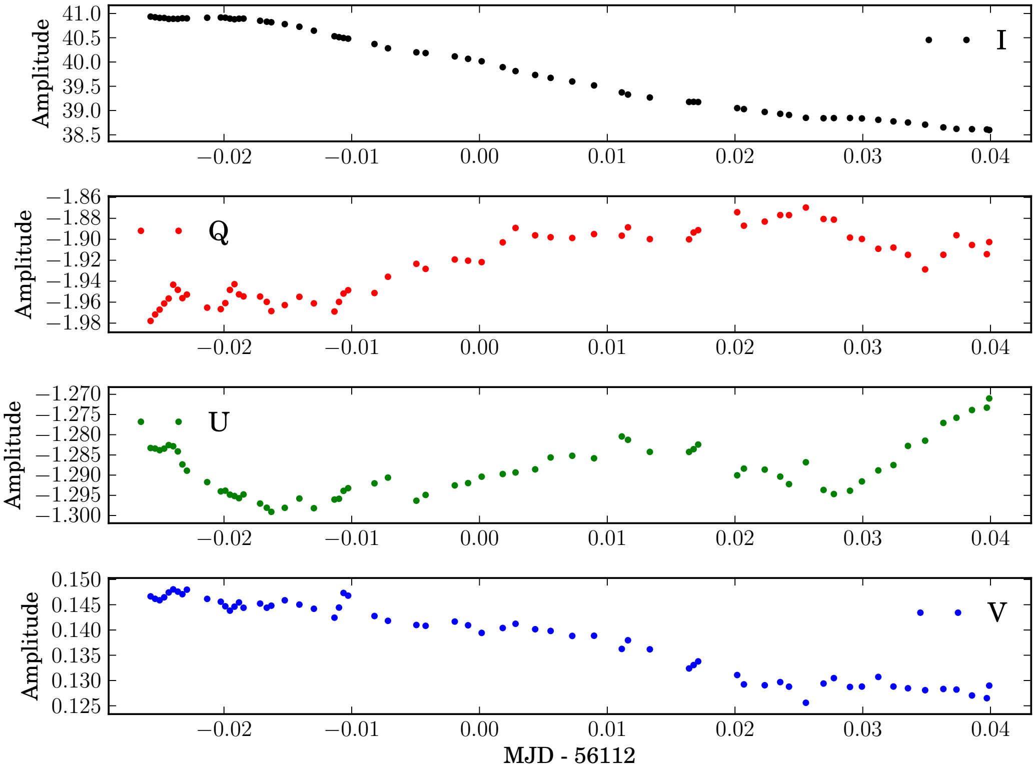

Figure 2.11: Temporal trend of the noise baseline averaged over 30-second subintegrations in the four Stokes parameters (from top to bottom, Stokes I, Q, U, V).

under investigation, as well as how to model matrix Ξ.
The following analysis are thus to be considered preliminary and partial.

The above discussion has implications not only for pulsar polarimetry. For example, a phase-resolved parameter, called *modulation index* m, is largely used in pulsar astronomy to study the variability (modulation) of Stokes I from pulse to pulse. The modulation index is defined as (Jenet and Gil, 2003):

$$m(\phi) = \frac{\sqrt{\langle I(\phi)^2 \rangle - \langle I(\phi) \rangle^2}}{\langle I(\phi) \rangle} = \frac{\sigma_{\rm I}(\phi)}{\langle I(\phi) \rangle} \tag{2.57}$$

where ϕ is the pulse longitude. It is possible to recognize in the numerator the square root of the first element of the covariance matrix. As the only bias removal to be applied to m in pulsar literature (Taylor et al., 1975; Cordes et al., 1978) is the one shown in Equations 2.52, we can conclude that the modulation index studies show still partially biased parameters.

Figure 2.12 shows the pulse profile of the Stokes parameter variances computed from the first 6 of these 8-second long groups, while Figure 2.13 shows the pulse profile of the Stokes parameter variances computed using all the single pulses of the data set.
From the two figures it is evident that for a vast range of phase longitudes, variance in Stokes I and along eigenvector S_1 are basically equal. In the very simplified hypotheses we assumed at the beginning of Section 2.5 (orthogonal and independent modes, similar mode intensities and comparable fractions of occurrence), this would be a hint for single, superposed or composite regime. However, the evident discrepancy between the variances along eigenvectors S_2 and S_3 would exclude the superposed regime. Indeed, no one of the aforementioned regimes predicts that the variances along eigenvectors S_2 and S_3 can differ. Moreover, several phase ranges (especially corresponding to the emission peaks) show a difference also between the variances in Stokes I and along eigenvector S_1. Clearly a neat explanation would requests us to null one or more of the initial hypotheses. For example, mode $\mathfrak{A}$ and $\mathfrak{B}$ may sum coherently or being non-orthogonal: as speculated in van Straten (2009) and van Straten (2010), this would inflate the variance of Stokes I with respect to the one along eigenvector S_1.
A thorough characterization of the covariance matrix in presence of coherent modes is under study, and it will be soon presented in an upcoming publication.

2.7 Summary on applications

We have presented a polarimetric analysis of 49 long-period pulsars discovered as part of the HTRU southern survey. We were able to compute the RM for 34 of them, while 9 objects show almost no polarized signal.

We found that the percentage of L among the pulsars in the sample is mainly around $15-20\%$, in agreement with previous studies (Gould and Lyne, 1998; Weltevrede and Johnston, 2008) for sources with $\dot{E}$ lower than 5×10^{33}erg s^{-1} and a characteristic age larger than 1 Myr. In addition, the mean degree of $|V|$, approximately 6%, is roughly compatible with expectations, although it

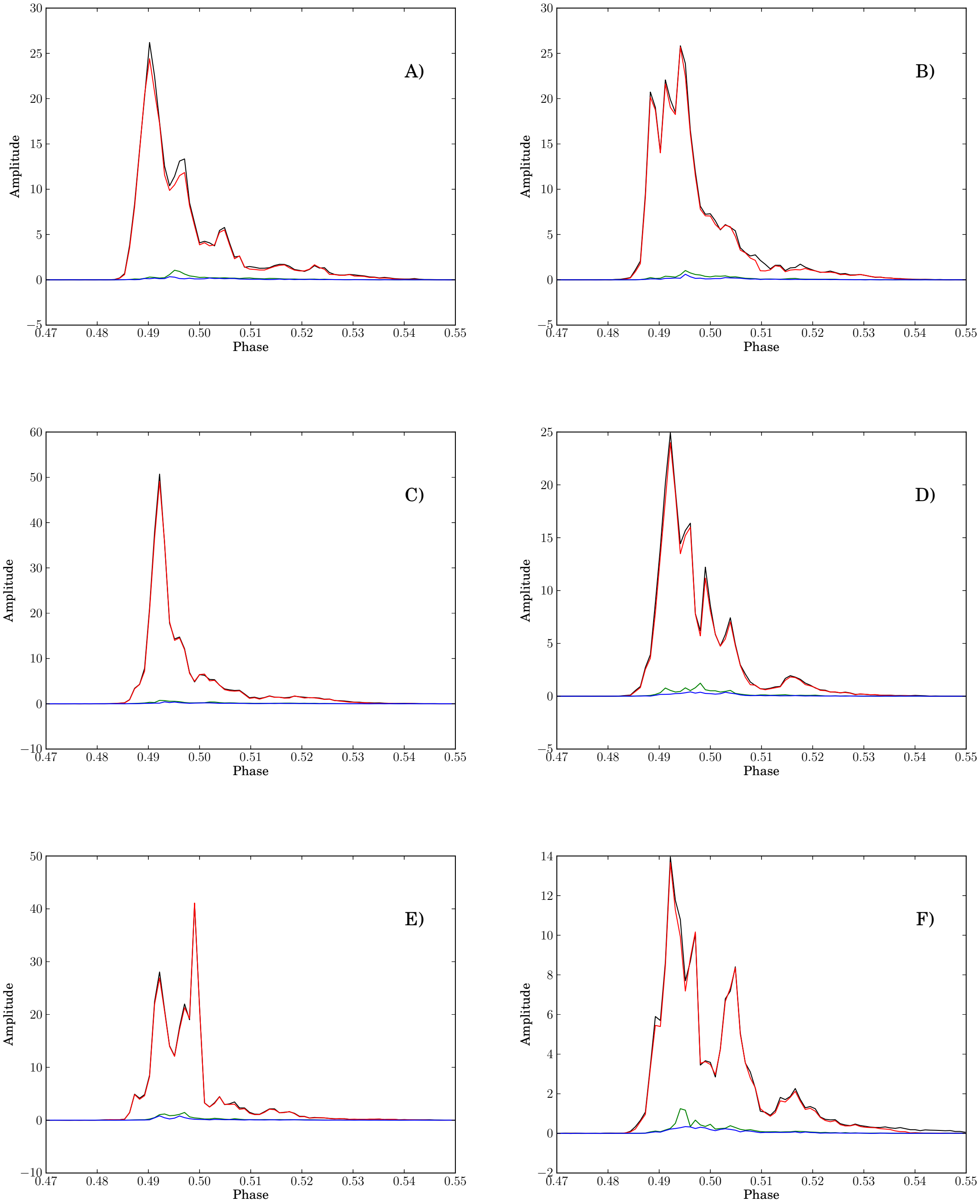

Figure 2.12: For each panel, black, red, green and blue lines show, respectively, the pulse profiles of the variance in Stokes I and along eigenvectors S_1, S_2, S_3 computed from 8 of the 8-second long groups.

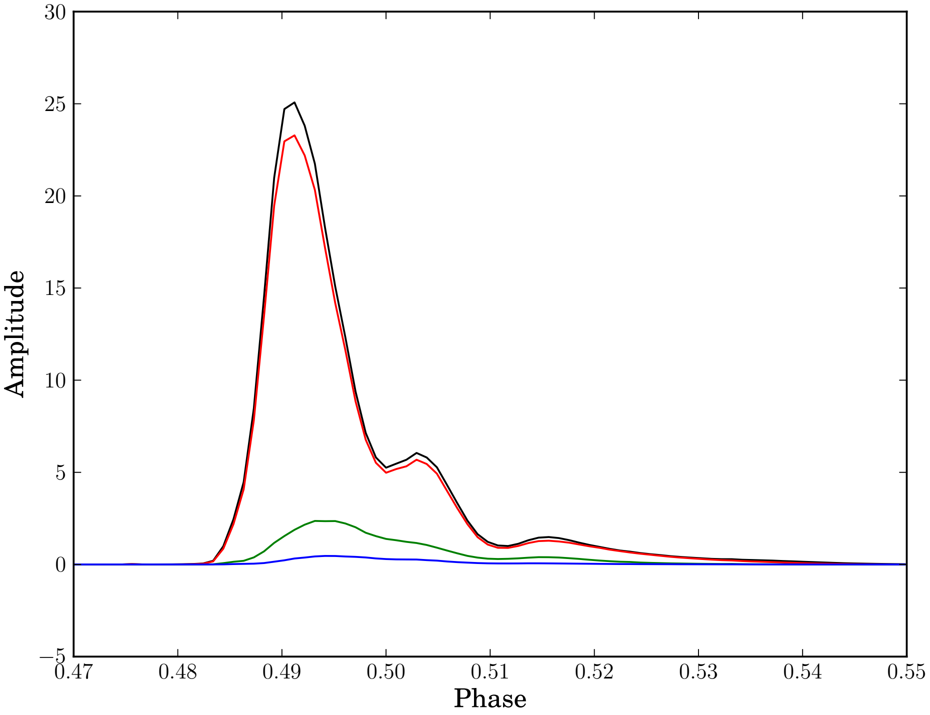

Figure 2.13: Black, red, green and blue lines show, respectively, the pulse profiles of the variance in Stokes I and along eigenvectors S_1, S_2, S_3 computed using all the single pulses in the data set.

does not show any sign of a minimum in the range of ages between 10^6 and 10^7 years as in Gould and Lyne (1998). This can be due to the smaller number of pulsars in our sample. However, we believe that these differences are not significant.

For the majority of the total power profiles, we recognized the presence of more than one component, as expected for a sample of "old" pulsars. In particular, we note the frequent occurrence of blended-double shaped profiles. According to the literature (i.e., Rankin 1983), this is an indication of a conal emission. The linear polarization profiles often mirror the total intensity shape, although the former are almost always narrower than the latter, as already noticed in Rankin (1983) while the fainter circular polarization profiles show a handedness reversal in a few cases. The PA swings vary from flat behaviors to mode jumps and some occurrences of RVM-like swings. For two of the analyses pulsars, the fit for the swing yields some geometrical constraints on the radio-beam. Both appear to be almost aligned ($\alpha << 45°$) rotators.

We have also carried out a preliminary analysis of the Galactic magnetic field resulting from the available sample of pulsars discovered so far in the HTRU southern survey that have a computable RM value, and we studied the implications of the results we obtained. The data do not support the model presented by Vallée (2005), whereas there is some agreement with the one proposed by Han et al. (2006) and Noutsos et al. (2008). In contrast with Vallée (2005), Han et al. (2006) and Noutsos et al. (2008) claim that the Galactic magnetic field has a counter-clockwise direction in the arms and a clockwise direction in between. However, given the limited number of pulsars in our sample and their proximity to the Sun, it is difficult to put significant constraints on more complicated large scale models for the Galactic magnetic field for the time being.

In the second part of the Chapter, we tested a technique to obtain and interpret the covariances of the Stokes parameters based on citealtvs09, and applied it to single pulse observations of the Vela pulsar obtained with the Parkes radio telescope.

As we can consider three regimes of polarization mode combination, starting from the hypothesis of orthogonal and independent modes, with similar intensities and occurrence frequencies, we find that no one of them fully represent the data. This leads to the obvious conclusion that one or more of the initial hypotheses have to be discarded. The most likely one is the assumption of mode independence, favoring the presence of mode covariance. Moreover, we recognize that the current bias removal technique to eliminate the noise contribution to the Stokes variances is not accurate enough. Our results are thus to be considered preliminary. Modulation index studies should be reconsidered once an appropriate bias removal procedure is fully developed.

Chapter 3

Constraining correlated signals in Pulsar Timing Array data

Based on *Constraining correlated signals in pulsar timing array data*, C. Tiburzi, G. Hobbs, M. Kerr, W. A. Coles, S. Dai, M. J. Keith, R. N. Manchester, A. Possenti, R. M. Shannon, W. van Straten, *in preparation*

As explained in Chapter 1, the main target of the Pulsar Timing Array (PTA) experiments is the direct detection of a stochastic and isotropic gravitational wave background. Such a signal is predicted to induce low frequency noise in the pulse time-of-arrival of a pulsar, that is correlated between pulsars pairs on the basis of a specific function. The detection will thus be achieved searching for this particular correlation signature. In this Chapter we study the impact of other correlated noises on this search. We have two main aims. The first is to obtain a deep knowledge of these other correlated signals, mainly errors in the clock time standards and in the planetary ephemeris, and understand if their presence can prevent a correct detection of the underlying gravitational wave background. The second is to test a series of mitigation routines to correct for the aforementioned signals and evaluate which are the costs of these routines in terms of loss of sensitivity in our search for the gravitational wave background.

3.1 Introduction

PTA projects aim to study phenomena that affect multiple pulsars. Such phenomena include irregularities in terrestrial time standards (Hobbs et al., 2012), poorly determined Solar System ephemeris (Champion et al., 2010), instrumental effects and, most important, gravitational waves (Jenet et al., 2005). In all these cases, the ToA series of the signals from a pulsar will be spatially and temporally correlated. PTA projects are based around determining the correlation $C(\theta_{\rm ij})$ between the time series of a pair of pulsars (labeled i and j) that are separated by an angle $\theta_{\rm ij}$. These coefficients are analyzed to identify the physical phenomenon that leads to the correlation.

For uncorrelated noise – such as that induced by the interstellar medium and intrinsic timing noise of each individual pulsar – we have that, on average, the angular correlation is:

$$C(\theta_{\rm ij}) = 0. \tag{3.1}$$

In Chapter 1 we introduced that pulse time of arrivals (ToAs) are referred to a realization of Terrestrial Time, TT. Two main realizations are used. Terrestrial Time as realized by International Atomic Time (TAI) is a quasi-real-time time standard. This is subsequently updated to produce the world best atomic time standard, i.e. the Terrestrial Time as realized by the Bureau International des Poids et Mesures (BIPM). For the work presented in this Chapter we use TT(BIPM2013). The difference between these two time standards, after fitting and removal a quadratic polynomial (see Hobbs et al. 2012), is shown in the upper panel of Figure 3.3 and, over the time span plotted, has a peak-to-peak amplitude of $\sim 2\,\mu$s. Any errors in the terrestrial time standard used will induce the same timing residuals in all pulsars, i.e.,

$$C(\theta_{\rm ij}) = 1. \tag{3.2}$$

We note that this monopolar signal in the correlations is only true for pulsar data sets that have an identical data span, fit parameters and observing cadence. The clock error does induce the same ToA fluctuations for each pulsar, but the determination of each pulsars' pulse, astrometric and orbital parameters as part of the timing procedure will modify the shape of the residuals for each pulsar.

Always in Chapter 1 we described how the pulsar timing procedure also relies upon knowledge of the position of the SSB with respect to the observatory. Let us assume that the position of the observatory with respect to the center of the Earth is precisely known. In this case, we can only consider possible errors in the Solar System ephemeris that is used to convert pulse ToAs from the Earth's center to the Solar System Barycentre (SSB). Instantaneously, the effect induced by an error in the planetary ephemeris on the pulsar timing residuals r is dipolar (with pulsars in the ecliptic plane having maximum ToA fluctuations assuming that the major uncertainty in the SSB position is within the ecliptic):

$$r_{\mathrm{i}}(t) = \frac{1}{c}(\vec{e}(t) \cdot \hat{k}_{\mathrm{i}}) \tag{3.3}$$

where c is the vacuum speed of light, $\vec{e}$ is the time-dependent error in position of the SSB position with respect to the observatory and $\hat{k}_{\mathrm{i}}$ is a versor pointed toward pulsar i.

The development of Solar System ephemerides is complex. An error in the Earth–SSB vector could arise from 1) the planetary mass estimates used when making the model or 2) Solar System objects that are not included in the ephemeris. Generally, if the error arises because of a single object, its time-dependency will be oscillatory with the period of the planetary orbit. If it arises because of multiple objects, a more complex time-dependent variations in the Earth-SSB error can occur. Averaged over a long time interval, the correlations between any two pulsars will not be anymore a pure dipolar signature.

In this Chapter we make use of the Jet Propulsion Laboratory (JPL) ephemerides, DE421 and DE414. DE421 includes more VLBI observations, more updated planet and satellite orbits and mass estimates. It is also valid until 2050 while DE414 is valid until 2201, and this ensures a better precision of DE421 on shorter time scales. The temporal trend of the SSB position difference between these two realizations of the planetary ephemeris, with the subtraction of a quadratic polynomial as for the case of the clock errors, is shown in the two lower panels of Figure 3.3.

We recall that a gravitational wave background (GWB) leaves on the angular correlation computed between the timing residuals of independent pulsar pairs is the Hellings and Downs curve, given by:

$$C(\theta_{\mathrm{ij}}) = \zeta(\theta_{\mathrm{ij}}) = \frac{3}{2}x\log(x) - \frac{x}{4} + \frac{1}{2} \tag{3.4}$$

where $x = [1 - \cos(\theta_{\mathrm{ij}})]/2$.

We note that also other effects can also lead to correlated timing residuals, such as instrumental effects and Solar Wind.

The search for the GWB is based on determining the correlation between the timing residuals for each pair of pulsars in a given PTA. An analysis is subsequently carried out to identify whether those correlations take the form of the Hellings & Downs curve. If they do, then a detection of the GWB will be claimed. We note that this functional form will never be perfectly matched in practice. First of all, the Hellings & Downs curve is not obtained through independent measurements of the angular covariance. For a given PTA, only a finite number of pulsar pairs exists and the measured correlations will not be independent as a given pulsar will contribute to multiple pairs. The Hellings & Downs curve is also the theoretical limit that would only be obtained by averaging a large number of individual universes. For our universe, the positions and properties of the black hole binaries along with the effect of the GWB passing each pulsar will lead to noise on the expected curve. Various researchers (Yardley et al., 2011; van Haasteren et al., 2011) have developed algorithms to search for the signature of the Hellings & Downs curve and have applied those algorithms to actual data sets.

To date, no detection has been made. As the first, direct detection of GWs will be of enormous astrophysical interest, the chance of false detections must be well understood. After a detection, the first step will be to determine an unbiased estimate of the properties of that background (such as its amplitude). It is therefore fundamental to verify whether any other physical effects could lead to an angular correlation that has the form of, or could be misidentified as, the Hellings & Downs curve. In this Chapter we:

- demonstrate how other correlated noise processes (such as errors in the terrestrial time standard and in the planetary ephemeris) degrade our ability to detect and measure the properties of the Hellings & Downs curve and emphasize that GWB detection codes need to account for such correlations.
- demonstrate that these other correlated noise processes can bias our determination of the GWB amplitude
- provide a method to correct for these effects
- demonstrate the reduction in sensitivity to a GWB that occurs after accounting for other correlations.

This research is carried out using simulated data sets. In 3.2 we describe those simulations, the algorithm used to measure the angular correlations and the

PSR name	Spin period [ms]	Distance [kpc]	RA [hh:mm:ss]	Dec [dd:mm:ss]	Ecliptic latitude [deg]
J0437−4715	5.757	0.16	04:37:15.8	−47:15:08.6	−67.9
J0613−0200	3.062	0.90	06:13:43.9	−02:00:47.1	−25.4
J0711−6830	5.491	1.04	07:11:54.2	−68:30:47.5	−82.9
J1022+1001	16.453	0.52	10:22:58.0	+10:01:53.2	−0.1
J1024−0719	5.162	0.49	10:24:38.6	−07:19:19.1	−16.0
J1045−4509	7.474	0.23	10:45:50.1	−45:09:54.1	−47.7
J1600−3053	3.598	2.40	16:00:51.9	−30:53:49.3	−10.1
J1603−7202	14.842	1.64	16:03:35.6	−72:02:32.7	−50.0
J1643−1224	4.622	0.42	16:43:38.1	−12:24:58.7	9.8
J1713+0747	4.57	1.05	17:13:49.5	+07:47:37.4	30.7
J1730−2304	8.123	0.51	17:30:21.6	−23:04:31.1	0.2
J1732−5049	5.313	1.81	17:32:47.7	−50:49:00.1	−27.5
J1744−1134	4.075	0.42	17:44:29.4	−11:34:54.6	11.8
J1857+0943	5.362	0.90	18:57:36.3	+09:43:17.3	32.3
J1909−3744	2.947	1.26	19:09:47.4	−37:44:14.3	−15.2
J1939+2134	1.558	5.00	19:39:38.5	+21:34:59.1	42.3
J2124−3358	4.931	0.30	21:24:43.8	−33:58:44.6	−17.9
J2129−5721	3.726	0.40	21:29:22.7	−57:21:14.1	−39.9
J2145−0750	16.052	0.57	21:45:50.4	−07:50:18.4	5.3
J2241−5236	2.187	0.68	22:41:42.0	−52:36:36.2	−40.4

Table 3.1: The PPTA pulsar sample simulated in this study

mitigation procedures. In 3.3 we show and discuss the results. In 4.5.3 we derive the conclusions.

3.2 Method

3.2.1 Simulated data sets

PTA data sets are subject to various complexities: different pulsars may have different data spans, the precision with which the ToAs can be determined is affected by the flux density of the pulsar and interstellar scintillation and the observational sampling is non uniform. In the work presented in this Chapter we choose to use much simpler, simulated data sets that have regular sampling, equal error bars and equal data spans. If we obtain incorrect determinations of the Hellings & Downs curve with these simulations then it is even more likely that features in the actual data would also lead to further problems. We simulate data sets for 20 of the millisecond pulsars (MSPs) observed by the PPTA (listed in Table 3.1). The coverage of the Hellings & Downs curve offered by these pulsars is shown by the empty dots in Figure 3.1. We note that the closest pulsar pair is PSR J2129−5721-PSR J2241−5236 with an angular distance of 11.36 degrees, and the most widely separated is PSR J1022+1001-PSR J2145−0750 with an angular distance of 170.57 degrees. Only nine pulsar

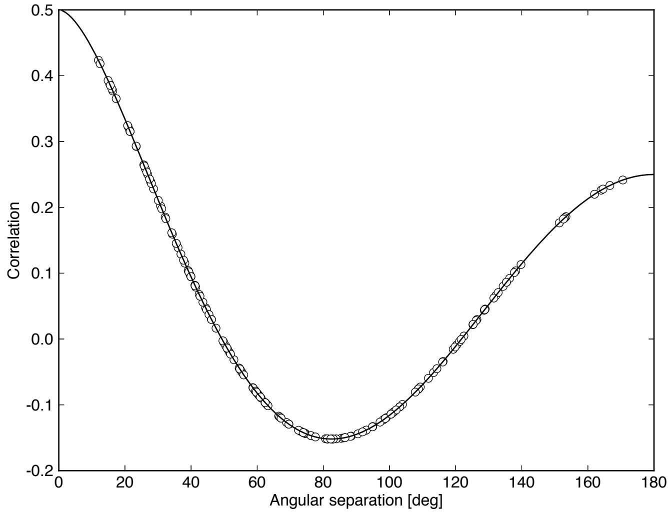

Figure 3.1: The continuous line represents the expected Hellings & Downs curve, the empty dots show the Hellings & Downs curve coverage offered by the PPTA (see Table 3.1).

Tag	Simulated effect
S0	White noise
S1	Uncorrelated red noise
S2	GWB (A=1×10^{-15})
S3	Errors in the clock conversion [TT(BIPM2013) - TT(TAI)]
S4	Errors in the SSB position [DE421 - DE414]
S2+S3	GWB (A=1×10^{-15}) and errors in the clock conversion [TT(BIPM2013) - TT(TAI)]
S2+S4	GWB (A=1×10^{-15}) and errors in the SSB position [DE421 - DE414]

Table 3.2: List of the produced simulations.

pairs have angular separations wider than 140 degrees. Where needed in the simulations, we assume distances for these pulsars as the values given in the pulsar catalogue [1].

We simulate the ToAs using the simulation routines within the TEMPO2 software package (Edwards et al., 2006). We form idealized ToAs (see Hobbs et al. 2009) for each of the 20 pulsars with the FORMIDEAL plugin from MJD 48000 to 53000 (a span of 5000 days/13.7 years), with an observing cadence of once every 14 days and a white noise level of 100 ns. These idealized ToAs are perfectly modeled by the input timing model, i.e. with that model they would produce zero, to within machine precision, residuals. We then add various offsets to these idealized arrival times. The ADDGAUSSIAN plugin

---

[1] http://www.atnf.csiro.au/people/pulsar/psrcat/

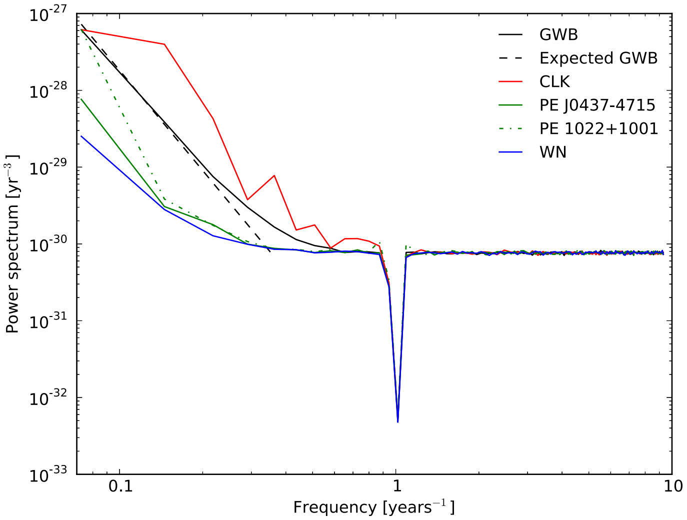

Figure 3.2: The blue, black, red continuous lines show the power spectrum caused by, respectively, only white noise, a GWB with an amplitude of 1×10^{-15} and an error in the clock conversion averaged over 1000 realizations for PSR J0437−4715, while the black dashed line indicates the expected power spectrum following Equation 3.5. The green continuous and dotdashed lines show the power spectrum caused by an error in the SSB position averaged over 1000 realizations for, respectively, PSR J0437−4715 and PSR J1022+1001.

simulates offsets caused by radiometer noise. Various other plugins exist, such as addRedNoise, addGWB, etc. that can add other physical effects (uncorrelated red noise and a GWB signal respectively, for these examples). A final data set based on the required physical effects is produced by using the createRealisation plugin. In all cases the initial, idealized ToAs are based on TT(BIPM2013) and the Solar System ephemeris JPL DE421. For all simulations we generate 1000 realizations of the noise. The simulations we create are summarized in Table 3.2:

- **S0**, we simulate a data set that only includes 100 ns of white, Gaussian noise.
- **S1**, we simulate a data set that includes 100 ns of white, Gaussian noise and spatially-uncorrelated red noise. This red noise is chosen to have the same power as expected from a GWB created by a large number of supermassive black hole binaries at high redshift ($A = 1 \times 10^{-15}$; Ravi et al. 2014);
- **S2**, we simulate white noise data sets and then add the offsets induced by

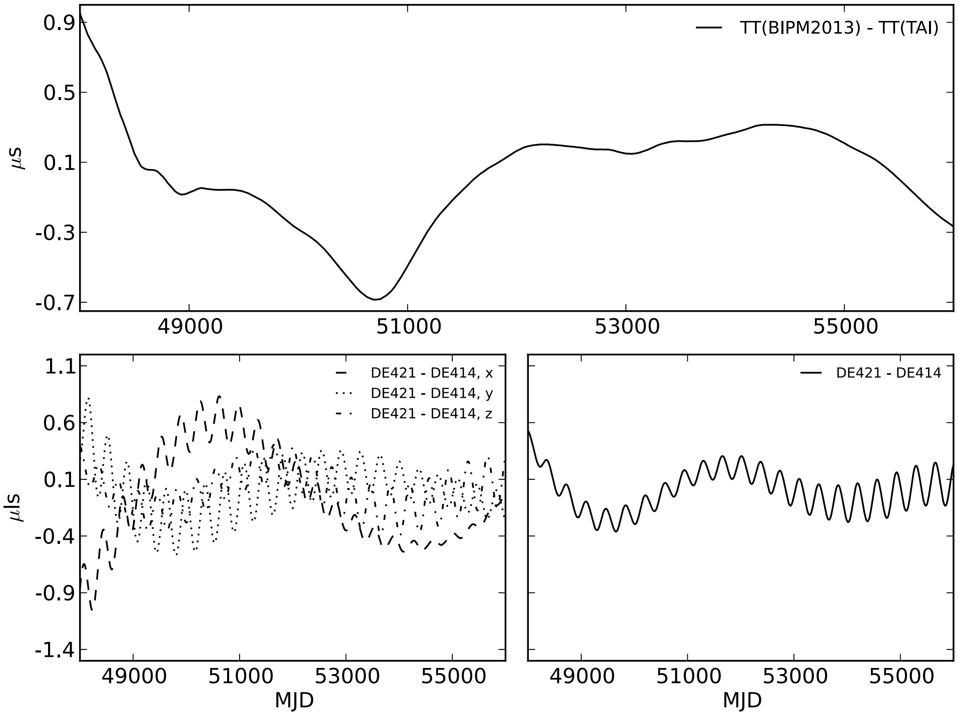

Figure 3.3: The upper panel shows the temporal trend of the difference between the two realizations of the terrestrial time TT(BIPM2013) and TT(TAI). In the lower row, the two panels show the temporal trend of the difference in the SSB position as computed via the planetary ephemeris DE421 and DE414. The left panel displays this difference as decompose in its three spatial components, the right panel displays the absolute difference.

a GWB with an amplitude of 1×10^{-15} via the TEMPO2 plugin ADDGWB;

- **S3**, we simulate white noise data sets as described for S0, based on the TT(BIPM2013) time standard. We then carry out all subsequent processing of the data using the TT(TAI) time standard.
- **S4**, we simulate white noise data sets based on DE421. We then carry out all subsequent processing of the data using the DE414 Solar System ephemeris.

We create two additional simulations, that will be only used in Section 3.3.4 to test the effects of the mitigation routines that we will describe in Sections 3.2.3 and 3.2.4:

- **S2+S3**, we simulate white noise data sets based on the TT(BIPM2013) time standard. Then we add the offsets induced by a GWB with an amplitude of 1×10^{-15} via the TEMPO2 plugin ADDGWB and we carry out all subsequent processing of the data using the TT(TAI) time standard.
- **S2+S4**, we simulate white noise data sets based on DE421. Then we add the offsets induced by a GWB with an amplitude of 1×10^{-15} via the TEMPO2 plugin ADDGWB and we carry out all the subsequent processing of the data using the DE414 Solar System ephemeris.

As one of our goals is to evaluate if a certain detection can be produced by white noise, uncorrelated red noise or the aforementioned correlated signals instead of a genuine GWB, we process all the realizations in S0, S1, S3 and S4 as simulations in S2. We thus use the model of the expected power spectrum given by a GWB (Equation 3.5) to fit each generated time series for spin period, its derivative, position and proper motion.

In order to estimate the impact of the various effects, we show (Figure 3.2) the resulting power spectra for simulations S0, S2, S3 and S4, averaged over 1000 realizations, for PSR J0437−4715. Note that since the resulting mean power spectrum for S1 is the same of S2, we do not display it for sake of clarity. As the Solar System ephemeris errors are strongly dependent upon the pulsar position we also show the resulting power spectrum for a pulsar in the ecliptic plane, PSR J1022+1001, for S4. The power-law spectrum for the GWB (S2) takes the expected form shown as a black, dashed line in Figure 3.2 (Detweiler, 1979):

$$P_{\mathrm{GWB}}(f) = \frac{A^2}{12\pi^2}\left(\frac{f}{f_{\mathrm{yr}}}\right)^{2\alpha-3} \tag{3.5}$$

where A is the GWB amplitude for a frequency $f = f_{\mathrm{yr}} = (1\mathrm{yr})^{-1}$, α sets the power-law slope, and it is predicted to be $-2/3$ for an isotropic and stochastic GWB (Phinney, 2001).

The spectrum of a clock error corresponding to the difference between BIPM2013 and TAI is at a higher level than that from the expected GWB. We estimate that it is comparable to the power induced by a GWB amplitude of 2.2×10^{-15}. However, the actual error in the terrestrial time standard used when analyzing actual PTA data is likely to be smaller. This is because 1) the largest errors are likely to be caused by errors in TT(BIPM2013) while the errors in TT(TAI) should be at a lower level and 2) much of the power comes from variations in the TT(TAI) around the year 2000 when the time standard was deliberately steered. Modern-day time standards are significantly more stable. However, this method does provide an upper bound on the expected variations that could occur due to the adopted time standard.

The power spectrum obtained from a Solar System ephemeris errors corresponding to the difference between versions DE421 and DE414, and averaged over all the 20 pulsars used in the simulations, is approximately equivalent to a GWB amplitude of 6×10^{-16}. As above, we expect that the actual errors in the planetary ephemeris will be at a lower level than that. This suggests that, even for pulsars situated in the ecliptic plane, the signal will be lower than that induced by the GWB. However, this consideration does not account for the possibility that an unknown object exists in the solar system that is not included in the existing ephemerides. It is unlikely that such an object exists, is massive enough and has a short enough orbital period to significantly change this conclusion in the ecliptic plane (which has been well probed by spacecraft), but it is not impossible that such an undetected object may exist in a non-ecliptic orbit.

3.2.2 Measuring the angular covariance

Measuring the correlation or covariance between different pulsars is not trivial because of the presence of steep red noise signal. Methods described in the literature are either optimal for data sets that are close to white, or have been optimized for a particular red noise spectrum. Yardley et al. 2011 (hereafter

Y11) presented a method that was optimal to search for the correlations induced by a GWB (with $\alpha = -2/3$).

In the Y11 technique, the covariance $A^2\zeta$ between every pair of pulsars is determined as a weighted mean over the frequency channels $f_{\rm k}$:

$$A^2_{\rm ij}\zeta(\theta_{\rm ij}) = \frac{12\pi^2 \sum_{\rm k} X_{\rm ij}(f_{\rm k}) k^{2\alpha-3}/\sigma^2_{\rm X_{ij}}(f_{\rm k})}{(T_{overlap})^{3-2\alpha} \sum_{\rm k} k^{4\alpha-6}/\sigma^2_{\rm X_{ij}}(f_{\rm k})} \tag{3.6}$$

where $\theta_{\rm ij}$ is the angular distance between the pulsars, $\sigma^2_{\rm X_{ij}}(f_{\rm k})$ is the variance of the k-th frequency channel of the cross-power spectrum $X_{\rm ij}$ between pulsars i and j, $T_{\rm overlap}$ is the data span covered by both the time series of pulsar i and pulsar j and ζ is the Hellings & Downs functional form (see Equation 3.4). The value for the squared GWB amplitude A^2 is obtained by fitting the Hellings & Downs curve to the resulting covariance estimates. To get an unbiased estimate of A^2, this routine (implemented as the DETECTGWB plugin in the TEMPO2 software package) needs an initial guess for the GWB amplitude, in order to properly weight the spectral frequency channels obtained from each time series. As initial guesses for all the simulations we choose 1×10^{-15}. As we stressed in Section 3.2, we search for the probability that a detection we think is given by a GWB is actually generated by a different source, thus we process all the simulations as we analyze S2.

With these initial guesses, we run DETECTGWB on each of the simulated realization. We choose A^2 as our statistics. The A^2 statistic will allow us to determine if the inclusion of other correlated noise processes can induce significant values of A^2 even when no GWB is present. The choice of A2 is therefore used as it is "optimally" sensitive to the GWB, but also provides a way to detect other non-Hellings & Downs systematic effects in the data.

It is common practice to apply GWB detection codes directly to a data set without attempting to account for other correlated noise processes (e.g., Yardley et al. 2011, van Haasteren et al. 2009, Demorest et al. 2013). However, if other forms of correlated noise have a well-defined signature in the timing residuals then it is also possible to attempt to remove or account for such correlated noises. We identified two possible methods: 1) remove the signals from the data sets before applying the GWB detection code and 2) to update the GWB detection code to account for the presence of such signals. In the Sections 3.2.3 and 3.2.4 we describe an implementation of these methods.

3.2.3 Mitigation of time standard errors

Our initial method (labeled here as CLK1) is to leave the data sets untouched, but to update the Y11 fitting algorithm to account for the possibility of correlated noise caused by errors in the time standard (by combining Equations 3.2 and 3.4). The Y11 algorithm is therefore updated to enable simultaneous fitting for the amplitude of the Hellings & Downs curve and an arbitrary offset. In theory, the offset would correspond to the clock error. In practice, we expect it to be covariant with the mean of the Hellings & Downs curve.

Our second method (labeled here as CLK2) is to measure, and subsequently remove, the errors in the time standard using the routines developed by Hobbs et al. (2012). In brief, we first search for a common signal in the timing residuals of all the pulsars by simultaneously fit the timing residuals of all pulsars with a grid of regularly-spaced, linearly-interpolated values. After measuring the common signal, we update the timing models for each pulsar to include (but do not subsequently fit for) the computed grid of values. As we mentioned, removing this common signal we remove the mean of the GWB signal as well, and it would be erroneous to fit the resulting angular covariances only with Equation 3.4. We will use:

$$C(\theta_{\rm ij}) = \zeta(\theta_{\rm ij}) = \frac{3}{2}x\log(x) - \frac{x}{4} + \frac{1}{2} + c \tag{3.7}$$

instead, with c being a new free parameter representing an offset. This technique has a single free parameter – the sampling of the grid. We use a 100 days grid spacing.

3.2.4 Mitigation of planetary ephemeris errors

Two published methods exist for measuring and removing planetary ephemeris errors. The first (PE1) is a generalization of the method to measure and remove the clock signal (see Deng et al. 2013 for a similar technique). In the process, we simultaneously fit for the three components of $\vec{e}(t)$ in Equation 3.3. This provides three time series, $e_{\rm x}(t)$, $e_{\rm y}(t)$, $e_{\rm z}(t)$, that can subsequently be included in the timing models for each pulsar.

The second (PE2) was first presented by Champion et al. (2010) and is used to measure uncertainties in the mass of a body in the Solar planetary system. This method is optimal for the known planetary objects, but cannot be applied to unknown objects. In this work we assume that the masses of the planets to Mars are well constrained. We also assume that any error in the planets further out than Saturn will have little effect on our current data sets. We therefore include a fit for the Jovian and Saturnian systems.

3.3 Results and discussion

3.3.1 Results from non mitigated simulations: angular covariances

In the left-hand panels of Figure 3.4, we show the angular covariance of an individual realization from the simulations without applying any correction. In the right-hand panels we show the angular covariance trend for the same simulations, but averaged over the 1000 realizations.

We note that the angular covariances (both from the individual realization and the averaged) for simulations S0 and S1 have a flat trend and are dispersed around zero, but the scatter of the S1 angular covariances is higher, as it is reasonable to expect.

We correctly recover the Hellings & Downs curve for simulation S2. For an individual realization there is significant scatter on the curve even though we are simulating very long data sets with a very low level of white noise rms. This scatter makes it challenging, but not impossible, to distinguish between the five simulations on the basis of an individual realization. The angular covariances for simulation S3 have no dependency with the angular separation, and show a significant offset with respect zero, as Equation 3.2 anticipated.

The shape of the angular covariance trend obtained from simulation S4 is more difficult to be interpreted. The instantaneous angular correlation given by an error in the SSB position can only be 1, -1 or 0, but the covariance rescales the correlation with respect the power induced by the effect. Moreover, since the error vector $\vec{e}$ is time-dependent, the derived angular covariance can change in time, and the final result is obtained via a time-integration. However, we can say that in general a close pulsar pair is likely to be positive correlated, and a widely-separated one is likely to be anticorrelated. This mirrors the trend that we observe for simulation S4.

The panels in the right-hand column clearly show that the average characteristics are different and that, with a large number of realizations, it is unlikely that the angular covariance trend for a GWB would be misidentified with another effect. For example, the main distinguishing feature between the GWB and the planetary ephemeris errors is seen at wide angular separations

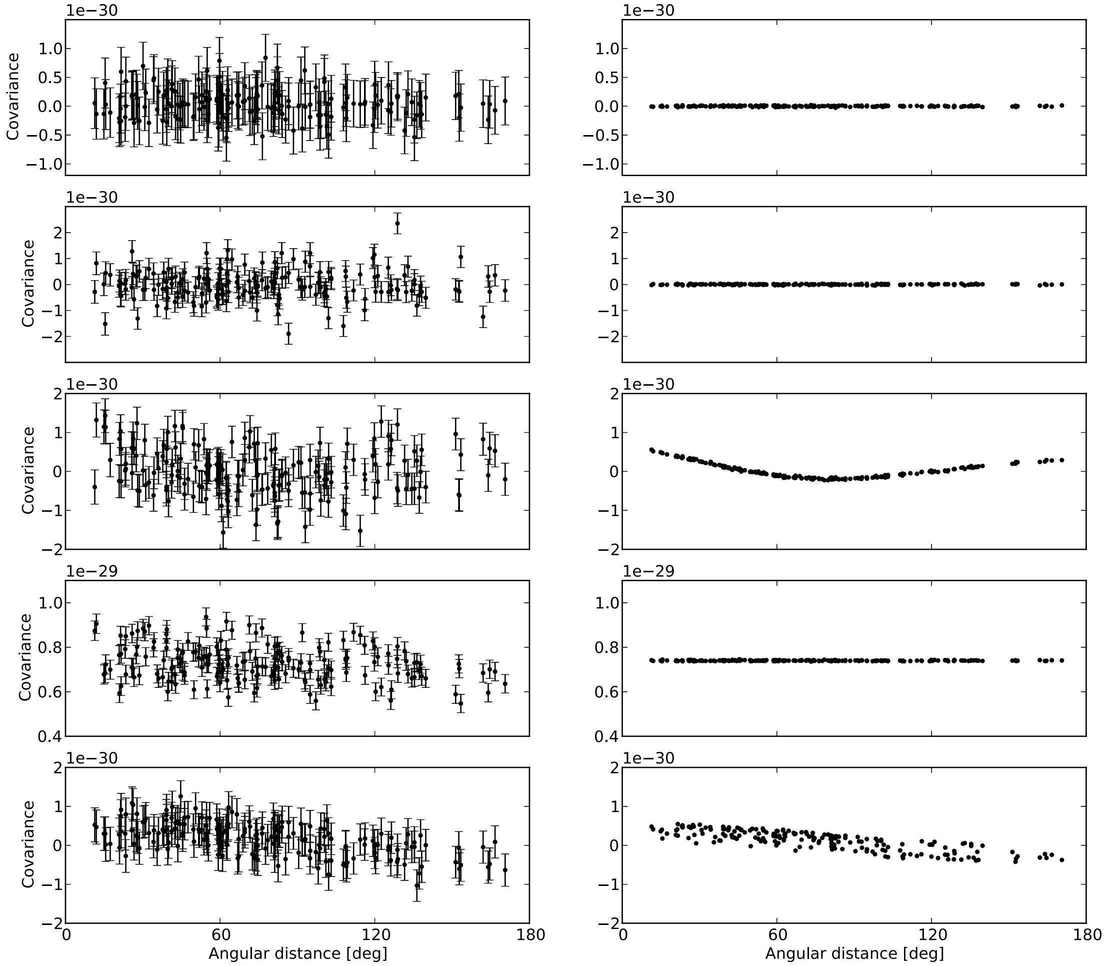

Figure 3.4: In the left-hand panels we show the angular covariance trends of an individual realizations for, respectively, simulations S0, S1, S2, S3 and S4 as computed by DETECTGWB. In the right-hand panels, we show the angular covariance trends for the same simulations, averaged over 1000 realizations.

Mitigation	**Simulation**	**Mean**	**Standard deviation**	**FAP 5%**	**FAP 1%**
NO	S0	$3.1e-34$	$1.3e-31$	$2.2e-31$	$3.4e-31$
NO	S1	$3.0e-34$	$2.6e-31$	$4.6e-31$	$6.6e-31$
NO	S2	$1.2e-30$	$5.6e-31$	–	–
NO	S3	$2.8e-30$	$3.1e-31$	$3.3e-30$	$3.6e-30$
NO	S4	$3.0e-31$	$1.3e-31$	$5.2e-31$	$6.3e-31$

Table 3.3: Means, variances and FAP levels at 5% and 1% for simulations from S0 to S4 without any correction applied.

where the GWB produces correlated timing residuals whereas the ephemeris produces anti-correlated residuals. Concerning the PPTA, unfortunately, it is in this region where we have poor sampling of the angular covariances (see Figure 3.1).

Even though it is hard to imagine mistaking the results from errors in the terrestrial time standard for a GWB signal, in the next Section we are going to show that the blind run of GWB detection algorithms could lead to false significant detections. Modern algorithms calculate a statistic that is sensitive to the GWB (in our case A^2 is such a statistic) for the actual data set and then determine the false alarm probability of achieving that value with data sets that do not include the GWB. In the following, this has been accomplished by comparing the chosen statistic obtained for GWB-affected simulations (S2) with the same parameter as computed from simulated data sets that include other kind of uncorrelated and correlated noise (S0, S1, S3 and S4). We will demonstrate how the false alarm probability must be modified in the presence of other correlated noise.

3.3.2 Results from non mitigated simulations: false alarm probability estimates

In Figure 3.5 we show the resulting A^2 histogram from simulation S2. The continuous line indicates the mean (approximately 1.2×10^{-30}) of the histogram, the error bar shows the standard deviation of the values with respect this mean (5.6×10^{-31}), and the dashed black line marks the injected GWB squared amplitude (1×10^{-30}). This demonstrates that the adopted algorithm is non-biased in this ideal case. We note that the A^2 distribution is not Gaussian and has significant outliers. It is not trivial to determine analytically the shape of the actual distribution (particularly for real PTAs in which the pulsars have different data spans, noise levels, etc.).

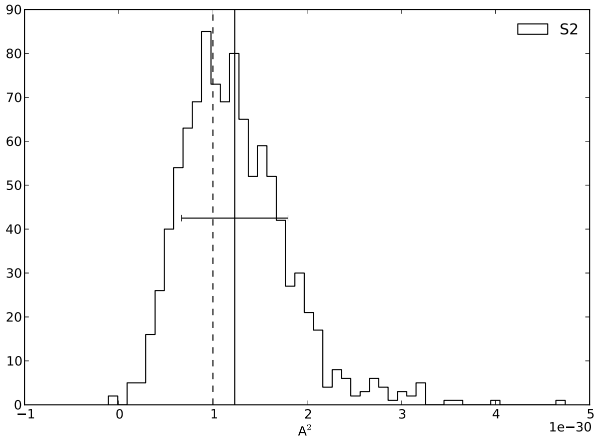

Figure 3.5: A^2 histograms for simulations S2. The continuous and dashed lines correspond, respectively, to the mean of the values and to $A^2 = 1 \times 10^{-30}$. The error bar shows the standard deviation of the values.

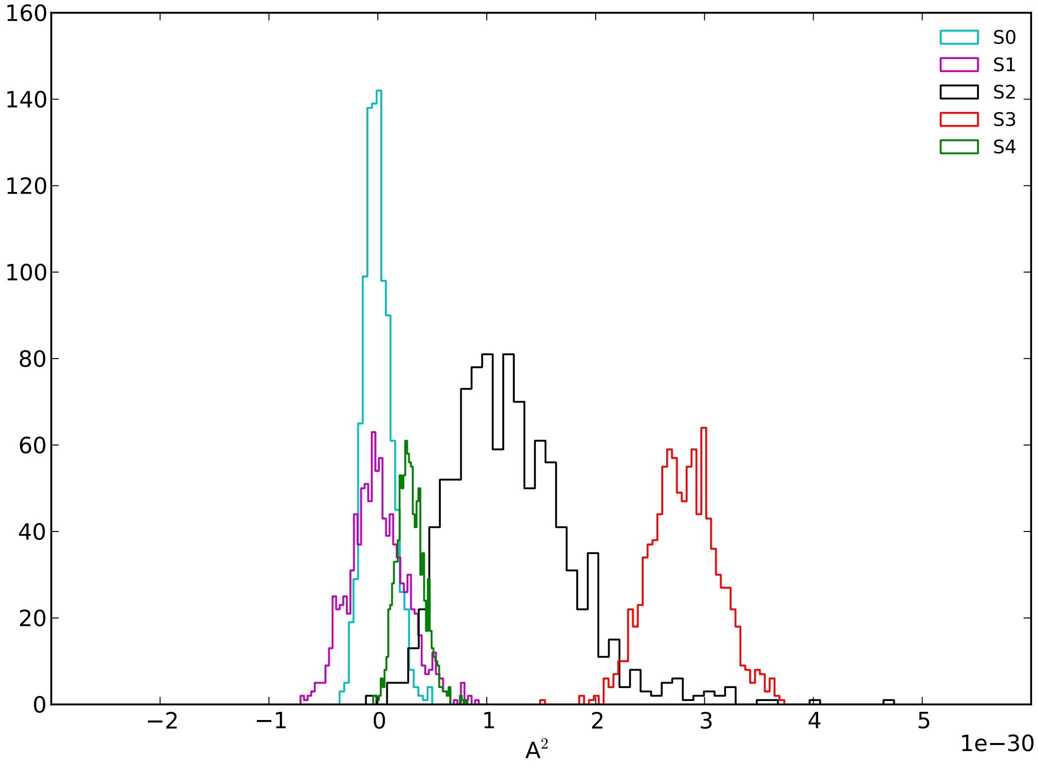

Figure 3.6: A^2 histograms obtained from simulations S0, S1, S2, S3 and S4 (respectively in cyan, magenta, black, red and green.)

In Figure 3.6 we show a comparison between the A^2 histograms obtained for simulations S0 to S4. The histogram means, standard deviations and false alarm probability (FAP) levels at 5% and 1% are reported in Table 3.3. The S0 histogram (white noise only case, cyan in the Figure) mean is $3.1e-34$: it is extremely close to zero, as it should be if there is no correlated signal resembling a GWB in the time series. Assuming a 5% FAP referred to S0, the corresponding A^2 threshold is 2.2×10^{-31}. Out of the 1000 realizations of the GWB (S2; black in the Figure), 992 exceed it. If we choose a 1% FAP instead, the corresponding A^2 threshold is 3.4×10^{-31}, and the percentage of S2 realizations above it is 99.8%. This demonstrates that, if the only comparison was with white noise at 100 ns level for all the pulsars, then a GWB with an amplitude of 1×10^{-15} could easily be detected with our simulated sample of pulsars. However, the timing residuals simulated for S2 do exhibit red noise that is clearly seen by eye. It is therefore more reasonable to select a false alarm rate based on data sets that include both white and uncorrelated red noise (S1; magenta in the Figure). A 5% FAP based on S1 gives an A^2 threshold of 4.6×10^{-31}, with the 95.6% of the S2 A^2 values above it. A 1% FAP, characterized by an A^2 threshold of 6.6×10^{-31}, gives that the 86.9% of the S2 A^2 values are greater than it. This means that the sensitivity to the GWB is reduced, but implies that a detection is possible.
However, the histogram obtained from S3 (error in the clock time standard, red in the Figure) exceeds almost completely the S2 results. The reasons for such an outcome are to be searched in the high equivalent amplitude of the simulated clock error, also shown in Figure 3.2. Simulations S3 show a 5% and 1% FAP of, respectively, $3.3e-30$ and $3.6e-30$, and only from an handful of realizations from S2 we get a squared amplitude that exceeds these levels.An error in the Solar System ephemeris (S4; green in the Figure) yields a 5% and 1% FAP of $5.2e-31$ and $6.1e-31$. Respectively, 92.8 and 87.8% of the S2 values are above the two thresholds. We deduce that although the overlap between the S2 and S4 results is not complete, also in this case the sensitivity to the GWB is reduced.

In summary, Figure 3.6 highlights that significant A^2 values can be obtained from data sets that do not contain a GWB, but do contain other correlated noise such as clock and planetary ephemeris errors. This therefore leads to biased A^2 estimates and, unless corrected, could potentially lead to false detections.

All these considerations are not surprising. In fact, even though the determination of A^2 is obtained from a method that is optimized for a GWB search, it will still detect correlated power in the residuals caused by other effects. In the next section we discuss the effectiveness of our proposed correction routines.

3.3.3 Results from mitigated simulations: modification of the false alarm probability estimates

We individually apply the mitigation procedures for clock and planetary ephemeris errors, respectively, on simulations S3 and S4 to test if the chosen mitigation procedures are able to correct for the corresponding errors and how much effective they are.

We find that both the clock correction procedures explained in Section 3.2.3 work well. Figure 3.7 shows a comparison between the A^2 histograms obtained from simulations S3 corrected for CLK1 (upper panel) and CLK2 (lower panel) with respect those obtained from simulations S3 and S2. The first two rows of Table 3.4 reports means and standard deviations of the A^2 histograms computed from mitigated S3 simulations given as fractions of the corresponding values listed in Table 3.3, along with FAPs at 5% and 1%. Both CLK1 and CLK2 successfully remove the majority of the effects of the clock errors from simulations S3: the means of the histograms are about three orders of magnitude less than the non-mitigated result. However, CLK1 leaves a significant scatter in the A^2 values, close to the original one, whereas the scatter left by CLK2 is roughly halved. This is because CLK1 does not work on the data, thus the original correlation between the simulated timing residuals is not removed. This causes the scattering of the A^2 values to remain basically unaltered. On the other hand, CLK2 acts directly on the data with the aim to remove the entire monopolar signature, and this induces a reduction of the A^2 spread as well. FAPs at 5% and 1% are greatly reduced by both of the mitigation procedures. After the implementation of CLK1, they fall from $3.3e-30$ and $3.6e-30$ to $5.1e-31$ and $7.5e-31$: more than, respectively, 93% and 81% of the A^2 values obtained from S2 exceed these thresholds. After CLK2, 5% and 1% FAPs are reduced to $2.3e-31$ and $3.1e-31$, with 992 and 985 A^2 S2 values out of 1000 above them. CLK2 seems thus to be the most effective mitigation routine for what it concerns the capability of reducing the FAP. Upper row of Figure 3.9 shows the averaged angular covariances obtained after the application of CLK1 (left panel) and CLK2 (right panel) to simulations S3. The initial monopolar signature is preserved by the application of CLK1, as it does not imply a modification of the data, while the power subtraction worked by the second mitigation routine is the reason for the negative offset when CLK2 is applied.

The application of the two planetary ephemeris corrections described in Section 3.2.4 is not as well effective. Figure 3.8 compares the A^2 distribution obtained from simulations S4 after being corrected for PE1 (upper panel) and PE2 (lower panel) with the results from simulations S4 and S2. The last two rows of Table 3.4 reports the fractional means and variances from the mitigated A^2 histograms, and FAPs at 5% and 1%, while lower row of Figure 3.9 shows the average angular covariances from simulations S4 following the mitigations for PE1 and PE2. A first clear consideration is about the negative histogram mean after correcting for PE1, induced by the trend of the angular covariances shown in the lower left panel of Figure 3.9, that is reversed with respect the original one (see right panel in the last row of Figure 3.4). This behavior is explained by the large number of extra degrees of freedom (we fit for three time series sampled every 100 days, adding in an extra 156 parameters to the fit), that absorbs a wide amount of power in the timing residuals. This does not happen with PE2. Evidently, PE2 is less effective in neutralizing the effects of errors in the planetary ephemeris, as the resulting histogram mean is lowered not more of the 61%. However, this is not unexpected: PE2 only adds in two extra degrees of freedom corresponding to the errors in Jupiter and Saturn masses, and only searches for these specific corrections. It can also been noticed from the lower right panel of Figure 3.9 that PE2 does not dramatically modify the angular covariance shape of simulations S4, although it reduces its diagonal trend. The 5% and 1% FAPs reductions mirror what discussed above. After PE1, they are diminished from $5.2e{-}31$ and $6.3e{-}31$ to $7.9e-32$ and $1.5e-31$. More than 99% of the A^2 values from S2 exceed these values, a result that resembles what obtained from simulations S0. After PE2, they are decreased to $3.4e-31$ and $4.3e-31$, exceeded by, respectively, 98% and 96.5% of the S2 values. It thus seems that PE1 is largely more effective than PE2. Moreover, we emphasize that PE2 can only be used if the masses of Jupiter and Saturn do dominate the errors in the ephemeris.

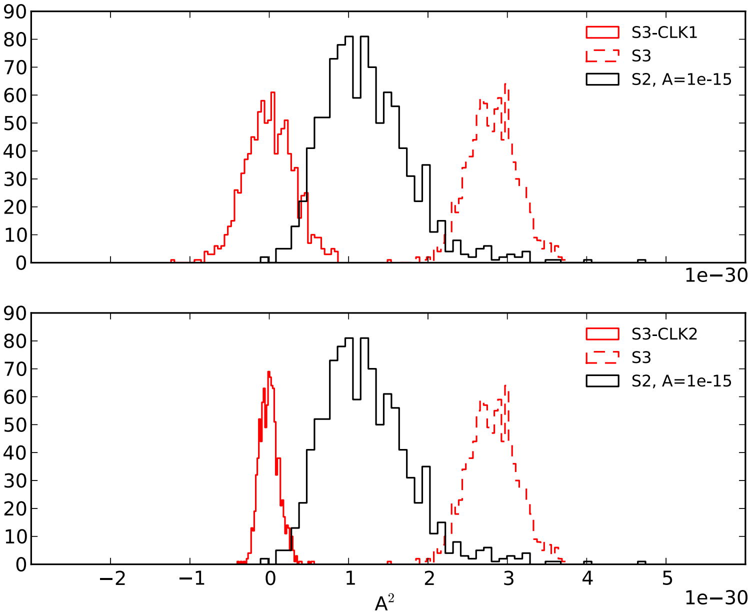

Figure 3.7: A^2 histograms obtained from the application of mitigation CLK1 (dashed histograms) and CLK2 (crossed histograms) to simulations S2 (upper panel) and S3 (lower panel)

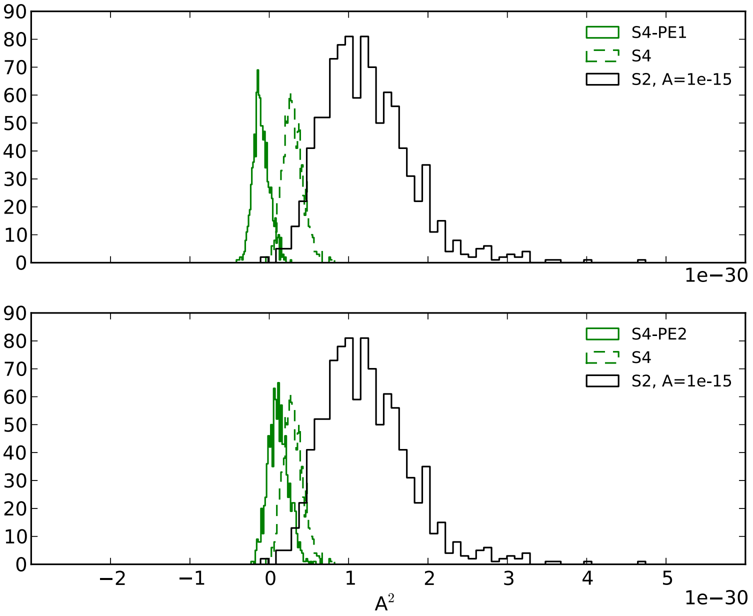

Figure 3.8: A^2 histograms obtained from the application of mitigation PE1 (dashed histograms) and PE2 (crossed histograms) to simulations S2 (upper panel) and S4 (lower panel)

Mitigation	**Simulation**	**Mean**	**Standard deviation**	**FAP 5%**	**FAP 1%**
CLK1	S3-CLK1	$1.7e-03$	$9.8e-01$	$5.1e-31$	$7.5e-31$
CLK2	S3-CLK2	$1.4e-03$	$3.9e-01$	$2.3e-31$	$3.1e-31$
PE1	S4-PE1	$-3.4e-01$	$8.1e-01$	$7.9e-32$	$1.5e-31$
PE2	S4-PE2	$3.9e-01$	$1.0e+00$	$3.4e-31$	$4.3e-31$

Table 3.4: Means, variances and FAPs at 5 and 1% for the individual application of clock and planetary ephemeris corrections on, respectively, simulations S3 and S4. Means and variances are normalized with respect the corresponding measurements reported in Table 3.3.

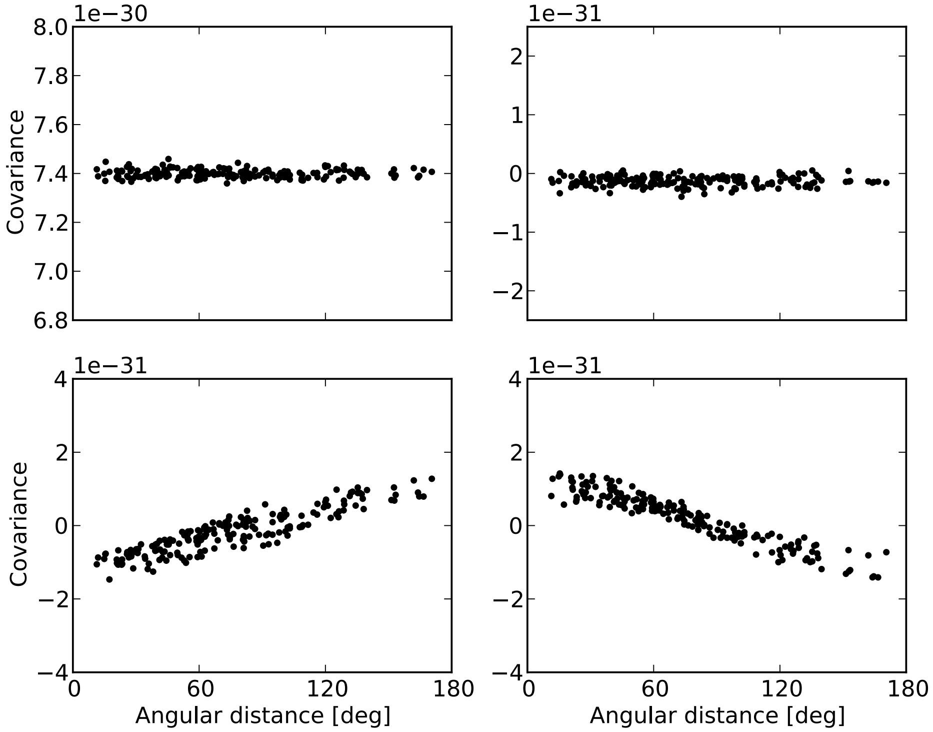

Figure 3.9: Averaged angular covariances obtained from the application of mitigation CLK1 (left upper panel) and CLK2 (right upper panel) to simulations S3 and of mitigation PE1 (left lower panel) and P2 (right lower panel) to simulations S4.

3.3.4 Results from mitigated simulations: loss in sensitivity

In the previous Section we showed the effectiveness of the proposed mitigation routines in diminishing the FAPs. However, to adopt a certain mitigation routine it is not sufficient to show that it works in the context for which it was designed. It is necessary to demonstrate that it does not affect the results if no signal to be corrected is present (as it happens, for example, in simulations S2). In other words, it should leave unaltered the detection code sensistivity.

Here we show and discuss the results from tests aimed to evaluate the loss in sensitivity introduced by these routines.

We perform two tests: 1) we apply the mitigation routines on simulations S2, and we successively run our detection code on the mitigated simulations, 2) we apply the clock and planetary ephemeris mitigation routines on, respectively, simulations S2+S3 and S2+S4 described in Section 3.2.

In the context of these tests, instead of running our detection code once (as we did until now) we iterate its application twice. The latest guess amplitude that we give to the code is the A^2 mean from the first run. This is to obtain a more stable convergence in the final result.

In the case of tests 1), only a GWB affects the timing residuals. If the mitigation procedures work properly, no correction should be caused by their implementation. In Figures 3.10 and 3.11 we show the A^2 distributions obtained from the application of, respectively, CLK1 and CLK2 and of PE1 and PE2 on simulations S2. Table 3.5 reports the histogram means and variances normalized with respect the corresponding S2 parameters from Table 3.3. Figure 3.12 shows the average angular covariances for the application of the four mitigation routines on S2.

It is evident that both of the clock mitigation routines do not bias the GWB signal recovery, with CLK1 being the less affecting of the two procedure as mean and standard deviation of the histogram are unaltered with respect the non-mitigated values. The first row of Figure 3.12 supports this conclusion, showing that the shape of the Hellings & Downs curve is preserved after the application of the mitigation procedure, although the mean angular covariances gain a certain degree of scattering with CLK2.

Concerning the planetary ephemeris corrections, Figure 3.11 and Table 3.5 indicate that PE1 absorbs the majority of the GWB signal from S2, decreasing the original histogram mean at its 36%. We identified two reasons for this.

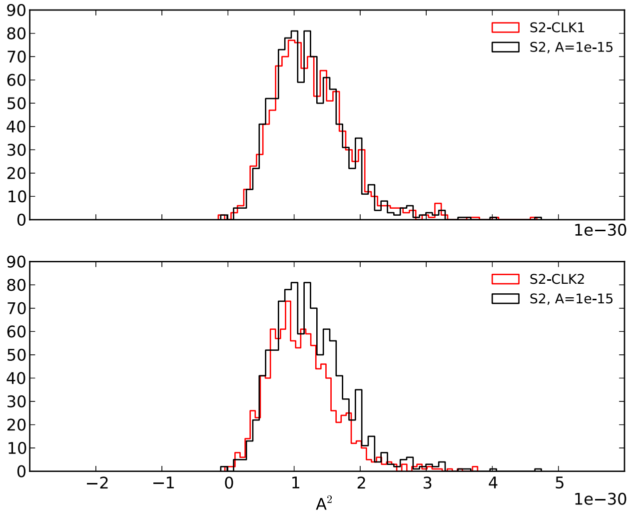

Figure 3.10: A^2 histograms obtained from the application of mitigation CLK1 (red histogram in the upper panel) and CLK2 (red histogram in the lower panel) to simulations S2 (black histograms)

First of all, the PE1 procedure adds in a large number of extra degrees of freedom (we fit for three time series sampled every 100 days, adding in an extra 156 parameters to the fit), thus it is more likely that the power induced by a GWB can be partially absorbed. Secondly, both the signatures left by an error in the SSB position and by a GWB are not purely, respectively, dipolar and quadrupolar. This means that while fitting for the former effect via Equation 3.3, it is extremely probable that part of the signal introduced by the latter would be assimilated. This is confirmed by the lower left panel of Figure 3.12. The signature left after the fitting closely resembles a quadrupole. In contrast, as already stated in Section 3.3.3, the PE2 method only adds in two extra degrees of freedom (the error in Jupiter and Saturn masses). The lower panel of Figure 3.11 shows that, although PE2 does not completely neutralize the planetary ephemeris signature when present (see Section 3.3.3), it leaves the parameters of the A^2 histogram basically unaltered with respect the non-mitigated simulations.

For tests 2), CLK1 and CLK2 are applied on simulations where, along with a GWB, also an error in the clock is present (simulations S2+S3). PE1 and PE2 are instead implemented on simulations where a GWB and an error in the SSB position are present (simulations S2+S4). If our routines work well, they should identify and correct for the respective spurious correlated

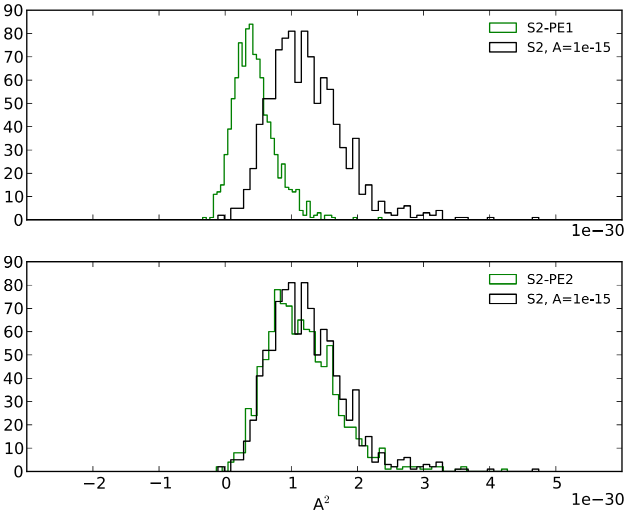

Figure 3.11: A^2 histograms obtained from the application of mitigation PE1 (green histogram in the upper panel) and CLK2 (green histogram in the lower panel) to simulations S2 (black histograms)

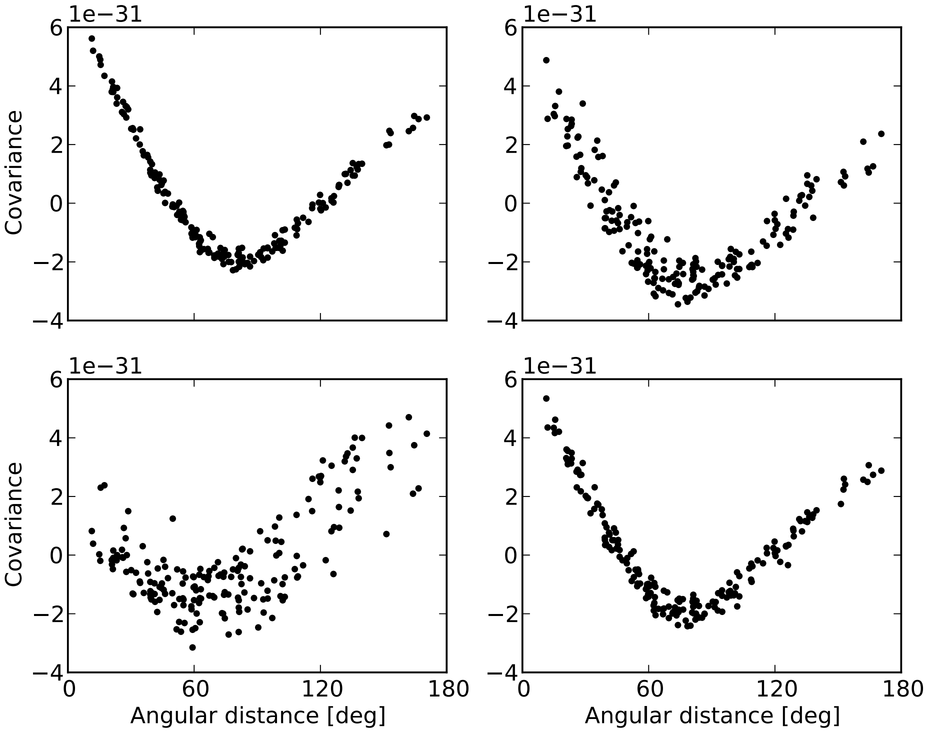

Figure 3.12: Averaged angular covariances obtained from the application of CLK1 (left upper panel), CLK2 (right upper panel), PE1 (left lower panel) and PE2 (right lower panel) to simulations S2.

noises only, leaving unbiased the underlying GWB signal. Eventually, the parameters of the computed A^2 distributions should reproduce the mean and variance of the histogram obtained from S2. In Figures 3.13 and 3.14 we show the A^2 histograms computed from the implementation of, respectively, CLK1 and CLK2 on simulations S2+S3 and of PE1 and PE2 on simulations S2+S4. Table 3.6 reports means and variances of the A^2 distributions normalized with respect the parameters for the A^2 histogram from S2, shown in Table 3.3. Figure 3.15 shows the average angular covariances.

Although the implementation of CLK1 on S2+S3 produces an A^2 distribution mean that is only 2% different with respect the non-mitigated S2, it is unable to reduce the value scattering. In fact, the variance is twice the original one. This is because, as already discussed in Section 3.3.3, CLK1 does not directly modify the data. This is also evident from the very high mean shown by the average angular covariances in the upper left panel of Figure 3.15. Thus, if CLK1 does not alter the timing residuals it does not neutralize the noise correlation in the data either. In the case of simulations S2+S3 we have two sources of correlated noise, and both of them contribute in increasing the A^2 value scattering. This spread remains practically unaltered by the implementation of CLK1, while the mean value is correctly recovered.

On the other hand, CLK2 is able to recover both the S2 histogram mean and the correct variance reduction, with only 10% of error. The good behavior of CLK2 shows also in the upper right panel of Figure 3.15, that closely reproduces the shape of the Hellings & Downs curve.

The implementation of the mitigation routines for a planetary ephemeris errors gives similar results to tests 1). PE1 absorbs the semi-dipolar signal generated by an error in the SSB position, but also a significant fraction of the GWB power. This is shown clearly by Figure 3.14 and Table 3.6, where the histogram mean is newly reduced of about 64%. The lower, left panel of Figure 3.15 confirms this result displaying an average angular covariance trend where the dipolar contribution to the Hellings & Downs curve is reduced, basically leaving the only quadrupolar shape. In contrast, Figure 3.14 and Table 3.6 indicate that PE2 allows a perfect recovery of the histogram mean and variance (the latter is incremented of about 10%), while the lower right panel of Figure 3.15 shows that the Hellings & Downs shape is recovered as well.

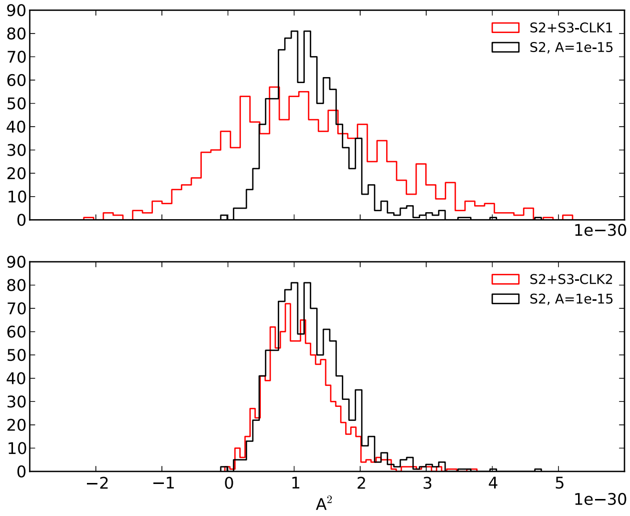

Figure 3.13: A^2 histograms obtained from the application of mitigation CLK1 (red histogram in the upper panel) and CLK2 (red histogram in the lower panel) to simulations S2+S3. As a reference, A^2 distribution from S2 is shown as well (black histograms).

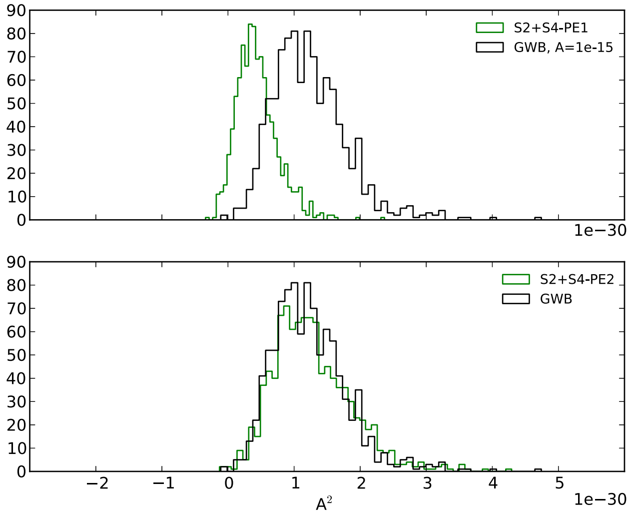

Figure 3.14: A^2 histograms obtained from the application of mitigation PE1 (green histogram in the upper panel) and CLK2 (green histogram in the lower panel) to simulations S2+S4. As a reference, A^2 distribution from S2 is shown as well (black histograms)

Mitigation	**Simulation**	**Mean**	**Standard deviation**
CLK1	S2+S3	$9.8e-01$	$2.1e+00$
CLK2	S2+S3	$9.1e-01$	$9.4e-01$
PE1	S2+S4	$3.6e-01$	$5.6e-01$
PE2	S2+S4	$1.0e+00$	$1.1e+00$

Table 3.6: Means and variances for the individual application of clock and planetary ephemeris corrections on simulations S2+S3 and S2+S4, normalized with respect the corresponding measurements for the S2 results reported in Table 3.3.

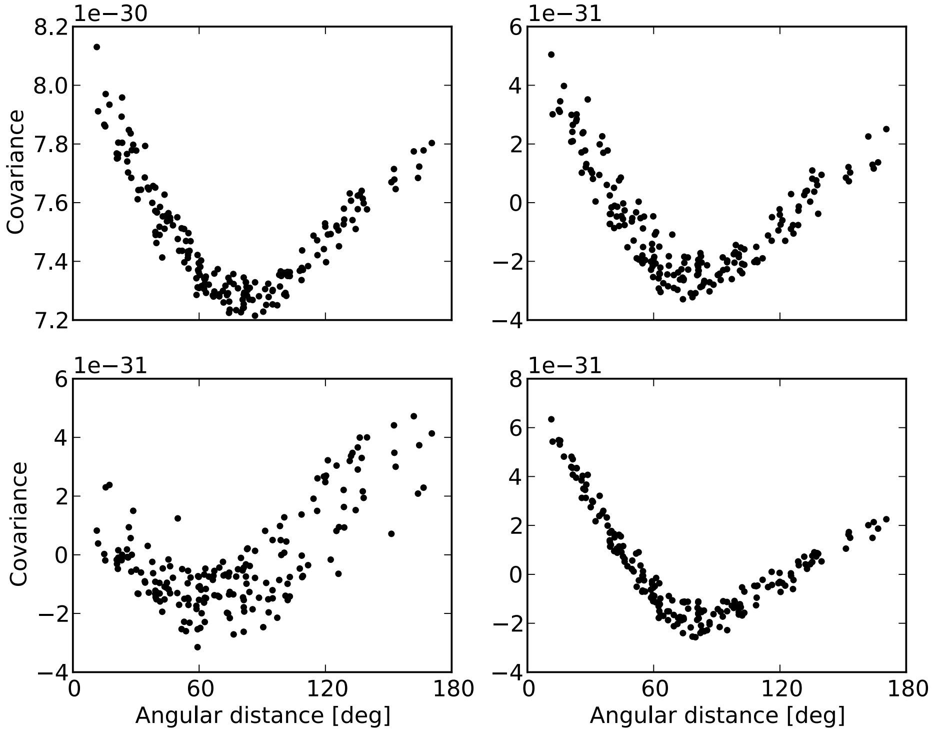

Figure 3.15: Averaged angular covariances obtained from the application of CLK1 (left upper panel), CLK2 (right upper panel) on simulations S2+S3, and from the application of PE1 (left lower panel) and PE2 (right lower panel) to simulations S2+S4.

3.4 Conclusions

Our study shows that even if the GWB detection codes work properly in the correct scenario, it is important to consider that other sources of correlated noise, such as errors in clock conversions and planetary ephemeris, can induce significant measures of A^2 if not corrected during the data processing.

Without attempting corrections, the effect with the major impact is given by uncertainties in the clock conversion. Figure 3.2 displays that it introduces a considerable amount of power in the timing residuals. Figure 3.6 also clearly shows that it generates non-zero measures of A^2. The amount of power introduced by an error in the planetary ephemeris is less affecting with respect the GWB search.

We identify two mitigation methods to accomplish for errors in the clock time standards (CLK1 and CLK2), and two to accomplish for errors in the SSB position (PE1 and PE2). CLK1 works only on the angular covariances, while CLK2 fits the clock signal directly from the time series, introducing a non-negligible number of new degrees of freedom. CLK1 is more effective in absorbing the clock signal when it is the only present signal, alongside with white noise, but generally the two mitigation procedures give good and comparable results in this scenario. When tested for the sensitivity reduction, CLK1 results unable (because of its method logic) to diminish the A^2 histogram variance if two correlated signals are present. This does not happen with CLK2, that preserves the detection code sensitivity. Nevertheless, we stress that CLK2 is dependent to an arbitrary number of grid steps.

In the case of errors in the planetary ephemeris, both the methods work on the time series. PE1 fits for the three components of the error vector introduced in Equation 3.3, PE2 only for the Jovian and Saturnian masses. When tested on data sets where only the signal given by an incorrect SSB position and white noise are present, PE1 results more effective than PE2 thanks to the large number of introduced degrees of freedom. On the other hand, this introduces an evident bias in the sensitivity of our detection code. Thus, PE1 it is obviously able to absorb the ephemeris signal, but it also incorrectly diminishes the GWB signal when present: it is, thus, unacceptable. PE2 is not as well effective in absorbing the ephemeris signal, but leaves basically unaltered the GWB signal when present.

Chapter 4

Millisecond pulsars profile variability

Based on *The European Pulsar Timing Array - Secular variability of millisecond pulsar profiles*, C. Tiburzi et al., in preparation.

In this Chapter we explore the hypothesis of temporal stability of millisecond pulsar profiles. This is an obvious topic to be assessed for the purposes of Pulsar Timing Array experiments, especially in view of sensitive, new-generation telescopes such as the Square Kilometer Array and the Five hundred meter Aperture Spherical Telescope. In fact, these new instruments will greatly reduce the white noise impact on pulsar timing.
In Section 4.1 we briefly summarize the studies of pulse profile variability. In Sections 4.2 and 4.3 we outline, respectively, the data set we use in our analysis and the followed pipeline. In Section 4.5 we describe the results of the analysis. In Section 4.5.3 we summarize the analysis outcomes.
We stress that this study is still ongoing, thus the results presented here are to be considered preliminary.

4.1 Introduction

As introduced in Chapter 1, the Pulsar Timing Array (PTA) experiments are built under the observational evidence that the targeted pulsars have a very high rotational stability (Detweiler, 1979; Jenet et al., 2005). Millisecond pulsars (MSPs) are extremely stable rotators (Matsakis et al., 1997), far more than the non-recycled pulsars: for this reason, PTA research teams monitor only samples of MSPs that are selected in order to obtain particularly precise measurements of ToAs.

Besides the rotational stability, an additional underlying hypothesis in collecting high quality ToAs is that the intrinsic integrated profile of a MSP at a given frequency is a non-evolving signature of the MSP itself. In the course of the years, this fundamental assumption has been reviewed few times, focusing in particular on the short time scales. In fact, it is renown that the individual pulses from the same pulsar undergo a wide range of variations, in flux, shape and phase position (Rankin, 1986). Usually, this variability becomes negligible by integrating a reasonably large amount of single pulses (Helfand et al., 1975). However, limits to the applicability of this rule have been found discovering that, in many pulsars, the root-mean-square of the timing residuals exceeds the predictions given by considering only the radiometer noise (Cordes and Downs, 1985). This phenomenon, called *jitter* or *stochastic wide-band impulse modulated self noise* (SWIMS), is indeed generated by a non sufficient, although generous, number of averaged single pulses to obtain the final integrated profile, that thus maintains significant shape differences with respect to the reference template with which is cross-correlated to generate a ToA. The onset of pulsar jitter, that mirrors an intrinsic instability of pulsars, depends on the source brightness, telescope sensitivity, integration time and, of course, on the pulsar tendency in undergoing to shape variations. A few cases of this kind of variability had been already reported, but only in the very last years, under the impulse of the studies related to PTAs, careful investigations have been undertaken. For instance, Osłowski et al. 2011 showed that the timing precision of the brightest MSP known, J0437−4715, is limited by the presence of SWIMS, and proposed a method, based on the principal component analysis, to recover part of the lost timing precision. A follow up of this work to include the polarized component of the observations (Osłowski et al., 2013) brought the capabilities of this method to improve the timing precision of MSP J0437−4715 up to the 40%. Shannon and Cordes 2012 shown that MSP J1713+0747 timing precision is as well affected by pulse jitter, and that this phenomenon has a correlation bandwidth. This was remarked by Shannon et al. 2014, who searched and found jitter evidences in 7 MSPs of the Parkes Pulsar Timing Array sample. Liu et al. 2012 stressed the importance of assessing the jitter problem since, with the commissioning of high-sensitivity telescopes like the Square Kilometer Array and the Five hundred meter Aperture Spherical Telescope, jitter will be the dominant limitation to the achievable timing precision. Another interesting, although debated (Hotan et al., 2004a), evidence of short term instability in MSPs was found by Kramer et al. 1999b in MSP J1022+1001. In the presented data set, this pulsar morphology changes in a way that is incompatible with the known shape variations in pulsars, and they were claimed to be intrinsic variations rather than due to instrumental errors or signal propagation effects.

In contrast with the case of short term variability, the literature about long term variability of MSP profiles is scarce, as these sources have been since long considered very good clocks over long timescales. Long term, intrinsic variability has been detected for long period pulsars: Lyne et al. 2010 found an interesting correlation between the variations in shape (parameterized by the pulse profile width at different altitudes or the effective width) shown by a sample of long period pulsars taken from the sample of Hobbs et al. 2010 and the fluctuations of the amount of spin period derivative. They confirmed the attribution of this behavior to magnetospheric variations. Another kind of shape variation in mildly-recycled binary pulsars (i.e., pulsars spun up to rotational periods of tens of milliseconds over a relatively short stage of mass and angular momentum transfer from a mid/low mass companion star), is given by the geodetic precession. This relativistic effect induces a precession of the misaligned rotational axis with respect to the total orbital momentum of the binary, and hence a varying intersection of the emission cone with respect to the observer line-of-sight, that results in a shape variation of the observed pulsar profile. Weisberg et al. 1989 found evidences for geodetic precession in PSR B1913+16 (Harrison and Tademaru, 1975), lately confirmed by Kramer 1998. Similar studies lead to recognize this phenomenon in PSR J0737-3039B (Breton et al., 2008) and PSR B1534+12 (Fonseca et al., 2014).

Concerning solitary MSPs, Shao et al. 2013 analyzed the cases of MSP J1744-1134 and J1939+2134. They put strong upper limits to any variation in the pulse profiles of these sources and, thanks to that, they were able to set extremely precise constraints on one of the parameters that characterize the preferred frame effects. This parameter is null in the context of the General Relativity of Einstein, and non-null in alternative gravity theories, based on the isotropic Lorenz violation in a particular frame.

No more systematic studies on the long term stability of MSP profiles, beside that of Shao et al. 2013, has been done to date. This can be explained, between the other reasons, with the lack of suitable data sets. Since the expected variations are (if any) very small, it is highly unlikely that they can be detected relying on data sets obtained by different instruments (backends or frontends, or even telescopes), or, for example, from incoherently dedispersed data. In fact, the quality of the latter data is significantly poorer than data taken, over the same bandwidth, in a coherent dedispersion mode. Furthermore, it is impossible for two frontends and/or backends to react in the same identical way to an incoming signal. This means that, whenever a frontend and/or a backend changes, a comparison between pulsar profiles obtained before and after the change can be biased by not accountable instrumental effects. Moreover, the time span of the data set must cover several years in order to match the typical data spans which are expected to be collected by the PTAs.

The data sets used by Shao et al. 2013 are indeed the best available choice that answers to the aforementioned constraints: it was obtained with the same telescope, receiver and backend, and it is coherently dedispersed. Besides the two aforementioned solitary pulsars, a larger sample of MSPs were observed as well, covering in total about 14 years of homogeneously-collected data: these are the observations that we examine in this Chapter.

4.2 Data set

The data sets were obtained with a circularly polarized, L-band receiver at the 100-mt Effelsberg Radio Telescope (Germany) between 1997 and 2011, that was replaced in 2009. The observing central frequency is 1410 MHz, while the bandwidth, divided into 32 frequency channels, usually does not exceed 50 MHz. Each observation was folded in a coherent dedispersion mode using the Effelsberg-Berkeley-Pulsar Processor (EBPP) backend, and is not provided with automatic calibration in polarization or flux. The EBPP backend (Backer et al., 1997) is a 4-bit device, schematically made of 4 boards that independently process a 8-channel wide sub-band of the incoming signal. The processing includes an automatic attenuation procedure (called *levelling*) based on the system temperature. Only two polarization channels are archived, corresponding to the self products of the voltages, along with a limited amount of information related to the observation itself.

The data are stored in files (EBPP-format archives) and contain an individual

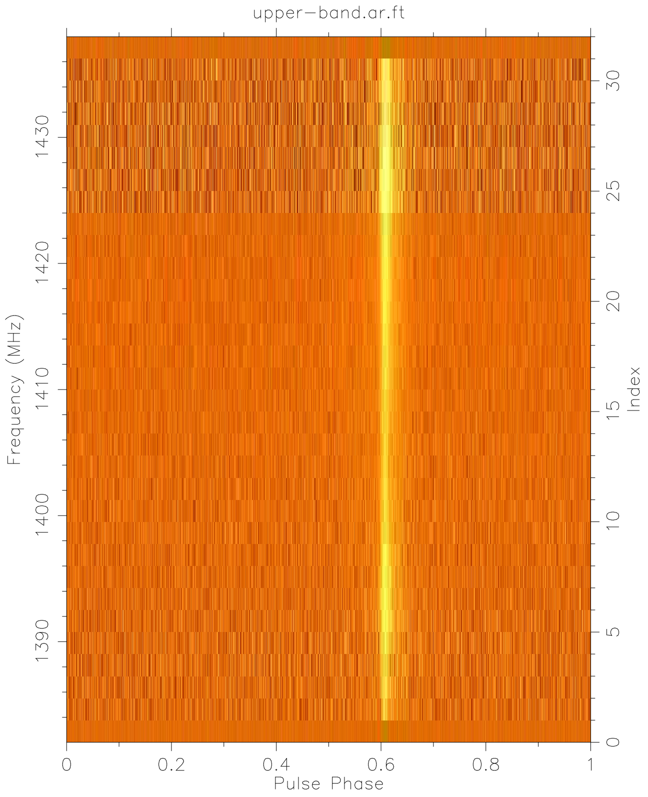

Figure 4.1: Frequency versus phase diagram of one of the PSR J1713+0747 observations. The first and the last frequency channels of the bandwidth have been manually removed. The plot shows the clear difference between the off-pulse noise level in the upper sub-band with respect to the lowest frequency sub-bands.

integration in time with full frequency and polarization resolution.

The original binning, set at the observing epoch, depends on the specific source, and varies from 1090 to 1990 phase bins.

An accurate investigation of the data unveil a potential problem, caused by interferences and an incorrect levelling, that affects the highest frequency sub-band. The off pulse noise of this sub-band, centered at 1431 MHz, is almost always systematically different with respect to the other three sub-bands. An example of this behavior is shown in Figure 4.1. The effects of this sub-band presence are still not completely assessed, although at least one of them is described in Section 4.5.2. Anyway, we opted for removing this sub-band in all the available observations.

4.3 Data Analysis

We analyze 10 MSPs: PSR J0613−0200, PSR J0751+1807, PSR J1012+5307, PSR J1640+2224, PSR J1643−1224, PSR J1713+0747, PSR J1744−1134, PSR J1857+0943, PSR J1939+2134, PSR J2145−0750. We reduce the data using the PSRCHIVE (Hotan et al., 2004b) and the TEMPO2 (Edwards et al., 2006) software packages.

For each pulsar we proceed as follows.

We set the phase resolution of all the observations to 1024 bins. For each archive with full resolution in frequency and polarization, we apply an algorithm for radio frequency interference (RFI) excision based on the comparison between the bandpass and a median smoothing of the bandpass itself computed on 10 frequency channels. The tolerance is set to four standard deviations. We then apply a second algorithm to excise the signal in those phase bins where the amplitude deviate for more than four standard deviations with respect the local mean. We visually inspect every archive and, if necessary, we complete the data cleaning, by zapping the frequency channels affected by RFIs. At this stage we also reject all the faint or damaged archives (typically in the order of 10-20 for pulsar). We then install the latest ephemeris computed by the EPTA collaboration and shared among its members [1] in each archive of the data set, and we combine together all the archives corresponding to an individual, original observations. We fix the central frequency to the nominal, central observing frequency (1410 MHz) and dedisperse every observation before averaging in time, frequency and polarization. We check the goodness of the installed ephemeris carrying on the timing analysis of the residuals using the TEMPO2 software package. During this step, we reject all the observations whose timing residuals are more than one standard deviation away from the mean. This step is usually repeated twice.

The subsequent analyses are usually performed on two series of pulse profiles per pulsar, obtained by binning all the available observations taken in a six month interval and, independently, in a one year interval (see Figure 4.2). For the brightest pulsars in our sample (PSRs J1713+0747, J1744−1134, J1939+2134, J2145−0750), we also use a third series of pulse profiles,

---

[1] http://www.epta.eu.org/wiki/doku.php

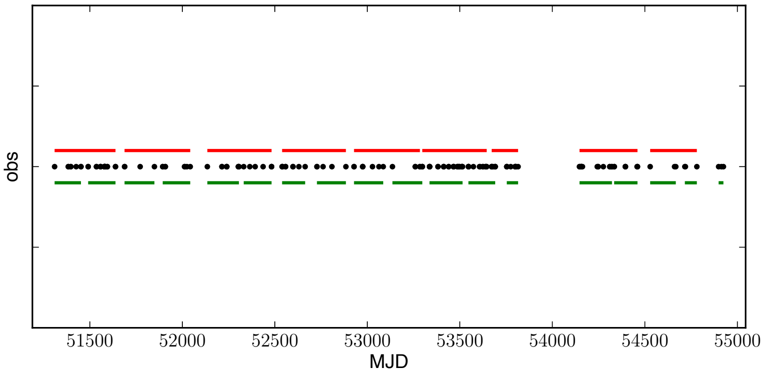

Figure 4.2: Temporal coverage of the EBPP observations for PSR J0613−0200 at 1410 MHz, and partition of the data span to form the average profiles. The black dots are the epochs of the observed data, the red and the green lines indicate respectively the 1 year and 6 month partitions.

corresponding to the individual observations.

We then select the first and last averaged (over 6 months or 1 year) observation of each series, and we compare the S/N of the profiles to select the brightest of the two as a reference profile (see Figure 4.3). All the observations that are averaged to obtain the reference profile are excluded from the subsequent analysis.

We then cross-correlate the observations to the reference profile to estimate both a scale factor and an offset that are subsequently applied to normalize the observations.

Once obtained the normalized pulse profiles for the available data series (1-year and 6-month averaged and, occasionally, the individual observations), we search for secular variations in the pulse profiles.

We mainly study the temporal trend of the pulse profile widths at different percentages of the main peak height, as well as the separation between the edges of two different peaks (if any), by adapting a method presented by Ferdman et al. 2013. Let us assume that we are measuring the width of a pulse profile component c at a percentage p of the main peak height, H.

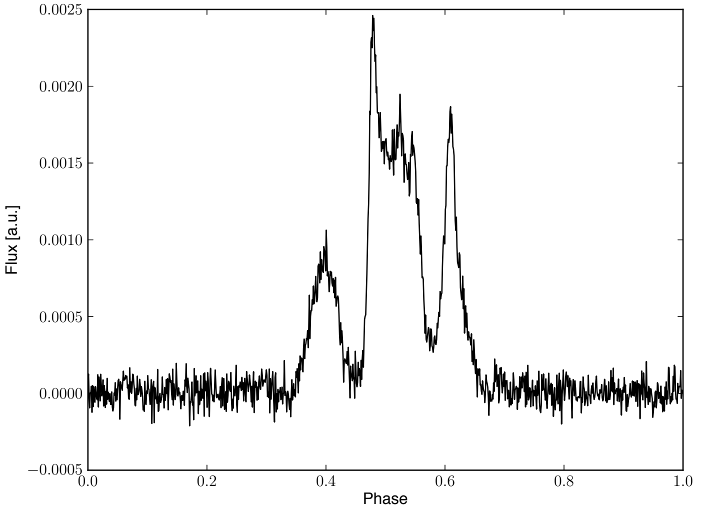

Figure 4.3: The chosen reference template for PSR J0613−0200, formed averaging the observations within the first year of the data span.

- We compute a guess for the phase longitudes at which the leading and trailing crossings of c at p percent of H occur, using an high S/N template. For this, we first select the range of phase longitudes that contains the main peak of the profile (see Figure 4.4, panel A), and we fit the chosen region with a fifth order polynomial (see same Figure, panel B), obtaining an estimate of the main peak height, h_{fit}. By intersecting the horizontal line $f(x) = h_{\text{fit}} \times p/100$ with c, we obtain the leading and trailing guessed values (see same Figure, panel C);
- we then select a shape-dependent range of phase longitudes around these guessed values, r_{leading} and r_{trailing}, and we keep them fixed during the following steps of the analysis (see same Figure, panel D);

We then use a Monte Carlo method with 10,000 realizations, each of them implying the following steps, to obtain the width of c and its uncertainty:

- we vary the amplitudes of the phase bins within the main peak region, r_{leading} and r_{trailing} by adding white noise whose amplitude equalizes the off pulse amplitude standard deviation (see Figure 4.5, panel A);
- we then fit the peak region with a fifth order polynomial in order to obtain the height, and, independently, the r_{leading} and r_{trailing} regions with a third

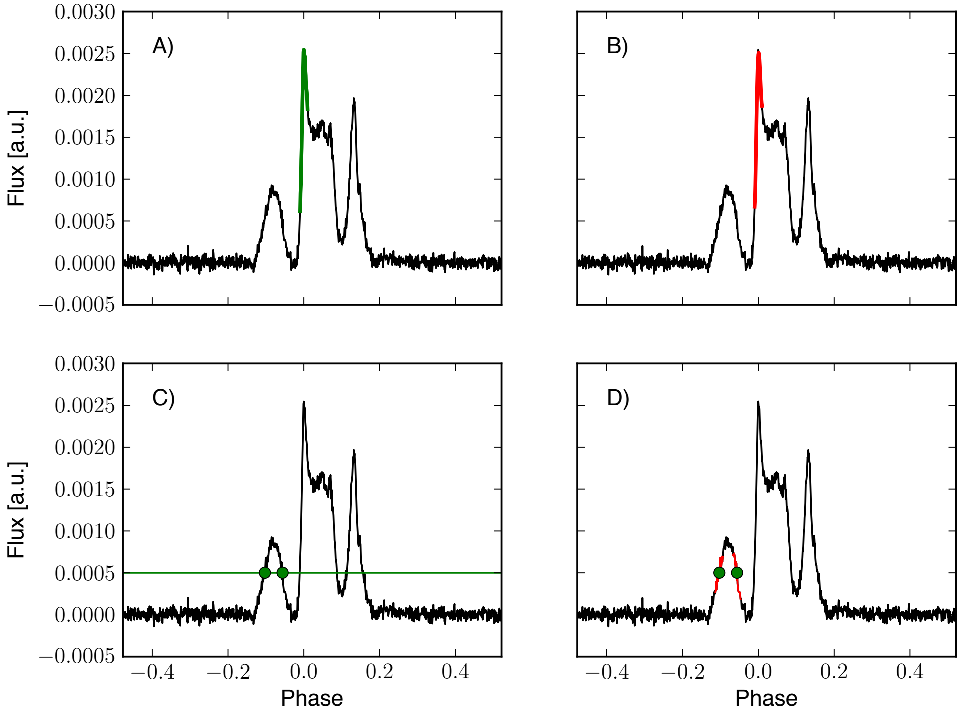

Figure 4.4: Analysis of the pulse profile width for the leading peak of the first 1-year averaged integrated profile of PSR J0613−0200. For each panel, the pulse profile is shown in black. *Panel A*, in green is shown the main peak region. *Panel B*, in red is shown the main peak region fitted with a fifth order polynomial. *Panel C*, the horizontal green line cuts the pulse profile at a queried altitude (in this case, 20% of the main peak height), the green dots are the computed leading and trailing intersection. *Panel D*, the green dots are the computed leading and trailing intersection, in red are shown the shape-dependent selections of longitudes around the guesses.

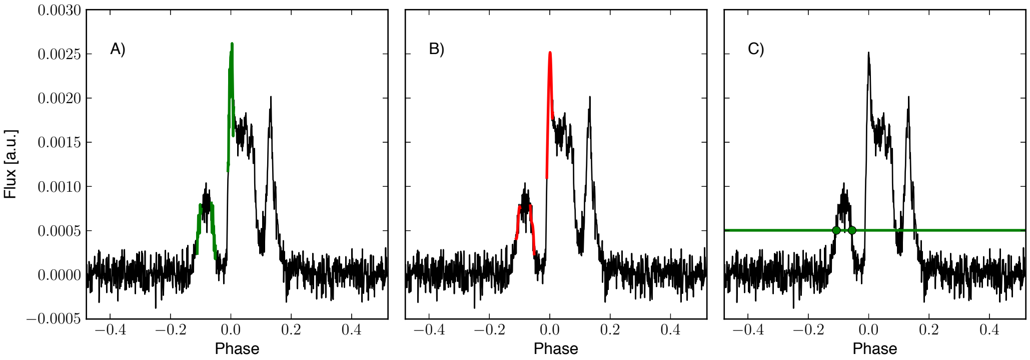

Figure 4.5: Analysis of the pulse profile width for the leading peak of the first 1-year averaged integrated profile of PSR J0613−0200. For each panel, the pulse profile is shown in black. *Panel A*, in green are shown the main peak phase bins and the leading and trailing regions, whose amplitude are varied by adding white noise. *Panel B*, in red are shown the fits for the fifth (on the peak region) and third (on the edges) order polynomials. *Panel C*, the horizontal green line cuts the pulse profile at a queried altitude (in this case, 20% of the main peak height), the green dots are the computed leading and trailing intersections.

order polynomial (see the same Figure,panel B);

- by computing the intersection between an horizontal line at the queried percentage of the fitted main peak height and the two computed polynomial, we finally obtain the width value (see the same Figure, panel C).

Internal steps of sanity checks and rejection of corrupted values are performed in every cycle of the Monte Carlo (for example, to discard negative widths or failed polynomial fits). In addition, the bulk of the widths collected at the end of the Monte Carlo is trimmed of its highest and lowest values (70 values per tail in the distribution are deleted).

The high number of obtained width values allows to produce histograms that are fit with a Gaussian function. The error bar for each bin of the histogram is assumed to be Poissonian (i.e., $\sqrt{N}$, where N is the number of values per bin) if the number of elements per bin exceeds 30. A correction is applied to the error bar if the number of elements per bin is lower than 30 (i.e., $1+\sqrt{N+0.75}$ according to Gehrels 1986). On the basis of a direct inspection of a large sample of resulting fits, we conclude that the obtained histogram

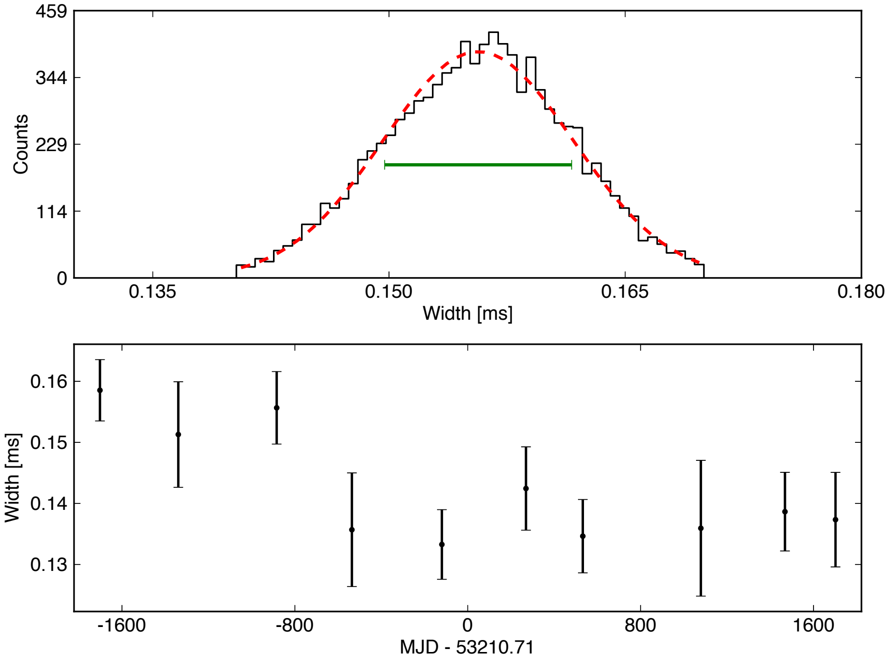

Figure 4.6: *Upper panel*, histogram of the widths from the leading peak of PSR J0613−0200 at 20% of the main peak height for the third 1-year pulse profile. The black contour shows the width histogram. In red and green are displayed, respectively, its Gaussian fit and the computed uncertainty. *Lower panel*, temporal evolution of the widths for the leading peak of PSR J0613−0200 at 20% of the main peak height for the 1-year pulse profile.

characterized by a Gaussian fit with reduced χ^2 less than 3 can be accepted. If the reduced χ^2 exceeds 3, the quality of the fit is prone to a visual inspection for a possible rejection. From the Gaussian fit of the width histogram a value of the component width and its uncertainty finally are released. The central width value corresponds to the peak of the Gaussian fit, while the uncertainty is computed in order to include at least the 68.2% of the width values from the Monte Carlo around the peak of the Gaussian (see Figure 4.6, upper panel).

Repeating the aforementioned steps for the same component c in all the pulse profiles representative of each epoch, we obtain a map of the temporal evolution of the widths for c (see same Figure, bottom panel). A follow-up analysis is performed to evaluate the possible presence of a trend in time that differs from a non-evolving width. We first fit the time series of the obtained widths for component c with a linear polynomial, using 2σ error bars on the widths to be more conservative. From this, we obtain a slope value a, its error σ_a and the reduced χ^2 of the fit. We group the results according to:

- *Flat trend* if $(a - 2\sigma_a) < 0 < (a + 2\sigma_a)$ and $\chi^2 < 1.5$;
- *Scatter plot* if $(a - 2\sigma_a) < 0 < (a + 2\sigma_a)$ and $\chi^2 > 1.5$;
- *Other trend* if $(a - 2\sigma_a) > 0$ or $(a + 2\sigma_a) < 0$.

Figure 4.7 reports an example for each classified trend. Every column of the Figure is dedicated to a profile cut of one of the examined pulsars: a cut at 20% of the main peak height of the leading component of PSR J0613−0200 yields a flat trend in time, a cut at 50% of the main peak height of the leading component of PSR J2145−0750 leading component yields a scatter plot, a cut at 30% of the peak height of PSR J1713+0747 shows a linear trend (i.e., other trend). The profile cuts are shown in the bottom panels. Upper panels display the temporal trends of the widths. The shaded regions are included between two lines characterized by the same offset of the best linear fit, and slopes equal to the best fit slope, respectively increased and decreased of twice the fit uncertainty σ_a. The central panels show the trend in the residual of the fit.

4.4 Comparison with previous results

Shao et al. 2013 performed an analysis of the temporal trends of the profile widths at various heights for PSR J1744−1134 and PSR J1939+2134. Their data set comprises the same observations used in this Chapter. As both of the mentioned sources are exceptionally bright, Shao et al. 2013 directly worked only on the individual observations (i.e., without analyzing averaged profiles with high S/N). Moreover, they added to the data sets a second series of data, as well obtained with the Effelsberg radio telescope at L-band, and processed with the EBPP backend. However, these data were collected after 2009, when the original 21-cm receiver was substituted. The central frequency of the new receiver changed as well, from 1410 MHz to 1360 MHz. In this work, we intentionally decide not to include the data at different frequency to preserve the uniformity in the data set and avoid the risk of detecting profile variations due to the natural frequency evolution of the pulsar profiles (Liu et al., 2014). In fact, Shao et al. 2013 included the 1360 MHz data after fitting for a width jump between the two series of data.

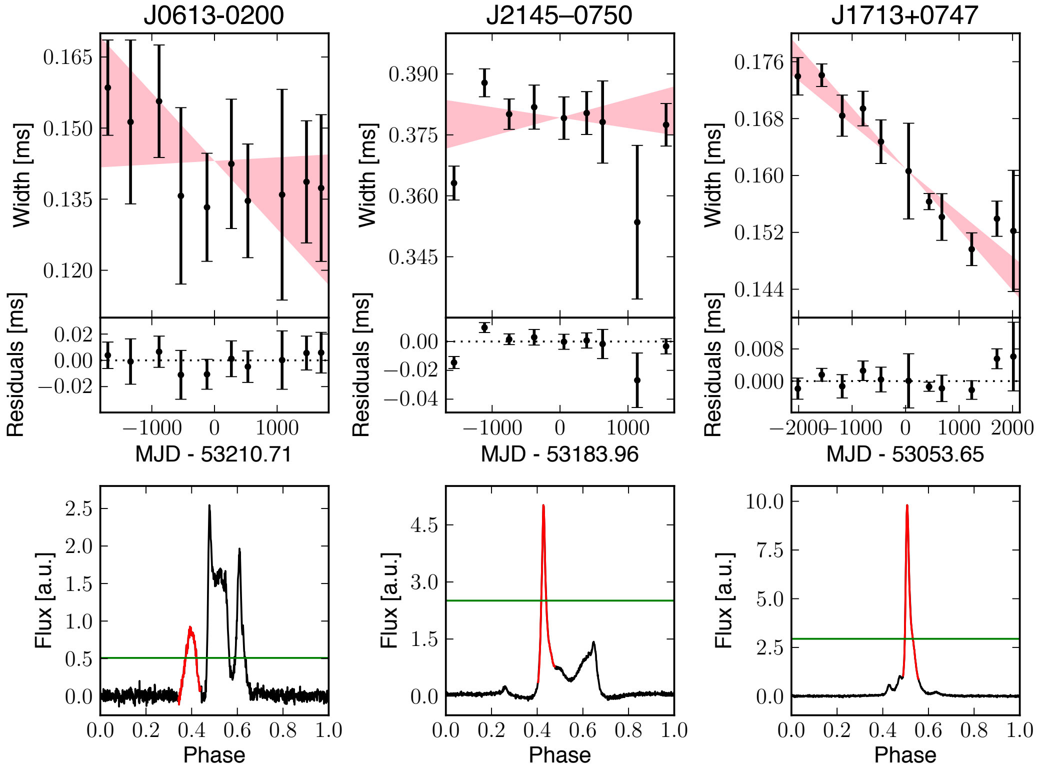

Figure 4.7: Examples of each class of results. *Upper panels*, trend of the widths for one of the inspected profile cuts performed on three chosen pulsars, whose names are reported at the panel top, displayed with 2σ error bars. The shaded regions are limited by lines characterized by the same offset resulting from the best linear fit performed on the widths, and by slopes that are, respectively, $2\sigma_a$ larger and smaller with respect to the slope of the best linear fit. *Central panels*, residuals obtained from the subtraction of the best linear fit from the widths. A dotted, black line is drawn at $y = 0$. *Lower panels*, the pulsar profile is shown in black. The profile component for which the width analysis is shown in the panels above is highlighted in red. The altitude of the profile cut is indicated by the green line.

Pulsar	**Peak and percentage**	**Source**	**Average width [deg]**	**Width time derivative [mdeg/yr]**	**Claimed trend**
J1744−1134	I, 50%	Shao et al. 2013	12.53(3)	1.3(72)	flat trend
		this work	12.30(3)	2(9)	flat trend
J1939+2134	I, 50%	Shao et al. 2013	8.281(9)	−3.2(34)	flat trend
		this work	8.325(7)	−5(3)	flat trend
J1939+2134	II, its 50%	Shao et al. 2013	10.245(17)	3.5(66)	flat trend
		this work	10.20(17)	−1(7)	flat trend

Table 4.1: Comparison between the results obtained by Shao et al. 2013 and our pipeline. The columns report, respectively: the source name, the peak and height percentage of the performed profile cut, the work reference, the averaged width, the slope obtained from a linear fit of the results (along with a 1σ error bar value), a qualitative evaluation of the trend.

Shao et al. 2013 computed the width values for PSR J1744−1134 via fitting 10^4 realization of its main component, obtained by adding white noise to the phase bin amplitudes, with a sum of three functions (one Gaussian and two Landau functions). From the fit they obtained 10^4 width values, that they collected in an histogram from which they derived a final width value, along with its uncertainty. The uncertainty was then rescaled with the reduced χ^2 of the fit.

PSR J1939+2134 was differently investigated. The width values were obtained by fitting a parabola on each of the three, easily recognizable components of the pulse profile. The uncertainties on the widths of the main pulse and interpulse of this pulsar profile are achieved via a propagation of the errors of the parabola parameters.

PSR J1744−1134 was analyzed by Shao et al. 2013 performing a pulse profile cut at 50% of the main peak height, while PSR J1939+2134 was analyzed searching for the full-width-half-maximum of the main peak and of the interpulse, the peak relative separations, and the internal and external separations of the two components. We repeat the analysis of Shao et al. 2013 using the method presented in Section 4.3 to check for the compatibility among the procedures.

Table 4.1 reports our results and a comparison with the values recovered from Table 1 of Shao et al. 2013. Figures 4.8 and 4.9 visually display the pulse profiles along with the altitude at which the cut is performed (upper panels) and the overlap between the results of Shao et al. 2013 (in green, private

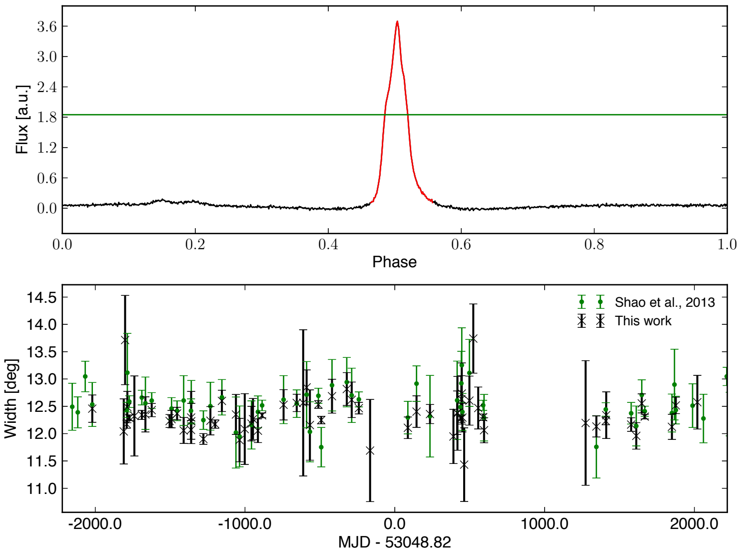

Figure 4.8: *Upper panel*, the pulse profile of PSR J1744−1134 is shown in black. The profile component for which the width analysis is performed is highlighted in red. The altitude of the profile cut is indicated by the green line. *Lower panel*, overlap of the widths obtained from the analysis performed on the component shown in the upper panel following the method described in Section 4.3 (black crosses and error bars) and the results obtained by Shao et al. 2013 (green dots and error bars, private communication by L. Shao).

communication by L. Shao) and the ones obtained by us following the method described in Section 4.3, applied on the individual observations of this pulsar (in black). It is possible to state that the slopes of a linear fit are always well in agreement. Although a visual inspection of the widths in the bottom panels of the aforementioned Figures suggests a good match between the two pipelines, we systematically observe an absolute offset, incompatible with the error bar sizes, between the averaged widths computed by Shao et al. 2013 and by us. This can be easily attributed to the different procedures used to calculate the profile widths.

4.5 Results

The altitudes at which the different profile cuts were performed for each pulsar are shown in Figure 4.10.

Not all the available components displayed by the sources in our sample are analyzed, depending on the pulse profile shape and the overall S/N. The label of

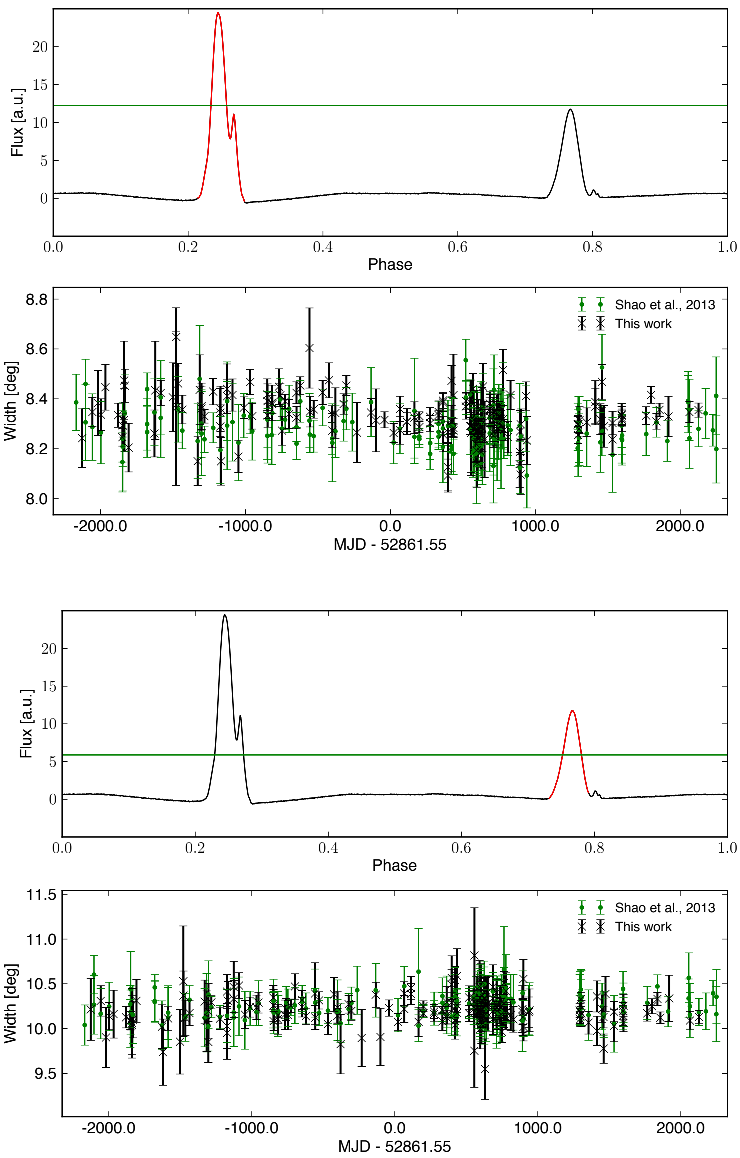

Figure 4.9: *Upper panels*, the pulse profile of PSR J1939+2134 is shown in black. The profile component for which the width analysis is performed (leading component in the first Figure and trailing component in the second one) is highlighted in red. The altitude of the profile cut is indicated by the green line. *Lower panel*, overlap of the widths obtained from the analysis performed on the component shown in the upper panel following the method described in Section 4.3 (black crosses and error bars) and the results obtained by Shao et al. 2013 (green dots and error bars, private communication by L. Shao).

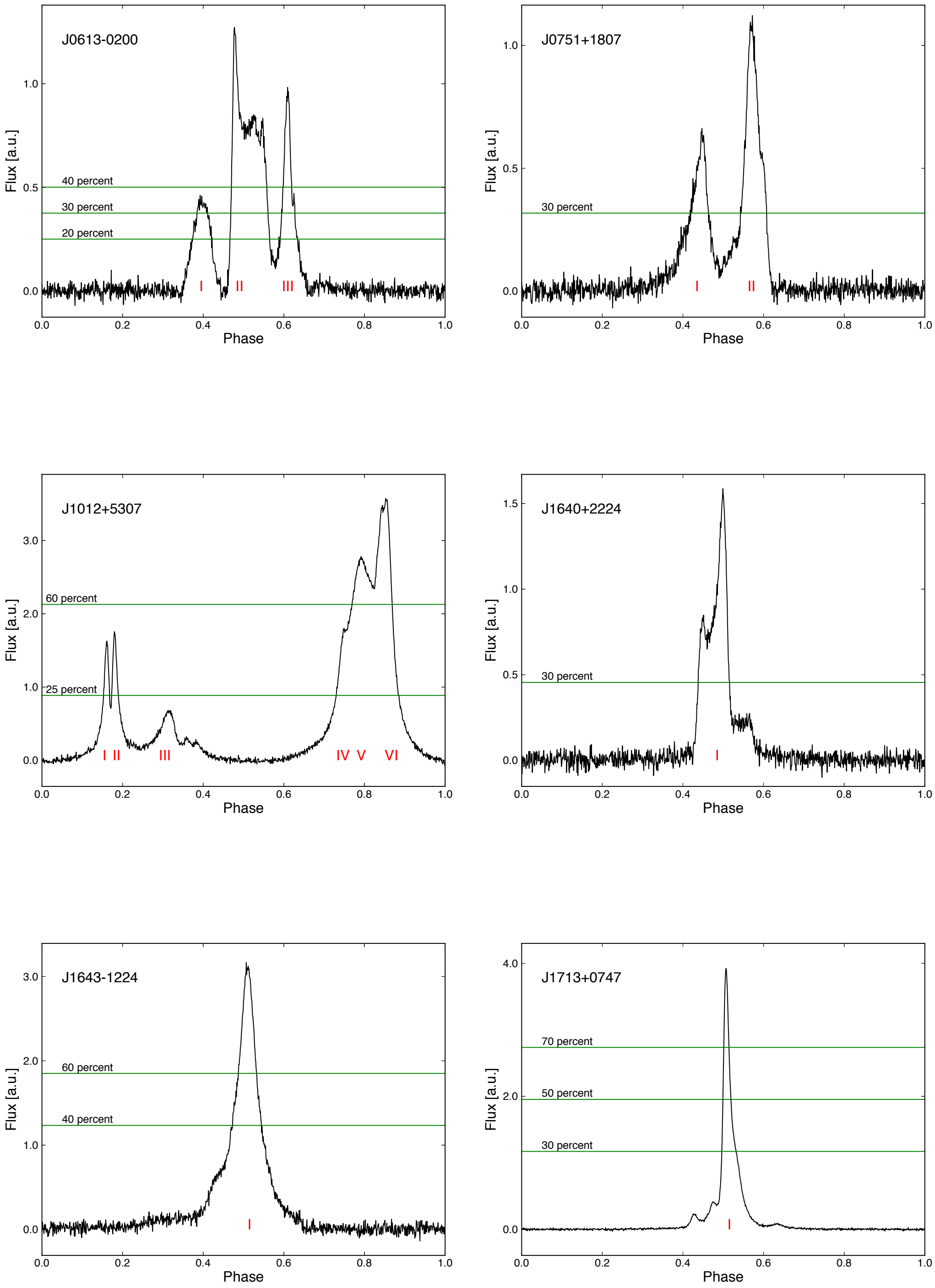

Figure 4.10: In black are presented the pulse profiles of the sources in our sample, along with the altitudes at which the profile cuts were performed, displayed in green. Peak labeling is indicated in red.

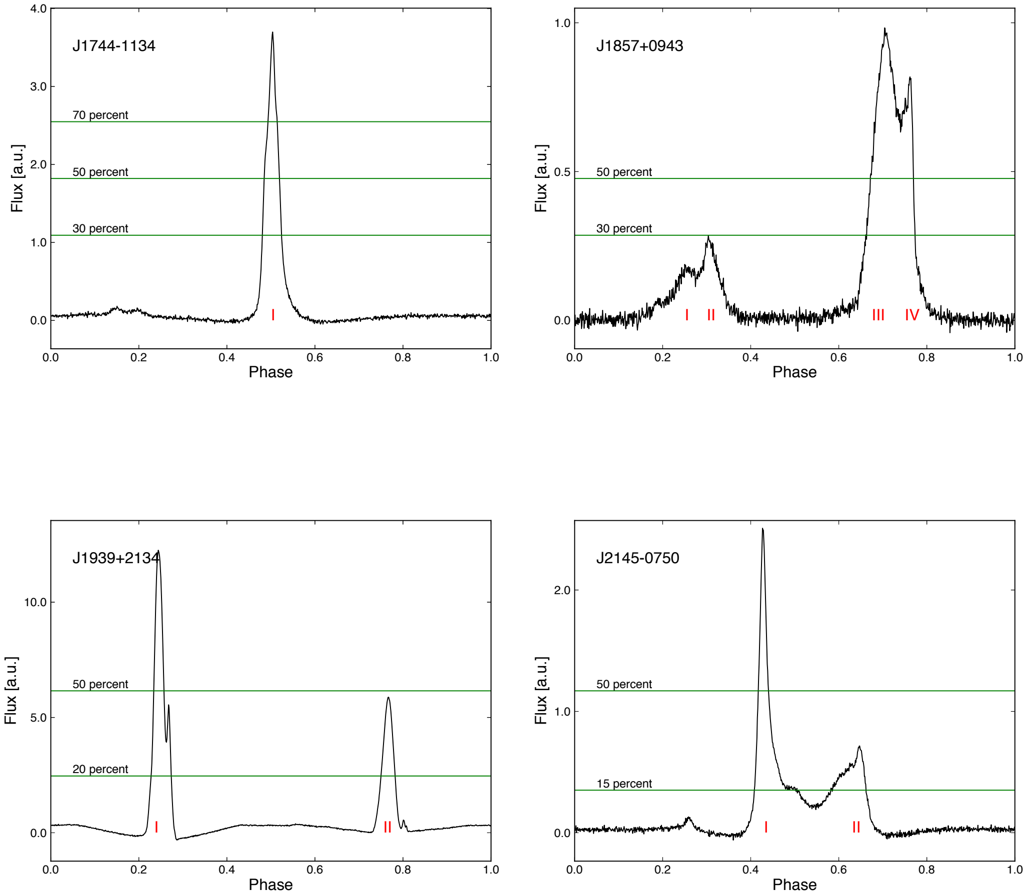

Figure 4.10: (continued)

the analyzed peaks per each pulsar, and the results from the analysis presented in Section 4.3 and performed on the 1-year and 6-month averaged profiles are reported in Table 4.2. Note that the width uncertainties were taken at 2σ to perform the linear fit. In Table 4.3 we report the results from the analyses performed on the individual observations for the brightest pulsars, while in Figure 4.11 we show how the results obtained from the individual observations nicely match with what computed for the high S/N averaged profiles. This is a confirmation that the high S/N profiles simply highlighted the underlying behavior of the individual observations, and supports the usage of the 1-year and 6-month series as a valid alternative data sets for those pulsars whose individual observations are too weak to apply the pipeline described in Section 4.3.

In the following part we describe in greater details the individual pulsars of the sample, with the exception of PSR J1713+0747 (see Section 4.5.2).

4.5.1 Pulsars in the sample

PSR J0613−0200, this source is characterized by a complex shape and a low S/N in L-band. Our analysis shows that its leading and trailing peaks have non-evolving widths in time (see Figure 4.12), while the central and brighter component displays a decreasing, linear temporal trend. At an altitude equivalent to the 30% of the main peak height, the width trend turns flat excluding, respectively, the first 3 and 4 points from the 1-year and 6-month profiles. At 40%, this happens by only excluding the first point from both the series (see Figure 4.13). In this last case, both the points are what now on we will call *outliers*. We define as *outliers* those points whose unique presence in the computed trends induces a deviation from a non-evolving behavior;

PSR J0751+1807, the pulse profile of this source is given by two peaks separated by an emission bridge. We only examine the 6-month profiles, as the 1-year series enumerates a scarce number of observations. Concerning the 6-month series, the temporal trends for the width of peak II and the separation between components I and II show a linear, decreasing trend with time. These trends disappear by eliminating the third point of the data set, that is thus identified as an outlier (see Figure 4.14). We do notice that the main peak of

Pulsar	**Peak**	**Percentage**	χ^2**/dof**	χ^2 **significance**	**Slope range**	**Trend evaluation**
J0613−0200	I	20	2.172/8	9.8e-01	-1.44e-05;7.50e-07	flat trend
			2.445/15	1.0e+00	-1.30e-05;1.95e-06	flat trend
J0613−0200	II	30	2.313/8	9.7e-01	-7.82e-06;-1.06e-06	linear trend
			4.143/15	1.0e+00	-7.67e-06;-1.07e-06	linear trend
J0613−0200	II	40	3.957/8	8.6e-01	-6.75e-06;-1.90e-07	linear trend
			4.444/15	1.0e+00	-7.26e-06;-1.80e-07	linear trend
J0613−0200	III	30	1.266/6	9.7e-01	-1.01e-05;1.35e-06	flat trend
			3.438/14	1.0e+00	-1.12e-05;1.06e-06	flat trend
J0613−0200	II+III	30	2.857/7	9.0e-01	-8.32e-06;1.16e-06	flat trend
			7.755/14	9.0e-01	-8.11e-06;8.90e-07	flat trend
J0751+1807	I	30				
			4.035/7	7.8e-01	-3.95e-05;3.40e-07	flat trend
J0751+1807	II	30				
			4.549/7	7.1e-01	-1.93e-05;-2.70e-07	linear trend
J0751+1807	I+II	30				
			3.191/7	8.7e-01	-3.58e-05;-4.00e-07	linear trend
J1012+5307	I+II	25	4.314/8	8.3e-01	-4.72e-06;3.60e-07	flat trend
			4.552/16	1.0e+00	-4.64e-06;2.40e-07	flat trend
J1012+5307	II+IV	25	1.569/8	9.9e-01	-5.96e-06;2.52e-06	flat trend
			2.910/15	1.0e+00	-5.01e-06;2.35e-06	flat trend
J1012+5307	II+VI	25	0.845/8	1.0e+00	-1.85e-06;6.91e-06	flat trend
			2.858/14	1.0e+00	-1.37e-06;6.95e-06	flat trend
J1012+5307	IV+V+VI	25	0.792/8	1.0e+00	1.00e-08;8.25e-06	linear trend
			2.560/16	1.0e+00	1.20e-07;7.52e-06	linear trend
J1012+5307	V+VI	60	2.885/8	9.4e-01	-2.65e-06;5.11e-06	flat trend
			4.412/16	1.0e+00	-2.55e-06;4.17e-06	flat trend

Table 4.2: Results from the analysis described in Section 4.3 on the 1-year and 6-month averaged pulse profiles of all the pulsars in our sample. The columns report, respectively: MSP name, the labeling of the studied peak, the main peak height percentage at which we computed the studied profile width, the χ^2 versus degrees of freedom ratio for a linear fit, its significance, the limits (upper and lower within 2 σ) of the computed linear slope, a qualitative evaluation of the width temporal trend as introduced in Section 4.3. For each examined component are displayed two rows, referred respectively to the results obtained using the 1-year and the 6-months averaged pulse profiles.

Pulsar	**Peak**	**Percentage**	χ^2**/dof**	χ^2 **significance**	**Slope range**	**Trend evaluation**
J1640+2224	I	30	1.026/5	9.6e-01	-6.71e-06;1.70e-07	flat trend
			2.676/12	1.0e+00	-6.04e-06;6.80e-07	flat trend
J1643−1224	I	40	3.535/7	8.3e-01	-1.82e-05;-3.00e-06	linear trend
			7.094/14	9.3e-01	-1.79e-05;-2.90e-06	linear trend
J1643−1224	I	60	1.724/7	9.7e-01	-1.15e-05;1.42e-06	flat trend
			4.132/14	9.9e-01	-1.12e-05;1.79e-06	flat trend
J1713+0747	I	30	11.140/9	2.7e-01	-8.56e-06;-6.18e-06	linear trend
			22.768/16	1.2e-01	-8.20e-06;-5.82e-06	linear trend
J1713+0747	I	50	17.764/9	3.8e-02	-3.87e-06;-2.89e-06	linear trend
			33.658/16	6.0e-03	-3.72e-06;-2.76e-06	linear trend
J1713+0747	I	70	5.427/9	8.0e-01	-2.05e-06;-1.23e-06	linear trend
			13.149/16	6.6e-01	-1.96e-06;-1.16e-06	linear trend
J1744−1134	I	30	13.197/7	6.7e-02	-2.44e-07;1.02e-06	scatter plot
			16.092/13	2.4e-01	-2.74e-07;9.58e-07	flat trend
J1744−1134	I	50	6.951/7	4.3e-01	-5.80e-07;8.12e-07	flat trend
			6.876/13	9.1e-01	-5.94e-07;8.14e-07	flat trend
J1744−1134	I	70	6.215/7	5.1e-01	-1.79e-06;9.39e-07	flat trend
			8.688/13	8.0e-01	-1.62e-06;9.95e-07	flat trend
J1857+0943	III+IV	30	2.145/7	9.5e-01	-1.14e-05;5.27e-06	flat trend
			2.660/10	9.9e-01	-9.96e-06;4.44e-06	flat trend
J1857+0943	III+IV	50	1.211/6	9.8e-01	-4.07e-06;5.09e-06	flat trend
			0.875/11	1.0e+00	-4.50e-06;3.66e-06	flat trend
J1939+2134	I	50	8.514/8	3.8e-01	-1.17e-07;3.76e-08	flat trend
			13.056/18	7.9e-01	-1.18e-07;3.30e-08	flat trend
J1939+2134	II	20	2.209/8	9.7e-01	-6.30e-08;3.65e-07	flat trend
			6.426/18	9.9e-01	-5.30e-08;3.67e-07	flat trend
J1939+2134	I+II	20	4.641/8	8.0e-01	-2.32e-07;1.23e-07	flat trend
			6.595/18	9.9e-01	-2.25e-07;1.20e-07	flat trend
J2145−0750	I	50	23.056/7	1.7e-03	-2.57e-06;4.55e-06	scatter plot
			29.803/14	8.1e-03	-3.27e-06;3.01e-06	scatter plot
J2145−0750	I+II	15	11.045/8	2.0e-01	-4.66e-06;9.82e-06	flat trend
			12.708/14	5.5e-01	-5.78e-06;6.86e-06	flat trend

Table 4.2: (continued)

Pulsar	**Peak**	**Percentage**	χ^2**/dof**	χ^2 **significance**	**Slope range**	**Trend evaluation**
J1713+0747	I	30	96.497/98	5.2e-01	-8.78e-06;-7.08e-06	linear trend
J1713+0747	I	50	168.848/110	2.6e-04	-3.97e-06;-3.37e-06	linear trend
J1713+0747	I	70	68.502/114	1.0e+00	-2.10e-06;-1.60e-06	linear trend
J1744−1134	I	50	21.155/65	1.0e+00	-4.87e-07;6.25e-07	flat trend
J1939+2134	I	50	72.962/172	1.0e+00	-1.25e-07;7.10e-09	flat trend
J1939+2134	II	50	38.027/172	1.0e+00	-1.87e-07;1.49e-07	flat trend
J2145−0750	I	50	100.872/79	4.9e-02	-3.02e-06;1.50e-06	flat trend
J2145−0750	I+II	15	68.644/78	7.7e-01	-6.52e-06;2.92e-06	flat trend

Table 4.3: Results from the analysis described in Section 4.3 on the individual observations of the brightest pulsars in our sample. The columns report, respectively: MSP name, the labeling of the studied peak, the main peak height percentage at which we computed the studied profile width, the χ^2 versus degrees of freedom ratio for a linear fit, its significance, the limits (upper and lower within 2 σ) of the computed linear slope, a qualitative evaluation of the width temporal trend as introduced in Section 4.3.

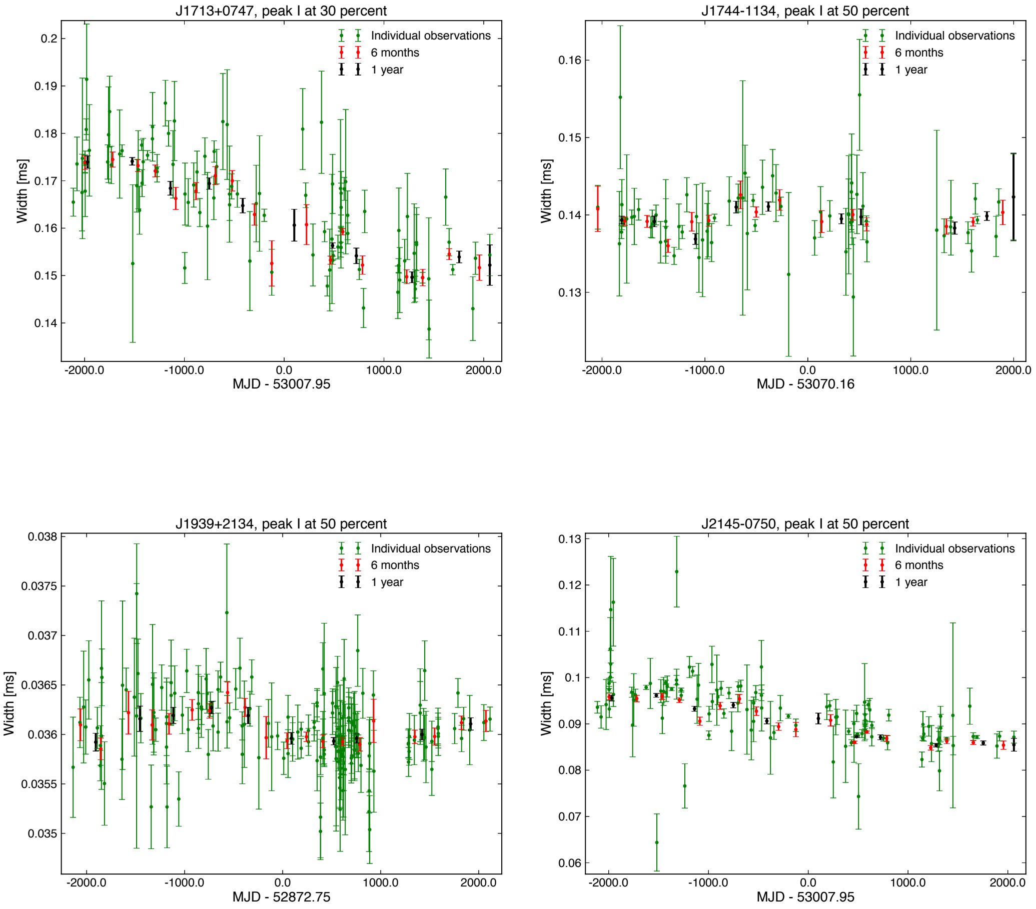

Figure 4.11: Overlap between the results of the width analysis performed on the 1-year (in black), 6-month (in red) and individual observation (in green) series for the pulsars where the latter data set is reasonably usable: PSR J1713+0747 (upper row, left panel) at 30% of the peak height, PSR J1744-1134 (upper row, right panel) at 50% of the peak height, PSR J1939+2134 (lower row, left panel) at 50% of the main peak height, leading component, and PSR J2145-0750 (lower row, right panel) at 50% of the main peak height, leading component.

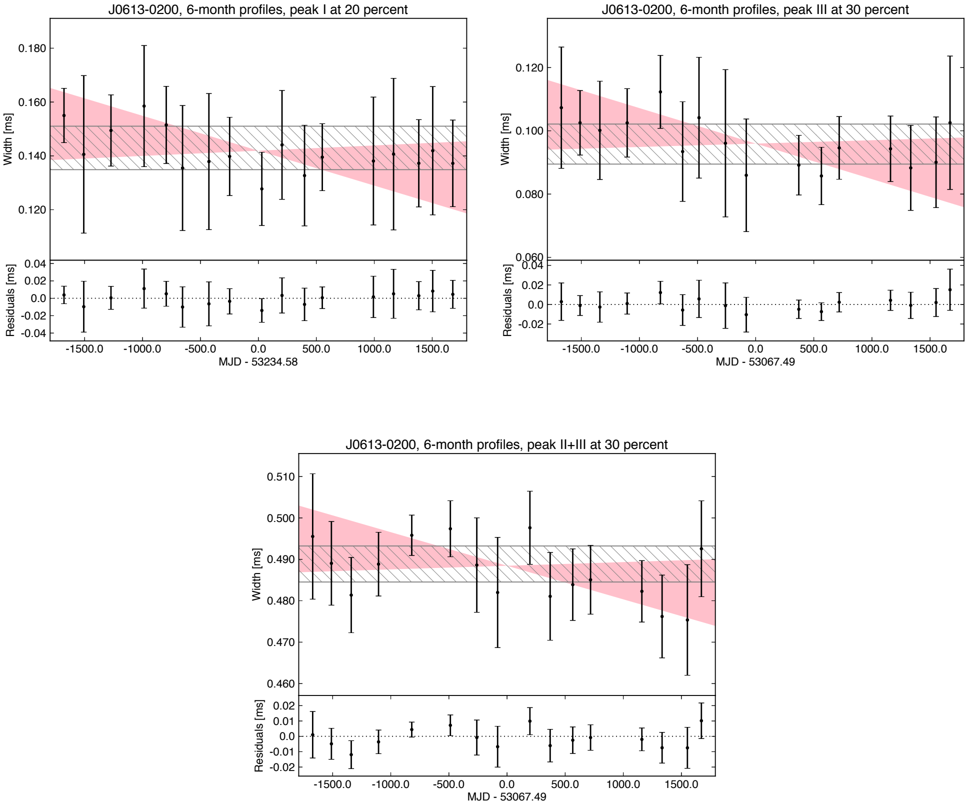

Figure 4.12: Samples of width trends characterized by a non-evolving behavior for PSR J0613−0200. Following a clockwise orientation, the plots are obtained for, respectively, component I at 20% of the main peak height, component III at 30% of the main peak height and the separation between the leading and the trailing edges of components II and III for the 6-month profiles. *Upper panels*, the observed widths and 2σ are displayed in black. The limits of the colored regions are lines characterized by the same offset of the best linear fit performed on the widths, and by slopes that cover a 2σ uncertainty range around the best fit value. The shaded areas cover a 2σ uncertainty region associated with the fit of the observed widths with an horizontal line (i.e., no time evolution in the data). *Lower panels*, residuals obtained by subtracting the best linear fit from the observed widths. A dotted, black line is drawn at $y = 0$.

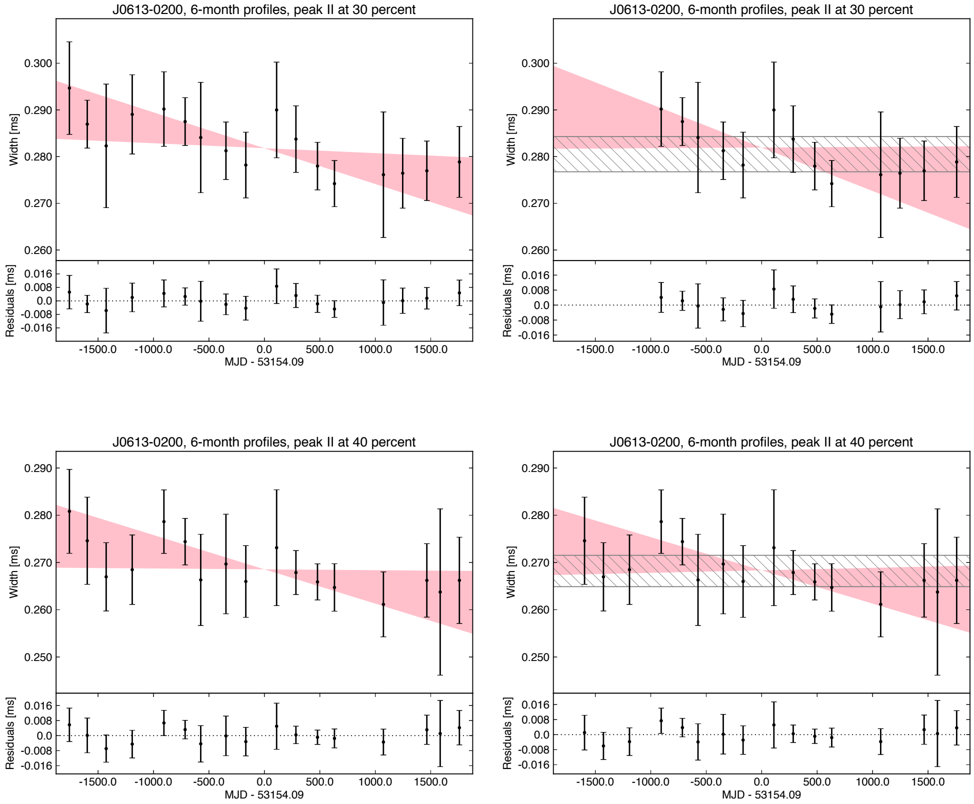

Figure 4.13: *Upper row*, comparison of the time-evolution for the width of component II of PSR J0613−0200 in the 6-month profiles, cut at 30% of the peak height, including (left panels) and excluding (right panels) the first 4 points of the series. *Lower row*, comparison of the time-evolution for the width of component II of PSR J0613−0200 in the 6-month profiles, cut at 40% of the peak height, including (left panels) and excluding (right panels) the first point of the series. See the caption of Figure 4.12 for explanation of the labels, markers and highlighted areas.

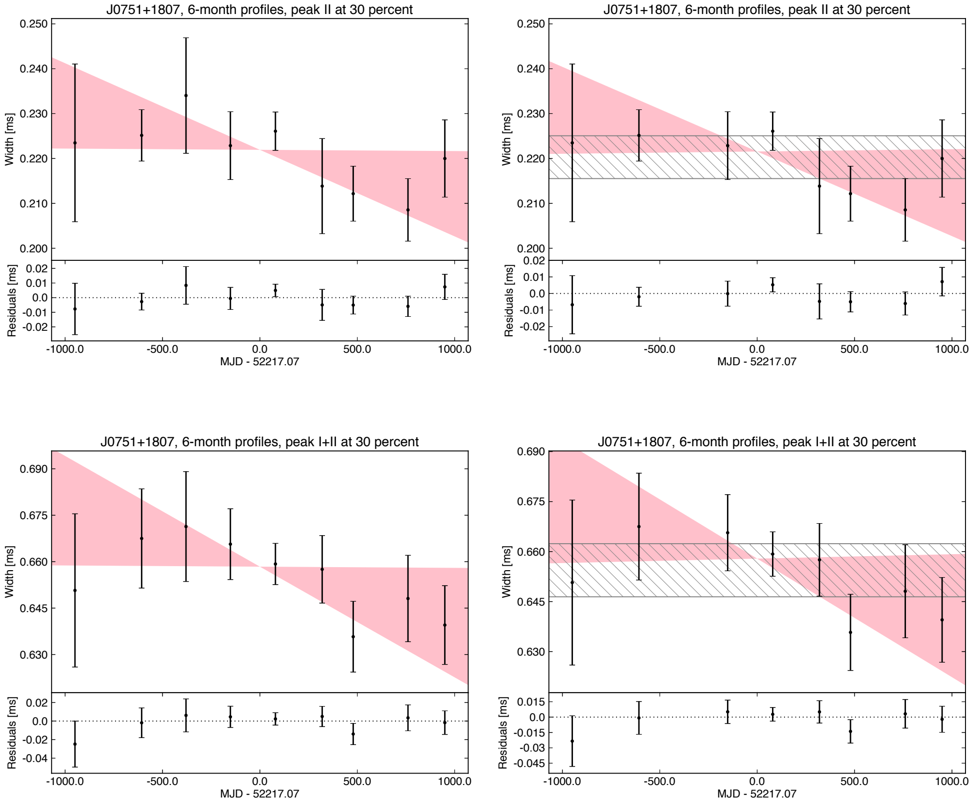

Figure 4.14: *Upper row*, comparison of the time-evolution for the width of component II of PSR J0751+1807 in the 6-month profiles, cut at 30% of the peak height, including (left panels) and excluding (right panels) the first 4 points of the series. *Lower row*, comparison of the time-evolution for the separation between the leading and the trailing edges of components I and II of PSR J0751+1807 in the 6-month profiles, cut at 40% of the peak height, including (left panels) and excluding (right panels) the first point of the series. See the caption of Figure 4.12 for explanation of the labels, markers and highlighted areas.

the averaged profile corresponding to the outlier is systematically weaker of the same feature in all the remaining profiles, as shown in Figure 4.15;

PSR J1012+5307, the pulse profile of this source is extremely noisy and complex, characterized by at least 6 components. We perform several profile cuts: we analyze the separation between the leading edge of peak I and the trailing edge of peak II (I+II), the width of the component that includes peaks IV, V and VI (IV+V+VI), and the width of the component that includes peaks V and VI (V+VI). We test as well the separation between the trailing edge of peak II and the leading and trailing edges of, respectively, peaks IV (II+IV) and VI (II+VI). No deviations from a flat trend are detected in any of these

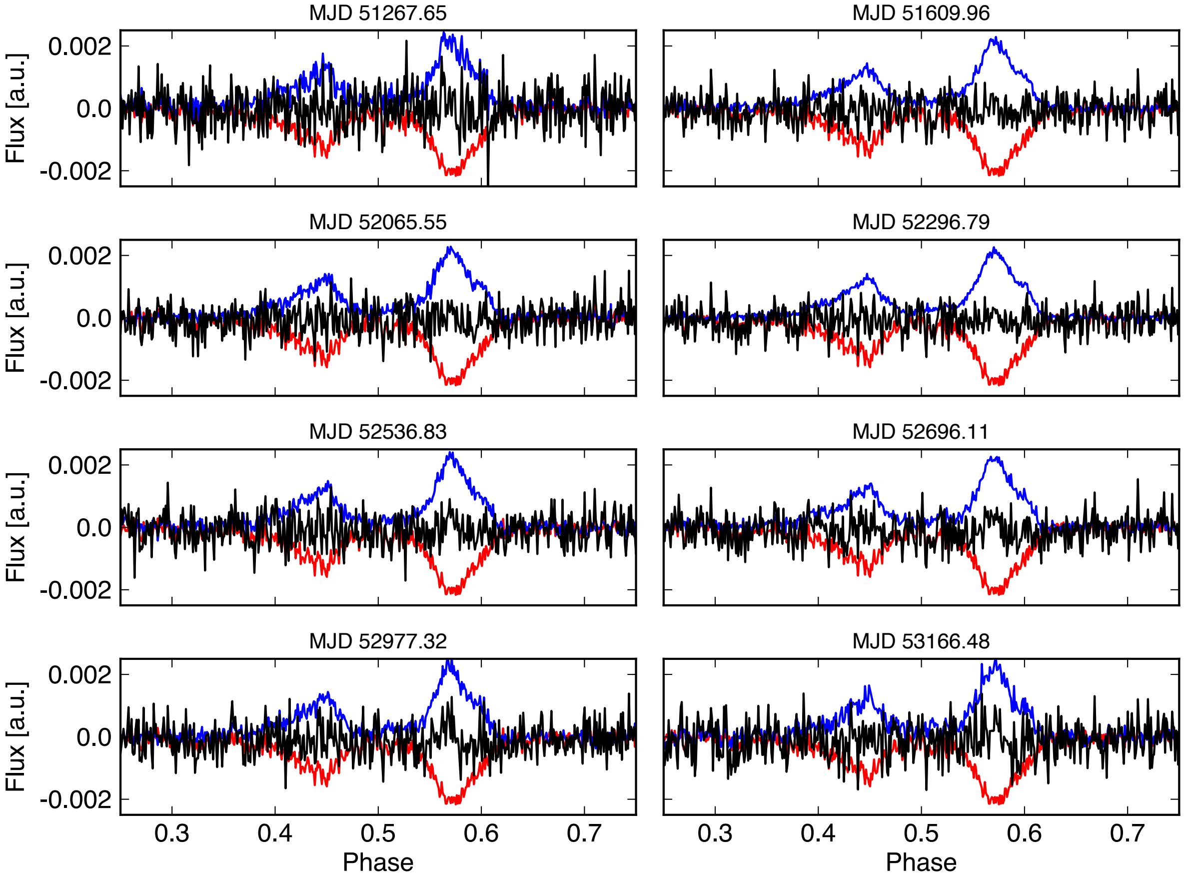

Figure 4.15: Each panel shows the difference (in black, three times magnified) between the third pulse profile in the 6-month series (in red, reversed the for sake of clarity) of PSR J0751+1807 and the remaining profiles of the series (in blue) relative to indicated MJDs.

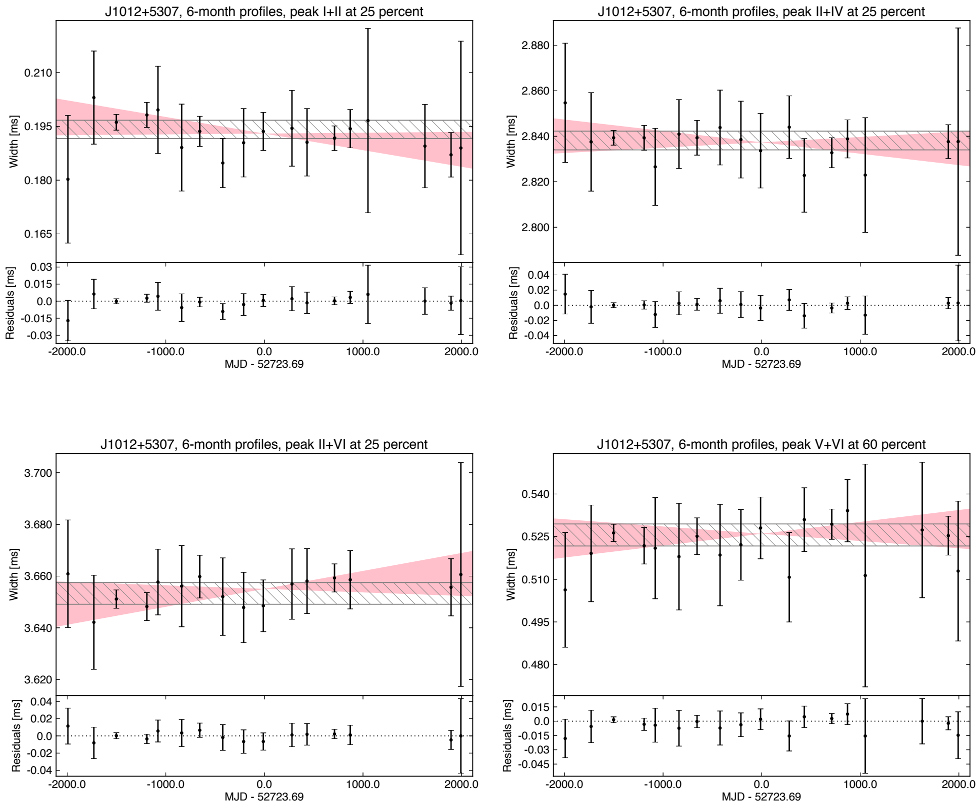
J1012+5307, 6-month profiles, peak I+II at 25 percent

J1012+5307, 6-month profiles, peak II+IV at 25 percent

J1012+5307, 6-month profiles, peak II+VI at 25 percent

J1012+5307, 6-month profiles, peak V+VI at 60 percent

Figure 4.16: Samples of width trends characterized by a non-evolving behavior for PSR J1012+5307. Following a clockwise orientation, the plots are obtained for, respectively, the separation between the leading and the trailing edges of components I and II, II and IV, II and VI at 25% of the main peak height and of components V and VI at 60% of the main peak height for the 6-month profiles. See the caption of Figure 4.12 for explanation of the labels, markers and highlighted areas.

cuts (see Figure 4.16), except for a linear, increasing trend for IV+V+VI. This appears to be in contrast with the non-evolving trends shown by the other profile cuts that include one of the peaks present in the combination (such as II+IV or II+VI). However, to compute the width trends for II+IV and II+VI we use a longitude range to fit the component edges that is smaller with respect the one for IV+V+VI. This is due to peak II, that is weaker than IV and VI, and it implies an increased uncertainty for the computed widths that can mask possible trends. The width trend for IV+V+VI turns flat excluding from the analysis the last point of the 1-year averaged series, identifying it as an outlier, and the two last points of the 6-month series (see Figure 4.17);

PSR J1640+2224: the weakness of this source and its steep edges allows us

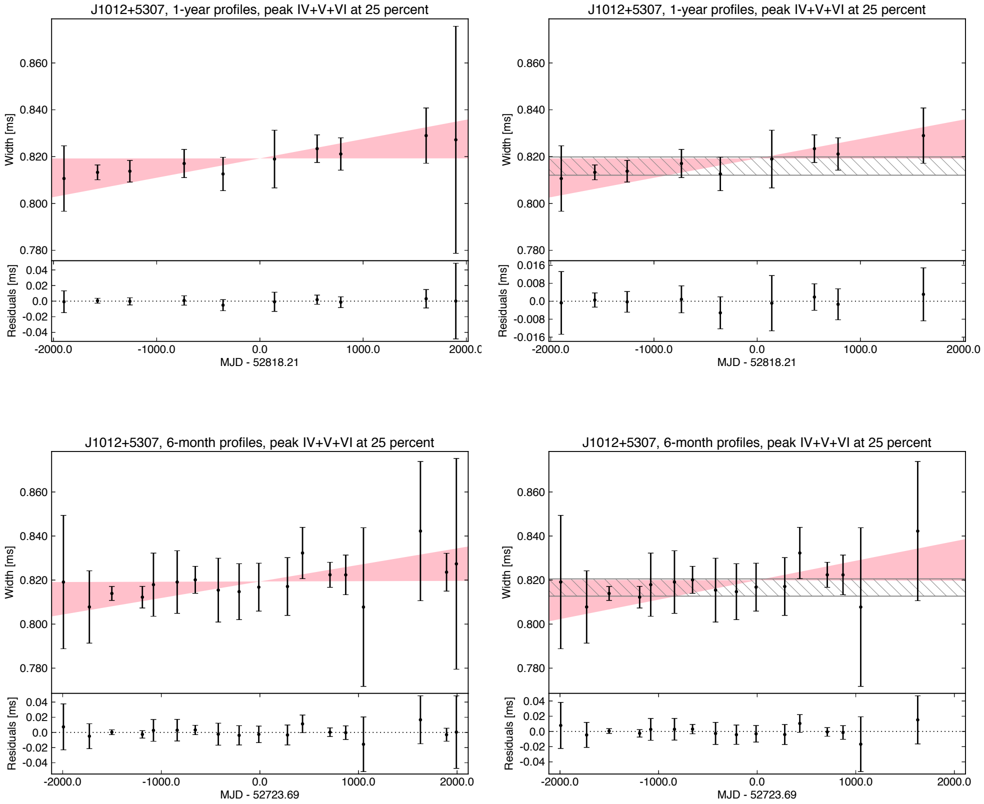

Figure 4.17: *Upper row*, comparison of the time-evolution for the widths of component IV+V+VI of PSR J1012+5307 in the 1-year profiles, cut at 25% of the peak height, including (left panels) and excluding (right panels) the last point of the series. *Lower row*, comparison of the time-evolution for the widths of component IV+V+VI of PSR J1012+5307 in the 6-month profiles, cut at 25% of the peak height, including (left panels) and excluding (right panels) the last two points of the series. See the caption of Figure 4.12 for explanation of the labels, markers and highlighted areas.

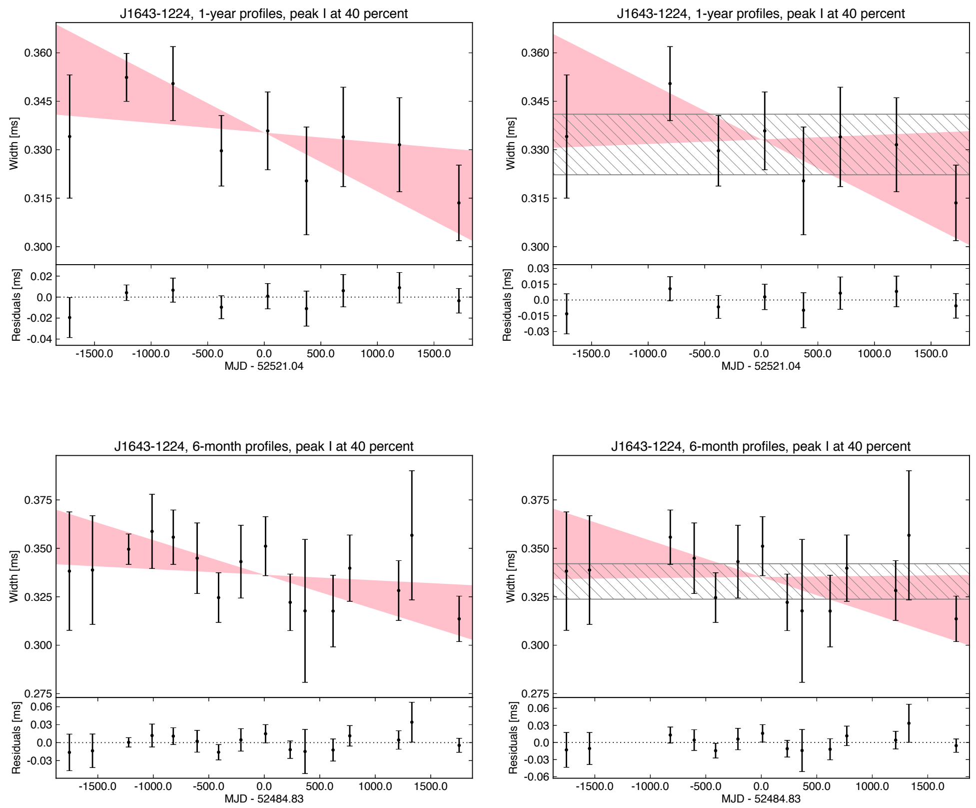

Figure 4.18: *Upper row*, comparison of the time-evolution for the widths of PSR J1643−1224 in the 1-year profiles, cut at 40% of the peak height, including (left panels) and excluding (right panels) the second point of the series. *Lower row*, the same as above in the 6-month profiles, including (left panels) and excluding (right panels) the second point of the series. See the caption of Figure 4.12 for explanation of the labels, markers and highlighted areas.

to satisfactorily perform only one profile cut, at 30% of the main peak height. Both in the 1-year and 6-month averaged profiles no signs of evolving trend have been detected;

PSR J1643−1224, we analyze the simple profile of this source at two altitudes, corresponding to the 40 and 60% of the peak height. Among these, the profile cut performed at 40% yields a linear, decreasing trend both in the 1-year and 6-month averaged profiles. The trend disappears eliminating from the analysis the second point in the 1-year series, identifying it as an outlier, and the third and fourth points in the 6-month series (see Figure 4.18);

PSR J1744−1134: this is one of the two sources that are in common with

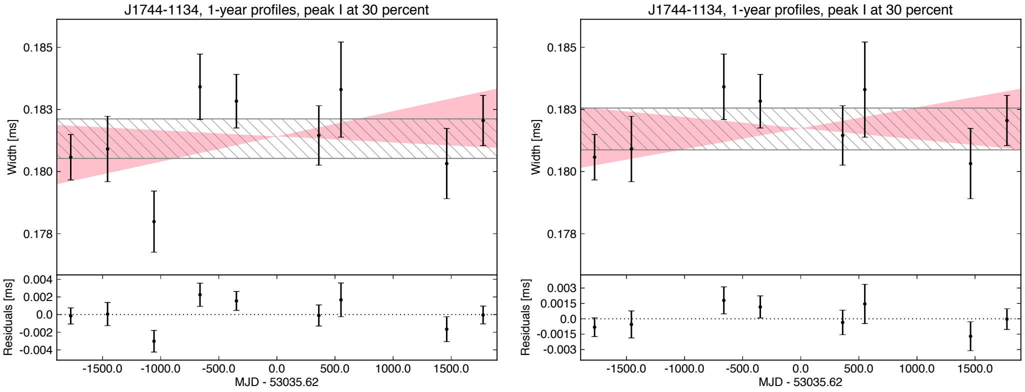

Figure 4.19: Comparison of the time-evolution for the widths of PSR J1744−1134 in the 1-year profiles, cut at 30% of the peak height, including (left panel) and excluding (right panel) the third point of the series. See the caption of Figure 4.12 for explanation of the labels, markers and highlighted areas.

Shao et al. 2013. The analysis of the profile width at 50% of the peak height performed on the individual observations, 6-month and 1-year averaged profiles, as well as at 70% on the 6-month and 1-year profiles and at 30% on the 6-month profiles reports a flat trend. However, the analysis of the width evolution at 30% of the peak height on the 1-year profile yields a statistically unacceptable linear fit. By excluding the third point of the 1-year series, a completely flat behavior is recovered (see Figure 4.19), identifying it as an outlier;

PSR J1857+0943: this pulsar has a complex and noisy pulse profile, made of two composite components. We are only able to analyze the trailing component at two heights (at 30 and 50% of the main peak). For both of them, for the 1-year and 6-months averaged profiles, the widths do not evolve with time;

PSR J1939+2134: this is the second pulsar that is in common with Shao et al. 2013. At all the examined heights, the widths of the source profiles are compatible with a non-evolving trend in time. However, it is worth noting that we initially tested an additional cut of component I, at 20% of the main peak height. Its temporal dependency results in a decreasing linear trend with a reduced χ^2 of, respectively, 0.8, 0.7 and 0.4 for the 1-year, the 6-month averaged profiles and the individual observations. We omit this result from Tables 4.2 and 4.3 because we deduce that is is caused by an artifact of the data

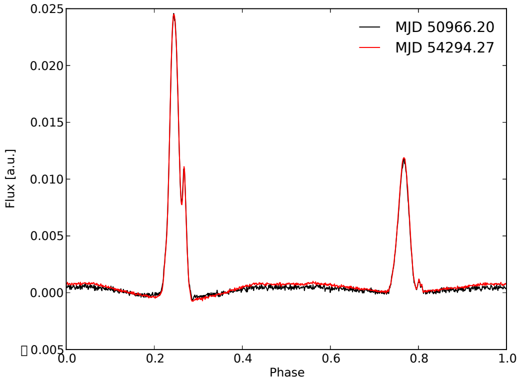

Figure 4.20: Temporal evolution of the digitalization artifact present in the used observations of PSR J1939+2134.

due to a digitalization issue of the signal (also shared with PSR J1744−1134), that generates two clear dips in the off-pulse baseline next to the pulse and the interpulse. This artifact evolves in time, as shown in Figure 4.20. In particular, the digitization dips next to the leading peak sink with time, inducing an increase of the off-pulse average amplitude (while the peak height remains approximatively the same). This means that a cut at 20% of the mean peak height should lead to an apparent shrinking of the profile across the years, due to the fact that the variable baseline induces us to cut at higher heights. Although the artificial width variation should affect the widths at every peak height percentage, in an absolute value it is higher for wider widths, closer to the dips. As a matter of fact, the spurious profile variation is likely not detectable (at the level of sensitivity of this analysis) at the main peak full-width-half-maximum.

PSR J2145−0750, this source shares the same digitization problems of PSRs J1744−1134 and J1939+2134. Although the profile cuts at 15% of the main peak height yield a flat trend both in the 1-year and the 6-month series, we obtain a scatter plots for the profile cuts performed at 50% of the main peak height. The scatter plots turn to a flat trend in the case of the 1-year profiles excluding from the analysis the first point of the series, identifying it as an outlier. The same result is obtained with the 6-month series eliminating the first three points from the 6-month series (see Figure 4.21).

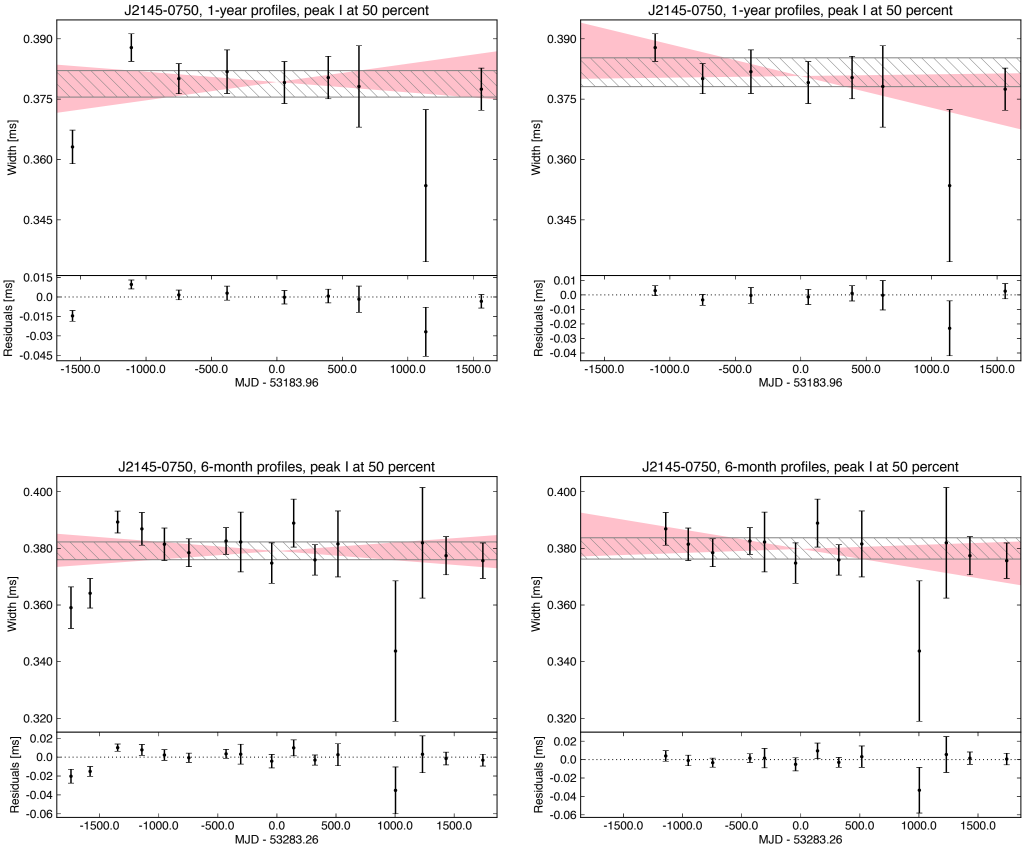

Figure 4.21: *Upper row*, comparison of the time-evolution for the width of component I of PSR J2145−0750 in the 1-year profiles, cut at 50% of the peak height, including (left panels) and excluding (right panels) the first point of the series. *Lower row*, the same as above in the 6-month profiles, including (left panels) and excluding (right panels) the first three points of the series. See the caption of Figure 4.12 for explanation of the labels, markers and highlighted areas.

4.5.2 The case of PSR J1713+0747

PSR J1713+0747 (Foster et al., 1993) is a bright MSP with a rotational period of about 4.57 ms. It is included in a binary system of about 68 days of orbital period, and it is characterized by a low DM value, about 16 $cm^{-3}pc$. Its pulse profile is relatively simple, given by a unique, bright peak and several weaker components with a flux of about 15 times smaller with respect to the peak.

PSR J1713+0747 is the only pulsar in our sample that shows a linear, decreasing trend in all the three series of observations (1-year averaged, 6-month averaged and individual observations), at all the performed profile cuts (at 30%, 50% and 70% of the peak height). Moreover, the spanned width excursus maintains approximatively the same ranges in each of the three data sets (see Figure 4.22).

The detected trend spans about 0.025 ms at 30% (corresponding to the 14% of variation in the profile width), 0.01 ms at 50% (corresponding to the 10% of variation) and 0.005 ms at 70% (corresponding to the 8% of variation). We stress that in the following discussion we often consider the cases for a profile cut at 30% of the peak height. In fact, the longitude range that we can use at this altitude for the purposes of the computation described in Section 4.3 is the largest, and we thus consider the width evaluation at 30% of the peak height as more precise with respect to the other profile cuts.

In this Section we study in details this behavior, exploring part of its possible causes.

Interstellar scattering

A first putative reason for the observed trends in the widths of PSR J1713+0747 is the profile broadening generated by a time-dependent interstellar scattering. To check for the reliability of this explanation, we simulate a scattered pulse profile of J1713+0747 by convolving the first of the 1-year averaged archives with an exponential scattering tail. We find that the maximum width excursus that affects the profile cut at 30% could be reproduced applying a scattering tail with a scattering time τ=0.02 ms. However, such a scattering tail yields a profile broadening at altitudes equivalent to the 50% and 70% of the profile peak of about 0.024 and 0.014 ms, far larger with respect to what we detect in the data.

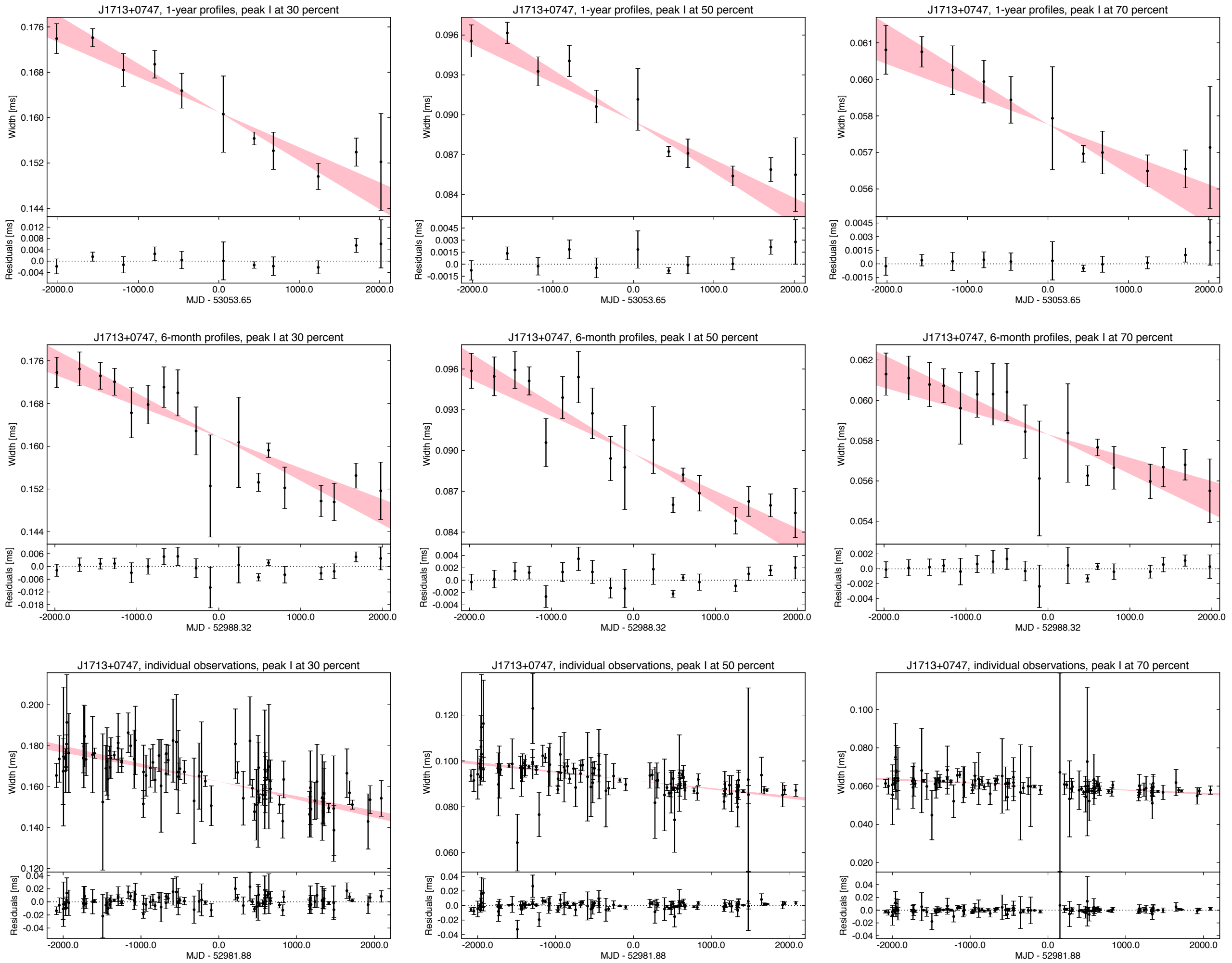

Figure 4.22: Width trends for PSR J1713+0747. Each column refers to a different altitude in the profile cuts: at 30% (left), 50% (central) and 70% (right) of the peak height. Each row refers to a series of data: 1-year (upper), 6-month averaged profiles (central) and individual observations (lower). See the caption of Figure 4.12 for explanation of the labels, markers and highlighted areas.

Moreover, the scattering time values associated to a pulsar at the location of PSR J1713+0747 that can be predicted from the literature (e.g., Cordes and Lazio 2002 and Bhat et al. 2004) are in the order of magnitude of 10^{-6} ms. Even assuming an uncertainty of two orders of magnitude, which is not uncommon in the predictions for the scattering time of a pulsar according to the available models, this value is strongly in disagreement with the outcome of the described simulation.

We therefore exclude the effect of a time-dependent interstellar scattering as a possible cause for the width trend computed in PSR J1713+0747.

Artifacts produced by the EBPP

PSR J1713+0747 is a bright and highly scintillating pulsar. The incoming signal in the EBPP is processed in a linear regime as far as the saturation level of the instrument is not reached. A reasonable test to be performed aims to check if high values of S/N in the incoming signal, maybe associated with peaks of the scintillation, trigger a different instrumental response with respect to a low S/N signal, leading to a bias in the observations.

We preliminary study if there exists a correlation between the width trend at 30% of the peak height in the individual observations and their S/N as computed by the PSRCHIVE tool *psrstat*. Figure 4.23 shows that no correlation is evident, mirrored by the low Pearson correlation coefficient, of about -0.15.

We therefore split the individual observations in two groups separated by the median S/N (again computed by *psrstat*), and we independently check the width trend at 30% of the peak height for the high and the low S/N data. The result is shown in Figure 4.24. In the left panel we report the temporal dependency of the pulse profile widths for the low S/N observations. In the right panel we report the same parameter for the high S/N observations. Table 4.4 shows the results of a linear fit on the two data series. Both of the two data series are in agreement with an evolving trend with time, and the slopes of the linear fits are fully compatible with respect to each other.

The EBPP processes the incoming signal by splitting the whole bandwidth in 4 sub-bands, that are independently handled by different boards. We

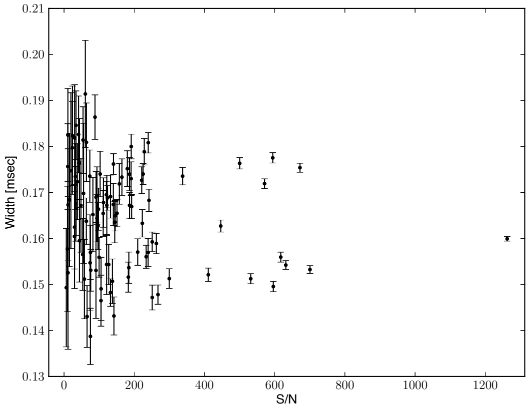

Figure 4.23: Evolution with respect to the S/N for the width of PSR J1713+0747 in the individual observations, cut at 30% of the peak height.

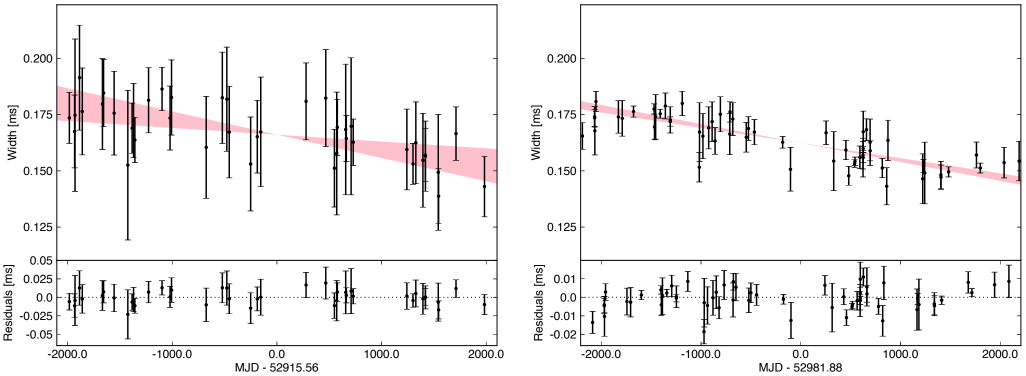

Figure 4.24: *Left panel*, time evolution for the width of PSR J1713+0747 in the low S/N individual observations, cut at 30% of the peak height. *Right panel*, time evolution for the width of PSR J1713+0747 in the high S/N individual observations, cut at 30% of the peak height.

S/N	**Percentage**	χ^2**/dof**	χ^2 **significance**	**Slope range**	**Trend evaluation**
Low	30	13.908/40	1.0e+00	-1.04e-05;-3.03e-06	linear trend
High	30	80.768/57	2.1e-02	-8.85e-06;-7.09e-06	linear trend

Table 4.4: Results from the analysis described in Section 4.3 on the low and high S/N individual observations of PSR J1713+0747. The columns report, respectively, the S/N class, the peak height percentage at which we computed the studied profile width, the χ^2 versus degrees of freedom ratio for a linear fit, its significance, the limits (upper and lower within 2 σ) of the computed linear slope, a qualitative evaluation of the width temporal trend as introduced in Section 4.3.

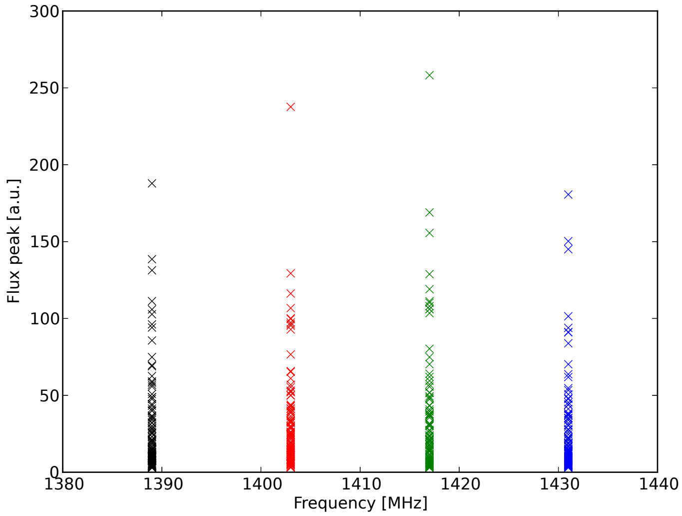

Figure 4.25: S/N of the profile peak (normalized with respect the off-pulse rms) per frequency sub-band.

thus also study the individual sub-bands, in order to detect a possible issue that may have generated the computed trend in the widths. For this, we split the individual observations in each of the four sub-bands, obtaining four archives per observation, each centered on a slightly different frequency. For the purposes of this test, we also include the upper band that is zapped for all the tests described in the previous and the following parts. We initially check for the S/N of the pulse profile peak (normalized with respect the off-pulse rms) of each of the sub-bands. The result is shown in Figure 4.25: we do not observe any significant difference among the four frequencies.

We then build an appropriate template for each sub-band, and we use it to normalize the observations as described in Section 4.3. Before computing the

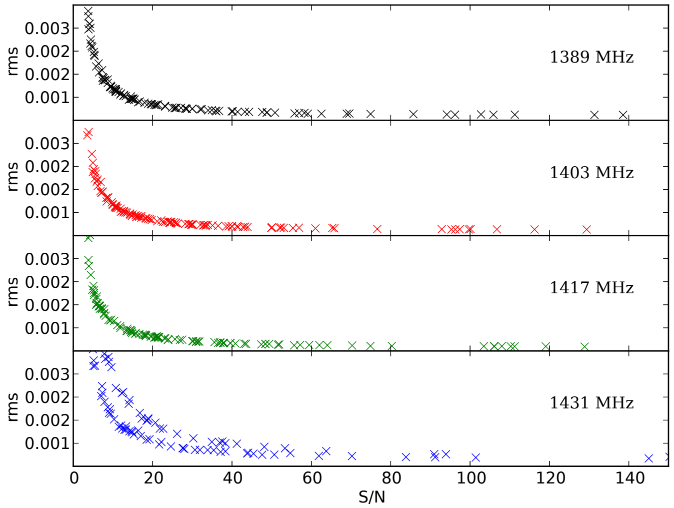

Figure 4.26: Rms of the subtraction of the reference template from the individual observations per sub-band with respect to the S/N per sub-band.

widths of each pulse profile in the four frequencies, we perform an additional test to check for the behavior of the sub-bands with respect the S/N of the observations. In particular, we subtract the template of each frequency to the individual observations, and we compute the rms of the residuals, plotting it against the S/N of the pulse profile peak (normalized with respect the off-pulse rms) of the observations. If a high S/N triggers the saturation regime, we would expect the rms to increase with the S/N. The result of this test is shown in Figure 4.26. We first notice that no high spread of the rms occurs at high S/N. Secondly, the upper band shows a bimodality in the rms with varying the S/N. The causes for this behavior are still under investigation, however, the peculiar feature supports the exclusion of this sub-band from the standard analysis of the pulsars in our sample.

We finally proceed with the analysis of the widths at 30% of the peak height per sub-band, following the same procedure described in Section 4.3. The results are shown in Figure 4.27, and in Table 4.5. All of the sub-bands present a linear, decreasing tendency in the width trend. The slope ranges of the two sub-bands with highest (1431 and 1417 MHz, the "protected frequency" for the Radioastronomy) and the lowest (1403 and 1389 MHz) central values are compatible. However, they are only marginally, or not in agreement ones with respect to the others. Possible causes for this behavior are under

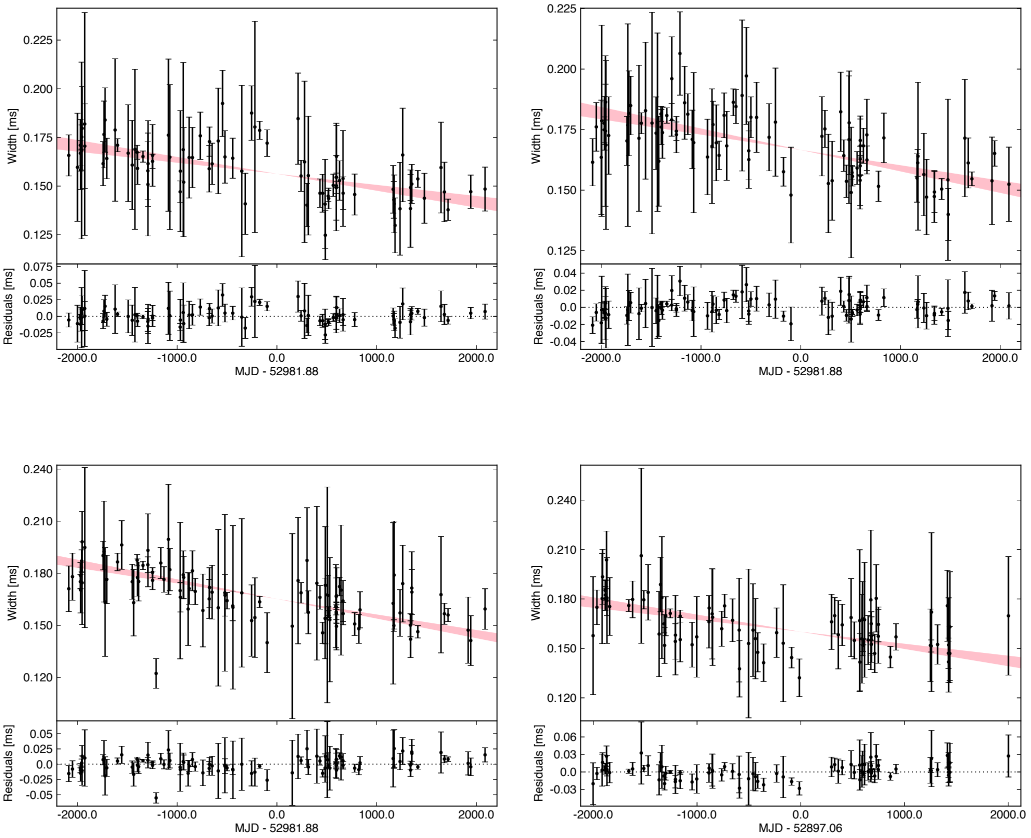

Figure 4.27: *Upper row, left panel*, time evolution for the width of PSR J1713+0747 in the frequency sub-band centered on 1389 MHz of the individual observations, cut at 30% of the peak height. *Upper row, right panel*, same as above in the sub-band centered on 1403 MHz. *Lower row, left panel*, same as above in the sub-band centered on 1417 MHz. *Lower row, right panel*, same as above in the sub-band centered on 1431 MHz. See the caption of Figure 4.12 for explanation of the labels, markers and highlighted areas.

exam, however, as a linear trend is present in all the sub-bands we reject the hypothesis that the detected width temporal evolution in PSR J1713+0747 is a band limited effect and/or an artifact of some of the four used boards of the EBPP backend.

We repeat the width analysis splitting the observations into the individual polarization channels, limiting the bandwidth to the sum of the three sub-bands with lowest frequencies. We thus obtain two archives per individual observation. The results are shown in Figure 4.28 and Table 4.6. This test

Frequency	**percentage**	**chi2/dof**	**chi2 significance**	**slope range**	**trend evaluation**
1389	30	87.633/84	3.7e-01	-8.69e-06;-5.69e-06	linear trend
1403	30	77.298/92	8.6e-01	-8.86e-06;-6.32e-06	linear trend
1417	30	126.785/96	1.9e-02	-1.13e-05;-8.92e-06	linear trend
1431	30	61.998/82	9.5e-01	-1.04e-05;-7.26e-06	linear trend

Table 4.5: Results from the analysis described in Section 4.3 on the four frequency sub-bands of the individual observations of PSR J1713+0737. The columns report, respectively: the centroid of each frequency sub-band, the peak height percentage at which we computed the studied profile width, the χ^2 versus degrees of freedom ratio for a linear fit, its significance, the limits (upper and lower within 2 σ) of the computed linear slope, a qualitative evaluation of the width temporal trend as introduced in Section 4.3.

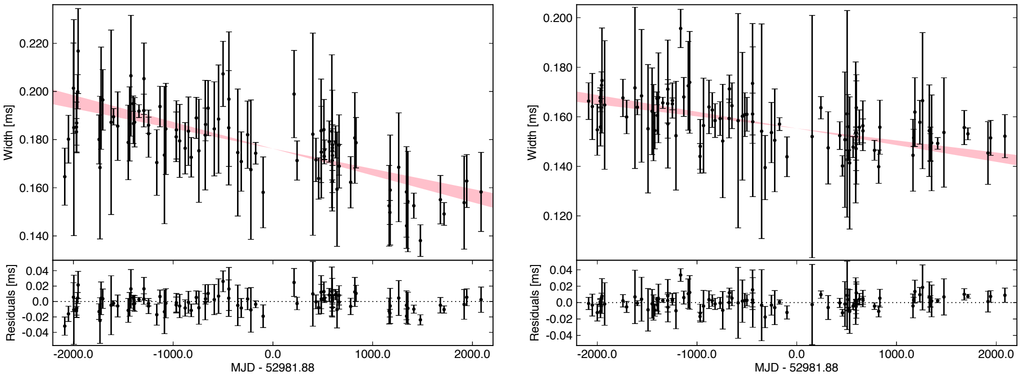

Figure 4.28: *Left panel*, time evolution for the width of PSR J1713+0747 in the first polarization channel of the individual observations, cut at 30% of the peak height. *Right panel*, same as above in the second polarization channel. See the caption of Figure 4.12 for explanation of the labels, markers and highlighted areas.

yields an outcome similar to the previous one: the slope of a linear fit is nominally incompatible at 2σ between the two polarization channels, but the descending trend is significantly present in both of the channels. Still, the reason of the difference in the slopes remains under study.

Lack of polarization calibration

The EBPP data are not polarization calibrated: gain imbalance and leakage between the feeds have, thus, not being corrected. As they can induce deformations in the pulse profile, we search which magnitude of these effects would be needed to explain the observed width variations by simulating (via a private software that will be presented in an upcoming paper from the Large

Polarization channel	**percentage**	**chi2/dof**	**chi2 significance**	**slope range**	**trend evaluation**
0	30	108.559/90	8.9e-02	-1.11e-05;-8.37e-06	linear trend
1	30	126.991/95	1.6e-02	-6.74e-06;-4.86e-06	linear trend

Table 4.6: Results from the analysis described in Section 4.3 on the two polarization channels of the individual observations of PSR J1713+0737. The columns report, respectively: the polarization channel labeling, the peak height percentage at which we computed the studied profile width, the χ^2 versus degrees of freedom ratio for a linear fit, its significance, the limits (upper and lower within 2 σ) of the computed linear slope, a qualitative evaluation of the width temporal trend as introduced in Section 4.3.

European Array for Pulsars, Lee et al. 2015 in preparation) pulse profiles affected by a wrong amount of polarization calibrations. We preliminary notice that the parallactic angle rotation does not affect the observations, thanks to the symmetry of the used circular polarization feeds: this also tells us that I and V are invariant with respect to the parallactic angle rotation.

To perform this test, we first select an high S/N, polarization calibrated pulse profiles of PSR J1713+0747, obtained with the Effelsberg radio telescope at L-band and processed with a ROACH (Reconfigurable Open Architecture Computing Hardware)-based backend, ASTERIX (Karuppusamy, 2011). This observation acts as our reference.

We first simulate the presence of a differential gain between the two feeds. This effect is described by two parameters: Δ, the factor of signal enhancement/weakening in a feed with respect to the other, and ϕ, that gives the signal phase delay/advance in a feed with respect to the other. The Jones matrix that describes the gain imbalance is given by (Lee et al. 2015, in preparation):

$$J = \begin{bmatrix} 1 & 0 \\ 0 & \Delta e^{i\phi} \end{bmatrix} \tag{4.1}$$

A combination of (Δ, ϕ) equal to (1,0) indicates the absence of gain imbalance. As the total intensity of the profile is given by the half-sum of the two polarization channels corresponding to the voltages self-product, ϕ is inconsequential for our data set. We thus only test the effect of a variable Δ value. We apply different values of Δ spanning from 0.01 to 100 (with $\Delta = 1$

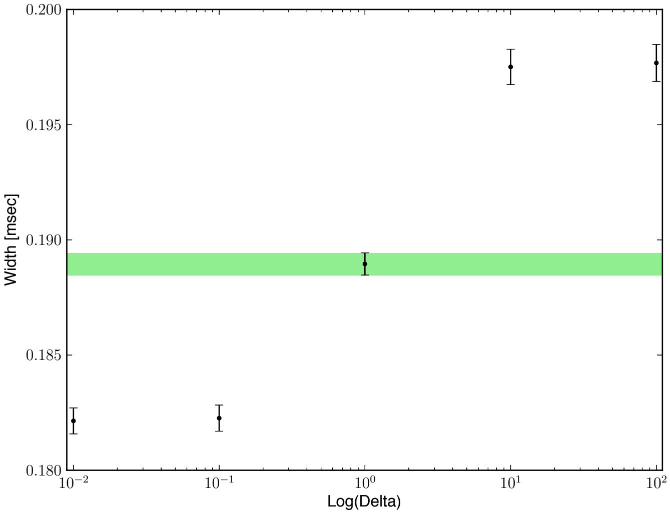

Figure 4.29: Effect of gain imbalance on the pulse profile widths as a function of Δ. The shaded region indicates the 1σ range of the width value obtained from the reference (i.e., unaltered, corresponding to $\Delta = 0$) pulse profile.

being the case of no gain imbalance), safely larger than what suggested by the expected properties of the receiver (K. Lee, private communication). We then compute the width at 30% of the pulse profile peak for the reference and the simulated profiles. The results are shown in Figure 4.29. The maximum excursus reached thanks a systematic Δ variation from 0.01 to 100 is about 0.014 ms, still insufficient to accomplish for the computed variability in the EBPP data.

However, if we consider that only the gain imbalance had a significant impact on the polarization calibration (implying that the leakage contribution was negligible) and that the fraction of circular polarization C is a time-invariant, it is possible to correct for the effect of the gain imbalace itself. In fact, in the case of circular feeds, the two polarization channels recorded by the EBPP and corresponding to the self product of the voltages recorded by the two feeds (A and B) are related to the Stokes parameters I and V that describe, respectively, the total intensity and the circular polarization as:

$$\begin{aligned} P_0 &= \langle A, A \rangle = (I + V)/2 \\ P_1 &= \langle B, B \rangle = (I - V)/2 \end{aligned} \tag{4.2}$$

thus:

$$C = \frac{V}{I} = \frac{P_0 - P_1}{P_0 + P_1} \tag{4.3}$$

A gain imbalance between the feeds as described by Equation 4.5.2 transforms the recorded voltages A and B in A' and B':

$$\begin{pmatrix} A' \\ B' \end{pmatrix} = \begin{pmatrix} 1 & 0 \\ 0 & \Delta e^{i\phi} \end{pmatrix} \begin{pmatrix} A \\ B \end{pmatrix} = \begin{pmatrix} A \\ \Delta B e^{i\phi} \end{pmatrix} \tag{4.4}$$

thus we have new polarization channels, P_0' and P_1':

$$\begin{gathered} P_0' = P_0 \\ P_1' = \Delta^2 P_1 = \kappa P_1 \end{gathered} \tag{4.5}$$

Expressing C as a function of the new polarization channels, we have that:

$$C = \frac{V'}{I'} = \frac{1 - \frac{1}{\kappa}\frac{P_1'}{P_0'}}{1 + \frac{1}{\kappa}\frac{P_1'}{P_0'}} \tag{4.6}$$

Knowing C from the polarization calibrated data, we can compute the parameter κ for each observation and correct the data for the gain imbalance. We perform this test using the EBPP observations for PSR J1713+0747 characterized by a S/N higher than the median S/N of all the available observations, and we then compute the widths at 30% of the peak of the newly generated observations. The result is shown in Figure 4.30. In the left panel are shown the widths of the original observations, in the right panel are displayed the widths of the corrected observations. No substantial changes appear, implying that the gain imbalance does not significantly affect this data set. Note that one should also consider the possiblity of cables being swapped during the time span covered by the data set (using $|V|$ instead of V), but this is neglected in the thesis.

We then simulate the presence of a cross-coupling between the two feeds, whose magnitude being D. We proceed like the test for the gain imbalance, applying a range of values for D from 0 to 0.1 (with $D = 0$ being the case of no feed cross-coupling). The tested variations in the values of D accounts for a maximum width variation of about 0.014 ms as well, still insufficient to explain the excursus observed in PSR J1713+0747 at 30% of the peak height. The upper limit of the tested range of D values was indicated as a reasonable value for the current set-up of the Effelsberg radio telescope receivers (K. Lee,

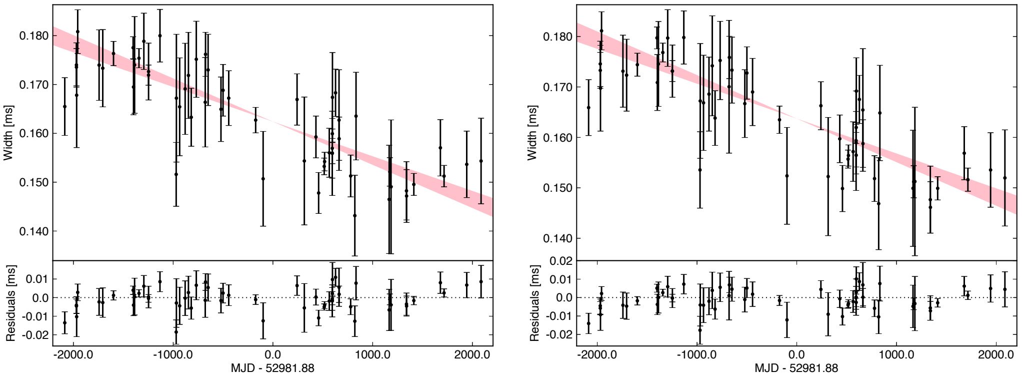

Figure 4.30: *Left panel*, time evolution for the width of PSR J1713+0747 in the high S/N individual observations, cut at 30% of the peak height. *Right panel*, time evolution for the width of PSR J1713+0747 in the high S/N individual observations, cut at 30% of the peak height, corrected for the gain imbalance. See the caption of Figure 4.12 for explanation of the labels, markers and highlighted areas.

private communication). We are currently investigating if higher values for the D parameter have possibly affected the receivers in the past.

Correlations with telescope elevation

The correlation between the width trend at 30% of the peak height and the telescope elevation at the observation epoch (see Figure 4.32) yields a Pearson correlation coefficient of -0.33. This weak evidence of correlation (that would imply that the higher is the telescope elevation, the narrower is the pulse profile) is currently under study to understand its implications with respect to other characteristics of the telescope, such as gain imbalance and leakage. A mechanical instability of the receiver feeds may possibly introduce (A. Jessner, private communication) a dependency of the conceivable gain imbalance parameters with respect to the elevation, in addition to the more predictable correlation of the amount of leakage with telescope elevation.

Further analysis

A follow-up of the tests on the lack of polarization calibration is to have a deeper understanding of the link between the elevation of the telescope and the magnitudes of the combined effects given by gain imbalance and leakage

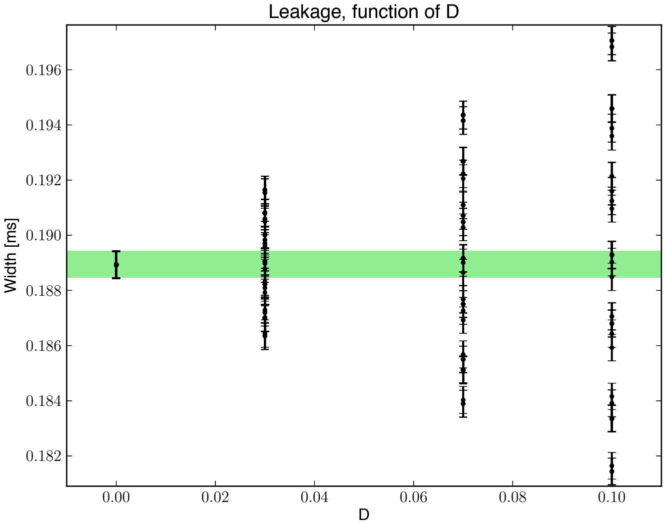

Figure 4.31: Effect of the leakage between the polarization channels on the pulse profile widths as a function of D. The shaded region indicates the 1σ range of the width values obtained from the reference (i.e., unaltered, corresponding to $D = 0$) pulse profile.

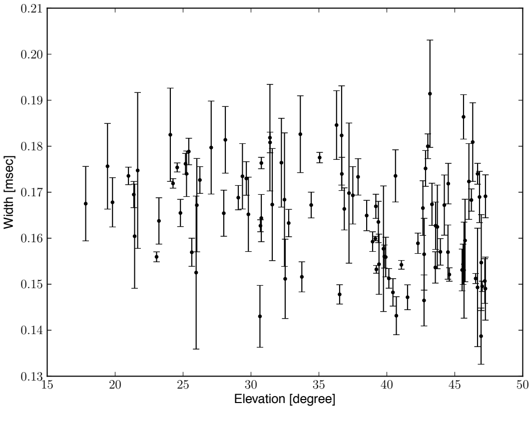

Figure 4.32: Evolution with respect to the telescope elevation for the width of PSR J1713+0747 in the individual observations, cut at 30% of the peak height.

between the feeds.

The next obvious step is to check for the ephemeris used to fold the data at the observation epoch. It is reasonable to expect that the precision of the timing parameters improved at each of their updates, implying a subsequent narrowing of the pulse profile. We are currently working to recover the original folding ephemeris from databases at the Effelsberg radio telescope. Once we will obtain them, we will use an individual baseband observation of PSR J1713+0737 to be folded with the different ephemeris set, in order to evaluate the possibility that the temporal trend we see in the EBPP data is an artifact.

If neither of the causes listed above will result sufficiently convincing to explain the width trend in PSR J1713+0747, the only possible explanation to be claimed is an intrinsic variation of the pulse profile of this source.

4.5.3 Summary of the results

In this Chapter we systematically tested the long term stability in time of MSP profiles, one of the main hypothesis at the base of the PTA experiments. We used coherently dedispersed data sets for 10 MSPs included in the EPTA targets, collected between 1997 and 2011 at the Effelsberg radio telescope in L-band and processed with the EBPP backend. For each pulsar, we analyzed the temporal trend of the profile widths at different altitudes with respect to the main peak height. This study is performed on high S/N profiles obtained by averaging the available observations for each pulsar over 6 months and 1 year. When the pulsar brightness is sufficient, the study is also performed on the individual observations: this happens for four pulsars, PSRs J1713+0747, J1744−1134, J1939+2134 and J2145−0750. PSRs J1744−1134 and J1939+2134 are in common with the study performed by Shao et al. 2013, who included the data sets used in this Chapter. The results from our and Shao et al. 2013's analysis are in agreement, letting alone a small offset in the absolute value of the widths due to the use of different procedures.

In nine pulsars over ten we detected either an absence of time evolution in the widths or, alternatively, the presence of only one or a small number of points in the temporal evolution of the widths standing out from an otherwise flat trend in time.

PSR J1713+0747 is the only pulsar that shows a linear, decreasing trend at all the percentages of the peak height at which we performed the analysis (30%, 50%, 70%), in all the tested series of data (1-year and 6-month averaged profiles and individual observations), independently on the choice of (i) the S/N of the selected observations, (ii) the adopted polarization channel, (iii) the examined frequency sub-band. The width excursus is approximatively 0.025 ms at 30% of the peak height, 0.01 ms at 50% and 0.005 ms at 70%.

The possibility that a time-dependent interstellar scattering event caused the trend has been ruled out.

As these data sets are not polarization calibrated, we also tested the effects of a possible gain imbalance and cross-coupling between the feeds. Spanning reliable ranges of values for the magnitude of these effects in the receiver that collected the data, it results that, taken independently, gain imbalance and cross-coupling between the feeds can explain only 0.014 ms of width variation each. This falls short in explaining the observed trend.

Some main tests need to be performed yet. In particular, we aim to understand the link (if any) between the telescope elevation and the effects given by the lack of polarization calibration, as well as to test the impact of the folding ephemeris (whose precision surely improved in the course of the years).

Conclusions

In this work of Thesis we have touched several aspects of pulsar astrophysics and its applications.

In Chapter 2 we showed two examples of the potentialities of the studies about pulsar polarization. First, we applied a standard polarization analysis to a sample of 49 long-period pulsars discovered by the High Time Resolution Universe (HTRU) southern survey and *were able to determine the Rotation Measure (RM) for 34 additional pulsars* among them. The measured linear and absolute circular polarization fractions of these pulsars are in agreement with the values that can be found in literature for long period pulsars, respectively around $15-20\%$ and 6%. The profile shapes, that often show the presence of two or more components, also mirror previous studies about aged pulsars. Linear polarization profiles trace the total intensity, although they become narrower at the edges. Circular polarization profiles occasionally show a handedness reversal in rough correspondence with the profile mid point. Polarization angle behaviors are hardly in accordance with what predicted by the rotating vector model except for two cases in the whole sample. We then combined the new determined values of the RM with those previously measured for the other pulsars discovered in the context of HTRU Survey and used this dataset for putting constraints on the Galactic magnetic field. *We found that the RM of the pulsar of our sample are not in disagreement with the models that claim that the Galactic magnetic field have a counter-clockwise direction in the spiral arms and a clockwise direction in between.*

In a second part of the Chapter we based on the study of the fourth moment of the electric field to compute the covariances between the Stokes parameters associated to a pulsar signal, in the aim of reexamining and clarifying the so far adopted classification of the composition of the modes of polarized emission of the pulsars. Following the procedure above and relying on the four hypotheses of orthogonal, independent, similarly intense and recurrent modes, we performed a preliminary analysis of a single pulse data set collected for the Vela pulsar. We find that, starting from these very simple assumptions, it is impossible to find any combination of modes that properly represent the data. This means that one or more of our hypotheses need to be discarded, likely the mode independence. Moreover, *our new procedure indicates that the methods so far applied to remove the bias induced by the noise from the computation of the Stokes parameters do not properly account for the amount of cross-coupling between the signal and the noise itself.* This implies that a different approach of bias removal, on which we are currently working, should be adopted.

In Chapter 3, we studied a problem related to the data analysis of the Pulsar Timing Array (PTA) experiments, i.e. how the occurrence of correlated signals caused by sources unrelated to the gravitational wave background (GWB) produced by coalescing supermassive black hole binaries at high redshift can impact on the search for the mentioned GWB in PTA data. In particular, we focused on correlated signals given by errors in the clock time standards and in the used planetary ephemeris. Our study demonstrate that, if not corrected, these kind of signals can potentially give significant detection in the course of a GWB searches. In particular, the study demonstrated that an error in the clock corresponding to the difference between two realizations of the Terrestrial Time (TT), the International Atomic Time (TAI) and the 2013 version of TT of the Bureau international des poids et mesures (BIPM), inject a considerable amount of power in the pulsar timing residuals, higher that the one introduced by a GWB. We also tested the effectiveness of two mitigation routines for each of the studied spurious signals, errors in the clock time standard (CLK1 and CLK2) and in the planetary ephemeris (PE1 and PE2), and their impact on the sensitivity of the used GWB detection code. CLK1 acts on the final product of the GWB detection procedure, the angular covariances between the timing residuals of pulsar pairs, to search and accomplish for the monopolar signature generated by a clock signal. CLK2 searches for the same feature to be fitted away from the time series, exploring them with a grid of samplings and thus introducing a variable number of degrees of freedom. CLK1 and CLK2 gave satisfactorily results, whether in terms of extracting the noise signal or of maintaining the detection code sensitivity. PE1 and PE2 both act on the time series. PE1 pipeline is alike to CLK2, as it simultaneously samples all the time series to search for the 3-component signature of the difference between the real position of the Solar System barycenter (SSB) and the one given by the erroneous planetary ephemeris. PE2, on the contrary, only searches for errors in the planet masses. PE1 results more effective than PE2 in correcting for the signal given by the planetary ephemeris error, thanks to the large number of introduced degrees of freedom. However, at the contrary of PE2, it also severely reduces the sensitivity of the detection code when a GWB is truly present. *In summary, the presence of correlated noise greatly increases the "false alarm" probability of an attempt to detect the GWB: this problem can be solved nicely for the clock error but not so well at the moment for the ephemeris error.*

In Chapter 4 we explore one of the main hypotheses at the base of the PTA experiments: the long-term temporal stability of the millisecond pulsars (MSPs) integrated profiles. We checked for the time-stability over a ~ 15 yr data-span of the integrated profiles at L-band (1400 MHz) for 10 MSPs observed with the Effelsberg radio telescope, exploiting the best dataset so far available in the world for this kind of study. The procedure we followed implies the study of the temporal evolution of the pulse profile widths at different altitudes with respect to the height of the main peak of the profile. For each pulsar we created two high S/N ratio data series to be tested, averaging all the observations for a specific pulsar over 6 months and over 1 year. If the pulsar was bright enough, we performed the same study on the individual observations too. Using confidence levels at 2σ, *in nine pulsars over ten we did not detect any secular evolution in the profile width. However, PSR J1713+0747 shows a linear, decreasing temporal trend in the profile widths* at all the percentages of the peak height at which we performed the analysis, that induces a shrinking of the profile width of 14% at 30% of the peak height, of 10% at 50% of the peak height and 8% at 70% of the peak height. The trend is detected in all the tested series of data (1-year and 6-month averaged profiles as well as individual observations and it seems to be independent on the S/N of the selected observations or on the adopted polarization channel or inspected frequency sub-band. Effects due to the interstellar scattering cannot explain the detected temporal evolution of the PSR J1713+0747 profile. We also tested the potential effects due to the lack of polarization calibration in the used data. We found that, taken independently, effects as gain imbalance and leakage between the feeds can account for only part (approximatively half) of the observed variation at 30% of the pulse profile. Some additional instrumental tests are in progress in order to finally conclude if the evolving profile width of PSR J1713+0747 is an intrinsic effect and to which extent that can affect the results of the timing observations of this bright pulsar.

Appendix A

Polarization profiles at 1369 MHz for the pulsars described in Section 2.4. The top panel of each plot shows the PA variation with respect to celestial north as a function of longitude. The PAs are corrected for RM and represent the (frequency independent) value at the pulsar, and are plotted if the linear polarization is above 2 σ. The lower panel shows the integrated profile in total intensity (thick black line), linear polarization (red line) and circular polarization (blue line).

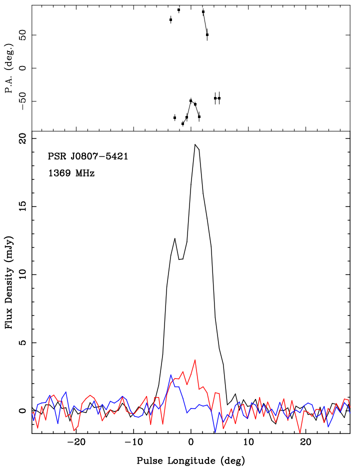
P.A. (deg.)
50
0
−50
PSR J0807−5421
1369 MHz
Flux Density (mJy)
0
5
10
15
20
−20
−10
0
10
20
Pulse Longitude (deg)

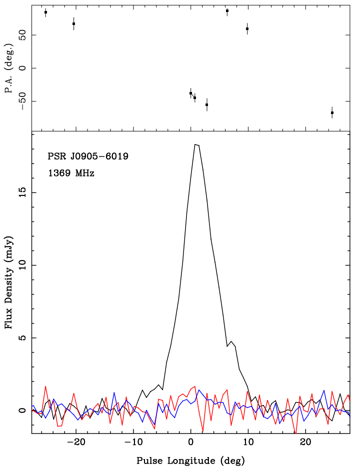
P.A. (deg.)
50
0
−50
PSR J0905−6019
1369 MHz
Flux Density (mJy)
0
5
10
15
−20
−10
0
10
20
Pulse Longitude (deg)

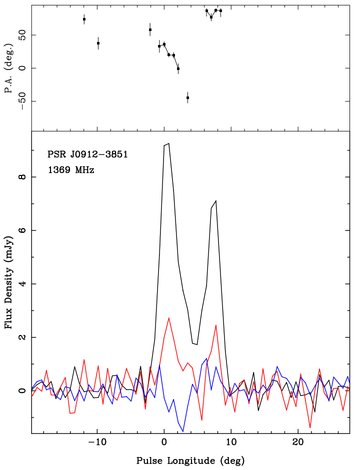
P.A. (deg.)
50
0
−50
PSR J0912−3851
1369 MHz
Flux Density (mJy)
0
2
4
6
8
−10
0
10
20
Pulse Longitude (deg)

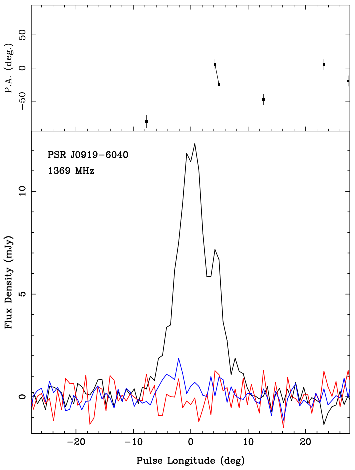
P.A. (deg.)
50
0
−50
PSR J0919−6040
1369 MHz
Flux Density (mJy)
0
5
10
−20
−10
0
10
20
Pulse Longitude (deg)

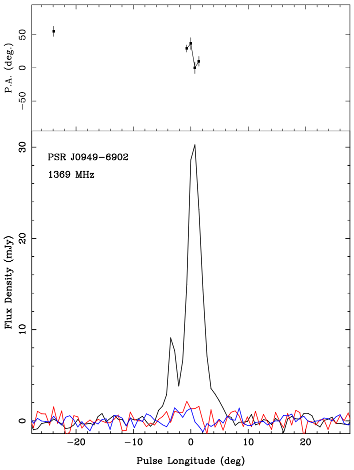
P.A. (deg.)
50
0
−50
PSR J0949−6902
1369 MHz
Flux Density (mJy)
0
10
20
30
−20
−10
0
10
20
Pulse Longitude (deg)

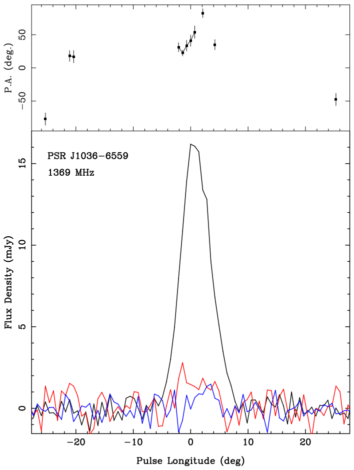
P.A. (deg.)
50
0
−50
PSR J1036−6559
1369 MHz
Flux Density (mJy)
0
5
10
15
−20
−10
0
10
20
Pulse Longitude (deg)

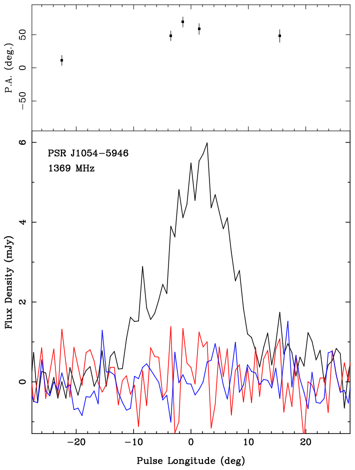
P.A. (deg.)
50
0
−50
PSR J1054−5946
1369 MHz
Flux Density (mJy)
0
2
4
6
−20
−10
0
10
20
Pulse Longitude (deg)

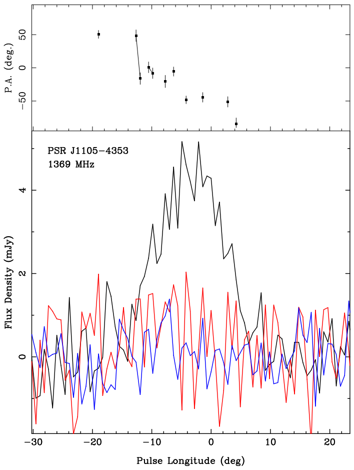
P.A. (deg.)
50
0
−50
PSR J1105−4353
1369 MHz
Flux Density (mJy)
0
2
4
−30
−20
−10
0
10
20
Pulse Longitude (deg)

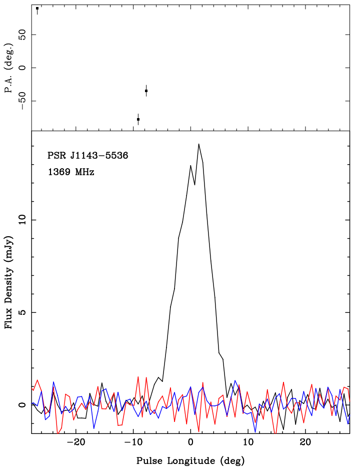
P.A. (deg.)
50
0
−50
PSR J1143−5536
1369 MHz
Flux Density (mJy)
0
5
10
−20
−10
0
10
20
Pulse Longitude (deg)

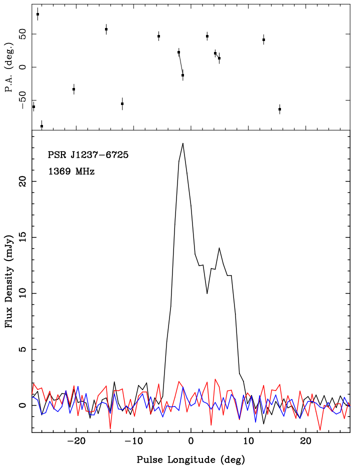
P.A. (deg.)
50
0
−50
PSR J1237−6725
1369 MHz
Flux Density (mJy)
20
15
10
5
0
−20
−10
0
10
20
Pulse Longitude (deg)

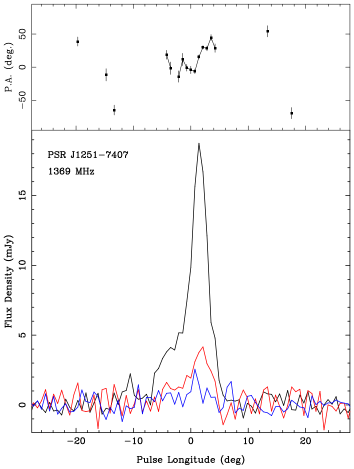
P.A. (deg.)
50
0
−50
PSR J1251−7407
1369 MHz
Flux Density (mJy)
15
10
5
0
−20
−10
0
10
20
Pulse Longitude (deg)

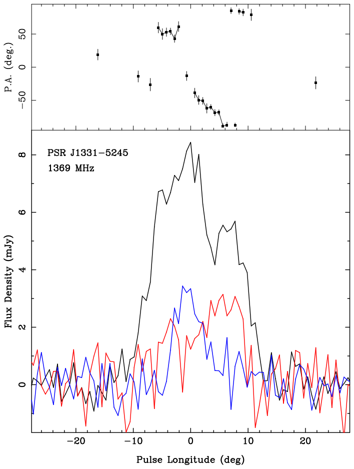
P.A. (deg.)
50
0
−50
PSR J1331−5245
1369 MHz
Flux Density (mJy)
8
6
4
2
0
−20
−10
0
10
20
Pulse Longitude (deg)

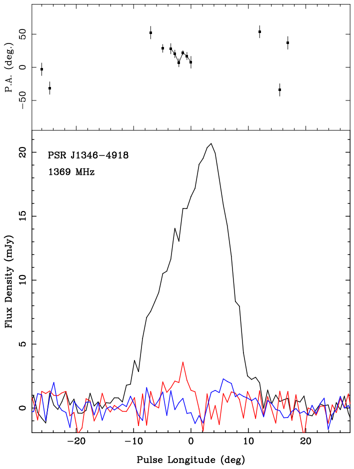
P.A. (deg.)
50
0
−50
PSR J1346−4918
1369 MHz
Flux Density (mJy)
20
15
10
5
0
−20
−10
0
10
20
Pulse Longitude (deg)

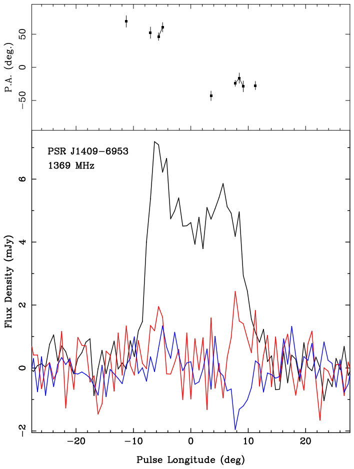
P.A. (deg.)
50
0
−50
PSR J1409−6953
1369 MHz
Flux Density (mJy)
6
4
2
0
−2
−20
−10
0
10
20
Pulse Longitude (deg)

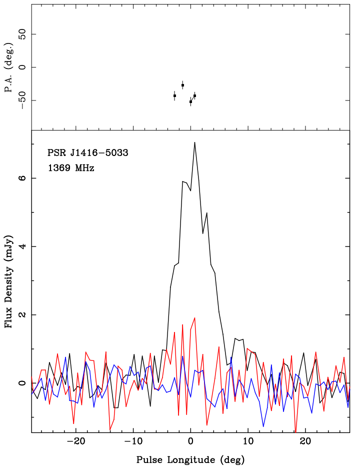
P.A. (deg.)
50
0
−50
PSR J1416−5033
1369 MHz
Flux Density (mJy)
6
4
2
0
−20
−10
0
10
20
Pulse Longitude (deg)

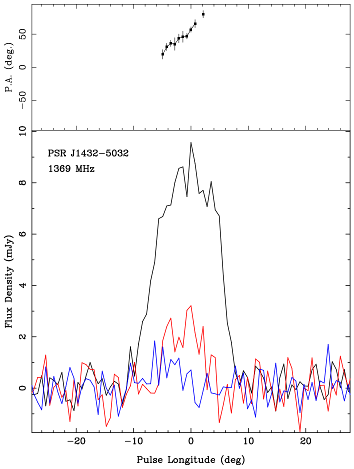
P.A. (deg.)
50
0
−50
10
PSR J1432−5032
1369 MHz
Flux Density (mJy)
8
6
4
2
0
−20
−10
0
10
20
Pulse Longitude (deg)

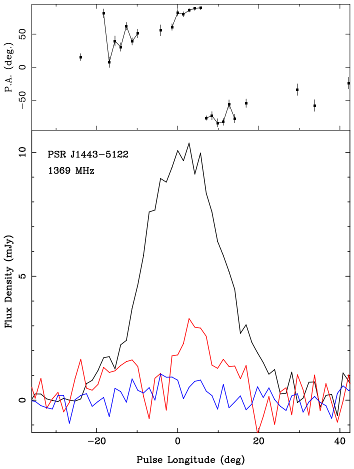
P.A. (deg.)
50
0
−50
PSR J1443−5122
1369 MHz
Flux Density (mJy)
10
5
0
−20
0
20
40
Pulse Longitude (deg)

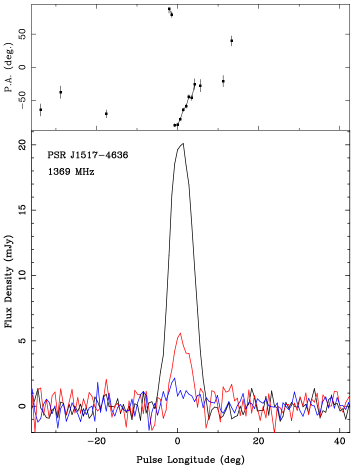
P.A. (deg.)
50
0
−50
PSR J1517−4636
1369 MHz
Flux Density (mJy)
20
15
10
5
0
−20
0
20
40
Pulse Longitude (deg)

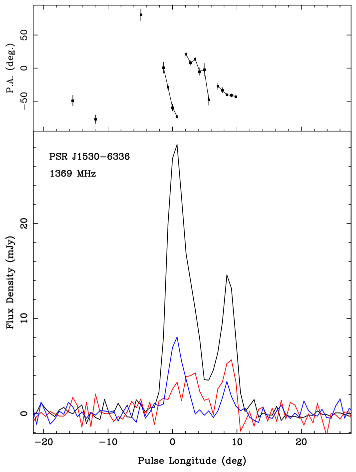
P.A. (deg.)
50
0
−50
PSR J1530−6336
1369 MHz
Flux Density (mJy)
0
10
20
−20
−10
0
10
20
Pulse Longitude (deg)

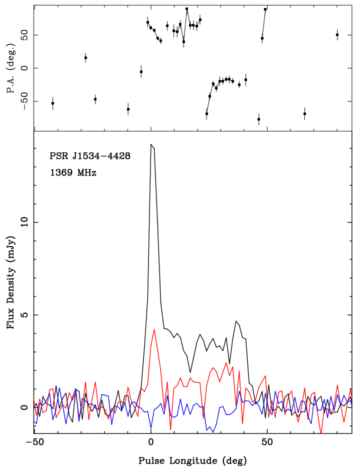
P.A. (deg.)
50
0
−50
PSR J1534−4428
1369 MHz
Flux Density (mJy)
0
5
10
−50
0
50
Pulse Longitude (deg)

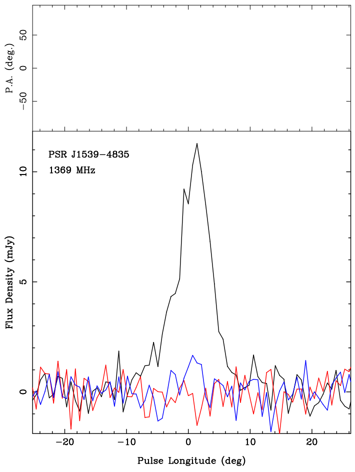
P.A. (deg.)
50
0
−50
PSR J1539−4835
1369 MHz
Flux Density (mJy)
0
5
10
−20
−10
0
10
20
Pulse Longitude (deg)

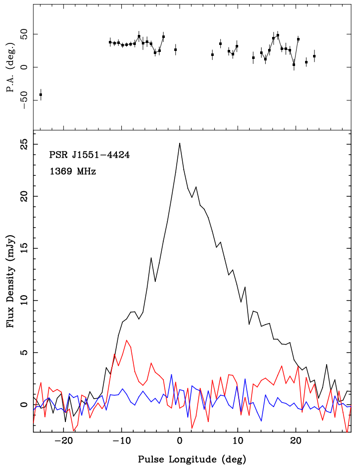
P.A. (deg.)
50
0
−50
PSR J1551−4424
1369 MHz
Flux Density (mJy)
0
5
10
15
20
25
−20
−10
0
10
20
Pulse Longitude (deg)

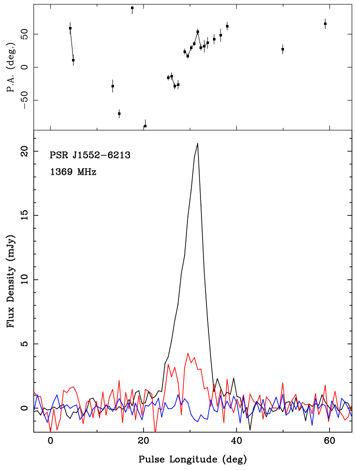
P.A. (deg.)
50
0
−50
PSR J1552−6213
1369 MHz
Flux Density (mJy)
0
5
10
15
20
0
20
40
60
Pulse Longitude (deg)

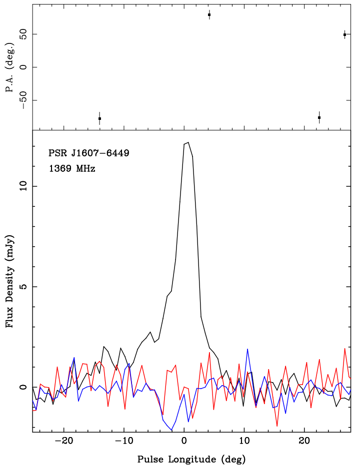
P.A. (deg.)
50
0
−50
PSR J1607−6449
1369 MHz
Flux Density (mJy)
0
5
10
−20
−10
0
10
20
Pulse Longitude (deg)

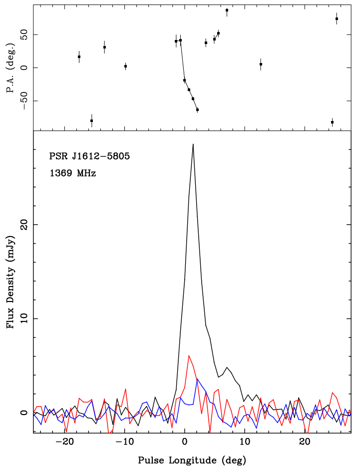
P.A. (deg.)
50
0
−50
PSR J1612−5805
1369 MHz
Flux Density (mJy)
0
10
20
−20
−10
0
10
20
Pulse Longitude (deg)

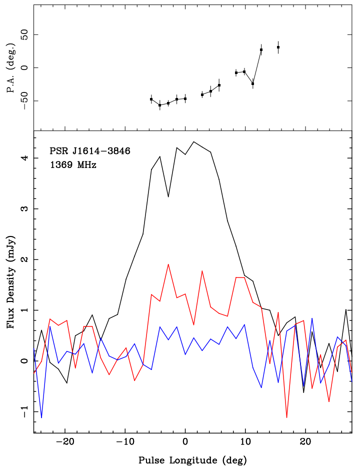
P.A. (deg.)
50
0
−50
PSR J1614−3846
1369 MHz
Flux Density (mJy)
−1
0
1
2
3
4
−20
−10
0
10
20
Pulse Longitude (deg)

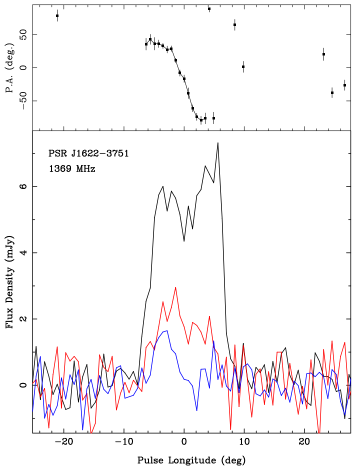
P.A. (deg.)
50
0
−50
PSR J1622−3751
1369 MHz
Flux Density (mJy)
0
2
4
6
−20
−10
0
10
20
Pulse Longitude (deg)

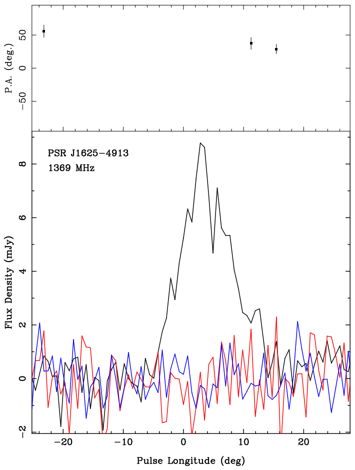
P.A. (deg.)
50
0
−50
PSR J1625−4913
1369 MHz
Flux Density (mJy)
8
6
4
2
0
−2
−20
−10
0
10
20
Pulse Longitude (deg)

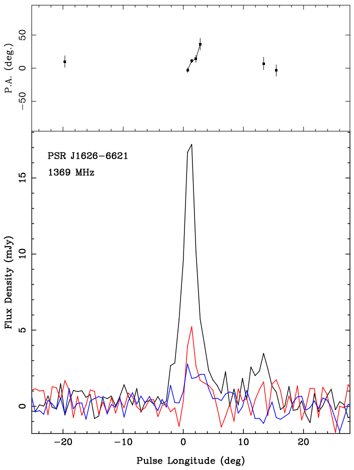
P.A. (deg.)
50
0
−50
PSR J1626−6621
1369 MHz
Flux Density (mJy)
15
10
5
0
−20
−10
0
10
20
Pulse Longitude (deg)

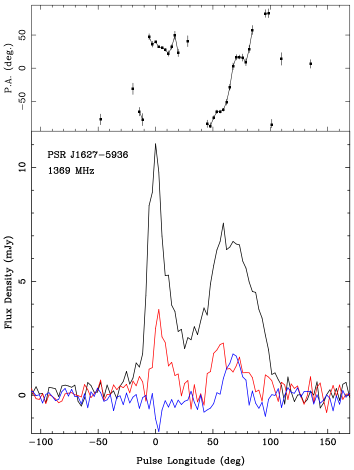
P.A. (deg.)
50
0
−50
PSR J1627−5936
1369 MHz
Flux Density (mJy)
10
5
0
−100
−50
0
50
100
150
Pulse Longitude (deg)

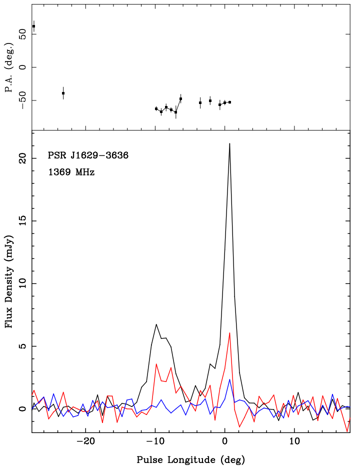
P.A. (deg.)
50
0
−50
PSR J1629−3636
1369 MHz
Flux Density (mJy)
20
15
10
5
0
−20
−10
0
10
Pulse Longitude (deg)

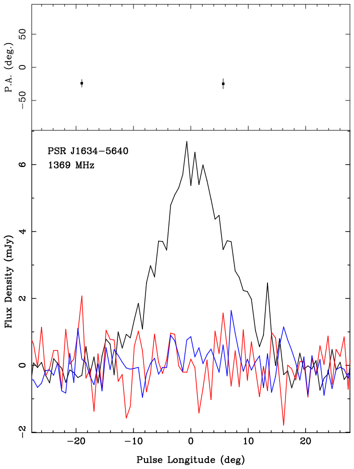
P.A. (deg.)
50
0
−50
PSR J1634−5640
1369 MHz
Flux Density (mJy)
6
4
2
0
−2
−20
−10
0
10
20
Pulse Longitude (deg)

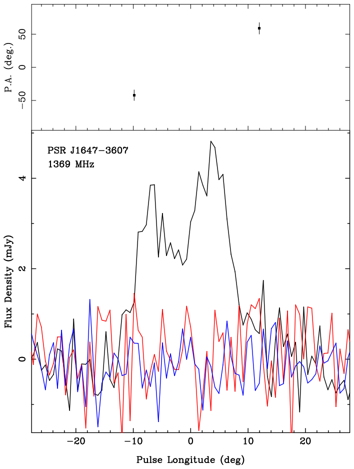
P.A. (deg.)
50
0
−50
PSR J1647−3607
1369 MHz
Flux Density (mJy)
4
2
0
−20
−10
0
10
20
Pulse Longitude (deg)

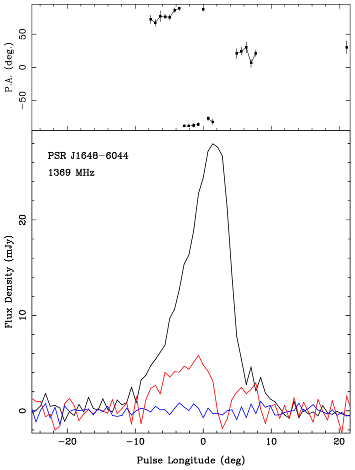
P.A. (deg.)
50
0
−50
PSR J1648−6044
1369 MHz
Flux Density (mJy)
20
10
0
−20
−10
0
10
20
Pulse Longitude (deg)

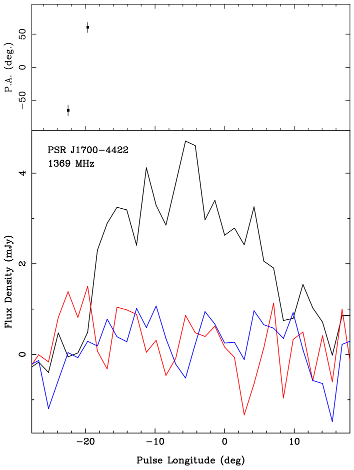
P.A. (deg.)
50
0
−50
PSR J1700−4422
1369 MHz
Flux Density (mJy)
4
2
0
−20
−10
0
10
Pulse Longitude (deg)

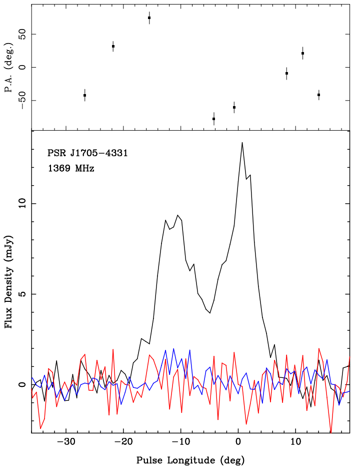
P.A. (deg.)
50
0
−50
PSR J1705−4331
1369 MHz
Flux Density (mJy)
10
5
0
−30
−20
−10
0
10
Pulse Longitude (deg)

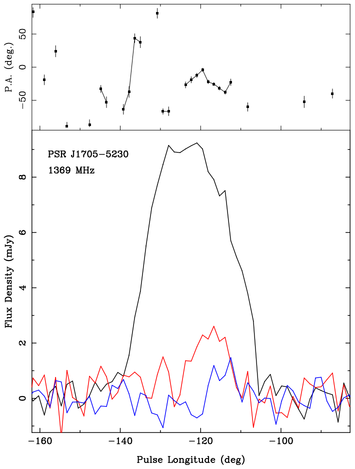
PSR J1705−5230
1369 MHz
P.A. (deg.)
50
0
−50
Flux Density (mJy)
0
2
4
6
8
−160
−140
−120
−100
Pulse Longitude (deg)

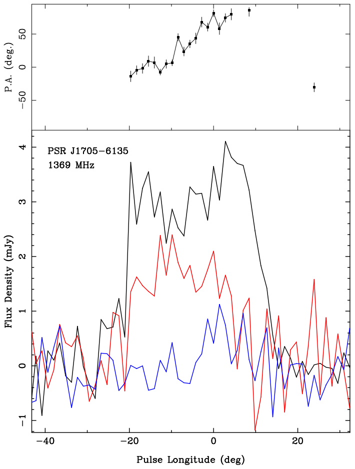
PSR J1705−6135
1369 MHz
P.A. (deg.)
50
0
−50
Flux Density (mJy)
−1
0
1
2
3
4
−40
−20
0
20
Pulse Longitude (deg)

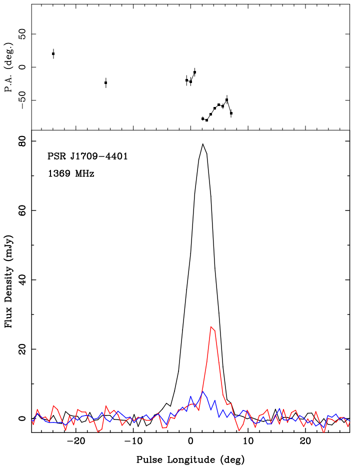
PSR J1709−4401
1369 MHz
P.A. (deg.)
50
0
−50
Flux Density (mJy)
0
20
40
60
80
−20
−10
0
10
20
Pulse Longitude (deg)

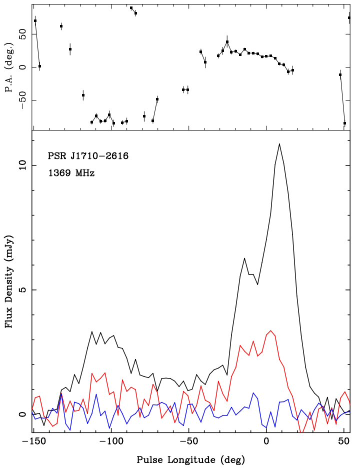
PSR J1710−2616
1369 MHz
P.A. (deg.)
50
0
−50
Flux Density (mJy)
0
5
10
−150
−100
−50
0
50
Pulse Longitude (deg)

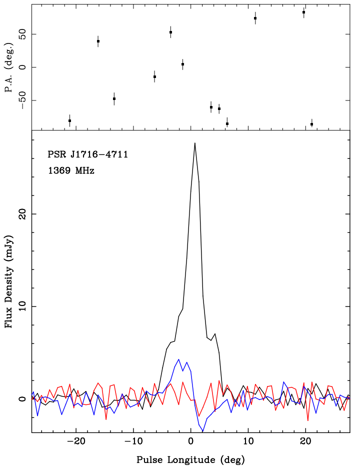
PSR J1716−4711
1369 MHz
P.A. (deg.)
50
0
−50
Flux Density (mJy)
0
10
20
−20
−10
0
10
20
Pulse Longitude (deg)

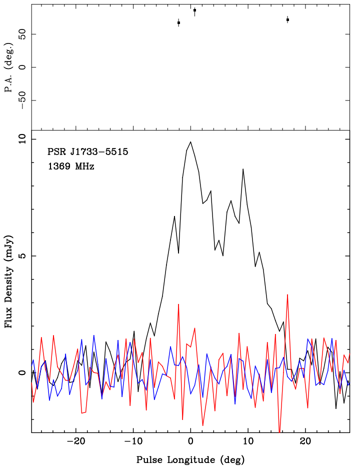
PSR J1733−5515
1369 MHz
P.A. (deg.)
50
0
−50
Flux Density (mJy)
0
5
10
−20
−10
0
10
20
Pulse Longitude (deg)

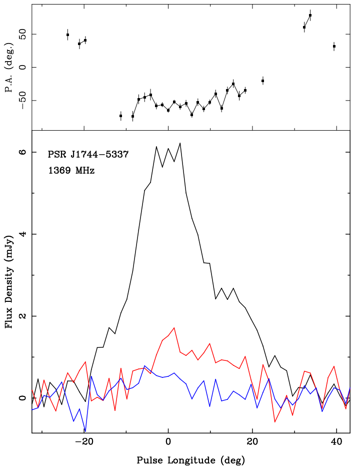
PSR J1744−5337
1369 MHz
P.A. (deg.)
50
0
−50
Flux Density (mJy)
0
2
4
6
−20
0
20
40
Pulse Longitude (deg)

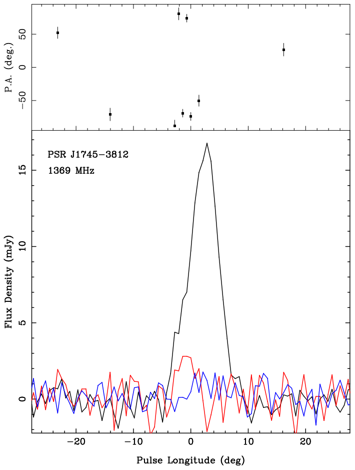
PSR J1745−3812
1369 MHz
P.A. (deg.)
50
0
−50
Flux Density (mJy)
0
5
10
15
−20
−10
0
10
20
Pulse Longitude (deg)

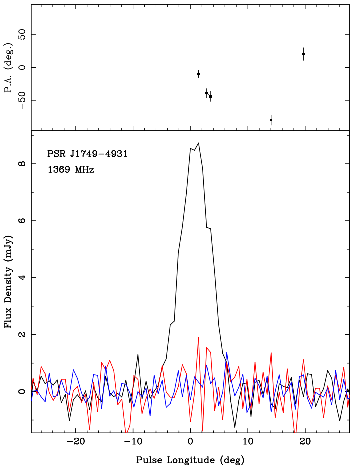
PSR J1749−4931
1369 MHz
P.A. (deg.)
50
0
−50
Flux Density (mJy)
0
2
4
6
8
−20
−10
0
10
20
Pulse Longitude (deg)

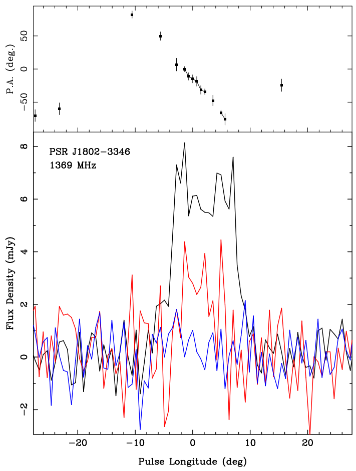
P.A. (deg.)
50
0
−50
PSR J1802−3346
1369 MHz
Flux Density (mJy)
8
6
4
2
0
−2
−20
−10
0
10
20
Pulse Longitude (deg)

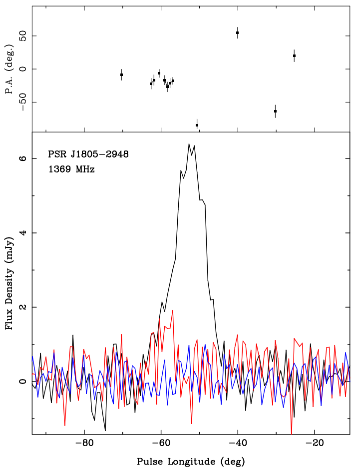
P.A. (deg.)
50
0
−50
PSR J1805−2948
1369 MHz
Flux Density (mJy)
6
4
2
0
−80
−60
−40
−20
Pulse Longitude (deg)

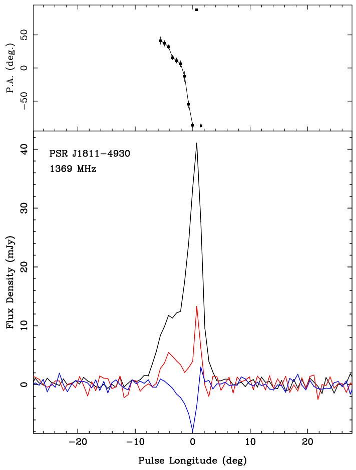
P.A. (deg.)
50
0
−50
PSR J1811−4930
1369 MHz
Flux Density (mJy)
40
30
20
10
0
−20
−10
0
10
20
Pulse Longitude (deg)

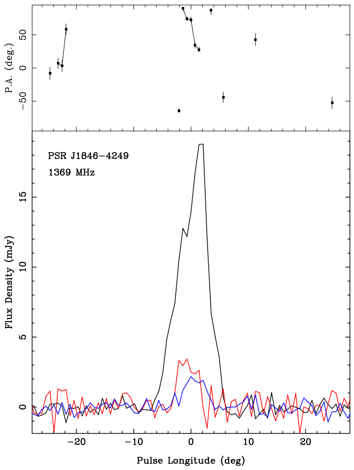
P.A. (deg.)
50
0
−50
PSR J1846−4249
1369 MHz
Flux Density (mJy)
15
10
5
0
−20
−10
0
10
20
Pulse Longitude (deg)

Appendix B

We show how we derived Equations 2.40, 2.45, 2.48.

Superposition regime, Equation 2.40 descends from Equation 2.35 if we substitute S with $A + B$:

$$\begin{aligned} C_{\text{superposed}} = & \quad \zeta^2[2\,(A+B)\otimes(A+B) - \eta(A+B)\circ(A+B)] \\ = & \quad \zeta^2[2A\otimes A + 2B\otimes B + 2A\otimes B + 2A\otimes B \\ & \quad -\eta A\circ A - \eta B\circ B - \eta A\circ B - \eta B\circ A] \\ = & \quad \zeta^2[C_{\text{A}}/\zeta_{\text{A}}^2 + C_{\text{B}}/\zeta_{\text{B}}^2 + \Xi/(\zeta_{\text{A}}\zeta_{\text{B}}) + \Xi^T/(\zeta_{\text{A}}\zeta_{\text{B}})] \end{aligned} \tag{7}$$

where:

$$\Xi = \zeta_{\text{A}}\zeta_{\text{B}}\,(2A\otimes B - A\circ B\eta) \tag{8}$$

Let us assume that the dimensionless variances for modes $\mathfrak{A}$ and $\mathfrak{B}$ are comparable and similar to ζ ($\zeta_{\text{A}} \sim \zeta_{\text{B}} \sim \zeta$) then:

$$C_{\text{superposed}} = C_{\text{A}} + C_{\text{B}} + \Xi + \Xi^T \tag{9}$$

Equations 2.45 and 2.48 do not descend from Equation 2.35. Equation 2.35 is in fact valid only if the source of signal is unique, or if more signals are superposed before being detected by the telescope receiver. Thus, its application to the composite and disjoint regimes requires further derivation.

Composite regime, Let us assume that the polarization state of a pulsar is in the composite regime, and let us focus on a single pulse from the pulsar at a defined longitude range, $\Delta\phi$. If we assume that only one of the modes, i.e. mode $\mathfrak{A}$, affects $\Delta\phi$, the Stokes vector S that we would obtain for the considered longitude range is the mean of the N samples A_i collected by the receiver during the interval $\Delta\phi$ itself:

$$\vec{S} = \frac{1}{N}\sum_{\mathrm{i}}^{N} A_\mathrm{i} \tag{10}$$

However, if both of the modes affects $\Delta\phi$, then the observed Stokes parameters are given by:

$$\vec{S} = \frac{1}{N}\left(\sum_{\mathrm{i}}^{N_\mathrm{A}} A_\mathrm{i} + \sum_{\mathrm{i}}^{N_\mathrm{B}} B_\mathrm{i}\right) \tag{11}$$

where $N = N_\mathrm{A} + N_\mathrm{B}$.

If we assume that the random samples A_i, B_i are drawn from populations $\mathfrak{A}$ and $\mathfrak{B}$ respectively, then their second order statistical characteristics are given by C'_A and C'_B. We thus have that the covariance matrix for an ensemble of Stokes vectors computed at the longitude range $\Delta\phi$ from different pulses:

$$C_\mathrm{composite} = \frac{1}{N^2}\left(N_\mathrm{A}C'_\mathrm{A} + N_\mathrm{B}C'_\mathrm{B}\right) = \frac{1}{N}\left(f_\mathrm{A}C'_\mathrm{A} + \left(1 - f_\mathrm{A}\right)C'_\mathrm{B}\right) \tag{12}$$

where $f_\mathrm{A} = N_\mathrm{A}/N$ and C'_A and C'_B are the covariance matrices of the populations A and B.

If only one mode was present at the longitude range $\Delta\phi$, then:

$$C = \frac{1}{N}C'_\mathrm{A} \tag{13}$$

or:

$$C = \frac{1}{N}C'_\mathrm{B} \tag{14}$$

If we define:

$$\begin{aligned} C_\mathrm{A} &= \frac{1}{N}C'_\mathrm{A} && (15)\\ C_\mathrm{B} &= \frac{1}{N}C'_\mathrm{B} && (16) \end{aligned}$$

then Equation 12 becomes:

$$C_\mathrm{composite} = f_\mathrm{A}C_\mathrm{A} + \left(1 - f_\mathrm{A}\right)C_\mathrm{B} \tag{17}$$

this is the final form shown in Equation 2.45.

Disjoint regime, Let us assume that the polarization state of a pulsar is in the disjoint regime, and let us focus on the same longitude range $\Delta\phi$ of a number $(N+M)$ of single pulses. Out of these $(N+M)$ impulses, N are drawn from mode $\mathfrak{A}$ population only, and M from mode $\mathfrak{B}$ population only. The mean Stokes vector is:

$$\bar{S} = \frac{NA + MB}{N+M} = F_{\mathrm{A}}A + (1 - F_{\mathrm{A}})B \tag{18}$$

where F_{A} is the fraction of mode $\mathfrak{A}$ samples present in $N+M$ impulses, and A and B are the mean Stokes parameters of mode $\mathfrak{A}$ and $\mathfrak{B}$ populations.
We recall that a possible definition of the covariance matrix C for a sample of N vectors x with mean $\bar{x}$ is:

$$C = \frac{\sum_{\mathrm{i}}^{N} x_{\mathrm{i}} \otimes x_{\mathrm{i}}}{N} - \bar{x} \otimes \bar{x} \tag{19}$$

where the brackets indicate an external product.
For Equations 18 and 19, the covariance matrix in the disjoint regime is:

$$C_{disjoint} = \frac{\sum_{\mathrm{i}}^{N} A_{\mathrm{i}} \otimes A_{\mathrm{i}} + \sum_{\mathrm{i}}^{M} B_{\mathrm{i}} \otimes B_{\mathrm{i}}}{N+M} - (\bar{S} \otimes \bar{S}) \tag{20}$$

If we assume that the random samples A_{i}, B_{i} are drawn from $\mathfrak{A}$ and $\mathfrak{B}$ respectively, and:

$$\begin{aligned} C_{disjoint} &= \frac{N\langle A \otimes A\rangle + M\langle B \otimes B\rangle}{N+M} - (\bar{S} \otimes \bar{S}) \\ &= F_{\mathrm{A}}\langle A \otimes A\rangle + (1 - F_{\mathrm{A}})\langle B \otimes B\rangle - (\bar{S} \otimes \bar{S}) \end{aligned} \tag{21}$$

where the angular brackets indicate an ensemble average. We then have that:

$$\begin{aligned} \bar{S} \otimes \bar{S} &= (F_{\mathrm{A}}\bar{A} + (1 - F_{\mathrm{A}})\bar{B}) \otimes (F_{\mathrm{A}}\bar{A} + (1 - F_{\mathrm{A}})\bar{B}) \\ &= F_{\mathrm{A}}^2(\bar{A} \otimes \bar{A}) + (1 - F_{\mathrm{A}})^2(\bar{B} \otimes \bar{B}) + F_{\mathrm{A}}(1 - F_{\mathrm{A}})(\bar{A} \otimes \bar{B} + \bar{B} \otimes \bar{A}) \end{aligned} \tag{22}$$

Replacing $F_{\mathrm{A}}^2(\bar{A} \otimes \bar{A})$ with $F_{\mathrm{A}}\langle A \otimes A\rangle - F_{\mathrm{A}}(1 - F_{\mathrm{A}})\langle A \otimes A\rangle$ we have that:

$$\begin{aligned} C_{disjoint} = {} & F_{\mathrm{A}} \quad C_{\mathrm{A}} + (1 - F_{\mathrm{A}})C_{\mathrm{B}} \\ & + \quad F_{\mathrm{A}}(1 - F_{\mathrm{A}})(A \otimes A + B \otimes B - A \otimes B - B \otimes A) \end{aligned} \tag{23}$$

thus:

$$C_{disjoint} = F_{\mathrm{A}}C_{\mathrm{A}} + (1 - F_{\mathrm{A}})C_{\mathrm{B}} + F_{\mathrm{A}}(1 - F_{\mathrm{A}})((A - B) \otimes (A - B)) \qquad (24)$$

that is the final form shown in Equation 2.48.

Bibliography

Alpar, M. A., Cheng, A. F., Ruderman, M. A., and Shaham, J. (1982). A new class of radio pulsars. *Nature*, 300:728–730.

Backer, D. C., Dexter, M. R., Zepka, A., D., N., Wertheimer, D. J., Ray, P. S., and Foster, R. S. (1997). A digital signal processor for pulsar research. *PASP*, 109:61.

Backer, D. C., Rankin, J. M., and Campbell, D. B. (1976). Orthogonal mode emission in geometric models of pulsar polarisation. *Nature*, 263:202–207.

Bailes, M., Bates, S. D., Bhalerao, V., Bhat, N. D. R., Burgay, M., Burke-Spolaor, S., D'Amico, N., Johnston, S., Keith, M. J., Kramer, M., Kulkarni, S. R., Levin, L., Lyne, A. G., Milia, S., Possenti, A., Spitler, L., Stappers, B., and van Straten, W. (2011). Transformation of a Star into a Planet in a Millisecond Pulsar Binary. *Science*, 333:1717–.

Bates, S. D., Bailes, M., Barsdell, B. R., Bhat, N. D. R., Burgay, M., Burke-Spolaor, S., Champion, D. J., Coster, P., D'Amico, N., Jameson, A., Johnston, S., Keith, M. J., Kramer, M., Levin, L., Lyne, A., Milia, S., Ng, C., Nietner, C., Possenti, A., Stappers, B., Thornton, D., and van Straten, W. (2012). The High Time Resolution Universe Pulsar Survey - VI. An artificial neural network and timing of 75 pulsars. *MNRAS*, 427:1052–1065.

Bates, S. D., Bailes, M., Bhat, N. D. R., Burgay, M., Burke-Spolaor, S., D'Amico, N., Jameson, A., Johnston, S., Keith, M. J., Kramer, M., Levin, L., Lyne, A., Milia, S., Possenti, A., Stappers, B., and van Straten, W. (2011). The High Time Resolution Universe Pulsar Survey - II. Discovery of five millisecond pulsars. *MNRAS*, 416:2455–2464.

Beskin, V. S. and Philippov, A. A. (2012). On the mean profiles of radio pulsars - I. Theory of propagation effects. *MNRAS*, 425:814–840.

Bhat, N. D. R., Cordes, J. M., Camilo, F., Nice, D. J., and Lorimer, D. R. (2004). Multifrequency Observations of Radio Pulse Broadening and Constraints on Interstellar Electron Density Microstructure. *ApJ*, 605:759–783.

Bhattacharya, D. and van den Heuvel, E. P. J. (1991). Formation and evolution of binary and millisecond radio pulsars. *Phys. Rep.*, 203:1–124.

Blanchet, L. and Damour, T. (1992). Hereditary effects in gravitational radiation. *prd*, 46:4304–4319.

Blaskiewicz, M., Cordes, J. M., and Wasserman, I. (1991). A relativistic model of pulsar polarization. *ApJ*, 370:643–669.

Born, M. and Wolf, E. (1980). *Principles of optics: electromagnetic theory of propagation ,interference and diffraction of light*. Pergamon, New York.

Boyle, L. A. and Buonanno, A. (2008). Relating gravitational wave constraints from primordial nucleosynthesis, pulsar timing, laser interferometers, and the CMB: Implications for the early universe. *prd*, 78(4):043531.

Braginskii, V. B. and Thorne, K. S. (1987). Gravitational-wave bursts with memory and experimental prospects. *nat*, 327:123–125.

Breton, R. P., Kaspi, V. M., Kramer, M., McLaughlin, M. A., Lyutikov, M., Ransom, S. R., Stairs, I. H., Ferdman, R. D., and Camilo, F. (2008). Relativistic spin precession in the Double Pulsar. *Science*.

Britton, M. C. (2000). Radio astronomical polarimetry and the Lorentz group. *ApJ*, 532:1240–1244.

Burgay, M., Bailes, M., Bates, S. D., Bhat, N. D. R., Burke-Spolaor, S., Champion, D. J., Coster, P., D'Amico, N., Johnston, S., Keith, M. J., Kramer, M., Levin, L., Lyne, A. G., Milia, S., Ng, C., Possenti, A., Stappers, B. W., Thornton, D., Tiburzi, C., van Straten, W., and Bassa, C. G. (2013). *MNRAS*. in press.

Burgay, M., D'Amico, N., Possenti, A., Manchester, R. N., Lyne, A. G., Joshi, B. C., McLaughlin, M. A., Kramer, M., Sarkissian, J. M., Camilo, F., Kalogera, V., Kim, C., and Lorimer, D. R. (2003). An increased estimate of the merger rate of double neutron stars from observations of a highly relativistic system. *Nature*, 426:531–533.

Caldwell, R. R., Battye, R. A., and Shellard, E. P. S. (1996). Relic gravitational waves from cosmic strings: Updated constraints and opportunities for detection. *prd*, 54:7146–7152.

Caraveo, P. A., De Luca, A., Mignani, R. P., and Bignami, G. F. (2001). The distance to the Vela pulsar gauged with Hubble Space Telescope parallax observations. *ApJ*, 561:930–937.

Champion, D. J., Hobbs, G. B., Manchester, R. N., Edwards, R. T., Backer, D. C., Bailes, M., Bhat, N. D. R., Burke-Spolaor, S., Coles, W., Demorest, P. B., Ferdman, R. D., Folkner, W. M., Hotan, A. W., Kramer, M., Lommen, A. N., Nice, D. J., Purver, M. B., Sarkissian, J. M., Stairs, I. H., van Straten, W., Verbiest, J. P. W., and Yardley, D. R. B. (2010). Measuring the Mass of Solar System Planets Using Pulsar Timing. *apjl*, 720:L201–L205.

Christodoulou, D. (1991). Nonlinear nature of gravitation and gravitational-wave experiments. *Physical Review Letters*, 67:1486–1489.

Clark, R. R. and Smith, F. G. (1969). Polarization of Radio Pulses from Pulsar CP 0328. *nat*, 221:724–726.

Cordes, J. M. (1978). Observational limits on the limits of pulsar emission regions. *ApJ*, 222:1006–1011.

Cordes, J. M. and Downs, G. S. (1985). JPL Pulsar timing observations. III. Pulsar rotation fluctuations. *ApJS*, 59:343–382.

Cordes, J. M., Kramer, M., Lazio, T. J. W., Stappers, B. W., Backer, D. C., and Johnston, S. (2004). Pulsars as tools for fundamental physics & astrophysics. *New Astron. Rev.*, 48:1413–1438.

Cordes, J. M. and Lazio, T. J. W. (2002). NE2001. I. A New Model for the Galactic Distribution of Free Electrons and its Fluctuations. *arXiv:astro-ph/020715*.

Cordes, J. M., Rankin, J. M., and Backer, D. C. (1978). Orthogonal modes of polarization from pulsar PSR 2020+28. *ApJ*, 223:961–972.

Crawford, F., Manchester, R. N., and Kaspi, V. M. (2001). Polarization Properties of Nine Southern Radio Pulsars. *AJ*, 122:2001–2007.

Damour, T. and Vilenkin, A. (2005). Gravitational radiation from cosmic (super)strings: Bursts, stochastic background, and observational windows. *Phys. Rev. D*, 71(6):063510.

Demorest, P. B., Ferdman, R. D., Gonzalez, M. E., Nice, D., Ransom, S., Stairs, I. H., Arzoumanian, Z., Brazier, A., Burke-Spolaor, S., Chamberlin, S. J., Cordes, J. M., Ellis, J., Finn, L. S., Freire, P., Giampanis, S., Jenet, F., Kaspi, V. M., Lazio, J., Lommen, A. N., McLaughlin, M., Palliyaguru, N., Perrodin, D., Shannon, R. M., Siemens, X., Stinebring, D., Swiggum, J., and Zhu, W. W. (2013). Limits on the Stochastic Gravitational Wave Background from the North American Nanohertz Observatory for Gravitational Waves. *ApJ*, 762:94.

Deng, X. P., Hobbs, G., You, X. P., Li, M. T., Keith, M. J., Shannon, R. M., Coles, W., Manchester, R. N., Zheng, J. H., Yu, X. Z., Gao, D., Wu, X., and Chen, D. (2013). Interplanetary spacecraft navigation using pulsars. *Advances in Space Research*, 52:1602–1621.

Detweiler, S. (1979). Pulsar timing measurements and the search for gravitational waves. *ApJ*, 234:1100.

Edwards, R. T., Hobbs, G. B., and Manchester, R. N. (2006). TEMPO2, a new pulsar timing package - II. The timing model and precision estimates. *MNRAS*, 372:1549–1574.

Einstein, A. (1916). Näherungsweise integration der feldgleichungen der gravitation. Sitz.-Ber. Preuß. Akad. Wiss., Berlin.

Ekers, R. D. and Moffet, A. T. (1969). Polarization of Pulsating Radio Sources. *apjl*, 158:L1.

Ellis, J. A., Siemens, X., and van Haasteren, R. (2013). An Efficient Approximation to the Likelihood for Gravitational Wave Stochastic Background Detection Using Pulsar Timing Data. *apj*, 769:63.

Everett, J. E. and Weisberg, J. M. (2001). Emission beam geometry of selected pulsars derived from average pulse polarization data. *ApJ*, 553:341–357.

Favata, M. (2009). Nonlinear Gravitational-Wave Memory from Binary Black Hole Mergers. *apjl*, 696:L159–L162.

Ferdman, R. D., Stairs, I. H., Kramer, M., Breton, R. P., McLaughlin, M. A., Freire, P. C. C., Possenti, A., Stappers, B. W., Kaspi, V. M., Manchester, R. N., and Lyne, A. G. (2013). *ApJ*, 767:85.

Fonseca, E., Stairs, I. H., and Thorsett, S. E. (2014). A Comprehensive Study of Relativistic Gravity Using PSR B1534+12. *apj*, 787:82.

Foster, R. S. and Backer, D. C. (1990). Constructing a pulsar timing array. *ApJ*, 361:300.

Foster, R. S., Wolszczan, A., and Camilo, F. (1993). A new binary millisecond pulsar. *ApJ*, 410:L91–L94.

Gangadhara, R. T. (1997). Orthogonal polarization mode phenomenon in pulsars. *aap*, 327.

Gangadhara, R. T., Xilouris, K. M., von Hoensbroech, A., Kramer, M., Jessner, A., and Wielebinski, R. (1999). Role of time resolution on polarization of pulsar radiation. *A&A*, 342:474–479.

Gehrels, N. (1986). Confidence limits for small numbers of events in astrophysical data. *ApJ*, 303:336–346.

Gould, D. M. and Lyne, A. G. (1998). Multifrequency polarimetry of 300 radio pulsars. *MNRAS*, 301:235–260.

Grishchuk, L. P. (2005). Relic gravitational waves and cosmology. *Phys. Uspekhi*, pages 1235–1247.

Gupta, Y. and Gangadhara, R. T. (2003). Understanding the Radio Emission Geometry of Multiple-Component Radio Pulsars from Retardation and Aberration Effects. *ApJ*, 584:418–426.

Hamaker, J. P. and Bregman, J. D. (1996). Understanding radio polarimetry. III. Interpreting the IAU/IEEE definitions of the Stokes parameters. *A&AS*, 117:161–165.

Han, J. L. and Manchester, R. N. (2001). The shape of pulsar radio beams. *MNRAS*, 320:L35–L40.

Han, J. L., Manchester, R. N., Lyne, A. G., and Qiao, G. J. (2002). Counterclockwise magnetic fields in the norma spiral arm. *ApJ*, 570:L17–L20.

Han, J. L., Manchester, R. N., Lyne, A. G., Qiao, G. J., and van Straten, W. (2006). Pulsar rotation measures and the large-scale structure of the galactic magnetic field. *ApJ*, 642:868–881.

Han, J. L., Manchester, R. N., and Qiao, G. J. (1999). Pulsar rotation measures and the magnetic structure of our Galaxy. *MNRAS*, 306:371–380.

Han, J. L. and Qiao, G. J. (1994). The magnetic field in the disk of our Galaxy. *A&A*, 288:759–772.

Harrison, E. R. and Tademaru, E. (1975). Acceleration of pulsars by asymmetric radiation. *ApJ*, 201:447–461.

Helfand, D. J., Manchester, R. N., and Taylor, J. H. (1975). Observations of pulsar radio emission. III. Stability of integrated profiles. *ApJ*, 198:661–670.

Hellings, R. W. and Downs, G. S. (1983). Upper limits on the isotropic gravitational radiation background from pulsar timing analysis. *ApJ*, 265:L39.

Hewish, A., Bell, S. J., Pilkington, J. D. H., Scott, P. F., and Collins, R. A. (1968). Observation of a Rapidly Pulsating Radio Source. *nat*, 217:709–713.

Hewish, A., Bell, S. J., Pilkington, J. D. H., Scott, P. F., and Collins, R. A. (1968). Observation of a rapidly pulsating radio source. *Nature*, 217:709–713.

Hibschman, J. A. and Arons, J. (2001). Polarization sweeps in rotation-powered pulsars. *ApJ*, 546:382–393.

Hobbs, G. (2013). The Parkes Pulsar Timing Array. *Classical and Quantum Gravity*, 30(22):224007.

Hobbs, G., Coles, W., Manchester, R. N., Keith, M. J., Shannon, R. M., Chen, D., Bailes, M., Bhat, N. D. R., Burke-Spolaor, S., Champion, D., Chaudhary, A., Hotan, A., Khoo, J., Kocz, J., Levin, Y., Oslowski, S., Preisig, B., Ravi, V., Reynolds, J. E., Sarkissian, J., van Straten, W., Verbiest, J. P. W., Yardley, D., and You, X. P. (2012). Development of a pulsar-based time-scale. *MNRAS*, 427:2780–2787.

Hobbs, G., Jenet, F., Lee, K. J., Verbiest, J. P. W., Yardley, D., Manchester, R., Lommen, A., Coles, W., Edwards, R., and Shettigara, C. (2009). TEMPO2: a new pulsar timing package - III. Gravitational wave simulation. *MNRAS*, 394:1945–1955.

Hobbs, G., Lyne, A. G., and Kramer, M. (2010). An analysis of the timing irregularities for 366 pulsars. *MNRAS*, 402:1027–1048.

Hotan, A. W., Bailes, M., and Ord, S. M. (2004a). PSR J1022+1001: profile stability and precision timing. *MNRAS*, 355:941–949.

Hotan, A. W., van Straten, W., and Manchester, R. N. (2004b). PSRCHIVE and PSRFITS: An Open Approach to Radio Pulsar Data Storage and Analysis. *PASA*, 21:302–309.

Hulse, R. A. and Taylor, J. H. (1975). Discovery of a pulsar in a binary system. *ApJ*, 195:L51–L53.

Jaffe, A. H. and Backer, D. C. (2003). Gravitational waves probe the coalescence rate of massive black hole binaries. *ApJ*, 583:616–631.

Janssen, G. H., Hobbs, G., McLaughlin, M., Bassa, C. G., Deller, A. T., Kramer, M., Lee, K. J., Mingarelli, C. M. F., Rosado, P. A., Sanidas, S., Sesana, A., Shao, L., Stairs, I. H., Stappers, B. W., and Verbiest, J. P. W. (2015). Gravitational wave astronomy with the SKA. *ArXiv e-prints*.

Jenet, F. A. and Gil, J. (2003). Using the Intensity Modulation Index to Test Pulsar Radio Emission Models. *apjl*, 596:L215–L218.

Jenet, F. A., Hobbs, G. B., Lee, K. J., and Manchester, R. N. (2005). Detecting the Stochastic Gravitational Wave Background Using Pulsar Timing. *ApJ*, 625:L123–L126.

Jenet, F. A., Lommen, A., Larson, S. L., and Wen, L. (2004). Constraining the properties of supermassive black hole systems using pulsar timing: Application to 3c 66b. *ApJ*, 606:799–803.

Johnston, S. (2004). Single pulses from PSR B1641-45. *MNRAS*, 348:1229–1235.

Johnston, S., Karastergiou, A., Mitra, D., and Gupta, Y. (2008). Multifrequency integrated profiles of pulsars. *MNRAS*, 388:261–274.

Johnston, S., van Straten, W., Kramer, M., and Bailes, M. (2001). High time resolution observations of the vela pulsar. *ApJ*, 549:L101–L104.

Johnston, S. and Weisberg, J. M. (2006). Profile morphology and polarization of young pulsars. *MNRAS*, 368:1856–1870.

Karastergiou, A. (2009). The complex polarization angles of radio pulsars: orthogonal jumps and interstellar scattering. *MNRAS*, 392:L60–L64.

Karastergiou, A. and Johnston, S. (2004). An investigation of the absolute circular polarization in radio pulsars. *MNRAS*, 352:689–698.

Karastergiou, A. and Johnston, S. (2006). Absolute polarization position angle profiles of southern pulsars at 1.4 and 3.1 GHz. *MNRAS*, 365:353–366.

Karastergiou, A. and Johnston, S. (2007). A new beam model for radio pulsars. *MNRAS*, 380:1678–1684.

Karastergiou, A., Johnston, S., and Manchester, R. N. (2005). Polarization profiles of southern pulsars at 3.1 GHz. *MNRAS*, 359:481–492.

Karastergiou, A., Roberts, S. J., Johnston, S., Lee, H., Weltevrede, P., and Kramer, M. (2011). A transient component in the pulse profile of PSR J0738-4042. *MNRAS*, 415:251–256.

Karuppusamy, R. (2011). The LEAP Hardware. In Burgay, M., D'Amico, N., Esposito, P., Pellizzoni, A., and Possenti, A., editors, *American Institute of Physics Conference Series*, volume 1357 of *American Institute of Physics Conference Series*, pages 89–90.

Keith, M. J., Jameson, A., van Straten, W., Bailes, M., Johnston, S., Kramer, M., Possenti, A., Bates, S. D., Bhat, N. D. R., Burgay, M., Burke-Spolaor, S., D'Amico, N., Levin, L., McMahon, P. L., Milia, S., and Stappers, B. W. (2010). The High Time Resolution Universe Pulsar Survey - I. System configuration and initial discoveries. *MNRAS*, 409:619–627.

Keith, M. J., Johnston, S., Bailes, M., Bates, S. D., Bhat, N. D. R., Burgay, M., Burke-Spolaor, S., D'Amico, N., Jameson, A., Kramer, M., Levin, L., Milia, S., Possenti, A., Stappers, B. W., van Straten, W., and Parent, D. (2012). The High Time Resolution Universe Pulsar Survey - IV. Discovery and polarimetry of millisecond pulsars. *MNRAS*, 419:1752–1765.

Kramer, M. (1998). Determination of the geometry of the PSR B1913+16 system by geodetic precession. *ApJ*, 509:856–860.

Kramer, M. (2004). Millisecond Pulsarsas Tools of Fundamental Physics. In Karshenboim, S. G. and Peik, E., editors, *Astrophysics, Clocks and Fundamental Constants*, volume 648 of *Lecture Notes in Physics, Berlin Springer Verlag*, pages 33–54.

Kramer, M., Bell, J. F., Manchester, R. N., Lyne, A. G., Camilo, F., Stairs, I. H., D'Amico, N., Kaspi, V. M., Hobbs, G., Morris, D. J., Crawford, F., Possenti, A., Joshi, B. C., McLaughlin, M. A., Lorimer, D. R., and Faulkner, A. J. (2003). The Parkes Multibeam Pulsar Survey - III. Young pulsars and the discovery and timing of 200 pulsars. *MNRAS*, 342:1299–1324.

Kramer, M. and Champion, D. J. (2013). The European Pulsar Timing Array and the Large European Array for Pulsars. *Classical and Quantum Gravity*, 30(22):224009.

Kramer, M., Johnston, S., and van Straten, W. (2002). High-resolution single-pulse studies of the Vela pulsar. *MNRAS*, 334:523–532.

Kramer, M., Lange, C., Lorimer, D. R., Backer, D. C., Xilouris, K. M., Jessner, A., and Wielebinski, R. (1999a). The characteristics of millisecond pulsar emission: III. From low to high frequencies. *ApJ*, 526:957–975.

Kramer, M., Stairs, I. H., Manchester, R. N., McLaughlin, M. A., Lyne, A. G., Ferdman, R. D., Burgay, M., Lorimer, D. R., Possenti, A., D'Amico, N., Sarkissian, J. M., Hobbs, G. B., Reynolds, J. E., Freire, P. C. C., and Camilo, F. (2006). Tests of General Relativity from Timing the Double Pulsar. *Science*, 314:97–102.

Kramer, M., Xilouris, K. M., Camilo, F., Nice, D., Lange, C., Backer, D. C., and Doroshenko, O. (1999b). Profile instbilities of the millisecond pulsar J1022+1001. *ApJ*, 520:324–334.

Kramer, M., Xilouris, K. M., Lorimer, D., Doroshenko, O., Jessner, A., Wielebinski, R., Wolszczan, A., and Camilo, F. (1998). The characteristics of millisecond pulsar emission: I. spectra, pulse shapes, and the beaming fraction. *ApJ*, 501:270–285.

Large, M. I., Vaughan, A. E., and Mills, B. Y. (1968). A pulsar supernova association. *Nature*, 220:340–341.

Lee, K. J., Karuppusamy, R., Liu, K., Stappers, B. W., Kramer, M., Smits, R., Purver, M. B., Janssen, G. H., and Perrodin, D. (2015). In preparation.

Levin, L., Bailes, M., Barsdell, B. R., Bates, S. D., Bhat, N. D. R., Burgay, M., Burke-Spolaor, S., Champion, D. J., Coster, P., D'Amico, N., Jameson, A., Johnston, S., Keith, M. J., Kramer, M., Milia, S., Ng, C., Possenti, A., Stappers, B., Thornton, D., and van Straten, W. (2013). The High Time Resolution Universe Pulsar Survey -VIII. The Galactic millisecond pulsar population. *MNRAS*, 434:1387–1397.

Levin, L., Bailes, M., Bates, S. D., Bhat, N. D. R., Burgay, M., Burke-Spolaor, S., D'Amico, N., Johnston, S., Keith, M. J., Kramer, M., Milia, S., Possenti, A., Stappers, B., and van Straten, W. (2012). Radio emission evolution, polarimetry and multifrequency single pulse analysis of the radio magnetar PSR J1622-4950. *MNRAS*, 422:2489–2500.

Li, X. H. and Han, J. L. (2003). The effect of scattering on pulsar polarization angle. *aap*, 410:253–256.

Liu, K., Desvignes, G., Cognard, I., Stappers, B. W., Verbiest, J. P. W., Lee, K. J., Champion, D. J., Kramer, M., Freire, P. C. C., and Karuppusamy, R. (2014). Measuring pulse times of arrival from broad-band pulsar observations. *MNRAS*, 443:3752–3760.

Liu, K., Keane, E. F., Lee, K. J., Kramer, M., Cordes, J. M., and Purver, M. B. (2012). Profile-shape stability and phase-jitter analyses of millisecond pulsars. *MNRAS*, 420:361–368.

Lommen, A. N. (2012). Pulsar Timing Arrays: No longer a Blunt Instrument for Gravitational Wave Detection. *Journal of Physics Conference Series*, 363(1):012029.

Lorimer, D. R. (2008). Binary and Millisecond Pulsars. *Living Reviews in Relativity*, 11:8.

Lorimer, D. R. and Kramer, M. (2005). *Handbook of Pulsar Astronomy.* Cambridge University Press.

Lorimer, D. R., McLaughlin, M. A., Champion, D. J., and Stairs, I. H. (2007). PSR J1453+1902 and the radio luminosities of solitary versus binary millisecond pulsars. *MNRAS*, 379:282–288.

Lyne, A., Hobbs, G., Kramer, M., Stairs, I., and Stappers, B. (2010). Switched Magnetospheric Regulation of Pulsar Spin-Down. *Science*, 329:408–.

Lyne, A. G., Burgay, M., Kramer, M., Possenti, A., Manchester, R. N., Camilo, F., McLaughlin, M. A., Lorimer, D. R., D'Amico, N., Joshi, B. C., Reynolds, J., and Freire, P. C. C. (2004). A double-pulsar system: A rare laboratory for relativistic gravity and plasma physics. *Science*, 303:1153–1157.

Lyne, A. G. and Manchester, R. N. (1988). The shape of pulsar radio beams. *MNRAS*, 234:477–508.

Lyne, A. G. and Smith, F. G. (1989). Pulsar rotation measures and the Galactic magnetic field. *MNRAS*, 237:533–541.

Lyne, A. G., Smith, F. G., and Graham, D. A. (1971). Characteristics of the radio pulses from the pulsars. *MNRAS*, 153:337–382.

Maggiore, M. (2000). Gravitational wave experiments and early universe cosmology. *Phys. Rep.*, 331:283–367.

Manchester, R. N. (1972). Pulsar rotation and dispersion measures and the galactic magnetic field. *ApJ*, 172:43–52.

Manchester, R. N., Hamilton, P. A., and McCulloch, P. M. (1980). Polarization characteristics of southern pulsars — III. 1612MHz observations. *MNRAS*, 192:153–177.

Manchester, R. N. and IPTA (2013). The International Pulsar Timing Array. *Classical and Quantum Gravity*, 30(22):224010.

Manchester, R. N. and Taylor, J. H. (1977). *Pulsars*. Freeman, San Francisco.

Manchester, R. N., Taylor, J. H., and Huguenin, G. R. (1975). Observations of pulsar radio emission II. Polarisation of individual radio pulses. *ApJ*, 196:83–102.

Matsakis, D. N., Taylor, J. H., and Eubanks, T. M. (1997). A statistic for describing pulsar and clock stabilities. *A&A*, 326:924–928.

McKinnon, M. (1997). Birefringence as a mechanism for the broadening and depolarization of pulse average profiles. *ApJ*, 475:763–769.

McKinnon, M. and Stinebring, D. (1998). A statistical model for the orthogonal modes of polarization in pulsar radio emission. *ApJ*, 502:883–897.

McKinnon, M. M. (2002). Statistical Modeling of the Circular Polarization in Pulsar Radio Emission and Detection Statistics of Radio Polarimetry. *ApJ*, 568:302–311.

McKinnon, M. M. (2003). Three-Dimensional Statistics of Radio Polarimetry. *ApJS*, 148:519–526.

McKinnon, M. M. (2004). On the Excess Dispersion in the Polarization Position Angle of Pulsar Radio Emission. *ApJ*, 606:1154–1166.

McKinnon, M. M. (2006). Orientation Angles of a Pulsar's Polarization Vector. *apj*, 645:551–555.

McKinnon, M. M. (2009). Polarization Patterns in Pulsar Radio Emission. *apj*, 692:459–469.

McKinnon, M. M. and Stinebring, D. R. (2000). The Mode-separated Pulse Profiles of Pulsar Radio Emission. *ApJ*, 529:435–446.

McLaughlin, M. A. (2013). The North American Nanohertz Observatory for Gravitational Waves. *Classical and Quantum Gravity*, 30(22):224008.

Naghizadeh-Khouei, J. and Clarke, D. (1993). On the statistical behaviour of the position angle of linear polarization. *A&A*, 274:968.

Ng, C., Bailes, M., Bates, S. D., Bhat, N. D. R., Burgay, M., Burke-Spolaor, S., Champion, D. J., Coster, P., Johnston, S., Keith, M. J., Kramer, M., Levin, L., Petroff, E., Possenti, A., Stappers, B. W., van Straten, W., Thornton, D., Tiburzi, C., Bassa, C. G., Freire, P. C. C., Guillemot, L., Lyne, A. G., Tauris, T. M., Shannon, R. M., and Wex, N. (2014). The High Time Resolution Universe pulsar survey - X. Discovery of four millisecond pulsars and updated timing solutions of a further 12. *MNRAS*, 439:1865–1883.

Noutsos, A., Johnston, S., Kramer, M., and Karastergiou, A. (2008). New pulsar rotation measures and the Galactic magnetic field. *MNRAS*, 386:1881–1896.

Noutsos, A., Karastergiou, A., Kramer, M., Johnston, S., and Stappers, B. W. (2009). Phase-resolved Faraday rotation in pulsars. *MNRAS*, 396:1559–1572.

Osłowski, S., van Straten, W., Demorest, P., and Bailes, M. (2013). Improving the precision of pulsar timing through polarization statistics. *MNRAS*, 430:416–424.

Osłowski, S., van Straten, W., Hobbs, G. B., Bailes, M., and Demorest, P. (2011). High signal-to-noise ratio observations and the ultimate limits of precision pulsar timing. *MNRAS*, 418:1258–1271.

Palfreyman, J. L., Hotan, A. W., Dickey, J. M., Young, T. G., and Hotan, C. E. (2011). Consecutive Bright Pulses in the Vela Pulsar. *apjl*, 735:L17.

Papitto, A., Ferrigno, C., Bozzo, E., Rea, N., Pavan, L., Burderi, L., Burgay, M., Campana, S., di Salvo, T., Falanga, M., Filipović, M. D., Freire, P. C. C., Hessels, J. W. T., Possenti, A., Ransom, S. M., Riggio, A., Romano, P., Sarkissian, J. M., Stairs, I. H., Stella, L., Torres, D. F., Wieringa, M. H., and Wong, G. F. (2013). Swings between rotation and accretion power in a binary millisecond pulsar. *nat*, 501:517–520.

Phinney, E. S. (2001). A Practival Theorem on Gravitational Wave Backgrounds. *e-prints (arXiv:astro-ph/0108028).*

Radhakrishnan, V. and Cooke, D. J. (1969). Magnetic poles and the polarization structure of pulsar radiation. *Astrophys. Lett.*, 3:225–229.

Radhakrishnan, V. and Rankin, J. M. (1990). Toward an empirical theory of pulsar emission: V. On the circular polarization in pulsar radiation. *ApJ*, 352:258–266.

Ramachandran, R., Backer, D. C., Rankin, J. M., Weisberg, J. M., and Devine, K. E. (2004). Effect of Quasi-Orthogonal Emission Modes on the Rotation Measures of Pulsars. *ApJ*, 606:1167–1173.

Rankin, J. M. (1983). Toward an empirical theory of pulsar emission. I. Morphological taxonomy. *ApJ*, 274:333–358.

Rankin, J. M. (1986). Toward an empirical theory of pulsar emission. III. Mode changing ,drifting subpulses and pulse nulling. *ApJ*, 301:901–922.

Rankin, J. M. (1993). Toward an empirical theory of pulsar emission. VI. The geometry of the conal emission region. *ApJ*, 405:285–297.

Ravi, V., Wyithe, J. S. B., Shannon, R. M., and Hobbs, G. (2014). Prospects for gravitational-wave detection and supermassive black hole astrophysics with pulsar timing arrays. *ArXiv e-prints*.

Rohlfs, K. and Wilson, T. L. (2000). *Tools of Radio Astronomy*. Springer-Verlag, Berlin.

Romani, R. W. (1989). Timing a millisecond pulsar array. In Ögelman, H. and van den Heuvel, E. P. J., editors, *Timing Neutron Stars*, pages 113–117.

Rybicki, G. B. and Lightman, A. P. (1979). *Radiative Processes in Astrophysics*. Wiley, New York.

Salaris, M. and Cassisi, S. (2005). *Evolution of Stars and Stellar Populations*. Wiley.

Sesana, A. (2013). Gravitational wave emission from binary supermassive black holes. *Classical and Quantum Gravity*, 30(24):244009.

Sesana, A., Barausse, E., Dotti, M., and Rossi, E. M. (2014). Linking the Spin Evolution of Massive Black Holes to Galaxy Kinematics. *apj*, 794:104.

Sesana, A., Vecchio, A., and Colacino, C. N. (2008). The stochastic gravitational-wave background from massive black hole binary systems: implications for observations with Pulsar Timing Arrays. *MNRAS*, 390:192–209.

Sesana, A., Vecchio, A., and Volonteri, M. (2009). Gravitational waves from resolvable massive black hole binary systems and observations with Pulsar Timing Arrays. *MNRAS*, 394:2255–2265.

Shannon, R. M. and Cordes, J. M. (2012). Pulse Intensity Modulation and the Timing Stability of Millisecond Pulsars: A Case Study of PSR J1713+0747. *apj*, 761:64.

Shannon, R. M., Osłowski, S., Dai, S., Bailes, M., Hobbs, G., Manchester, R. N., van Straten, W., Raithel, C. A., Ravi, V., Toomey, L., Bhat, N. D. R., Burke-Spolaor, S., Coles, W. A., Keith, M. J., Kerr, M., Levin, Y., Sarkissian, J. M., Wang, J.-B., Wen, L., and Zhu, X.-J. (2014). Limitations in timing precision due to single-pulse shape variability in millisecond pulsars. *MNRAS*, 443:1463–1481.

Shannon, R. M., Ravi, V., Coles, W. A., Hobbs, G., Keith, M. J., Manchester, R. N., Wyithe, J. S. B., Bailes, M., Bhat, N. D. R., Burke-Spolaor, S., Khoo, J., Levin, Y., Oslowski, S., Sarkissian, J. M., van Straten, W., Verbiest, J. P. W., and Want, J.-B. (2013). Gravitational-wave limits from pulsar timing constrain supermassive black hole evolution. *Science*, 342:334–337.

Shao, L., Caballero, R. N., Kramer, M., Wex, N., Champion, D. J., and Jessner, A. (2013). A new limit on local Lorentz invariance violation of gravity from solitary pulsars. *Classical and Quantum Gravity*, 30(16):165019.

Simmons, J. F. L. and Stewart, B. G. (1985). Point and interval estimation of the true unbiased degree of linear polarisation. *A&A*, 142:100.

Sofue, Y. and Fujimoto, M. (1983). A bisymmetric spiral magnetic field and the spiral arms in our Galaxy. *ApJ*, 265:722–729.

Stairs, I. H., Thorsett, S. E., and Camilo, F. (1999). Coherently-dedispersed polarimetry of millisecond pulsars. *ApJS*, 123:627–638.

Stinebring, D. R., Cordes, J. M., Rankin, J. M., Weisberg, J. M., and Boriakoff, V. (1984). Pulsar polarization fluctuations. I - 1404 MHz statistical summaries. *ApJS*, 55:247–277.

Stinebring, D. R., Cordes, J. M., Rankin, J. M., Weisberg, J. M., and Boriakoff, V. (1984). Pulsar polarization fluctuations. I. 1408 MHz statistical summaries. *ApJS*, 55:247–277.

Sudou, H., Iguchi, S., Murata, Y., and Taniguchi, Y. (2003). Orbital Motion in the Radio Galaxy 3C 66B: Evidence for a Supermassive Black Hole Binary. *Science*, 300:1263–1265.

Taylor, J. H. and Cordes, J. M. (1993). Pulsar distances and the Galactic distribution of free electrons. *ApJ*, 411:674–684.

Taylor, J. H., Manchester, R. N., and Huguenin, G. R. (1975). Observations of pulsar radio emission. I. Total–intensity measurements of individual pulses. *ApJ*, 195:513.

Taylor, J. H., Manchester, R. N., and Lyne, A. G. (1993). Catalog of 558 pulsars. *ApJS*, 88:529–568.

Thomson, R. C. and Nelson, A. H. (1980). The interpretation of pulsar rotation measures and the magnetic field of the Galaxy. *MNRAS*, 191:863–870.

Urama, J. O. and Okeke, P. N. (1999). Vela-size glitch rates in youthful pulsars. *MNRAS*, 310:313–316.

Vallée, J. P. (2005). Pulsar-based Galactic magnetic map: A large-scale clockwise magnetic field with an anticlockwise annulus. *ApJ*, 619:297–305.

van Haasteren, R. and Levin, Y. (2010). Gravitational-wave memory and pulsar timing arrays. *MNRAS*, 401:2372–2378.

van Haasteren, R., Levin, Y., Janssen, G. H., Lazaridis, K., Kramer, M., Stappers, B. W., Desvignes, G., Purver, M. B., Lyne, A. G., Ferdman, R. D., Jessner, A., Cognard, I., Theureau, G., D'Amico, N., Possenti, A., Burgay, M., Corongiu, A., Hessels, J. W. T., Smits, R., and Verbiest, J. P. W. (2011). Placing limits on the stochastic gravitational-wave background using European Pulsar Timing Array data. *MNRAS*, 414:3117–3128.

van Haasteren, R., Levin, Y., McDonald, P., and Lu, T. (2009). On measuring the gravitational-wave background using Pulsar Timing Arrays. *MNRAS*, 395:1005–1014.

van Straten, W. (2003). *High-Precision Timing and Polarimetry of PSR J0437–4715*. PhD thesis, Swinburne University of Technology.

van Straten, W. (2004). Radio Astronomical Polarimetry and Point-Source Calibration. *ApJS*, 152:129–135.

van Straten, W. (2009). The statistics of radio astronomical polarimetry: Bright sources and high time resolution. *ApJ*, 694:1413–1422.

van Straten, W. (2010). Erratum: "the statistics of radio astronomical polarimetry: Bright sources and high time resolution". *apj*, 719:985.

von Hoensbroech, A., Lesch, H., and Kunzl, T. (1998). Natural polarization modes in pulsar magnetospheres. *A&A*, 336:209–219.

von Hoensbroech, A. and Xilouris, K. M. (1997). Does Radius-to-Frequency mapping persist close to the pulsar surface? *A&A*, 324:981.

Wardle, J. and Kronberg, P. (1974). The linear polarization of quasi-stellar radio sources at 3.71 and 11.1 centimeters. *ApJ*, 194:249.

Weisberg, J. M., Cordes, J. M., Kuan, B., Devine, K. E., Green, J. T., and Backer, D. C. (2004). Arecibo 430 MHz pulsar polarimetry: Faraday rotation measures and morphological classifications. *ApJS*, 150:317–341.

Weisberg, J. M., Romani, R. W., and Taylor, J. H. (1989). Evidence for geodetic spin precession in the binary pulsar 1913+16. *ApJ*, 347:1030–1033.

Weltevrede, P. and Johnston, S. (2008). Profile and polarization characteristics of energetic pulsars. *MNRAS*, 391:1210–1226.

Xilouris, K. M., Kramer, M., Jessner, A., von Hoensbroech, A., Lorimer, D., Wielebinski, R., Wolszczan, A., and Camilo, F. (1998). The characteristics of millisecond pulsar emission: II. Polarimetry. *ApJ*, 501:286–306.

Yan, W. M., Manchester, R. N., van Straten, W., Reynolds, J. E., Hobbs, G., Wang, N., Bailes, M., Bhat, N. D. R., Burke-Spolaor, S., Champion, D. J., Coles, W. A., Hotan, A. W., Khoo, J., Oslowski, S., Sarkissian, J. M., Verbiest, J. P. W., and Yardley, D. R. B. (2011). Polarization observations of 20 millisecond pulsars. *MNRAS*, 414:2087–2100.

Yardley, D. R. B., Coles, W. A., Hobbs, G. B., Verbiest, J. P. W., Manchester, R. N., van Straten, W., Jenet, F. A., Bailes, M., Bhat, N. D. R., Burke-Spolaor, S., Champion, D. J., Hotan, A. W., Oslowski, S., Reynolds, J. E., and Sarkissian, J. M. (2011). On detection of the stochastic gravitational-wave background using the Parkes pulsar timing array. *MNRAS*, 414:1777–1787.

Yu, M., Manchester, R. N., Hobbs, G., Johnston, S., Kaspi, V. M., Keith, M., Lyne, A. G., Qiao, G. J., Ravi, V., Sarkissian, J. M., Shannon, R., and Xu, R. X. (2013). Detection of 107 glitches in 36 southern pulsars. *MNRAS*, 429:688–724.

Acknowledgements

I am grateful to a handful of people that I consider my "scientific mentors" and helped me through these years (in a chronological order of interaction!): Dr. Andrea Possenti, Dr. Simon Johnston, Dr. Willem van Straten, Dr. Stefan Oslowski, Dr. George Hobbs.

There is a huge number of people that have been directly part of my “PhD world” that I would like to thank personally. The reasons may take several pages, but I’m feeling merciful: I’ll spare the reader. Thanks to the OAC group, especially Dr. Noemi Iacolina, Dr. Sabrina Milia, Dr. Andrea Saba, Mauro Pili and Dr. Silvia Casu. A special thanks to Alessandro "Aho" Ridolfi. Thanks to the PPTA team that warmly welcomed me onboard and thought me great science and heavy ping pong. A mention to Dr. Jim Casdwell, an old time gentlemen that I’m honored to have known. Thanks to Dr. Cherry Ng, to the kind and helpful "angels" of the Parkes radio telescope, John Sarkissian, Brett Preisieg, Harold the sheep.

Out of the scientific environment, my thanks are going to very obvious people. Thanks to my boyfriend, Roberto. I don’t think I would have started the PhD if it wasn’t for him. And as I would really like to give him long-term, daily-based annoyances, well, I hope that it won’t take long to eventually be at least in the same continent. mh!

Thanks to my parents and family, who never missed to give me advices and love.

Thanks to my friend in the always beloved Emilia Romagna, and many other friends that are spread around the world.